High-Power Target Development for Accelerator-Based Neutron Capture Therapy

by

Brandon William Blackburn

M.S. Nuclear Engineering (1997)
Massachusetts Institute of Technology

B.S. Nuclear Engineering (1995)
Texas A&M University

Submitted to the Department of Nuclear Engineering in
Partial fulfillment of the requirements for the degree of
Doctor of Philosophy in Nuclear Engineering

At the

Massachusetts Institute of Technology

February 2002

©2002 Massachusetts Institute of Technology
All rights reserved

MASSACHUSETTS INSTITUTE OF TECHNOLOGY
DEC 0 5 2003
LIBRARIES

Signature of Author.....
Department of Nuclear Engineering

Certified by.....
Jacquelyn C. Yanch
Professor of Nuclear Engineering and
Whitaker College of Health Sciences and Technology
Thesis Supervisor

Read by.....
Dr. Robert E. Klinkowstein
Newton Scientific Inc.
Thesis Reader

Accepted by.....
Professor Jeffrey Coderre
Chairman, Department Committee on Graduate Students

ARCHIVES

MIT Libraries
Document Services

Room 14-0551
77 Massachusetts Avenue
Cambridge, MA 02139
Ph: 617.253.5668 Fax: 617.253.1690
Email: docs@mit.edu
http://libraries.mit.edu/docs

DISCLAIMER OF QUALITY

Due to the condition of the original material, there are unavoidable flaws in this reproduction. We have made every effort possible to provide you with the best copy available. If you are dissatisfied with this product and find it unusable, please contact Document Services as soon as possible.

Thank you.

Some pages in the original document contain color pictures or graphics that will not scan or reproduce well.

High-Power Target Development for Accelerator-Based Neutron Capture Therapy

by

Brandon William Blackburn

Submitted to the Department of Nuclear Engineering
on January 25, 2002
in partial fulfillment of the requirements for the degree of
Doctor of Philosophy in Nuclear Engineering

Abstract

The production of clinically sufficient dose rates in Accelerator-based Neutron Capture Therapies (ABNCT) requires targets that can withstand ion beams of 2-10 kW or higher. Designing such a target requires knowledge of the current density profile which can exceed 1 mA/cm^2. A method has been developed to quantify the two-dimensional current intensity by utilizing the positrons emitted from the products of either the ^{12}C(d,n) or ^{11}B(p,n) reaction. A desktop scanner was used to convert the dose profile measured with MD-55-2 radiochromic film into a map of beam current intensity. Analytic calculations coupled with Monte Carlo methods determined the resolution of this technique to be 0.22±0.01 mm. Liquid gallium metal was investigated as a possible coolant. Qualitative and quantitative comparisons between single submerged impinging jets of liquid gallium and water at low flowrates were supplemented with computational fluid dynamics. Experiments using an array of submerged jets were conducted to determine area-averaged Nusselt number correlations for water and gallium over a Reynolds number range of 7000<Re<38000. The spreading factor, β_{max}, was introduced into the gallium correlation to account for surface wetting effects. Area-averaged heat transfer coefficients, $\bar{h}$, produced by an array of gallium jets were found to exceed those of water for Re>13500. At a Reynolds number of 35000 an $\bar{h}$ of 10^5 W/m^{2}K was measured with the gallium array compared to 5.5×10^4 W/m^{2}K for water. Simulations of the thermal and mechanical stresses found that a gallium-cooled beryllium target could withstand beam powers of up to 20.2 kW. Because of its low melting-point, lithium targets were able to achieve 10 kW only if the beam power density was kept below 11.6 MW/m^2. No significant difference in figures of merit used to characterize neutron beams for ABNCT were found when water was replaced by liquid gallium as the cooling fluid.

Thesis Supervisor: Jacquelyn C. Yanch
Title: Professor of Nuclear Engineering and Whitaker College of Health Sciences and Technology

Thesis Reader: Dr. Robert E. Klinkowstein
Title: Director of Research and Development at Newton Scientific Inc. (NSI)

Acknowledgements

It would be impossible for me to acknowledge all the people with whom I have worked, played, studied, agonized, and celebrated during my years at M.I.T. I can say without reservation that if it were not for Professor Yanch, none of this would have been possible. I would not be receiving a degree if it were not for her willingness to help me out. She is not only a fantastic advisor and mentor, but she is also a true friend. It has been an honor and a privilege to work with her. In addition, it has been a wonderful experience working with and getting to know Rachel Batista. I'm sure I drove her crazy during the writing of my thesis, but she was always willing to take time out and talk. She was always there to offer and helping hand, a listening ear, or a compassionate heart. Over the past year I needed each of those from her and she always knew exactly which one I needed at the time.

David Chichester has been and continues to be one of my closest friends. We both came to M.I.T at the same time and our mutual interests drew us together from the very beginning. During your life, there are only a handful of people that you meet whom you would trust with your life. David is one of those individuals. His integrity, loyalty, intellect, and honesty are without question. The same can be said of David Campos whom I have known longer than just about anyone. I will always remember the fact that during the last months of writing my thesis, Campos remembered to call me every week just to make sure I was OK. That meant a great deal. I would also like to mention my roommate of the past three years, David Gierga. In many ways we came from completely opposite worlds and went about life in different ways, but I have always respected the manner in which he approached his work and personal life. Whether he realizes it or not, I have learned a great deal from my three years of living with DPG.

There are a number of faculty and staff who have assisted me during my time at M.I.T. I would like to extend a special thank you to Dr. John Bernard, Dr. Richard Lanza, Prof. Kim Molvig, and Prof. Neil Todreas. Dr. Bernard was especially instrumental during my time of studying and preparing for the doctoral exam. Many students, including myself, owe him a great deal for his willingness to help with the test preparation. I also have to thank Dr. Bob Klinkowstein from Newton Scientific, who happens to be one of the smartest individuals I know.

I have been fortunate to be a part of a wonderful group of students at LABA. I would especially like to mention Haijun Song, Jo O'Meara, Susan White, Ray Albritton, Mark Sitek, Mike Folkert, and Jingli Liu. Ray is one of the most unselfish individuals I have ever met. If it were not for him and Mike Folkert, I might not have finished my thesis. During a time when they had plenty of their own stuff to do, they spent several hours on the Monday before my defense saving my computer, which had picked a most inopportune time to die. Somehow they managed to resurrect it from the dead. Thanks guys!!!

Mom and dad, you have always been there for me. No one in this world has prayed more, fought harder, given support, and believed in me like you guys. Thank you for always setting a Godly example for Skoo and I. Both of you are truly a blessing and a gift from God. Thank you Skoo, KP, Kel, Stacy, Mimi, Morgan, Mason, Preston, and Parker for always being supportive and encouraging. I realize that if it were not for your prayers, encouragement, and love I could not have gotten this far.

Beatka, Moja Kochana, it is fitting that this chapter of my life closes with thoughts of you. You truly are the light and love of my life. Words are not adequate to express how much I cherish you. Your compassion, energy, honesty, beauty, intelligence, and devotion astound me day after day. Each day I grow to love you more and more. As I often like to tell you....I love you immensely!!! I know its probably not the proper Polish, but....Kocham ciebie na zawsze!

Table of Contents

List of Figures

List of Tables

Chapter 1 Introduction and Presentation of the Problem

1.1 Introduction to High-Power Target Development

Accelerator-Based Boron Neutron Capture Therapy (ABNCT) is a two-part procedure that uses neutrons to irradiate tissue which has been loaded with ^{10}B. Neutrons which are produced through charged-particle reactions are then moderated to energies which increase the probability of capture in the ^{10}B-loaded tissue. In the case of Boron Neutron Capture Therapy (BNCT)[1-8] the tissue of concern could be a cancerous tumor, such as a glioblastoma multiforme.[4, 9, 10] For Boron Neutron Capture Synovectomy (BNCS)[11-16], inflamed synovium tissue caused by rheumatoid arthritis would be the targeted tissue. Capture of a neutron leads to the $^{10}B(n,\alpha)^7Li$ reaction which releases two heavy charged particles that deposit their energy in a very short distance. If the ^7Li produced in the reaction goes immediately to the ground state, the alpha particle and lithium nucleus share the 2.79 MeV released. In this case, the alpha will have an energy of 1.47 MeV and a range in tissue of 9.9 μm. The lithium nucleus, on the other hand, will carry away the remaining 0.84 MeV and travel a distance of 5.4 μm. When the $^{10}B(n,\alpha)^7Li$ reaction leads to the excited state, however, emission of a 478 keV photon leaves only 2.31 MeV available for the alpha and lithium nucleus. In both cases, however, the range of the products in tissue is less than the dimension of a cell. Damage caused by the delivery of dose to the tissue is intended to lead to cell death. Because the range of the alpha particle and lithium nucleus are so short, healthy tissue surrounding the affected cell is spared.

The rate at which dose can be delivered to the targeted tissue is directly proportional to the flux of useful neutrons at the patient position. Generation of a dose rate sufficient to allow reasonable therapy times, therefore, is directly dependent on the ability of the neutron producing target to withstand bombardment of charged-particle beams of up to 2-10 kW or higher.[2, 4-8, 13, 14] Figure 1-1 illustrates a simplified flow chart which highlights the individual components of neutron capture therapy. This figure helps to illustrate the need for high-power targets in ABNCT. At a fixed beam energy (E), the amount of beam power (Q) produced by the accelerator is the product of the current (I) and energy, $Q = I \bullet E$. Since the beam is completely stopped in the target, the amount of power which must be removed in steady-state is equal to Q. It follows, therefore, that the amount of neutrons produced is linearly proportional to the amount of current on target multiplied by the thick target yield. More power on target produces a greater amount of neutrons which translates to a larger dose rate at the patient position.

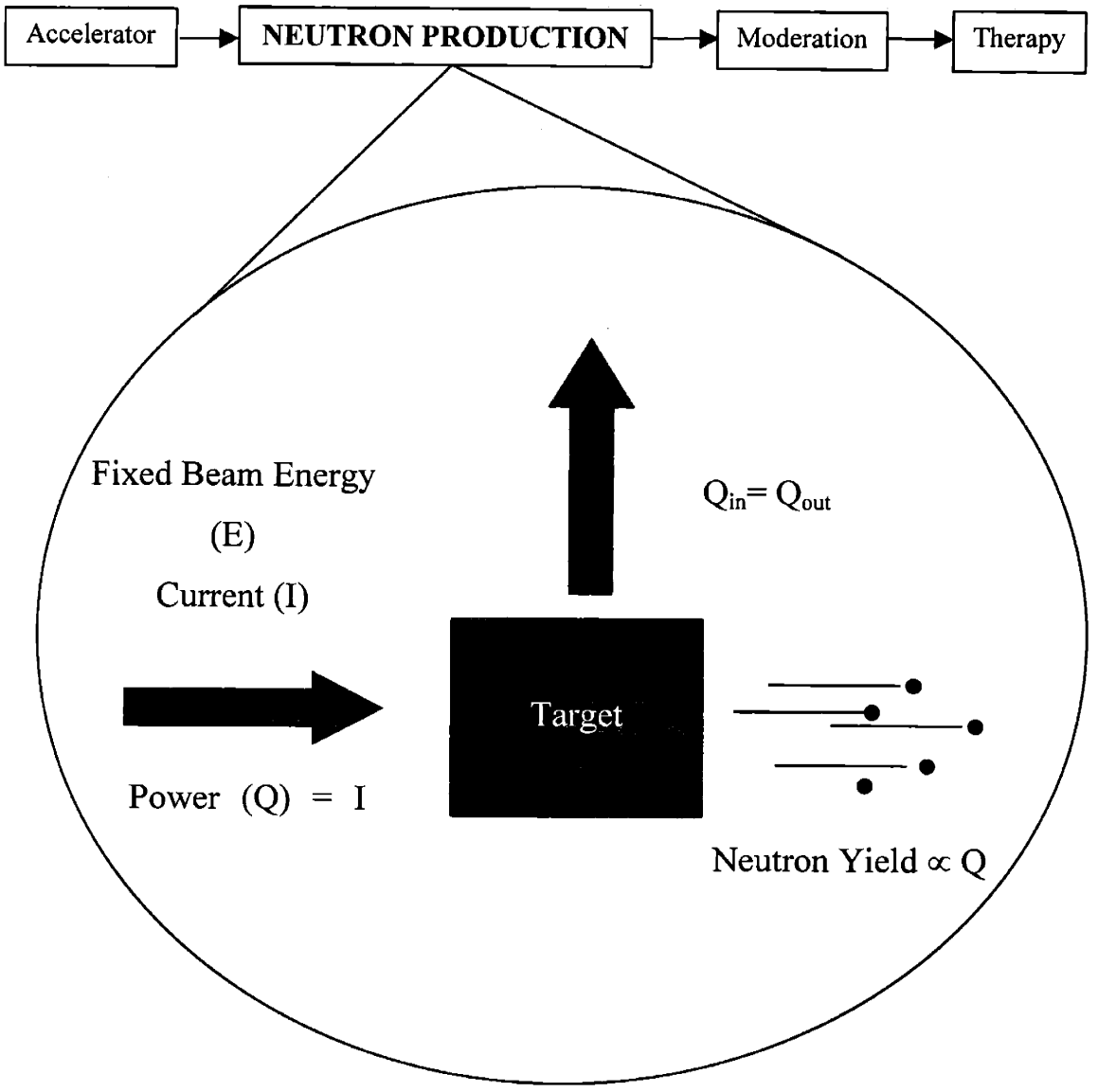

Figure 1-1. Representation of the steps required for ABNCT which illustrate the relationship between the beam power on target and the production of neutrons.

Successful development of a high-power neutron-producing target for neutron capture therapy (NCT) requires that certain fundamental problems encompassing different engineering disciplines be solved. These can be broken down into two general areas: (1)theoretical neutronic optimization of a moderator reflector assembly (MRA); (2)thermal/mechanical engineering of an integrated target/MRA and the resulting neutronics. Although several different research groups have investigated accelerator-NCT, the area of target development has not been, to any significant extent, systematically studied.[6,17-18] To date, the majority of work regarding accelerator-NCT targets has been primarily simulation studies directed at optimizing the

composition and dimensions of the MRA for neutronic purposes. It is the goal of this thesis to investigate both the engineering and neutronic aspects of integrating a target and MRA in an accelerator-NCT system.

When accelerator-BNCT was initially proposed, the problem of how to efficiently moderate a beam of fast neutrons down to a useful therapeutic range was treated extensively while thermal/mechanical issues were given only passing mention. As a result, many of the initial system designs presented significant engineering problems with regards to integrating a working target system into the MRA. Because of this decoupled approach toward the neutronic and thermal hydraulic problem, many of the initial neutronic designs were shown to be flawed when it came to implementing the target into a complete accelerator-NCT system. For example, one of the earliest studies to look at the coupled problem first optimized the neutronics for a target which had a diameter of 5 cm. Simple calculations, however, indicated that it was not possible to maintain target integrity unless the target diameter was increased to 25 cm.[19] This increase would therefore require totally different optimization of the neutronics. Likewise, a 1998 study quoted an epithermal flux based on target bombardment at a certain current level. Simulations of the target temperature, however, indicated that the target could not be kept from melting unless current levels were reduced by over 60%.[20]

Proper understanding of the various issues involved in target design requires a basic description of the various components involved in a complete accelerator-NCT system. Although the bulk of the following description applies to the Laboratory for Accelerator Beam Applications (LABA) accelerator facility, enough generality is included so that applications can be made to other types of accelerator facilities.

1.2 Components of an Accelerator-NCT System

There are three basic components which must be integrated into a completed accelerator-NCT system (as shown in Figure 1-2): (1) the accelerator, (2) neutron-producing target and associated cooling system, and (3) a moderator/reflector assembly (MRA). An accelerator produces a beam of charged particles, usually protons or deuterons, which can have current levels of a few milliamperes and energies of a few MeV. The accelerator in service at LABA is designed to generate currents in excess of 2 mA at energies up to 4.1 MeV.

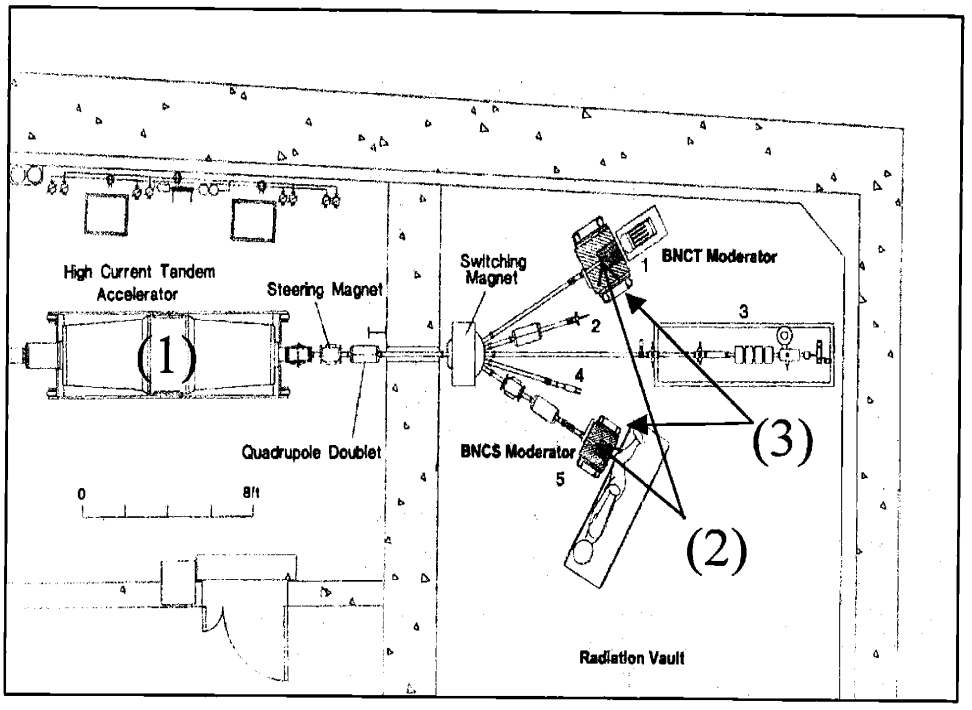

Figure 1-2. Illustration of a complete accelerator-NCT system (beams 1 and 5) in operation at LABA. The three components of the system are shown: (1) accelerator (2) neutron-producing target (3) MRA. The cooling system associated with the target is not shown.

Once the charged particle beam exits the accelerator, it must be focused and steered toward the neutron-producing target by a series of external optical components. The LABA accelerator uses three optical components in order to steer and focus beam. Two of the components, a beam steering magnet and a focusing quadrupole doublet, are located directly after the accelerator itself, while the third component, a switching magnet, is located in the radiation vault area. Figures 1-3 and 1-4 illustrate the various optical components of the LABA accelerator.

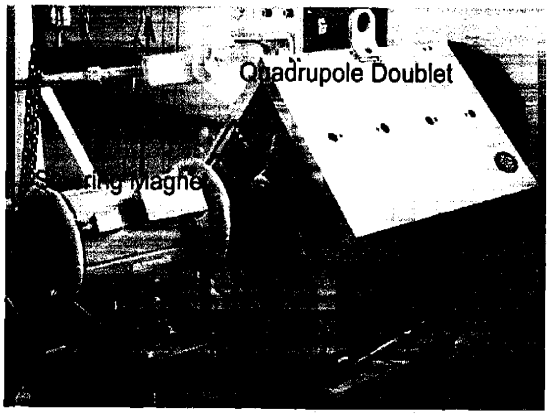

Figure 1-3. Photograph of the beam steering magnet and quadrupole doublet

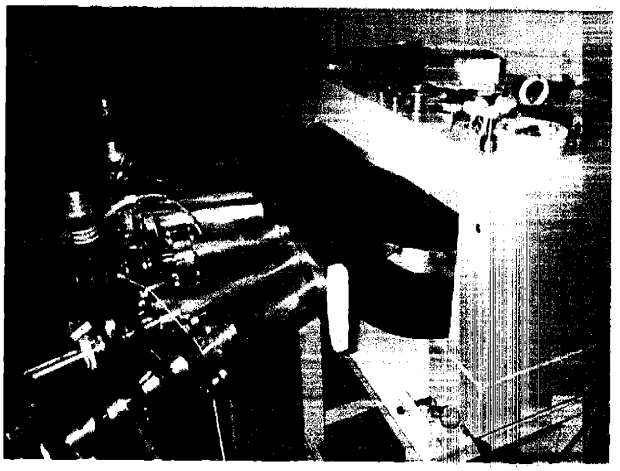

Figure 1-4. Switching magnet used to direct beam to one of five separate target locations.

Having been focused by the optical components, the beam must strike a neutron-producing target in order to generate the required flux. With beam energies limited to around 4 MeV, the targets must be constructed of low-Z materials which have (p,n) or (d,n) cross sections sufficient to produce a large neutron flux. Since the ultimate goal of an accelerator-NCT system is to produce a large neutron flux which has an energy spectrum tailored to the therapy being considered, the target must be housed in a moderator/reflector assembly (MRA). The two moderator/reflector assemblies used at LABA are shown in Figure 1-5. Upon irradiation, targets are subjected to heat loads which result from stopping of the charged particle beam. Total beam power (Q_{beam}) which must be removed from the target can be calculated simply by multiplying the beam energy (E_{beam}) by the beam current (I_{beam}).

$$Q_{beam} = I_{beam} E_{beam} \tag{1.1}$$

Removal of this heat load must be accomplished by the target cooling system. Not only must the cooling system be sufficient to remove enough heat to keep the target thermally and mechanically stable, it must also be capable of being installed into the MRA without detrimentally affecting the neutronics of the system. Successful implementation of either BNCS or BNCT as a clinical modality requires integration of all three components of an accelerator-based system. The accelerator must produce the required beam current at the proper energy. This beam must then be converted into neutrons by the target material which must be kept thermally stable by the target cooling system. Finally, a useful neutron beam can be created only by placing the complete target assembly into a moderator/reflector.

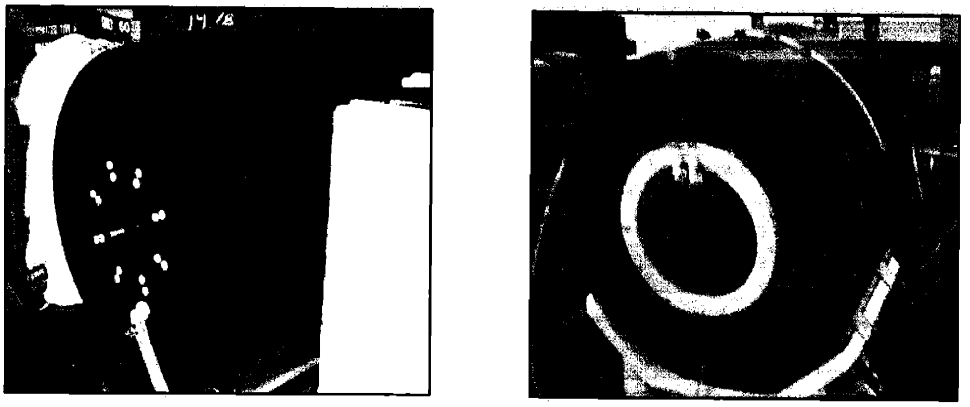

Figure 1-5. Graphite (left) and lead (right) reflectors with D_2O moderators located in LABA facility.

1.3 Neutronics of Accelerator-NCT

The primary function of an accelerator-NCT system is to convert a beam of charged particles into a flux of neutrons which exit the MRA at the patient position with an energy spectrum tailored to the specific type of therapy. Although this final energy spectrum will vary depending on the type of therapy, every ion-beam/target combination produces a unique spectrum of neutrons which depends on target material, charged particle species, and incoming particle energy. When investigating possible reactions for accelerator-NCT, certain characteristics such as yield, average and maximum neutron energy, prompt photons, and angular distribution are important. Table 1-1 lists a number of the most prominently studied neutron producing reactions.

Table 1-1. Several proposed BNCT reactions including beam energy and yield.[4, 21-23]

Reaction (ion beam energy)	Yield (n / s-mA)	Maximum Neutron Energy
$^{7}Li(p,n)^{7}Be$ (2.5 MeV)	8.96×10^{11}	800 keV
$^{9}Be(p,n)^{9}B$ (3.7 MeV)	7.77×10^{11}	1.9 MeV
$^{9}Be(p,n)^{9}B$ (4.0 MeV)	1.51×10^{12}	2.2 MeV
$^{9}Be(d,n)^{10}B$ (1.5 MeV)	3.3×10^{11}	>7 MeV
$^{9}Be(d,n)^{10}B$ (2.6 MeV)	1.0×10^{12}	>8 MeV
$^{12}C(d,n)^{13}N$ (1.5 MeV)	6.0×10^{10}	1.5 MeV
$^{13}C(d,n)^{14}N$ (1.5 MeV)	1.9×10^{11}	>6 MeV

It is widely agreed that the most desirable neutron producing reaction for both BNCT and BNCS is $^{7}Li(p,n)^{7}Be$ at proton energies of around 2.5 MeV. It has a very high yield and a soft spectrum which requires little moderation to bring the neutron energy down into the therapeutic range. As a result, most of the initial studies into accelerator-NCT based beam optimizations on a solid lithium target. The other candidate reactions based on beryllium have been shown to be

feasible, but they generally suffer from higher fast neutron doses due to harder neutron spectra. Regardless of the reaction, however, none are suitable for use in capture therapy without the neutrons first being reduced from fast to lower energies by a moderator reflector assembly.

To create a usable beam, a target constructed of these materials must be housed within a moderator reflector assembly (MRA). The MRA structure is a cylindrical structure consisting of a moderating material surrounded by an outer layer of neutron-reflecting material. As a moderator, it lowers the energy of the source neutrons from several hundred keV or even a few MeV down to (0.025eV-10 keV)[13, 14] for BNCS or (1eV-100keV)[3, 6, 17, 24] for BNCT. A successful MRA must moderate neutrons, have a large isotropic scattering cross section, and have a low (n,γ) cross section. Because the moderation of neutrons causes loss due to absorption or scattering, the moderating material should be composed of low-Z materials which moderate quickly yet have small capture cross sections. Choices for moderator material have included aluminum oxide (Al_2O_3), beryllium oxide (BeO), titanium deuteride (TiD_2), magnesium oxide (MgO), light water, and heavy water.[3, 22] Due to the fact that it is a good moderator and has a low (n,γ) cross section, heavy water has been extensively used as the moderator material for accelerator-NCT studies.

Neutrons which would otherwise be lost due to leakage from the side of the moderator are conserved by the reflector material which surrounds the moderator. Satisfactory reflector materials should have a large scattering cross-section which is isotropic in the laboratory frame. Such a cross section allows for an equal probability that the neutron is scattered back in the direction of the moderator as opposed to scattering deeper into the reflector. The reflector material should also not produce photons either as a result of inelastic scattering or upon neutron capture since extraneous photons will add unnecessary background dose. Heavy materials such as lead serve two purposes when placed around the moderator. Because it is a high-Z element, the scattering cross section is nearly isotropic in the laboratory frame of reference. Secondly, lead is a good photon shield and produces few additional contaminating photons due to neutron capture. The original MRA reflector assembly constructed at LABA used a lead reflector surrounding a D_2O moderator. Subsequent beam optimization showed that graphite could also be a good reflecting material. Originally it was thought that graphite was too moderating to be used as a reflector, but it was shown that by optimizing the moderator size and reflector dimension, graphite could produce a useful therapeutic beam for BNCS.[3, 14] The second MRA built for the LABA facility consisted of a graphite reflector surrounding a heavy-water moderator.

Although several different research groups have proposed MRA's which differ slightly in composition and arrangement, the general size and layout are quite similar. Figure 1-6 depicts the cross-section of a typical MRA, while comparisons of dimensions from three different research groups are given in Table 1-2.

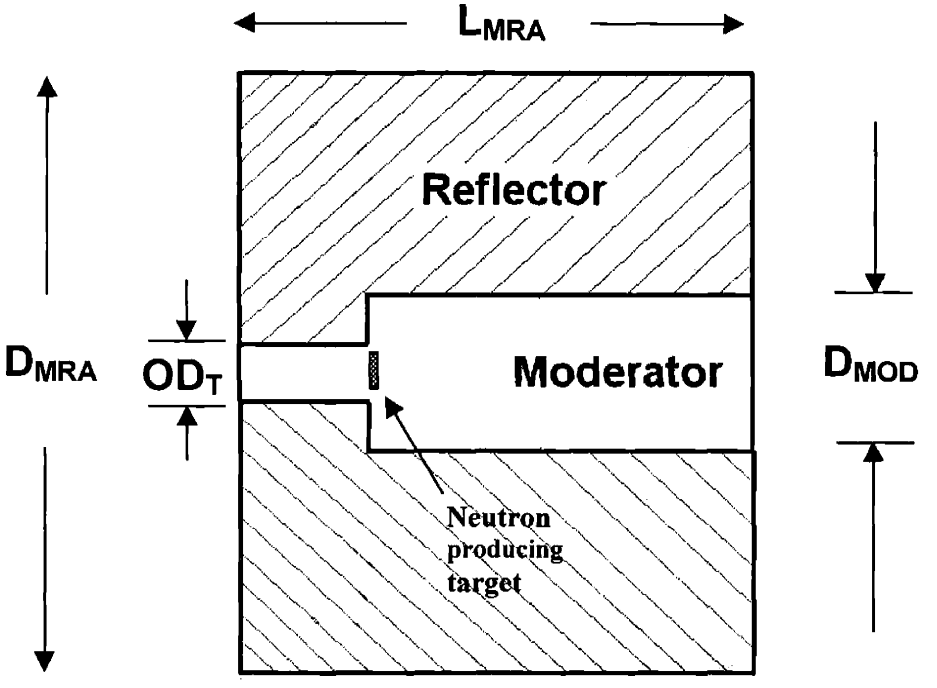

Figure 1-6. Cross-section of a typical MRA and some of the critical dimensions. The relative position of the target inside the MRA is also illustrated.

Table 1-2. Dimensions of moderators proposed by various research groups investigating accelerator-NCT.[7,24]

Research Group	D_{MRA} (cm)	L_{MRA} (cm)	D_{MOD} (cm)	OD_T (cm)
MIT LABA	56	48	20	9
Berkeley	85	65	25	10
Univ. Birmingham	55-60	N/A (orthogonal beam)	25	6

1.4 The Problem Statements

The balance between neutronics, thermal hydraulics, and structures completely bounds the problem of target development for accelerator-NCT. Targets must first produce enough neutrons when irradiated by a suitable ion beam. This beam should be as large as possible to spread the heat load, but still must remain small so that no unnecessary neutrons are lost. Because the ion beam generates heat as it is stopped, a cooling system must be designed which keeps the target thermally and mechanically stable. This entire cooled target-assembly must be integrated into the moderator/reflector assembly in order to lower the neutron energy for use in therapy. Integration, however, must be done in such a way as not adversely effect the neutron beam either by reducing the flux or altering the desired energy spectrum. Subsequent sections of this chapter will define the thermal/mechanical and neutronic problems encountered in integrating a target in an MRA.

1.4.1 Ion Beam Current Density Measurement and Reconstruction

In order to arrive at the dimensions given in Table 1-2, extensive optimization studies have been conducted in order to design MRA's which provide properly tailored neutron beams using both lithium and beryllium as the target material. In these studies, however, the targets used in the MCNP simulations were modeled as ideal neutron sources produced by uniformly distributed ion beams.[3, 19, 24, 25] Real beams, however, will certainly not be spatially uniform. Ion beam profiles will generally have Gaussian profiles which can vary substantially from irradiation to irradiation due to changes in accelerator parameters or optical components.

Accurate predictions of both the thermal and neutronic performance of a high current target, depend on having accurate information on both the size and current density of the incoming beam. Obtaining such information is complicated by the fact that beam currents can range from several hundred μA to as many as 1-2 mA for BNCS[13, 14], and from 4-50 mA for BNCT.[3, 8, 24] Beams which have energies of a few MeV and currents in the milliampere range cannot be investigated by standard profiling techniques such as helical wire beam profilers, quartz windows, or scintillators. Beam profiling equipment is generally limited to current levels in the 10's of μA.[26] Some beam profiling harps which consist of a grid of thin meshed wires can handle current levels up to 100 μA.[27] Quartz windows or scintillators can be used at current levels less than 10 μA, but give no detailed information on current density.

Determining information such as beam size or current density requires that a technique be developed which will allow interrogation at current levels which are typical of BNCS and BNCT. Information gained can then be used to accurately reconstruct the beam profile for use in

predicting both the thermal and neutronic performance of the target. Once developed, this process will allow detailed beam information to be derived at current levels not previously possible.

The technique being developed to image high current beams involves a short deuteron irradiation of a ^{12}C target to produce ^{13}N, a positron emitter. The β^+ emitter has a half-life of 9.97 minutes with a maximum positron energy of 1.19 MeV. Positrons created during this irradiation are then used to image the beam with MD-55 Gafchromic Dosimetry Media.[28] Once this film has been exposed to the target, it is scanned using a standard desktop image scanner which produces a grayscale image of the exposed film. This grayscale image can then be processed with software such as MATLAB, to generate an image of the beam. MCNP is also being used to determine the resolution accuracy of the technique which can be affected by scattering, background radiation, and uneven energy deposition in the film by the positrons.

1.4.2 Thermal and Mechanical Considerations

As noted previously, initial research regarding the viability of accelerator-NCT focused on the use of pure lithium. Neutron production from the lithium reaction is high, and the relatively soft energy spectrum requires less moderation than that produced using a beryllium target. Neutrons produced through any of the beryllium reactions at bombarding energies sufficient to obtain the same yield are more energetic and require more moderation than the lithium produced neutrons, resulting in a lower epithermal neutron flux at the patient position. Despite the need for increased moderation, beryllium has become an attractive alternative for accelerator-NCT targets because of its superior thermal and mechanical properties. Lithium, however, remains the preferred target material from a neutronic standpoint. Both materials will be investigated in this thesis.

Based on estimates of current levels needed for therapy, 1-2 kW (for BNCS) to 10kW or more (for BNCT) could be encountered and must therefore be removed efficiently in order to keep a target at sufficiently low temperatures. Removing total powers of these magnitudes from an accelerator-NCT target is hindered primarily by two factors: (1) size and distribution of the ion beam and (2) the confining nature of the MRA which must entirely surround a target and its associated cooling system. These factors give rise to both thermal and mechanical constraints which will be addressed in this thesis.

1.4.2.1 Thermal Considerations

Consider a 2.5 mA beam of protons which has an energy of 4.0 MeV striking a beryllium target as shown in Figure 1-7.

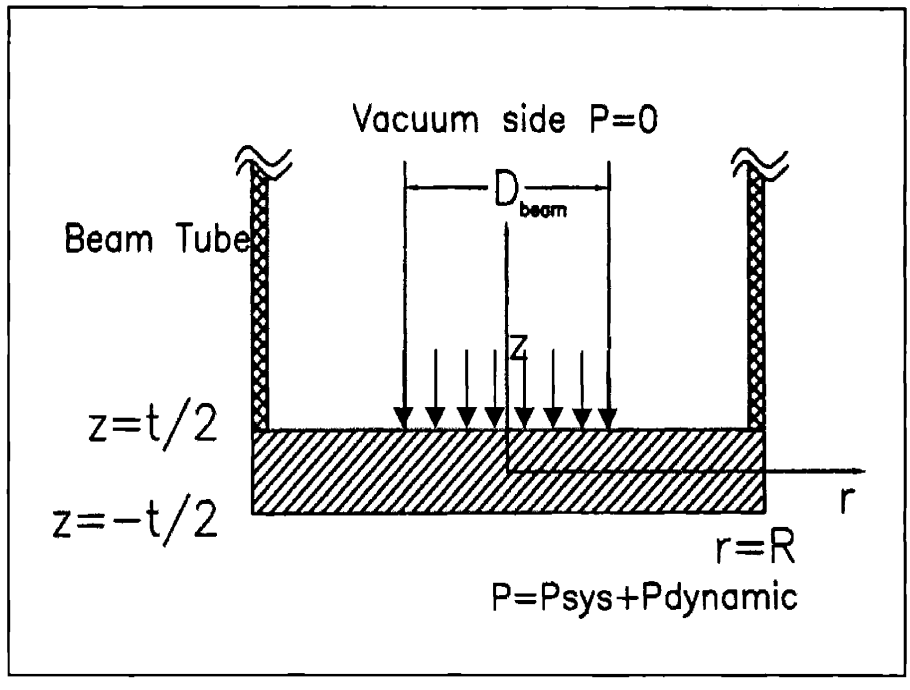

Figure 1-7. Schematic of a beryllium target (single cross-hatch)being irradiated by an ion beam.

The beam is assumed to have a radius (R) of 2.5 cm (D_{beam}=5 cm) and a standard deviation (σ_{beam}) of 1 cm. For ion beams it is typical to assume that 95% is located within $2.5\sigma_{beam}$ of the centerline. Considering a Gaussian distribution in only the r direction with no azimuthal variation, the heat flux striking the target, q"(r), can be expressed in cylindrical coordinates as

$$q''(r) = q''_{max}\, exp(-\frac{r^2}{2\sigma^2_{beam}}) \tag{1.2}$$

where,

$$I_{beam}E_{beam} = Q_{beam} = q''_{max} \int_0^{2\pi} d\theta \int_o^R exp(-\frac{r^2}{2\sigma^2_{beam}}) rdr\,. \tag{1.3}$$

When evaluated, the following expression for q''_{max} can be derived

$$q''_{max} = \frac{Q_{beam}}{2\pi\sigma^2_{beam}\left(1 - exp(-\frac{R^2}{2\sigma^2_{beam}}\right)} \tag{1.4}$$

Plugging in values for Q_{beam} (10 kW) and R (2.5 cm) gives a maximum heat flux at (r=0) of 16.64 MW/m^2. This is a value that is over three times higher than the heat flux value for a uniform beam. At the same power, a uniformly distributed beam would impart a heat flux load at (r=0) of 5.09 MW/m^2. From this calculation it is apparent that cooling of accelerator-NCT targets will require removing power densities on the order of 1-10 MW/m^2 over areas of several square centimeters.

Heat flux values of these magnitudes raise the concern that critical heat flux (CHF) conditions could be encountered in an accelerator-NCT target. One of the most promising techniques for removing power densities of this magnitude is submerged jet impingement.[29] This cooling configuration consists of injecting a high velocity jet of water through a static region of coolant before striking the center of the target normal to its surface. A schematic of this type of configuration is shown in Figure 1-8.

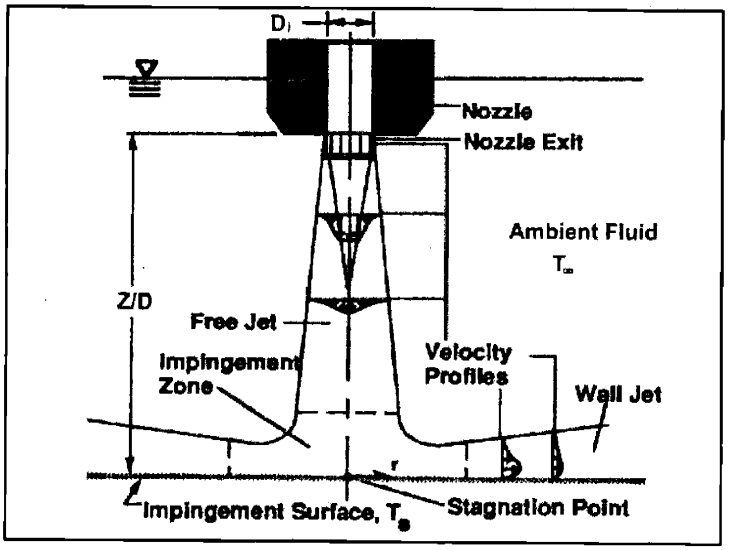

Figure 1-8 Geometry of a submerged impinging jet.[30]

Single-phase submerged jet impingement has been shown to be capable of generating stagnation point heat transfer coefficients of over 2x10^5 W/mK while removing a heat flux of 17 MW/m^2.[31] One advantage of submerged jet impingement is that the maximum coolant rates are

achieved at the stagnation region of the jet which can easily be directed to the location where beam strikes. A second advantage over simple convective cooling is that the dynamic pressure, $1/2\rho V_j^2$, created by the fluid striking the target raises the saturation temperature of the coolant and helps delay the critical heat flux crisis. This advantage comes at a price, however. In order to obtain high heat transfer coefficients, jet velocities (V_j) of 20-50 m/s are required. Generating these velocities poses a significant engineering difficulty due to the confined nature of the MRA in which the complete target must be housed. For example, a 1.0 cm diameter jet operating at 50 m/s requires that 62.2 GPM be introduced into and removed through a very restrictive space (refer to the OD_T dimensions in Figure 1-6 and Table 1-2). Because of these restricted spaces and the required large jet velocities, the pressure losses which scale as V_j^2 and pumping power which scales as V_j^3 will be quite large in a cooling system which requires flowrates of this magnitude.

1.4.2.2 Mechanical Considerations

An accelerator-NCT target (refer to Figure 1-7) will be subjected to stresses resulting from three types of loading. Because the target must have one side which sees vacuum while the other side (P_{sys}) is at or above atmospheric pressure, significant radial and hoop stresses will be generated. Additional stresses will be contributed by the dynamic pressure loading due to the coolant. For jet impingement, this pressure loading will have a Gaussian distribution centered about the stagnation point. In radial coordinates this pressure loading can be written as

$$P(r) = P_{sys} + \tfrac{1}{2}\rho V_j^2 \exp\left(-\frac{r^2}{2\sigma_p^2}\right). \tag{1.5}$$

In addition to stress generated by the system and dynamic pressure, thermal stresses resulting from temperature gradients will be present. In order to rigorously analyze the temperature profile in the target, the general steady-state heat transfer equation would have to be solved in three dimensions subject to the appropriate boundary conditions at the interfaces z = ±t/2 and r=R.

$$\frac{1}{r}\frac{\partial}{\partial r}\left(k(T) r \frac{\partial T}{\partial r}\right) + \frac{1}{r^2}\frac{\partial}{\partial \phi}\left(k(T)\frac{\partial T}{\partial \phi}\right) + \frac{\partial}{\partial z}\left(k(T)\frac{\partial T}{\partial z}\right) + q'''(r,\phi,z) = 0 \tag{1.6}$$

The resulting temperature profile will generate thermal stress in the target which generally scale as[32]

$$\frac{E\alpha(T_{max} - T_o)}{1-\nu} \tag{1.7}$$

where,

E: Young's Modulus

α: Coefficient of thermal expansion

T_{max}: Maximum target temperature

T_o: Temperature of unstressed plate.

ν: Poisson's ratio.

Consideration of the thermal/mechanical problem will begin with investigating how the different sizes and distributions of a real ion beam affects the temperature profile of both lithium and beryllium based targets. In order to do so, analytical calculations will be supplemented by extensive numerical heat transfer simulations using the finite element code ADINA. In order to accurately reconstruct the heat loads in these calculations, the beam profiling technique mentioned in the previous section will be utilized.

In order to answer the question of how to best cool the target, comparisons will be made between submerged jet cooling with water and liquid gallium metal. Area-averaged Nusselt number correlations for turbulent flows of liquid gallium will be presented and compared to experiment. Gallium metal seems to be an attractive alternative to water because of its ability to generate large heat transfer coefficients at comparatively low flowrates which minimizes unnecessary mechanical stress on the target. Additionally, it eliminates the concerns of CHF due to the fact that it has a liquid range which extends beyond 2000 °C.

Consideration of the thermal and mechanical stress will be investigated primarily with the ADINA code. Use of ADINA will allow for a number of target parameters such as thickness, radius, materials, shape, and mounting schemes (fixed-edge, simply supported edge, etc.) to be analyzed. Distortion energy theory will be used in combination with the ADINA simulations to predict the operational limits of both lithium and beryllium targets.

1.4.3 Target/MRA Integration and Neutronics

The final problem which must be addressed in this thesis deals with the integration of a properly cooled target assembly into a moderator/reflector assembly. Integration into the MRA is essential for accelerator-NCT. A target which has a cooling system which cannot be placed into an MRA does little to solve the problem of integration. A usable target must not only maintain its thermal and mechanical integrity, but it must also be properly instrumented so that accurate measurements of values such as current and temperature can be made. Secondary-electron effects which result from electrons being ejected from surfaces bombarded with ion beams will be dealt with specifically since it has been observed to alter target current measurements by as much as 40%.

It is apparent that a properly designed target and cooling assembly will differ, possibly significantly, from the ideal neutron source created by a uniformly distributed ion beam used in initial accelerator-NCT studies. As stated previously, the balance of thermal hydraulics, structures, and neutronics is the bottom-line in NCT. It is therefore necessary to confirm that a cooled target which has been integrated into the MRA does not adversely affect the neutronics of the system. Based on the conclusions of the previous sections, MCNP will be used to predict the effect that target design and a cooling system will have on the neutronics of the system as reflected by parameters such as therapy time and skin dose.

1.5 Thesis Contributions

It is the goal of this thesis to contribute to the field of high-power target development for accelerator-NCT. In response to the problems presented in this chapter, subsequent chapters will deal specifically with the integration of a working target into a moderator reflector assembly and the resulting neutronics from the complete system. Chapter 2 will focus on the area of accurately determining the size and current density of high-power beams. Techniques developed in this chapter will be the first such procedures for investigating certain beam parameters at current and energy levels previously unattainable. Building on the results of Chapter 2, thermal and mechanical engineering questions are addressed in Chapter 3. Theoretical calculations of thermal and mechanical target performance will be supplemented by detailed numerical simulations and experiments. A novel approach for cooling high heat flux targets using liquid gallium metal will be discussed. Area-averaged Nusselt number correlations for liquid gallium cooling with submerged jets will be presented. Comparisons will be made between this technique and standard water cooling. Having developed a method suitable for cooling accelerator-NCT targets,

procedures for integrating and instrumenting the target in an MRA will be presented in Chapter 4. No complete study regarding the integration of such a target has been done previously. This thesis will conclude with a presentation of the actual neutronics to be expected from the integrated system. Such neutronic information will greatly assist in the eventual implementation of an accelerator-based NCT system as a viable clinical modality.

1.6 References

1. W. B. Howard, J. C. Yanch, S. M. Grimes, T. N. Massey, S. I. Al-Quaraishi, D. K. Jacobs and C. E. Brient, "Measurement of the ^{9}Be(p,n) thick target spectrum for use in accelerator-based boron neutron capture therapy," Nucl. Sci. Tech., submitted (1998).

2. S M White, "Beam Characterization for Accelerator-Based Boron Neutron Capture Therapy using the 9Be(d,n) Nuclear Reaction," M.S. thesis, Massachusetts Institute of Technology, 1998.

3. J.C. Yanch, X-L. Zhou, R.E. Shefer and R.E. Klinkowstein, "Accelerator-based epithermal neutron beam design for neutron capture therapy," Med Phys, **19:** 709-721 (1992).

4. W.B. Howard, "Accelerator-based boron neutron capture therapy," Ph.D. thesis, Massachusetts Institute of Technology, 1997.

5. D.L. Bleuel, R.J. Donahue, B.A. Ludewigt and J. Vujic, "Designing accelerator-based epithermal neutron beams for boron neutron capture therapy," Med Phys, **25:** 1725-1734 (1998).

6. R.E. Shefer, R.E Klinkowstein, J.C. Yanch and G.L. Brownell, *A versatile new accelerator design for boron neutron capture therapy: Accelerator design and neutron energy considerations*, In *Neutron Beam Design Development and Performance for Neutron Capture Therapy*.th Edition, edited by O.K. Harling, J.A. Bernard, and R.G. Zamenhoff et al (Plenum ,New York, 1990) pp 259-270.

7. D.A. Allen, T.D. Beynon and S. Green, "Design for an accelerator-based orthogonal epithermal neutron beam for boron neutron capture therapy," Med Phys, **26:** 71-76 (1999).

8. C.-K. Chris Wang, T. E. Blue and R. Gahbauer, "A Neutronic Study of an accelerator-based neutron irradiation facility for boron neutron capture therapy," Nuclear Technology, **84:** 93-107 (1988).

9. M. Chadha, J. Capala, J. A. Coderre, E.H. Elowitz, J. Iwai, D.D. Joel, H.B. Liu, L. Wielopolski and A.D. Chanana, "Boron neutron-capture therapy (BNCT) for glioblastoma multiforme (GBM) using the epithermal neutron beam at the Brookhaven National Laboratory," Int J Radiat Oncol Biol Phys, **40:** 829-834 (1998).

10. A.Z. Diaz, A.D. Chanana, J. Capala, M. Chadha, J.A. Coderre, E.H. Elowitz, J. Iwai, D.D. Joel, H.B. Liu, R. Ma, M. Shady, D.N. Slatkin, G.W. Tyson and L. Wielopolski, "Safety and efficacy of BNCT for glioblastoma multiforme: results from the initial dose escalation studies," to be published in the Proceedings of the 8th International Symposium on Neutron Capture Therapy for Cancer, La Jolla, CA, Spetember, 1998.

11. E. Binello, R.E. Shefer and J.C. Yanch, "Neutron Beam Design for Boron Neutron Capture Synovectomy," *Advances in Neutron Capture Therapy*, vol. II, (Elsevier Science, Amsterdam, 1997) pp. 459-463.

12. E. Binello, J.C. Yanch, S. Shortkroff, C. Vivieros, G. Young, A.G. Jones, C.B. Sledge and A. Davison, "Research in boron neutron capture synovectomy," in *International Conference: Neutrons in Research and Industry*, George Vourvopoulos, Editor, Proc. SPIE 2867, pp. 68-71,1997.

13. D.P. Gierga, J.C. Yanch and R.E. Shefer, "Development and construction of a neutron beamline for accelerator-based neutron capture synovectomy," Med Phys, **27:** 203-214 (2000).

14. D.P. Gierga, "Neutron delivery for boron neutron capture synovectomy," Ph.D. thesis, Massachusetts Institute of Technology, 2001.

15. J. C. Yanch, R. E. Shefer and E. Binello, "Design of low-energy neutron beams for boron neutron capture synovectomy," in *International Conference: Neutrons in Research and Industry*, George Vourvopoulos, Editor, Proc. SPIE 2867, pp. 31-40,1997.

16. J. C. Yanch, S. Shortkroff, R. E. Shefer, S. Johnson, E. Binello, D. Gierga, A. G. Jones, G. Young, C. Vivieros, A. Davison and C. Sledge, "Boron Neutron Capture Synovectomy: Treatment of Rheumatoid Arthritis Based on the $^{10}B(n,\alpha)^{7}Li$ Nuclear Reaction," Med Phys, **26:** 364-375 (1999).

17. C.K. Wang and T.E. Blue, "An accelerator neutron source for boron neutron capture therapy," Trans. Am. Nuc. Soc., **54:** 302-304 (1987).

18. N. Gupta, J. Niemkiewicz, T.E. Blue, R. Gahbauer and T.X. Qu, "Effect of head phantom size on ^{10}B and $^{1}H(n,\gamma)^{2}H$ dose distributions for a broad field accelerator epithermal neutron source for BNCT," Med Phys, **20:** 395-404 (1993).

19. R.E. Blue, T.X. Qu, R.N. Christensen, P. Guo and J.W Blue, *An integrated neutronic and thermal-hydraulic design study for an accelerator neutron irradiation facility*, In *Progress in Neutron Capture Therapy for Cancer*.th Edition, edited by B.J. Allen, D.E. Moore, and B.V. Harrington et al (Plenum ,New York, 1992) pp 113-117.

20. J.W. Kim and J.S. Chai, "Design study of a linear accelerator system for neutron capture therapy," in *17th Particle Accelerator Conferece, PAC-97*, Vancouver, B.C.3, pp. 3825-3827,1997.

21. W.B. Howard, J.C. Yanch, S.M. Grimes, T.N. Massey, A.I. Al-Quaraishi, D.K. Jacobs and C.E. Brent, "Measurement of the $^{9}Be(p,n)$ thick target spectrum for use in accelerator-based BNCT," Med Phys, **23:** 1233-1235 (1996).

22. C.K. Wang and B.M. Moore, "Thick beryllium target as an epithermal neutron source for neutron capture therapy," Med Phys, **21:** 1633-1638 (1994).

23. N. Colonna, L. Beaulieu, L Phair, G.J. Wozniak, L.G. Moretto, W.T. Chu and B.A. Ludewigt, "Measurements of low-energy (d,n) reactions for BNCT," Med Phys, **26:** 793-798 (1999).

24. B.A . Ludewigt, "Clinical requirements and accelerator concepts for BNCT," in *17th Particle Accelerator Conferece, PAC-97*, Vancouver, B.C.3, pp. 3791-3795,1997.

25. D.A. Allen and T.D. Beynon, "What is the best proton energy for accelerator-based BNCT using the $^{7}Li(p,n)^{7}Be$ reaction?," Med Phys, **26:** 1113-1118 (2000).

26. NTG Neue Technologien GmbH, "Rotating wire scanner Type DS 040 (Equipment Manual)"

27. NTG Neue Technologien GmbH, "Beam Profile Measuring System (Grid, Harp) Type DG070 (Equipment Manual)"

28. International Specialty Products, "ISP Data Sheet", Wayne, N.J. 07470

29. J.H. Lienhard, R.S. Dahbura, H.F. Younis and C.H. OH, "Large area jet-array cooling modules for high heat fluxes," High Heat Flux Engineering III, **SPIE 2855:** 66-81 (1996).

30. P.F. Sullivan, S. Ramadhyani and F.P. Incropera, *Use of smooth and roughened spreader plates to enhance impingement cooling of small heat sources with single circular liquid jets.*, Topics in Heat Transfer, ASME HTD, Vol. 206-2, 1992.

31. J.H. Lienhard, H.F. Younis, R.S. Dahbura and D. Michels, "Liquid jet-array cooling modules for high heat fluxes.," AIChe, **44, No.4:** 769-779 (1998).

32. D.J. Johns, *Thermal Stress Analyses*Oxford: Pergammon Press, 1965.

Chapter 2 Ion Beam Current Density Measurement

In many accelerator-based applications including BNCT and BNCS, knowledge of the ion beam current density is important. For example, heavy ion therapy at facilities such as HIMAC requires that beam intensity and uniformity be maintained within +/- 2%.[1] Knowledge of current intensity is also crucial in thin film deposition and electron microscopy.[2] In accelerator-based neutron capture therapies, the primary rationale for evaluating the current density profile is to understand the heat distribution in the target. Unfortunately, the ability to measure current density profiles in beams of 100 μA or more is extremely difficult with existing technology. This chapter presents a technique for measuring the intensity profiles of high current ion beams using induced radioactivity in a target to create an image in radiochromic film. Evaluation of the current density is accomplished by processing the irradiated film with a desktop scanner. Development of this technique is described from the process of selecting suitable target material, through the physics of the individual steps which contribute to overall resolution, and finally to application of the technique to measure ion beams having currents of several hundred μA.

2.1 Why is the Measurement of Current Density Important in NCT?

Accurate measurement of current density is necessary for the viability of both types of accelerator-based neutron capture therapies. This necessity stems initially from the fact that ion beams used in these therapies have large total beam powers (1-2 kW for BNCS; >10kW for BNCT). In order to generate the required neutron flux with a usable energy spectrum, the neutron-producing target must be housed within the moderator/reflector assembly (MRA). As indicated in the previous chapter, optimized MRA designs from several research groups have found that the target and associated cooling system should be housed in an area which is 5-10 cm. in diameter. This confinement coupled with high beam power generates significant heating in the target. Design of a target which will maintain its thermal and mechanical integrity under such extreme heating conditions requires measurement of the local beam current density.

While other applications will utilize accelerator targets differently, the ultimate purpose of a neutron producing target in NCT is for use in therapy. Planning a therapy requires knowledge of both the intensity and energy spectrum of the neutron flux (ϕ_n). Generation of this flux is accomplished through neutron-producing charged particle reactions in the target followed by neutron scattering and loss in the MRA. Final distribution of the therapeutic neutron flux is

therefore dependent on the initial beam current density (I_{beam}). This process can be represented as a convolution of the beam current density with various point-spread functions as indicated in Equation 2.1:

$$\phi_n(x,y,z,E) = I_{beam}(x,y,E) * \Omega_{production}(x,y,z,E) * \Omega_{MRA}(x,y,z,E) \quad (2.1)$$

$\Omega_{production}$: represents the spreading due to the production and emission of neutrons from the target at various angles and energies based on the charged particle reaction kinematics.

Ω_{MRA}: represents the spreading due to the moderation, reflection and attenuation of the neutrons as they pass through the moderator/reflector.

*: denotes the convolution operator

The ability to analyze the size, shape, and density of a high-current ion beam is a necessary component of neutron capture therapy, and will have use in other areas of accelerator applications as well. From a targetry standpoint, the overriding rationale for determining the current density is to ensure the thermal and mechanical integrity of the target. Beyond the thermal and mechanical concerns, however, knowledge of the current density assists in the planning of a neutron capture therapy by allowing accurate simulations of neutron beam parameters based on actual ion beam distributions.

2.1.1 Thermal and Mechanical Integrity

Ion beams used to produce neutrons through charged particle reactions deposit heat in the target causing temperature gradients to develop. These temperature gradients, in turn, result in the build-up of thermal stresses. Design of a cooling system that can sufficiently handle this heat load and a target that is mechanically sound under the resulting stress requires information about the heating source. While details regarding design of the target and the cooling system will be presented in Chapter 3, the following illustration will indicate why an understanding of the ion beam current density is important.

Consider the ion beam illustrated in Figure 1-7 consisting of 2.5 mA of protons at 4 MeV which generates a peak heat flux (q''_{max}). The target is solid beryllium with a thickness (t) of 2 mm and a radius (R) of 3 cm. The average heat transfer coefficient (h) on the back of the target ($z = -t/2$) is assumed constant at 1.0×10^5 W/m^{2}K with a bulk temperature (T_∞) of 20 °C. For this example, the thermal conductivity (k) of the target is constant at 200 W/mK. To first order, the solution of the general steady-state heat transfer equation, given in Equation 1.6, can be made

with a 1-D approximation which neglects radial heat transfer. Equations 2.2 and 2.3 can be arranged to solve for the temperature at (r=0, z=t/2) as shown in Equation 2.4. This is the peak temperature encountered in the target. The quantity q''_{max} is derived using Equation 1.4.

$$q'' = h\left(T_{z=\frac{-t}{2}} - T_{\infty}\right) \tag{2.2}$$

$$q'' = -k\left(\frac{T_{z=\frac{t}{2}} - T_{z=\frac{-t}{2}}}{\frac{-t}{2} - \frac{t}{2}}\right) \tag{2.3}$$

$$T_{z=\frac{t}{2}} = q''\left(\frac{1}{h} + \frac{t}{k}\right) + T_{\infty} \tag{2.4}$$

Substituting for h, k, $q''= q''_{max}$, and T_{∞} the temperature at the hottest spot in the target can be calculated for both a Gaussian-shaped and uniform heat flux. The convention used to determine beam size defines the radius such that it encompasses 95% of the total current. In terms of the standard deviation in the current density profile, σ_{beam}, the beam radius is set at $2.5\sigma_{beam}$. Based on Equation 2.4, the resulting temperatures are calculated to be; T_{max}= 352.8 °C(σ_{beam}=1 cm); T_{max}= 121.8 °C(σ_{beam}= ∞). Results of a more rigorous numerical calculation using the ADINA code, which takes into account 2-D heat transfer as well as temperature variations in thermal conductivity are shown in Figure 2-1 and Figure 2-2.

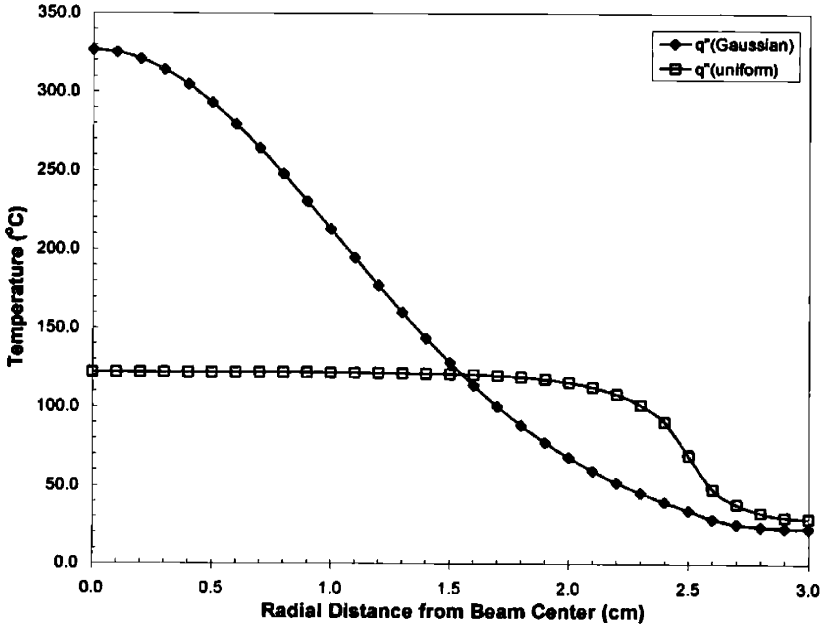

Figure 2-1. Radial variation of temperature on the beam side of the target. All distances are measured along the r-axis from (r=0, z=t/2) to (r=R, z=t/2).

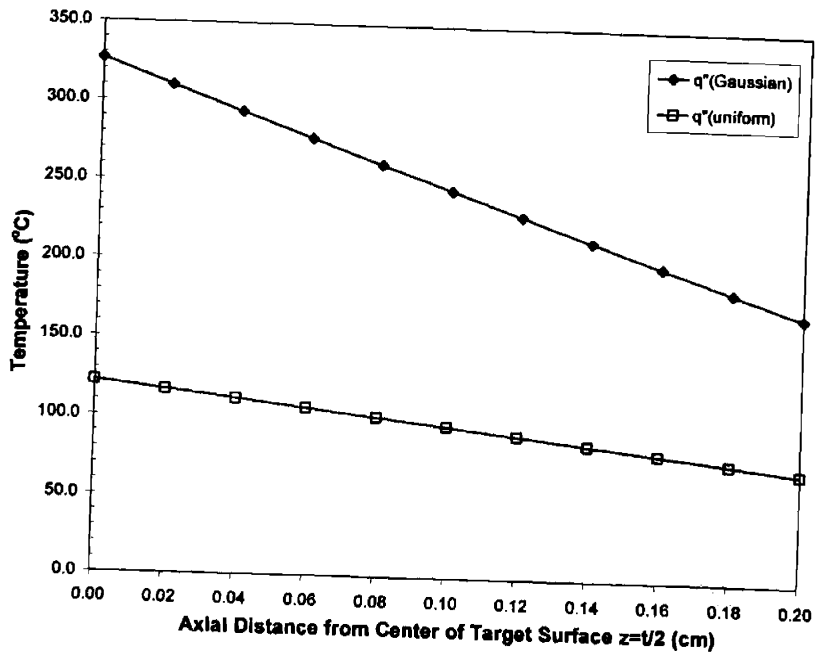

Figure 2-2. Axial temperature variation through the center of the target. All distances are measured along the z-axis from (r=0, z=t/2) to (r=0, z=-t/2).

From the 1-D and 2-D calculations it is evident that a beam which has a Gaussian-shaped heat flux will generate temperature profiles substantially different from those of a uniform heat flux. These differences will be amplified as σ_{beam} values decrease when the beam is focused. Simply basing the design of the target on a uniformly distributed heat source could lead to a serious under-prediction of the cooling requirements, resulting target temperatures, or thermal stresses. Thermal and mechanical design clearly requires the ability to measure current density.

2.2 Typical Methods for Monitoring Current Density

Initial research involving the measurement of current density was undertaken for applications such as thin film deposition and electron microscopy.[2] In an attempt to address this issue, a procedure for determining the intensity profile of electron beams was outlined in ASTM standard E986-86.[3] This procedure, which has also been applied to ion beams, involves rastering the beam over a sharp edge and measuring the current. While this technique can be used to determine beam size and shape, it is not designed to give a spatial measurement of beam intensity.[4] Although several techniques have been developed for the determination of beam size or shape, few techniques exist for accurately measuring the current density of ion beams. In fact,

most techniques are applicable only in ion beams of low power (0-100 W). The following sections briefly describe some of the most common techniques used to monitor ion beams.

2.2.1 Beam Profilers and Harps

Two of the most common devices for measuring current density are helical-wire profilers and harps. Both devices are direct measuring devices and operate on similar principles. Illustrations of these devices are shown in Figure 2-3.

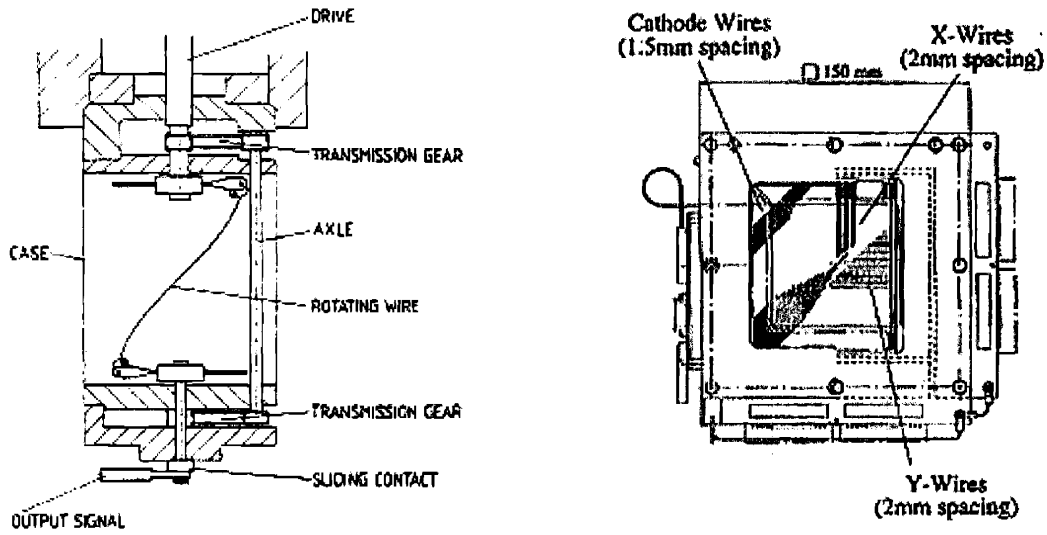

Figure 2-3. Diagrams of a helical beam profiler (left) and beam harp (right) devices.[1, 5, 6]

In order to measure profile intensity, a portion of the beam is stopped either in the wire or harp grid. For particles having a range greater than the dimension of the wires, the secondary electrons are gathered. Charge which is collected either by direct beam interaction or secondary emission generates a voltage proportional to current density. Resolution in these systems varies, but is on the order of 0.5-2 mm.[6] Advantages of these systems include on-line use in order to get real time information and sensitivity to currents as low as 100 pA. Both types of sensors, however, are limited to maximum currents around 100 μA depending on beam energy.[5, 6]

2.2.2 Quartz Windows

When struck by charged particle beams, quartz windows fluoresce by emitting light which has wavelengths in the visible spectrum. This allows quartz windows to be placed directly on the end of a beam tube and used as a target for the beam. In this configuration the beam can be viewed directly, and real-time images of the beam shape and size can be obtained. This imaging technique is often useful when constructing beam lines to ensure proper alignment of the tubes. It is also helpful in determining the operation of optical components such as focusing quadrupoles or beam steering magnets. Because the quartz window has to be viewed directly, it is difficult to cool the window while simultaneously allowing for visualization of the beam spot. Gas cooling can be used, but it must be configured so that line of sight from the window is not impaired.

While quartz windows allow for convenient monitoring of beam size and shape, it is uncertain whether they can be used to determine current density information since the light yield may not be linear with beam power.[7] The biggest limitation to its use as a window is the fact that quartz is a poor thermal conductor as well as extremely brittle. This limits the usable range of quartz to currents of tens of μA. At room temperature quartz has a thermal conductivity of 10.4 W/mK parallel to the crystalline axis and 6.21 W/mK perpendicular to the axis. For a 2 mm thick quartz window supported on a KF-50 flange a natural convection heat transfer coefficient of 10 W/m^2K can be assumed if no forced cooling is provided. Under these conditions, numerical calculations using ADINA have indicated the effective stress resulting from the irradiation of a uniformly-distributed 1 cm diameter beam with a total power of only 15 W will approach 1.0×10^7 Pa. While this is under the tensile yield stress limit, it is higher than the working design stress of 0.68×10^7 Pa recommended in a 1995 GE User's Guide.[8]

2.2.3 CCD Cameras and Phosphors

Another device for beam monitoring utilizes the same fluorescence phenomenon as the quartz window. Windows coated with phosphors such as zinc sulfide (ZnS) can be directly coupled to a CCD camera which in turn is mounted in the path of the beam. Resolution in these systems is quite good and can approach the micron level. A typical phosphor/CCD camera combination is shown in Figure 2-4. While these systems have good resolution and allow for real-time monitoring of the beam profile, they are limited to power levels which cannot exceed the damage threshold either for the conversion plate or the electronics. A typical value for the damage threshold is 50 W/cm^2, which corresponds to only 26 μA for a 1.5 MeV beam distributed evenly over a 1 cm diameter spot.

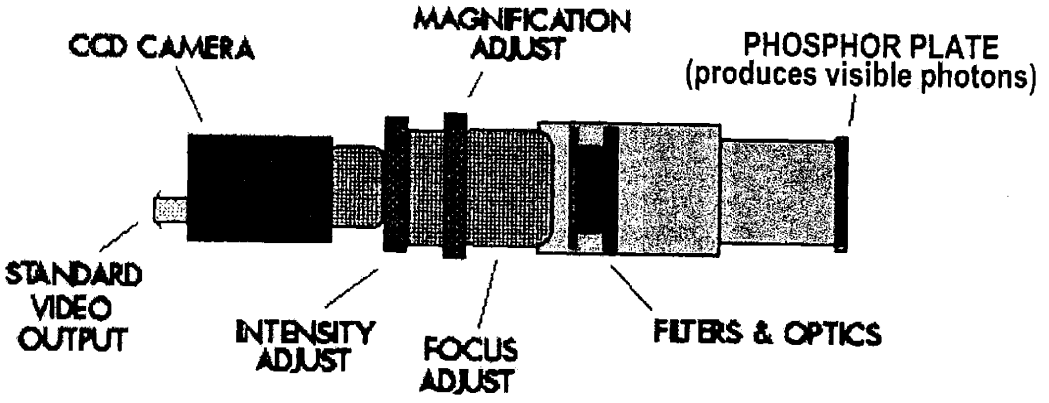

Figure 2-4. Illustration of a typical phosphor/CCD camera used to measure current intensity profiles.[9]

2.2.4 Kapton Film

Direct irradiation of Kapton film has been used to measure the current density profile of ion beams. This technique utilizes the color change in Kapton film which occurs when an ion beam strikes the film directly. Images which are burned onto the film are representative of the beam intensity and can be scanned in order to be quantified. Response of the film has been shown to be linear and can resolve beam spots as small as 250 μm.[7] This technique can only be used for small total beam powers due to rapid heating of the film. Beams having currents of ~18 nA and total powers of 1.5 mW were used in the study by Guharay et. al.

2.2.5 Infra-Red (IR) Systems

Techniques listed in §§2.2.1-2.2.4 are categorized as direct imaging techniques since they rely on interactions with the beam itself to obtain current density measurements. IR systems are indirect devices that generate a picture based on heat radiated from a sample. These systems are sensitive to photons having wavelengths of a few microns. IR devices, which can cost tens of thousands of dollars, have temperature resolutions (0.1-2 °C) which are comparable to standard thermocouples and can have spatial resolutions in the sub-millimeter range depending on lens configuration. Because this type of monitoring system does not directly interact with the ion beam, it is not subjected to beam heating. The camera, however, must be positioned to view the vacuum side of a target from some distance away. This orientation necessitates the camera being inclined at some angle to the beam and limits the spatial resolution which can be achieved.

While positioning obstacles could probably be overcome, ultimately the limiting factor for an IR system is the amount of lateral heat spreading in the target. An IR camera simply detects the thermal radiation emitted from the target and converts that information into a temperature reading. If the heat transfer in the target were simply in one dimension, the IR system could be calibrated so that the temperature measurement would directly reflect the current density of the incoming beam. Since ion beams, in general, are small and can have Gaussian distributions with small standard deviations, however, it is to be expected that the radial and azimuthal spreading of heat in a target will limit the spatial resolution for this type of system. In order to quantify the extent of this effect, numerical simulations of heat transfer due to the impingement of a 1 cm diameter Gaussian-shaped beam of varying power levels were conducted with the ADINA code. Resulting temperature profiles on the target surface were compared to the original heat flux distributions from the beam. It was found that the amount of spreading depended on both the power of the beam and the heat transfer coefficient used to cool the target. For a beam with a power of 1.5 kW, the full-width-half-maximum (FWHM) value of beam temperature increased from 2.35 mm to 2.5 mm when an h value of 10^5 W/m^{2}K was used. This value further increased to 2.65 mm when h was reduced to 25000 W/m^{2}K. Looking at the beam periphery, however, a much more profound difference was noticed. For the Gaussian beam, it is assumed that the beam edge occurs at $2.5\sigma_{beam}$ (5 mm) in the case of a 1 cm diameter beam. This is a typical convention which assumes 95% of the total current is located within the dimension defined as the beam radius. Comparison of the resulting temperature spatial profile to the $2.5\sigma_{beam}$ value of 5 mm for the true Gaussian shaped beam found that even for the (1.5 kW; h=10^5 W/m^{2}K) case, the beam edge as defined by the temperature increased to 7 mm. These results indicate that the unavoidable effect of radial temperature spread will limit the resolution in measurements of current intensity especially in regions of the beam periphery. Also, it indicates that the use of an IR system to measure current density requires a detailed knowledge of the target cooling.

The preceding sections have described many of the existing techniques used to monitor ion beam performance, obtain shape and size measurements, and to quantify current intensity profiles. While each of these methods is suitable in certain instances, none proves to be a robust, efficient, accurate, and inexpensive method for measuring the current density profile, especially at high current. The following section describes the development and evaluation of a quick and inexpensive method for obtaining detailed spatial information not only of the beam size and shape, but on the current intensity profile as well. It will be seen that this technique is usable at current levels far above those currently available and can even be implemented using previously existing targets.

2.3 Profiling Intensity Using Positrons from (p,n) and (d,n) Reactions

The following sections detail the theory and procedure for utilizing positrons created by either a (p,n) or (d,n) reaction to quantify various ion beam parameters. By definition, the use of reaction products to ascertain information about the beam size, shape, and intensity is an indirect profiling technique. Because it is an indirect method, the reactions chosen must have cross-sections which produce sufficient yield at the beam energy and current of interest. Current intensity measurements also require that detector response remain linear over the range of beam parameters being measured. Resolution of the acquired information must be as good or better than existing techniques, therefore it must be on the order of 0.5-1 mm. In addition, the technique must be capable of handling large total beam powers which are of interest in neutron capture therapies.

The beam profiling method consists of three basic steps which are outlined here for reference and described in detail in the following sections. First, an appropriate target material is selected depending upon beam species. Irradiation of the target produces a short lived radioisotope which emits positrons from its surface. Usually a short period (a few minutes) of decay is allowed before placing radiochromic film on the target. While on the target surface, dose from the positrons causes a color change in the film. Exposure of the film requires only a few minutes and is followed by removal of the film from the radiation field. This film can then be scanned in order to generate a dose profile which can be used to quantify the current intensity, beam shape, and size.

2.3.1 Selection of the Target Material

In order to measure current intensity using activation products from a charged particle reaction, the choice of appropriate target materials is crucial. The LABA accelerator is designed generate protons or deuterons with a maximum energy of 4.1 MeV. In this energy range, prolific charged particle reactions are limited to low-Z target materials. This restriction imposed by reaction kinematics and the Coulomb barrier is generally less important for deuterons which, because of the loosely bound neutron, will have more exothermic reactions and lower reaction thresholds than protons of equal energy. Stable elements up to Z=20 are located on or along the line Z=N, thus (p,n), (d,n), (p,γ), or (d,γ) reactions utilizing these nuclei will produce isotopes which are positron emitters. Some rare exceptions undergo electron capture or emit charged particles, but these are generally weak emissions or occur promptly and have no value with regards to beam profiling. In elements up to Z=5 there are no reactions which are useful for this

technique which requires irradiation followed by delivery of dose to a film. All reaction products from these low-Z elements have half-lives ranging from milliseconds to 10^{-22} seconds. At Z=5, however, half-lives become long enough to allow for production and decay in times on the order of minutes. Table 2-1 lists reactions which were considered along with their threshold energies.

Table 2-1. Positron producing reactions in low-Z materials and their corresponding thresholds.

Reaction	Energy Threshold (MeV)
$^{10}B(p,n)^{10}C$	4.492
$^{11}B(p,n)^{11}C$	3.001
$^{13}C(p,n)^{13}N$	3.262
$^{14}N(p,n)^{14}O$	6.004
$^{15}N(p,n)^{15}O$	3.792
$^{17}O(p,n)^{17}F$	3.827
$^{18}O(p,n)^{18}F$	2.792
$^{10}B(d,n)^{11}C$	0.000
$^{12}C(d,n)^{13}N$	0.679
$^{14}N(d,n)^{15}O$	0.000
$^{16}O(d,n)^{17}F$	1.896
$^{17}O(d,n)^{18}F$	0.000

From this table it is apparent that very few low-Z elements are possible candidates for this technique. Some can be ruled out immediately because the threshold energy is too high. Other reactions are based on target materials which constitute a small fraction of the naturally occurring element. Boron and carbon, however, appear to fit all the requirements for a target material. Boron produces a daughter product, ^{11}C, with a half life of 20.3 minutes and carbon produces ^{13}N, with a 9.97 minute half life. They also have cross-sections which rise quickly at energies above the threshold.

The following calculation, based on the $^{12}C(d,n)^{13}N$ reaction at 1.5 MeV, describes the steps used to test whether a given element would make a suitable target. Deuterons at 1.5 MeV are of interest because the $^{9}Be(d,n)^{10}B$ reaction at this energy is extensively used for BNCT and BNCS studies at LABA. While this calculation involves a specific reaction, it can be modified for use at other energies and for other particle/target combinations.

2.3.1.1 Target Irradiation

A uniformly distributed beam of deuterons (directed along the z-axis) having an area (A), energy (E) of 1.5 MeV, and current (I_{beam}) strikes a thick target of ^{12}C which has a density (ρ) of 2.26 g/cm^3. The number of particles per unit area striking the target per second, ϕ_{beam}, is given in Equation 2.5.

$$\phi_{beam} = \frac{I_{beam}}{Ae} \quad (e=1.602\text{x}10^{-19}\,\text{C}) \tag{2.5}$$

These particles have a range in the target which can be calculated from the stopping power (-dE/dz) as shown in Equation 2.6 or can be determined from Monte Carlo programs such as (S)topping and (R)ange of (I)ons in (M)atter -SRIM 2000. For 1.5 MeV deuterons in carbon, this distance is about 14 microns.

$$Range = \int_0^E (-dE/dz)^{-1} dE \tag{2.6}$$

Incoming ions will encounter (n) target atoms. Using Equation 2.7, n is evaluated to be 1.588x 10^{20} atoms for a 1 cm^2 beam.

$$n = \frac{\rho N_a}{M} A \cdot Range \tag{2.7}$$

(N_a is Avogadro's number; M is the molecular weight of target)

In thick targets the charged particle will slow from energy E to 0. Integration of the cross-section over all energies from E to 0, yields an effective thick-target cross-section. Evaluation of Equation 2.8, yields a cross-section of 87 mbarns for deuterons at 1.5 MeV in ^{12}C.

$$\sigma = \frac{1}{E}\int_0^E \sigma(E)dE \tag{2.8}$$

Combining Equations 2.5-2.8, activity produced in the target as a function of the irradiation time (t) is given by the standard activation equation (Equation 2.9). Analytical calculation of the saturation activity, $n\sigma\phi_{beam}$, gives a value of 2.33 mCi/μA, which is extremely close to the

experimentally derived value of 2.3 mCi/μA.[10] For many common reactions, the saturation activity has been experimentally measured and can be found in databases such as the National Nuclear Data Center.

$$A(t) = n\phi_{beam}\sigma(1 - e^{-\lambda t}) \tag{2.9}$$

(λ is decay constant for produced isotope)

For a given beam energy, the only parameter in Equation 2.9 which must be selected is the irradiation time, t. This time should only be as long as is required to produce a sufficient amount of the radioactive product. Long irradiation times introduce the possibility that beam characteristics could change, thereby altering the measurement of current density.

2.3.1.2 Decay Subsequent to Irradiation

Following the irradiation of the target, a short period of decay (t') provides time for removal of the target from the beamline and relocation to an area where the film irradiation can take place. Depending on the location of the target and the difficulty removing cooling lines and instrumentation, it is estimated that this decay time will be on the order of 5-10 minutes. Equation 2.10 gives the target activity at the end of the decay period, A(t').

$$A(t') = A(t)e^{-\lambda t'} \tag{2.10}$$

2.3.1.3 Film Irradiation

The final step requires irradiation of radiochromic film via the positrons emitted by the activated target to form an image. Details regarding the characteristics and performance of radiochromic film will be given in §2.3.3. After irradiation for a time, t, and subsequent decay for a period, t', the target has a ^{13}N activity of A(t'). Positrons from ^{13}N are emitted isotropically from the target surface where they immediately interact with and deposit dose in the film which induces a color change. This color change can be correlated with beam intensity as long as the amount of dose deposited remains within the linear range of the film. Several experiments have shown the linear range of the film to be 1-100 Gy.[11, 12] In order to remain within the dynamic range of the film and to allow for slight variations resulting from beam size or irradiation times, a value of 25 Gy was selected as a target dose level. Having selected a target dose, the time of film irradiation must be calculated. ^{13}N (λ=1.15872x10^{-3} sec^{-1}; β^{+}_{max}=1.190 MeV) has an average

emitted positron energy of approximately 0.4 β^{+}_{max}= 0.48 MeV. At this energy positrons lose 260 eV/μm in the film which has a density of 1.3 g/cm^3. The sensitive layer of the film has a total thickness of 30 μm which results in an average energy deposition of 7.8 keV/particle. Using a constant energy loss approximation for the positrons is justified since the overall thickness of the film (279 μm) will alter the stopping power by only 6-10%. Based on this approximation, the total dose deposited in the film per particle can be estimated using Equation 2.11.

$$D(Gy/particle) = \left(\frac{7800eV}{particle}\right)\left(\frac{1.602e^{-19}J}{eV}\right)\left(\frac{cm^2}{3.9e^{-6}Kg}\right)\left(\frac{1}{Acm^2}\right) \qquad (2.11)$$

It might seem redundant requiring the use of the beam area *a priori* to calculate the dose which needs to be given to the film, especially since this method is used to determine beam area. This fact, however, does not detrimentally affect the results since beam areas will vary by factors of a few as opposed to orders of magnitude. In fact final determination of the beam current intensity, beam size, and beam area do not depend on the total dose given to the film. Equation 2.11 is used only to ensure that the dose given to the film remains in the linear range and to test the feasibility of various charged particle reactions. Using this equation, the dose delivered to the film for a 1.0 cm^2 beam is found to be 3.204x10^{-10} Gy per particle passing through the film. Delivery of 25 Gy to the film, therefore requires the decay of 1.56x10^{11} atoms. Since the positrons are emitted isotropically, it is assumed that half of all emitted particles pass through the film. The total number of particles passing through the film is determined by integrating Equation 2.10 from 0 to T, where T is the time of film irradiation. This result is multiplied by 0.5 to account for the isotropic positron emission. Equation 2.12 combines the previous equations to give a general expression used to evaluate the validity of the $^{12}C(d,n)^{13}N$ reaction for measuring beam intensity. All constants from Equation 2.12 are collected in Equation 2.13, which indicates that the dose delivered to the film is proportional to the current density of the ion beam. As long as film response remains linearly dependant on dose, current intensity can be calculated based on the amount of color change. Equation 2.12 serves as the basis of the entire technique.

$$D(Gy) = \left(\frac{I_{beam}}{e}\right)\left(\frac{\rho N_a}{M}\right)(Range\cdot\sigma)(1-e^{-\lambda t})(e^{-\lambda t'})\left(\frac{1-e^{-\lambda T}}{\lambda}\right)\left(\frac{3.204e^{-10}\cdot 0.5}{A}\right) \qquad (2.12)$$

$$D(Gy) = C\left(\frac{I_{beam}}{A}\right)\left(1 - e^{-\lambda t}\right)\left(e^{-\lambda t'}\right)\left(1 - e^{-\lambda T}\right) \qquad (2.13)$$

-all times (sec)

-A (cm^2)

-I_{beam} (μA)

-C = 11.922 (the value of this constant was modified following MCNP simulations described in §2.4.2)

Using Equation 2.13, it was possible to evaluate times and currents needed for the procedure. Many permutations of I_{beam}, t, t', T, and A will give a dose of 25 Gy to the film, but several assumptions can be made to narrow the possibilities. Since this procedure is designed for high currents, a minimum value for I_{beam} was taken to be 100 μA. Beam size was set at 1 cm^2, and it was assumed that 5 minutes would be required to remove the target from the beamline after irradiation. Short irradiations are desirable since beam conditions might vary over long timescales, so the irradiation time, t, was set at 2 minutes. Delivery of 25 Gy to the film, therefore, would require 227 seconds, and the entire procedure can be completed in slightly over 10 minutes.

Utilization of Equation 2.12, with modifications made for different target materials, demonstrated that for beam energies of 0-4 MeV boron, carbon, nitrogen, and oxygen all are satisfactory targets for the (d,n) reaction. Only ^{13}C and ^{11}B, however, are suitable for use with the (p,n) reaction. In addition to time and cross-section requirements, consideration was also given to the fact that the chosen material must be suitable for fabrication into a target which can handle large beam powers. Carbon and boron both are suitable for use with high currents.

2.3.2 Target Construction and Irradiation Procedure

Having illustrated that carbon was a suitable target material, a simple target was designed and tested in order to determine the best procedure for obtaining beam information. The target constructed at LABA for testing consisted of a ^{12}C target disk which was machined and attached to an aluminum KF-50 beam stop using high temperature, thermally-conductive epoxy. A photograph of the completed target along with a schematic is shown in Figure 2-5. The carbon protrudes slightly (0.6 mm) from the face of the aluminum so that the radiochromic film can rest flush against the target surface. Cooling is provided by a 1.1 cm diameter channel cut in the aluminum backing. Coolant lines can quickly be disconnected to allow easy removal from the beamline.

A measurement using this technique begins by determining the desired beam parameters such as current level and energy. If the beam has already been tuned and needs no optimization then the following step can be omitted and irradiation of the carbon target can proceed directly. At LABA, tuning of the beam is done using an all-aluminum beam stop identical in size and shape to the carbon target. Optimizing beam parameters on this target avoids unnecessary production of ^{13}N. The beam also produces a witness mark on the aluminum which can be used to make a rough estimate of the beam area for use in Equation 2.13. In practice, it is helpful to make a rough first estimate of times required in the procedure. Setting a current level and irradiation time leaves only the decay time and film irradiation time to be adjusted to achieve the desired target dose level.

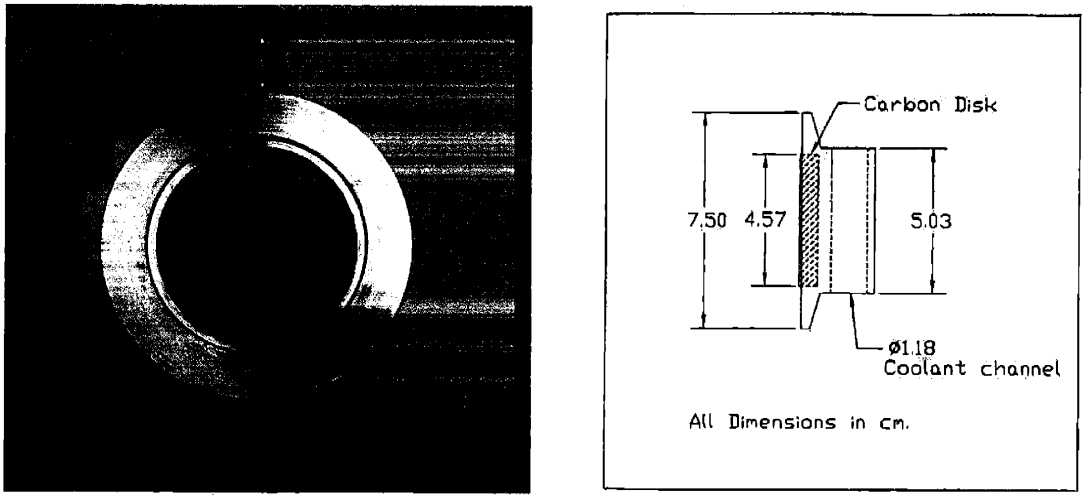

Figure 2-5. Photograph and schematic of the carbon target housed in a water-cooled KF-50 flange made of aluminum.

Irradiation begins by starting a current integrator connected to the target. Current is increased to the desired level, and a timer is started once the current level is reached. At the end of the predetermined irradiation time, the beam is shut off and the current integration is stopped. Because some isotope production occurs during ramping up of the current level, the appropriate average current level is determined by dividing integrated charge by the total time of the irradiation. The resulting value of I_{beam} and t are used in Equation 2.13 to adjust the decay time and film irradiation times which were estimated before the irradiation.

The decay period between the end of the target irradiation and the beginning of the film irradiation serves two functions. After the beam is shut off, there is a certain amount of time required to enter the radiation vault, close the gate valve, remove cooling lines, and remove the target from the beamline. For the LABA beamline, this procedure requires 3-5 minutes.

Secondly, the decay period minimizes the personnel dose during the remainder of the procedure. Reference to Equation 2.13 indicates that even short irradiations with high current beams will generate amounts of radioisotope which will be on the order of tens of millicuries. Assuming the ^{13}N activity is A_n, dose to tissue can be approximated by modeling the target as a point source of 511 keV photons. Neglecting attenuation, the dose to tissue can be calculated using Equation 2.14.

$$\dot{D}\left(\frac{mR}{hr}\right) = \frac{A_n E \cdot 1.1547 x 10^3}{r^2} \tag{2.14}$$

A_n: ^{13}N activity in mCi

E: photon energy in MeV

r: distance from source to tissue

Proximity to the target during the decay period will result in dose being delivered to the hand as well as the whole body. Noting the dimensions in Figure 2-5, the average distance to the hand is about 6 cm while the average distance to the torso is about 30 cm for an individual transporting the target by hand. At these distances dose rates of 16.4 mR hr^{-1} mCi^{-1} to the hand and 0.66 mR hr^{-1} mCi^{-1} to the body will be encountered. From the standpoint of dose limits, the ^{13}N activity must be lower than 3.81 mCi to ensure that the dose rate from the annihilation photons is kept below the legal limit of 2.5 mR/hr.

At the end of the decay period, a small piece of radiochromic film is placed flat on the carbon surface and left there for a given length of time, T. Dose from the positrons expose the film causing it to turn progressively darker blue. Once the film irradiation time is complete, the film is removed. The exposed film can then be scanned and the information processed to determine information about the beam.

2.3.3 Radiochromic Film and Scanners

The procedure for obtaining information about current density from an irradiated target which is emitting positrons requires radiochromic film to be placed on the surface of the target where it is exposed by the delivery of dose. Before irradiation the film is nearly colorless, and exposure to ionizing radiation causes the film to turn progressively more blue depending on the amount of dose delivered. After irradiation, the film contains a permanent record of the shape, size, and intensity of the beam. This film can then be scanned with a common desktop scanner to process the information contained on the film. Although typical dosimetry studies using

radiochromic film utilize densitometers, use of a common desktop scanner has proven to be a reliable, inexpensive method for obtaining high resolution information from the irradiated film. Use of a scanner has also been experimentally shown to have a higher signal-to-noise ratio than broadband densitometry.[12]

Radiochromic film has been investigated since 1965 as a means to determine dose with high spatial resolution without requiring any additional development other than the exposure to radiation.[11] Early radiochromic films were responsive to very high doses (10^4-10^6 Gy). Investigations at LABA, initially utilized GafChromic DM-1260 film, but the sensitive range of 50-2500 Gy required unnecessarily high ^{13}N activity. Subsequent experiments utilized the GafChromic MD-55-2 film which has a sensitive range of 1-100 Gy.

Extensive information about the development, properties, and use of MD-55-2 film can be found in the product description of the film issued by the distributor, International Specialty Products, or in the Recommendations of the AAPM Radiation Therapy Committee regarding radiochromic film dosimetry.[11, 13] The film consists of two pieces of polyester base each having a thickness of 67.3 μm. Coating one side of the base layer is 15 μm of radiosensitive gel. These two base/gel layers are held together by a third piece of polyester base (25 μm thick) coated with 44.5 μm of pressure sensitive adhesive. The complete assembly is a seven-layer film having a total thickness of 278.6 μm. While the composition of each layer varies slightly, the elemental composition consists only of carbon, hydrogen, nitrogen, and oxygen. The overall density of the film is 1.3 g/cm^3, and the sensor material is similar in its electron stopping powers and energy absorption coefficients for photons over 100 keV to water and muscle.[14]

A requirement of this technique is that the color change in the film remain linear as a function of dose. Not only must the color change remain linear, it must be independent of dose rate since different irradiations may involve dose rates that are not equal. Large amounts of data exist regarding the linearity of the film in the range of 1-100 Gy. In most studies the net optical density (O.D.) was determined at wavelengths of 610 nm and 660 nm. Studies using densitometers at these wavelengths illustrated that the optical density per unit dose varied by only 3.2% in the range of 0-30 Gy, while the variation at 50 Gy was 11.2% and at 100 Gy the variation was 13.9%.[11] Linearity has also been established in the visual wavelengths which is important to this study since scanning is to be performed with an optical scanner. Tests using an optical document scanner confirms information provided by the vendor indicating linearity within ±6% in the range of 15-60 Gy.[12, 13] Deviation from linear outside this range was less than 10% up to 100 Gy. From the previous section, it was calculated that the dose rate delivered to the film

will be on the order of 6-10 Gy/min. Color change in MD-55-2 film has been shown to be insensitive to changes in dose rate up to 80 Gy/min.[15] Two final properties of MD-55-2 film are important to this technique, resolution and timing of the scan. Resolution of the film has been determined to be better than 0.8 μm (1200 cycles/mm).[14] At this level, the resolution of the film is two orders of magnitude greater than the resolution of the scanner. Scanning of the film should be done at least 24 hours after irradiation. Color change has been shown to vary by 16% in the first 24 hours after irradiation, but less than 1% after the first 24 hours.[16] It is recommended that all scans be performed at least 24 hours after the irradiation of the film. For all experiments conducted at LABA, 48 hours were allowed between the irradiation and subsequent scanning of the film.

2.4 Prediction of Overall Resolution

Knowledge of the current density of high current ion beams is important for many reasons. This information is critical in determining the thermal and mechanical response of a target subjected to ion beam heating. Numerical simulations of target heating have already illustrated that peak target temperatures can vary by factors of three or higher due to differences between a uniform and Gaussian-shaped beam. It has also been stated that available measurement techniques having resolutions of 0.5-2 mm are limited to beams having currents less than 100 μA. With these factors in mind, it is evident that a technique which can resolve variations in the beam intensity on the order of 0.5-1 mm is necessary. The following discussion addresses the question of the overall resolution of the process including beam irradiation, deposition of dose, and scanning of the film.

2.4.1 Phenomena Affecting Overall Resolution

The image which is contained on the radiochromic film is not a direct replication of the two-dimensional current density profile. Correlation between the image which is scanned from the film and the original beam profile requires deconvolution of the point spread functions associated with each step in the process. The relation between the scanned image contained on the film $I_{film}(x,y)$ and the current density profile $I_{beam}(x,y)$ is given in Equation 2.15.

$$I_{film}(x,y) = I_{beam}(x,y,E) * \Omega_{cp}(x,y) * \Omega_{ee}(x,y) * \Omega_{film}(x,y) * \Omega_{scanner}(x,y) \qquad (2.15)$$

Ω_{cp}: point spread function due to charged particle scattering and isotope production

Ω_{ee}: point spread function due to isotropic positron emission and dose deposition

Ω_{film}: point spread function due to the inherent resolution of the film

$\Omega_{scanner}$: resolution loss due to scanning and digitizing the film

Recovery of information in the spatial domain requires determination of the point spread functions due to the processes of proton scatter/isotope production, positron emission, and the film response. These point spread functions can then be combined with the modulation transfer function of the scanning process through multiplication in Fourier space to arrive at an estimation of the overall resolution.

2.4.1.1 Charged Particle Scattering and Isotope Production

Ω_{cp} takes into account the combined effect of both lateral spreading of the charged particles and the location of isotope production. When deuterons at 1.5 MeV strike the target surface, Coulombic scattering with the carbon electrons causes the ions to lose energy. Each scattering event transfers only a small amount of energy from the deuteron, so the resulting angular deviations are small. These deviations and the rate of energy loss, however, progressively increase as the ion loses more and more energy. As the deuterons slow down they also produce ^{13}N at a rate proportional to the reaction cross-section which itself is a function of energy. Determination of lateral spreading and ^{13}N production was accomplished by simulation of the deuteron transport through carbon with SRIM2000.[17] Simulations were carried out using carbon targets of varying thickness which were less than the range of the deuteron. At each thickness, 5000 particles were run and the average lateral spread of the ions leaving the target was calculated. Figure 2-6 plots the calculated lateral spread of the deuterons as a function of depth into the carbon target. At the surface there is essentially zero lateral spreading of the ions, while at a distance of 10 microns, spreading has increased to ~0.14 microns. Concurrent with the spreading of the deuterons as they pass through the target is the production of ^{13}N. Location of ^{13}N production in the target was determined by calculating the cross-section as a function of depth. Calculation of this quantity began by determining the energy of the ions passing through the target.

Again using SRIM2000, simulations of 1.5 MeV deuterons striking a thick carbon target were performed. A simulation of 10000 particles gave -dE/dz as a function of depth at intervals of 1500Å. Since these bins were sufficiently small, E(z) was determined by integrating -dE/dz for each bin. Total energy lost in each bin was subtracted from the energy in the previous bin. This curve was fit with a 6^{th}-order polynomial function which provided an analytic expression for E(z).

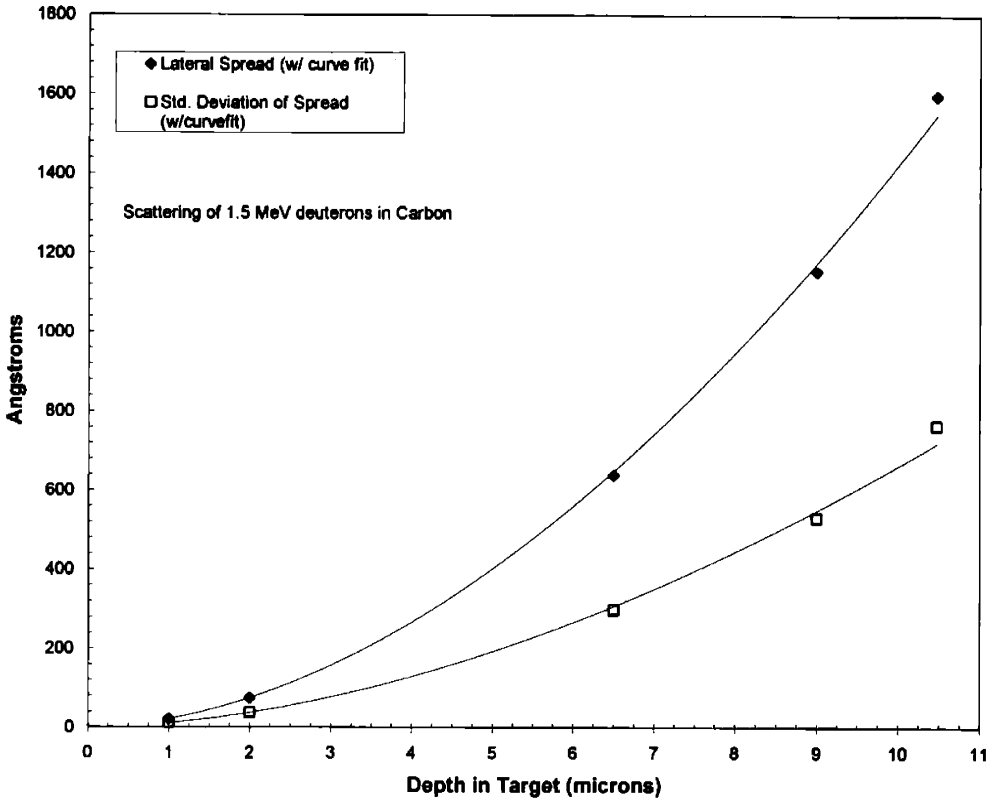

Figure 2-6. Calculation of the lateral spread and associated standard deviation of deuterons as a function of depth in carbon. Power functions were fit to each curve to generate analytic expressions for the quantities.

The $^{12}C(d,n)^{13}N$ cross-section, which increases sharply at energies above the threshold of 0.679 MeV has been determined experimentally by Fiorouzbahkt et. *al.* A plot of the cross-section data is shown in Figure 2-7. These measurements were also fit with a 6^{th}-order polynomial resulting in an analytic expression for $\sigma(E)$. Combining the expressions for $\sigma(E)$ and E(z) resulted in an analytic expression for $\sigma(E(z))$, which is plotted in Figure 2-8.

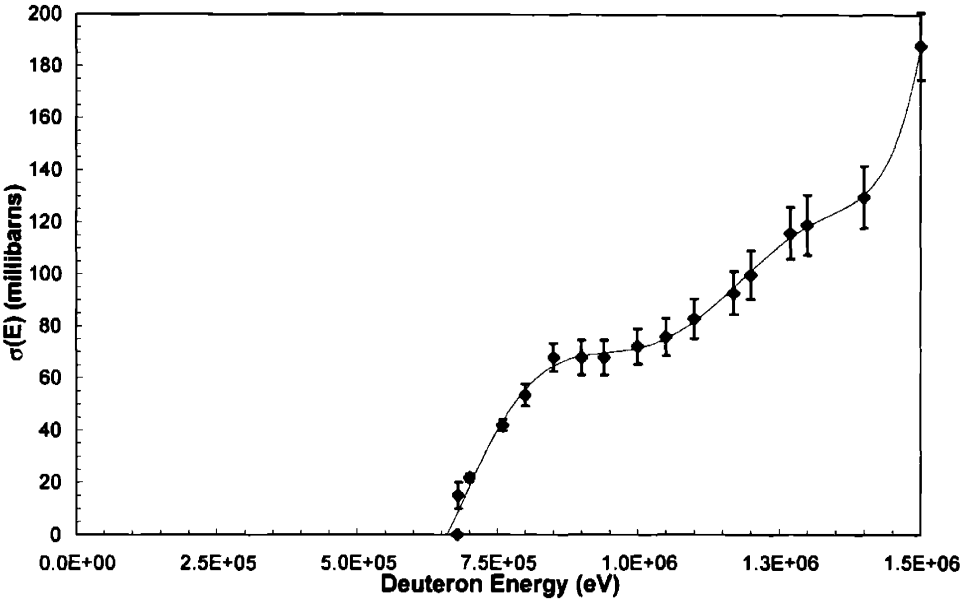

Figure 2-7. Experimentally determined $^{12}C(d,n)^{13}N$ cross-sections[10] and the resulting analytic expression for $\sigma(E)$.

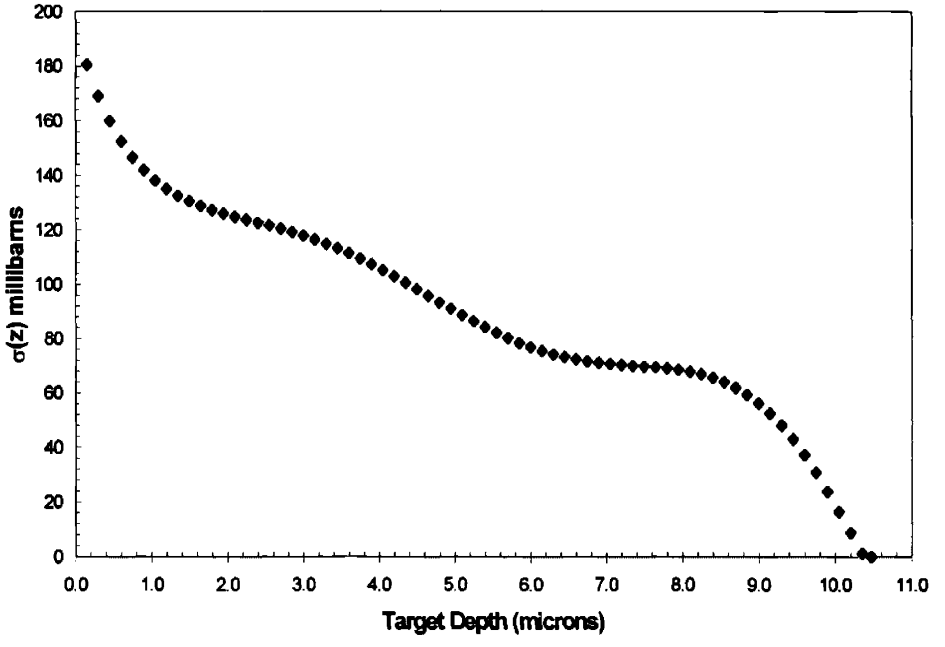

Figure 2-8. Plot of calculated ^{13}N production as a function of depth in the target.

Using an analytic expression for σ(z), the fraction of total ^{13}N produced at depth, z, in the interval dz could be evaluated as shown in Equation 2.16. The upper limit of 10.4 μm is the point at which the deuteron energy falls below the threshold of 0.679 MeV.

$$N^{13}_{fraction}(z) = \frac{\sigma(z)}{\int_0^{10.4\,micron} \sigma(z)dz} \quad \text{subject to the condition}$$

$$\int_0^{10.4\,micron} N^{13}_{fraction}(z) = 1 \tag{2.16}$$

This fractional production as a function of depth allowed the incorporation of isotope production into the deuteron spreading effect. By weighting the magnitude of the spread at a distance, z, by the fraction of ^{13}N produced in the interval dz, an effective total spreading could be determined. For 1.5 MeV deuterons in a thick carbon target, the average spreading weighted by ^{13}N production was calculated to be 0.0367±0.0174 microns. As will become evident in §2.4.1.3, the effect on resolution due to charged particle scattering, Ω_{cp}, is four orders of magnitude less than that due to positron emission, and thus will contribute no detectable blurring in the image which is obtained on the film.

2.4.1.2 Film Resolution

Although the film itself does have a finite resolution, which has been determined to be at least 1200 lines/mm (600 cycles/mm), it contributes no perceptible changes in either the image which is obtained by scanning the film or the final current intensity measurement. The ability of the film to resolve dose distributions on the micron scale results from the extremely small size and localized effect of the crystals in the sensitive layers of the film.[18] Even upon convolution of the two point spread functions due to charge particle scatter, $\Omega_{cp,}$ and film resolution, Ω_{cp}, the combined spread has a width of only about 1 micron. This can be seen in Figure 2-9.

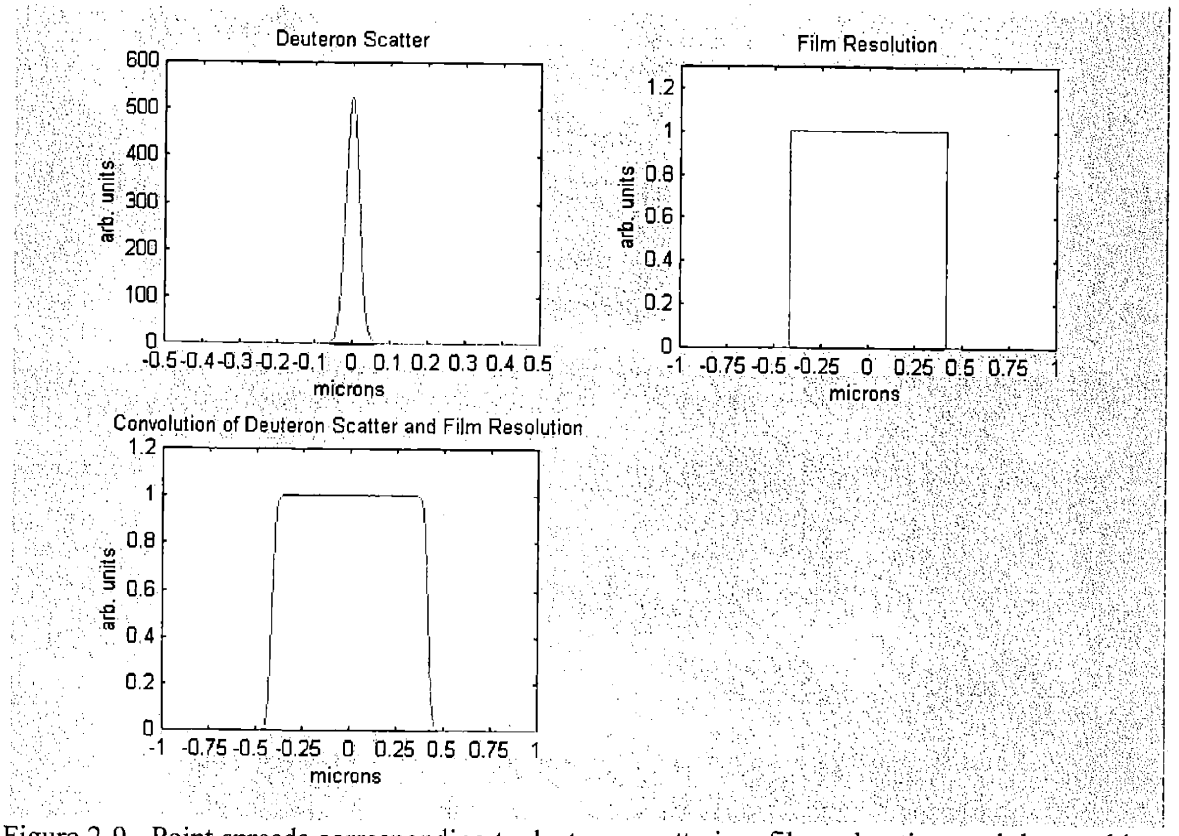

Figure 2-9. Point spreads corresponding to deuteron scattering, film coloration, and the resulting convolution of the individual functions.

2.4.1.3 Positron Emission and Dose Deposition

Determining the point spread function resulting from the emission of positrons and the deposition of dose in the film is not a trivial process. If electrons could simply be modeled like protons which travel along essentially straight lines and deposit energy according to -dE/dz, an analytical expression for dose deposition could be developed with relatively good accuracy. In this simplified case, the film response would be governed by -dE/dz, an inverse-square drop due to distance, and a cos(θ) dependence due to the increasing angle from the point source at increasing radial distances. Electrons, however, travel in torturous paths which cannot be accurately analyzed using straight line approximations. Calculation of the point spread, therefore, was determined by Monte Carlo simulation of the electron trajectory and energy loss.

MCNP4B was utilized to determine how positrons emitted from the carbon target interact with the film which is positioned directly on the surface. The target, which is pictured in Figure 2-5, was modeled in MCNP as was the radiochromic film using the dimensions and atomic composition given in the product data sheet. Plots generated by MCNP, which depict the entire target as well as two close-up views, are shown in Figure 2-10.

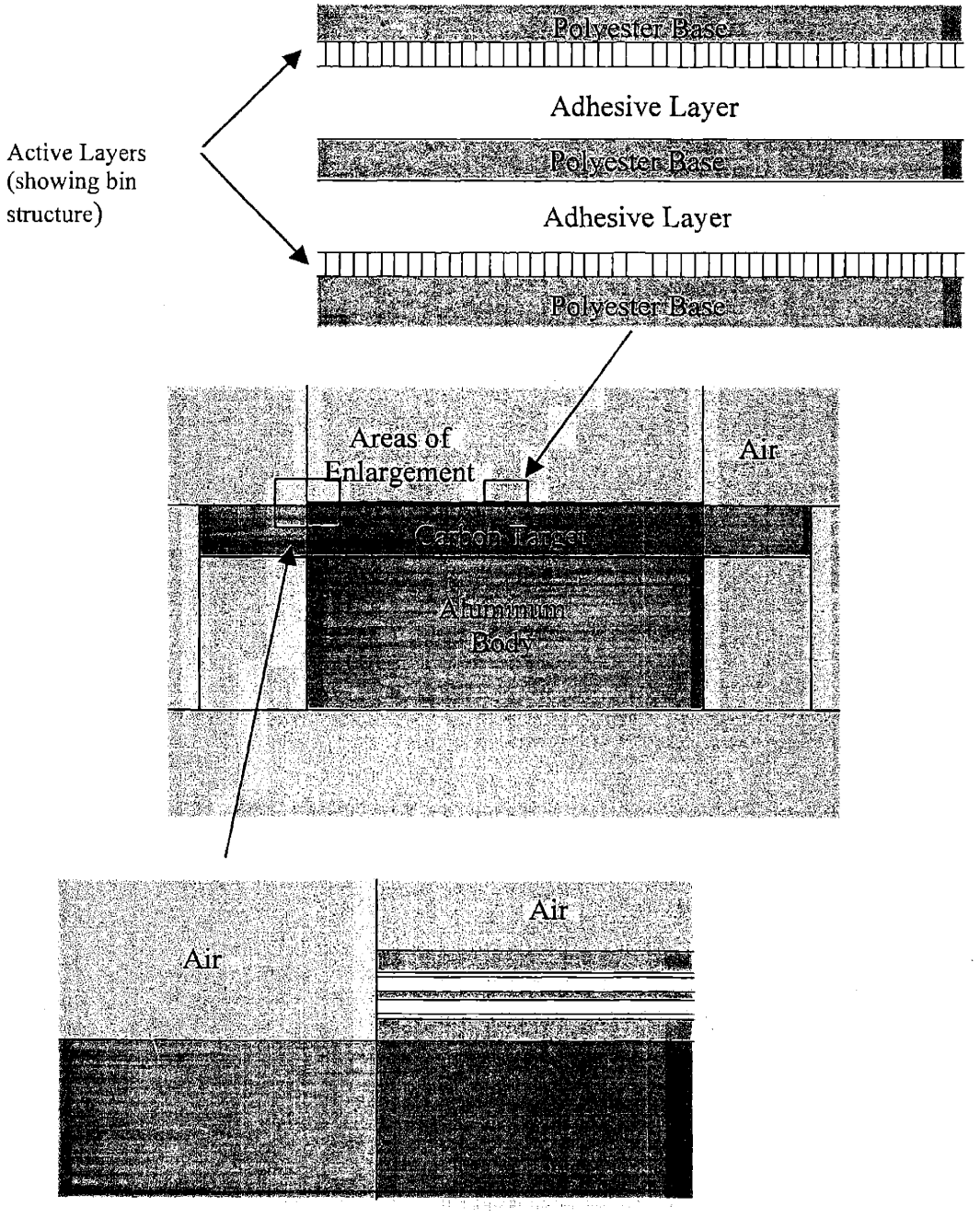

Figure 2-10. MCNP generated plots of the target and two enlarged views of the individual film layers used to model the positron emission point spread function.

Concentric cells were generated in both sensitive layers of film at increasing radial distances in increments of 4.233×10^{-3} cm. This distance was chosen because it represents half the pixel size used to scan the film. Some attempts were made to divide the bins even smaller, but the extremely small volumes resulted in poor statistics even after long run times. In generating the model, it was important to consider the extremely small dimensions of the cells, which had volumes on the order of 10^{-7} to 10^{-8} cm^3. For MCNP to accurately determine the electron trajectory an estep modification was added to each of the material cards making up the film layers. In MCNP, the electron trajectory is divided into a number of major steps (s) and substeps (m). Angular deflections and production of secondary particles are sampled at each of these subdivisions. The estep default, which determines the number of electron substeps, is m=3, but for cells with extremely small volumes this value does not allow for enough substeps to accurately calculate the electron trajectory. Increasing the estep value in important cells having small volumes allows for more accurate electron transport. MCNP recommends that at least ten substeps be considered in any important area in the problem.[19] In the non-sensitive (polyester base - adhesive) layers, therefore, the estep value was increased to 500, while the value was increased to 1500 in the sensitive layers.

MCNP does not allow positrons to be used as source particles. While modeling electrons instead makes no difference to the physics governing energy loss of the particles, the annihilation photons cannot be modeled explicitly in the code. To account for the additional dose due to the 511 keV photons, three additional runs were conducted with varying photon source geometries. The resulting dose from these additional runs were simply added to the electron dose to get a cumulative positron/annihilation photon dose. Positrons which start on the carbon surface are emitted isotropically. On average, half of the particles will be directed into the carbon where they slow rapidly. Using the continual slowing approximation, the range of positrons (or electrons) in carbon is 0.09 cm based on the average positron energy of 0.48 MeV from N^{13}. Modeling the photons which result from the annihilation of these positrons was performed by starting source photons with an energy of 511 keV in a hemispherical volume in the carbon which had a radius of 0.09 cm. Similar approximations were made for the photons which would start from within the film itself and from the air above the film.

Simulation of the positron (modeled as electron) point spread function was accomplished by modeling the dose deposition in the sensitive film cells illustrated in Figure 2-10. Because the film is to be scanned after irradiation to analyze the color change, dose to the bottom and top cells were added to give a total dose value at each radial location. All particles were started in the carbon along a line which passed through the origin at (0,0,0) which corresponds to the center of

the top surface of the target. Starting energies were sampled according to the probability distribution derived from the Fermi theory of beta-decay. According to the theory, the number of positrons emitted with energy (E) from ^{13}N which has an endpoint energy (Q) of 1.1984 MeV, can be expressed as $N(E)=C(E^2+2Em_ec^2)^{0.5}(Q-E)^2(E+m_ec^2)$. The constant C is normalized so that the integrated number emitted over all energies is unity. The average particle energy started during the simulation was computed by MCNP to be 0.48418 MeV. This compares well to the standard average energy approximation for positron emission of 0.4Q, 0.47936 MeV. Starting positions for the particles were weighted by the fractional production values indicated in Figure 2-8. Depths into the target were selected according to the production fractions in discrete increments of 1500 Å, and energies were selected according to the continuous energy distribution. Directionality of the particles was isotropic. Several runs were conducted using total numbers of starting positrons from $1x10^6$ to $3x10^6$ in order to achieve statistics with less than 2% error. Photon errors were less than 10% for all cells except the cell at r=0 which had an error of 15% due to its extremely small volume. The resulting dose distributions were used to calculate the point spread function.

Table 2-2 and Table 2-3 give the results of the Monte Carlo simulations for both the positron and 511 keV photon dose deposition. Distances given are in centimeters and represent radial locations in the center of each bin. The doses given for each distance are in units of MeV/g per starting positron.

Table 2-2. Dose deposition per starting particle resulting from positron emission of N^{13}.

Radius (cm)	Total Dose (MeV/g)	Total Dose Error (MeV/g)
0.00E+00	3193.45	22.30
6.35E-03	2313.23	11.35
1.06E-02	1492.54	6.98
1.48E-02	1014.36	5.09
1.91E-02	725.96	3.80
2.33E-02	540.90	2.99
2.75E-02	416.06	2.42
3.18E-02	325.37	2.00
3.60E-02	258.63	1.73
4.02E-02	210.89	1.44
4.45E-02	172.32	1.26
4.87E-02	143.81	1.08
5.29E-02	119.62	0.95
5.72E-02	101.25	0.83
6.14E-02	85.10	0.76
6.56E-02	74.22	0.69
6.99E-02	62.52	0.60
7.41E-02	54.53	0.53
7.83E-02	47.39	0.48
8.26E-02	40.06	0.44
8.68E-02	34.50	0.41
9.10E-02	30.20	0.39
9.53E-02	26.15	0.34
9.95E-02	22.92	0.30

Table 2-3. Dose deposition per starting particle resulting from annihilation of N^{13}.

Radius (cm)	Total Dose (MeV/g)	Total Dose Error (MeV/g)
0.00E+00	0.380	0.0537
6.35E-03	0.537	0.0371
1.06E-02	0.483	0.0299
1.48E-02	0.496	0.0243
1.91E-02	0.499	0.0217
2.33E-02	0.523	0.0206
2.75E-02	0.509	0.0188
3.18E-02	0.497	0.0180
3.60E-02	0.473	0.0155
4.02E-02	0.465	0.0148
4.45E-02	0.465	0.0142
4.87E-02	0.459	0.0134
5.29E-02	0.464	0.0129
5.72E-02	0.456	0.0125
6.14E-02	0.398	0.0108
6.56E-02	0.417	0.0109
6.99E-02	0.394	0.0102
7.41E-02	0.407	0.0103
7.83E-02	0.369	0.0094
8.26E-02	0.339	0.0086
8.68E-02	0.354	0.0090
9.10E-02	0.330	0.0083
9.53E-02	0.315	0.0077
9.95E-02	0.310	0.0077

From these results it is clear that the photon dose is insignificant even at the extreme edges where the positron dose is small. Combined doses from all annihilation photons are 3-4 orders of magnitude lower than that from the positrons. In fact, the entire photon dose is similar in magnitude to the positron dose error and can, therefore, be neglected in further consideration of the positron emission point spread function. Normalization of the positron dose distribution (dose = 1 at r=0) illustrates the effect of the blurring due to the isotropic emission as well as the image magnification due to the source/film geometry. Figure 2-11 is a plot of the normalized dose as a function of radial distance and represents the positron emission point spread function.

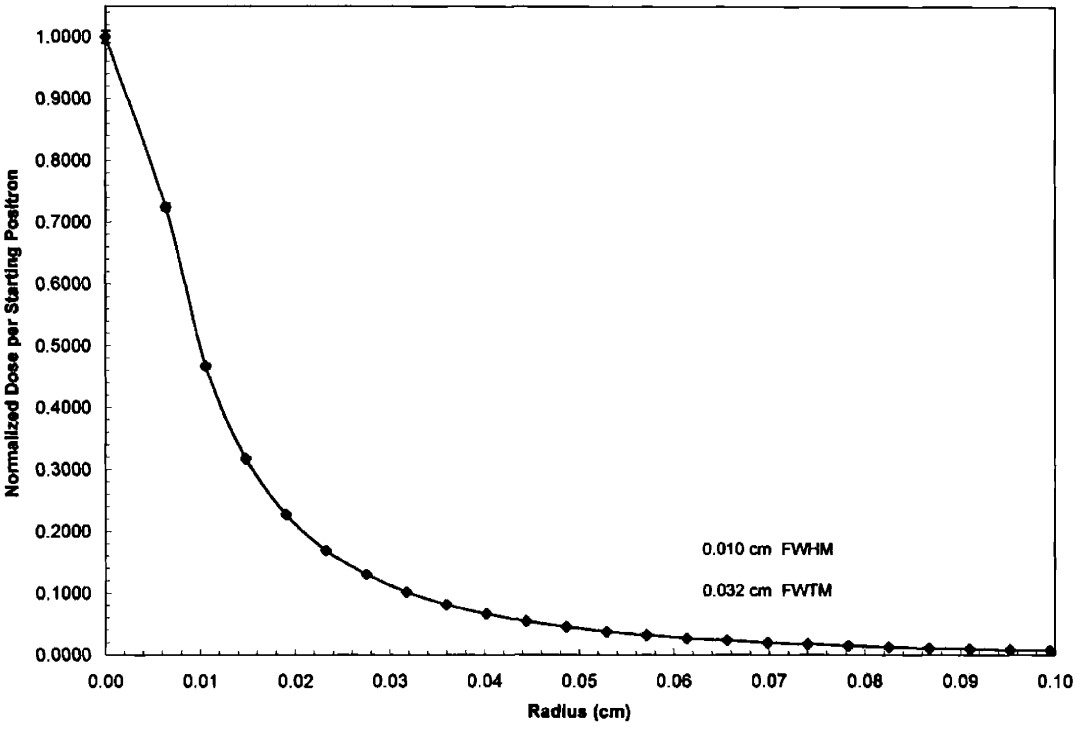

Figure 2-11. Normalized positron dose having a FWHM of 0.010 cm and a FWTM of 0.032 cm. For most radial points the positron dose error is smaller than the point indicator.

2.4.1.4 Film Scanning

The final process affecting resolution is the scanning of the radiochromic film in order to extract spatial dose deposition information. Quantification of the loss in resolution resulting from the scanning and digitizing of the film image was accomplished by measuring the modulation transfer function (MTF). For any type of imaging process, the modulation transfer function represents how an input signal is altered during the process. For example, consider an input signal Ψ which varies in intensity according to

$$\Psi(f_x) = \Psi_0 \cos(2\pi f_x x) \tag{2.17}$$

This function has a spatial frequency, f_x, which is measured in cycles per unit distance and will have a maximum intensity of Ψ_{max} and a minimum intensity Ψ_{min}. If this signal is input into an imaging device with perfect resolution, the amplitude and frequency of the output signal will not change. Real components such as the scanner in question, however, degrade the signal by altering the frequency and amplitude of the signal. The amount of change in the output signal

will vary depending on the spatial frequency of the input signal and is calculated by using Equation 2.18.

$$MTF(f_x) = \frac{\Psi_{max}(f_x) - \Psi_{min}(f_x)}{\Psi_{max}(f_x) + \Psi_{min}(f_x)} \tag{2.18}$$

The resulting MTF for a particular process is normalized to unity at a spatial frequency of 0.0 cycles per unit distance. Normalized MTF's for different imaging processes can be combined simply by multiplying the individual MTF's. This process is equivalent to multiplication of the Fourier transform of a point spread function.

For the MICROTEK scanner (described in detail in §2.5.1) used at LABA, quantification of the MTF was accomplished using the Kodak TL-5003 Digital Science Imaging Test Chart.[20] This chart contains test patterns having spatial frequencies ranging from 1.18 to over 20 cycles per millimeter (cycles/mm or line-pairs/mm are equivalent units). Similar test patterns at frequencies less than 1.0 cycle/mm were created using a Hewlett Packard 4500 laser printer and the PhotoImpact software package. All scans (using the process described in §2.5.1) were conducted using the "256 Shades of Gray" setting which resulted in perfectly black sections having a scanner signal of 0, while perfectly white sections gave a signal of 255. The 0.0 cycle/mm measurement was obtained by scanning a perfectly black and perfectly white block on the test sheet and using the resulting signals in Equation 2.18. Test patterns at each spatial frequency consisted of five alternating white and black bars of equivalent width. A scan of each pattern resulted in a 2-D matrix of values ranging from 0-255. The matrix was exported to MATLAB where the maximum and minimum signals along with their respective standard deviations were calculated. Values calculated in this manner represented Ψ_{max} and Ψ_{min} and the respective error at a particular spatial frequency. For each spatial frequency Equation 2.18 was used to calculate the MTF. These quantities were then normalized to the 0.0 cycle/mm measurement such that MTF(0.0)=1.0. Figure 2-12 represents the normalized MTF derived for the MICROTEK scanner at a scanning resolution of 300dpi.

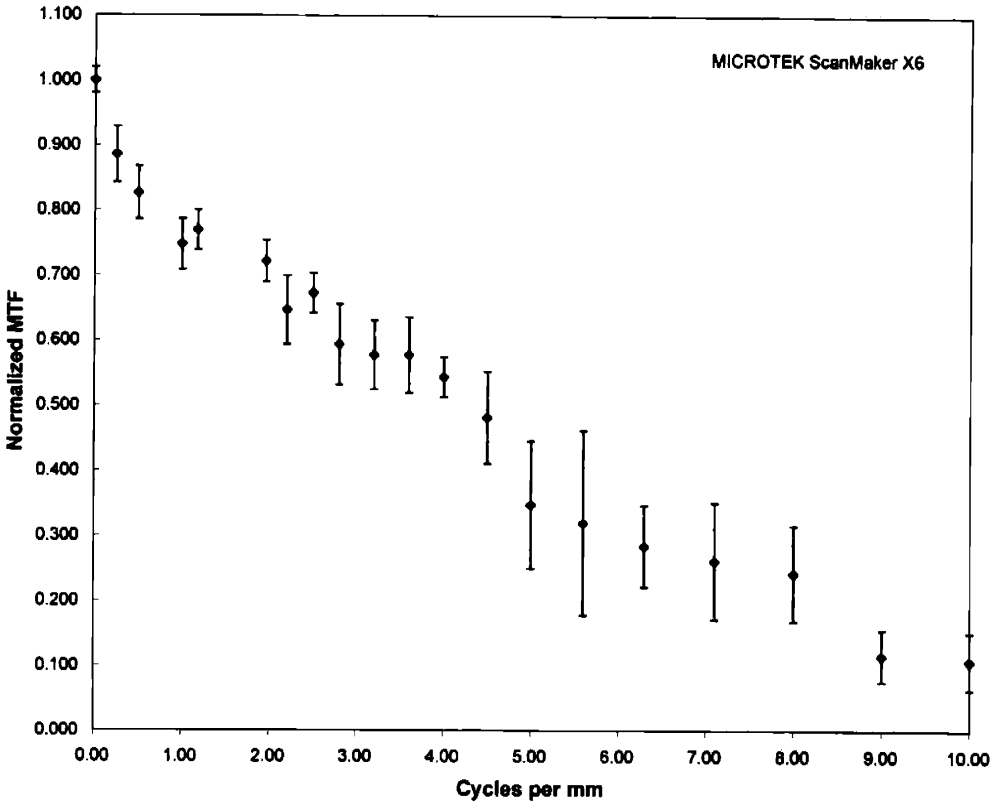

Figure 2-12. Normalized MTF for the MICROTEK scanner at a scanning resolution of 300dpi.

2.4.2 Overall Resolution

Having quantified the resolution loss associated with each step in the process, an overall technique resolution could now be calculated. Results from §2.4.1.1 and §2.4.1.2 indicated that the charged particle scattering and film coloration contribute negligible loss in resolution. Positron emission and scanning, therefore, determine the overall resolution. Using the results of the MCNP simulations, the Fourier transform of the point spread function resulting from the emission of positrons was obtained using the 1-D Fast Fourier Transform (FFT) algorithm in MATLAB. Multiplication of the point spread Fourier transform with the experimentally derived scanner MTF resulted in an overall process MTF which is illustrated in Figure 2-13. By convention, the cut-off (limiting) spatial frequency is defined as the point where the process MTF is 0.1, and the limiting resolution is simply the reciprocal of the limiting frequency. Based on the overall MTF illustrated in Figure 2-13, the limiting resolution of the entire process is calculated to be 4.6±0.2 cycles/mm (0.22±0.01 mm).

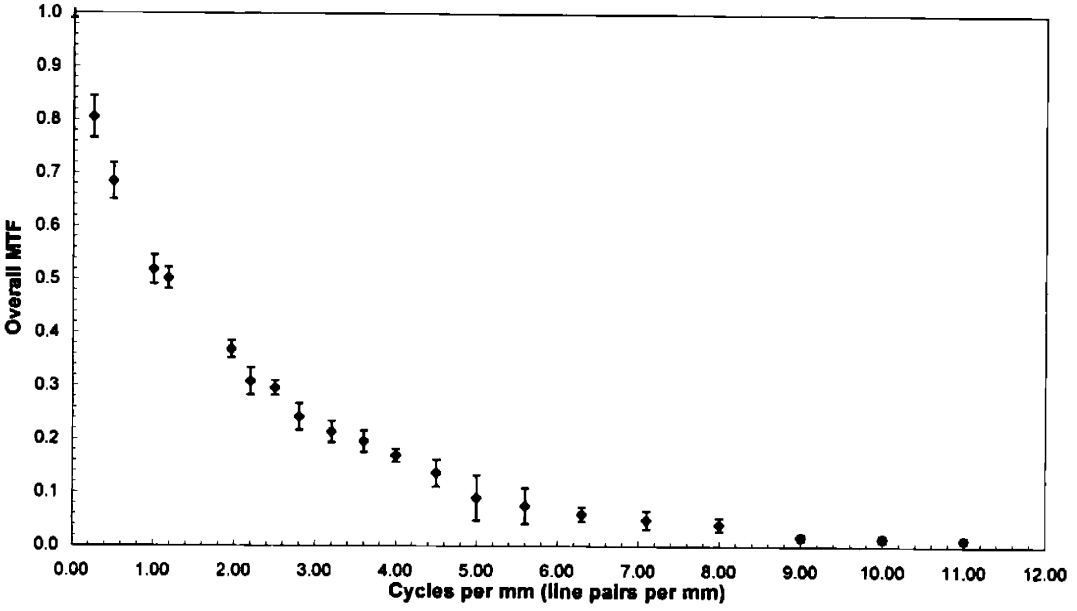

Figure 2-13. Overall Modulation Transfer Function of the current density measurement technique.

Utilizing the configuration described in this chapter, information about the beam current density can be resolved to 0.22±0.01 mm, which exceeds the limits (0.5-1 mm) achievable with beam profilers or harps. This value represents limitations based on positron emission and film scanning using 1.5 MeV deuterons on carbon. While other scanners will have properties different than that used in this experiment it is reasonable, however, to assume that most will have resolutions which are comparable to the limit imposed by the positron emission. Simulations have indicated that target thickness has little effect on the resolution limits for deuterons at 1.5 MeV. At this energy deuterons have a range of only 14 microns in carbon, and cross-sections fall off dramatically with decreasing energy, resulting in the majority of radioisotope being produced within a few microns of the surface. Over half of the total ^{13}N is produced within 4 microns of the surface. If, however, this technique were used at higher energies or if protons were used, serious consideration would have to be given to the positron spreading since more and more production would occur at deeper depths. At high bombarding energies resolution will undoubtedly suffer when thick targets are used. Particle ranges in carbon and boron for energies of 4 MeV are 120 μm for protons and 80 μm for deuterons. Lateral spreading at these higher energies also increases by a factor of 100 over the 0.0367 μm value given in §2.4.1.1. The maximum thickness required would have to be large enough to produce enough radioisotope to deposit sufficient dose in the film. Optimization of target thickness is discussed in greater detail in §2.6. Finally, improvement to the derivation in §2.3.1.3 was achieved using MCNP

simulations, although it did not change the conclusions presented in that section. Using a constant value of 260 eV/μm for -dE/dz, it was calculated that 1.56×10^{11} starting particles would be needed to reach the target dose of 25 Gy. The more accurate MCNP simulations make it clear that this number of particles is high by about a factor of three. Based on the stopping power derivation, each decay was found to deposit 1.602×10^{-10} Gy in the film. MCNP simulations determined that 5.116×10^{-10} Gy will be deposited per decay. When calculating irradiation times using Equation 2.13, using 38.072 as the constant will give more accurate dose predictions. Reasons for this difference are variations in stopping power with energy and the random walk of the positrons. Stopping power increases as the positron slows, causing those particles which start at depth in the carbon to lose energy at a greater rate in the film than those emitted from the surface. The greatest difference between the first approximation and the simulation, however, is that the positron scattering will increase the dose deposited per particle. Not only will some of the particles which start away from the film be scattered upwards and deposit dose, the positron tracks are highly nonlinear. Increasing the path length of each particle within the film will increase dose.

2.5 Experimental Verification of the Technique

2.5.1 Dose Linearity

The first experiment using MD-55-2 film involved verifying linearity of the radiochromic film and the scanning method which would be used in subsequent measurements. By ensuring linearity of the film response and scanning method over the dose ranges expected in the current intensity measurements, results should not exhibit saturation which would lead to an underestimation of current. This test also established a process by which irradiated films can be tested to confirm that the deposited dose had remained in the linear range.

MD-55-2 film is shipped in a light tight package and comes in five separate sheets each measuring 12.7x12.7 cm. Because the film can be exposed by UV radiation emitted from fluorescent lamps, it was important to keep the film in a dark container before and after use. The manufacturer also recommends that it not be exposed to extreme temperature variations. All film used in this and subsequent experiments was taken from Lot #H1146MD55. The scanner used to process the film after irradiation was a MICROTEK ScanMaker X6 which has a maximum resolution of 378 dots/mm. It was driven by MICTROTEK ScanWizard software Version 2.54. All images were processed using the Photoimpact software for Windows.

The film was cut into 30 individual squares measuring approximately 1 cm on a side. These samples were taken to the X-ray irradiation facility at the Massachusetts General Hospital which has a 250 kVp Siemens Stabilipan X-ray machine (Serial # 01067) operating at 12 mA with 2 mm of aluminum filter. The dose rate of the machine, which is routinely calibrated using ion chambers, measured 2.08 Gy/min. Isodose curves located on the table ensured that all samples located within the inner curve received 2.08 Gy/min. Samples placed on a rotating table located 20 cm below the machine were centered using a crosshair projection. Three separate petri dishes, each containing nine pieces of film, were arranged in a triangular pattern centered about the crosshairs on the irradiation table. Care was taken to ensure that no films overlapped or were vertically resting against the side of the dish. Three additional pieces of film were cut and processed but were not irradiated. These films served as the control representing a dose of 0 Gy. Irradiation began after warming the X-ray machine for about five minutes. A timer which automatically controlled power to the machine was used to start and stop the machine to ensure accurate dose delivery. This timer, which had a resolution of 0.01 minutes, was programmed to run for 2.40 minutes delivering a dose of 4.996 Gy to the films. After the irradiation, one piece of film was removed from each dish and placed into a light-tight container labeled with the delivered dose. The films left in the dishes could then be irradiated such that the desired cumulative dose could be delivered. This process was repeated up to 30 Gy in increments of 5 Gy. Subsequently the timer was changed, and cumulative doses of 40, 50, and 80 Gy were delivered. All films including the 0 Gy controls were then transported back to LABA and kept in a dark storage area for 48 hours before scanning.

After the 48 hour waiting period, the films were prepared for scanning. The scanner was set to a resolution of 11.8 dots/mm, and the color setting was set to 256 shades gray. At this setting, a completely white image will have a scanner signal of 255, while a completely black image will have a signal of 0. No artificial contrast or brightening was used during the scans. A single piece of white paper served as a backdrop for all films during the scanning process. All three pieces of film corresponding to each dose point were placed on the scanner glass underneath the paper and scanned simultaneously. To avoid irregularities which could have resulted from the cutting and handling of the film, edges were digitally cropped. The final image, which represented the center region of each film, was 90x90 pixels.

Processing of the digital image was conducted by loading data from the scanned film into the MATLAB program. MATLAB handles each image as a 90x90 matrix with the raw scanner signal data at each (i,j) location. A mean scanner signal and standard deviation was calculated using data from the 8100 pixels in each film. Standard deviations in the scanner matrix data

ranged from 0.8% for the 0 Gy films to 3.3% for the 80 Gy films, indicating good film uniformity and low noise in the scanning process. Averaging the mean signals from the three films gave an overall scanner signal representing each dose level. Propagation of the separate standard deviations resulted in total signal error ranging from 0.48% at 0 Gy up to 1.63% at 80 Gy. Verification of film image and scanner stability over time was tested by scanning the 25 Gy films after 24 and 48 hours. These same films were also scanned over two months later. Between 24 and 48 hours the scanner signal changed by 13.2%, but changed by only 2.5% over a period of more than two months. Measurements of film response are given in terms of net optical density (O.D.) as indicated by Equation 2.19.

$$\Delta O.D. = log(\frac{S_0}{S}) \tag{2.19}$$

where,

S_0: raw scanner signal for 0 Gy film

S: raw scanner signal at dose level

Plotting net O.D as a function of dose indicates that the film response and scanning process is, in fact, extremely linear over the range of interest. A linear regression taken from the data (R^2=0.981) found that dose delivered to film which is then scanned in this manner could be determined by the relationship: Dose=191.2±18.4 x net (O.D.). Results of the experiment are plotted in Figure 2-14. While absolute measurement of dose is not a crucial part of the technique, accurate determination of current density relies on the fact that the change in optical density is proportional to the delivered dose. Based on results of this experiment and on data in the literature[11, 13] keeping the maximum dose delivered to any part of the film below 100 Gy assures that the color change remains in the linear range. Using the relationship determined in this experiment, all films used in subsequent experiments will be checked to ensure that they are within the linear range.

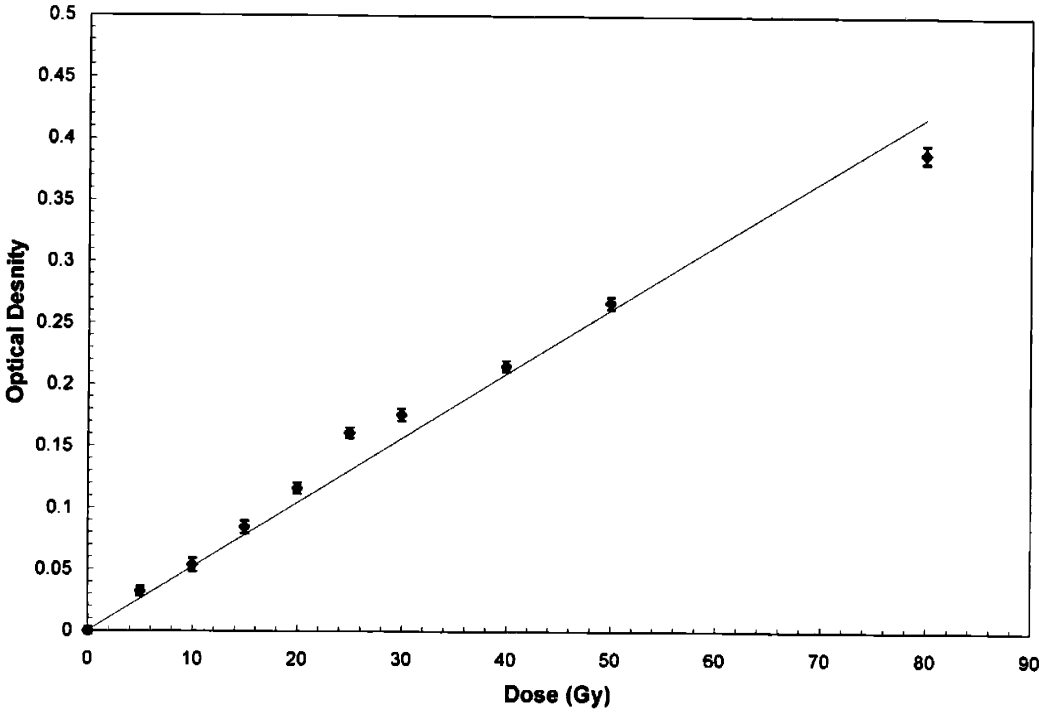

Figure 2-14. Optical density plotted as a function of dose for MD-55-2 film irradiated with 250 kVp X-rays.

2.5.2 Establishing a Measurement Protocol

The first experiments to verify this technique were conducted to establish a measurement protocol and to design an algorithm by which to analyze the information contained on the irradiated film. Three separate measurements were made at currents between 200-250 μA. Irradiated films were analyzed with a signal processing algorithm written with the MATLAB software, and the resulting current density profiles were measured. Dose levels were checked against the calibration curve from the previous section to ensure that the film response remained in the linear range.

2.5.2.1 Experimental Procedure

Each experiment began by tuning the accelerator on an aluminum beam stop which is exactly the size and shape of the target shown in Figure 2-5. Using an aluminum beam stop instead of the carbon allowed for irradiation of the target immediately following the tuning without having to wait for isotope decay. A water-cooled collimator, which facilitated centering of the beam, was located directly in front of the beam stop. Minimization of the current on the aperture using the steering magnets and focusing quadrupoles ensured that the beam was focused

and would hit the center of the graphite once the aluminum surrogate was replaced. After the accelerator had been tuned, the graphite target was positioned, and the cooling tubes and current measurement leads were connected.

For the three films used in this experiment, irradiation times (t), decay times (t'), and film irradiation times (T) were determined using Equation 2.13 with the improved constant of 38.072. Earlier accelerator runs at the settings used in these experiments had indicated that the beam was approximately 2 cm^2 in size. Times were set such that doses of 25-30 Gy would be delivered to the film. Experiments were conducted at current levels of 225, 240, and 200 μA with irradiation/decay times determined to allow $1.1x10^{11}$ decays to occur during the film irradiation. Irradiations began by starting a current integrator and timer connected to the target. Terminal voltage was set to 0.75 MV and the beam was brought up to the desired current level. After 30 seconds of irradiation at the peak current level, the beam was shut off and the current integrator was stopped. Although the irradiation time was designed to be 30 seconds, increasing current from zero to its maximum value required about 50 seconds, making the total irradiation time about 80 seconds. The effect of this transient beam current is discussed in §2.5.2.3. After irradiation the target was allowed to decay for a short period before it was disconnected from the beamline. It was then placed on a polyethylene stand in the radiation vault away from the beamline with the graphite surface facing upwards. At the end of the decay time, t', the film was placed directly on the target surface, and the lights in the vault were turned off. Although the sensitivity to the UV portion of fluorescent lighting is small, it is desirable to minimize the exposure to UV since it causes darkening over an extended period. The film was left on the target for a time, T, before being removed and placed into a light-tight storage container where it was stored for 48 hours. All films were scanned at least 48 hours after the irradiation to allow for the color change to stabilize.

2.5.2.2 Experimental Results

Results of the film irradiations were processed using a MATLAB program which converted the scanned information into net optical density, dose, and current density. Films were scanned at a resolution of 11.8 dots/mm. Files generated in the scanning process were 300x300 matrices with pixels ranging in value from 0-255. Net optical density (OD) was determined for each pixel using Equation 2.19 with a 0 Gy signal (S_o) of 240.2763. Figure 2-15 is a plot of the net OD based on the raw scanner signal for the 225 μA beam.

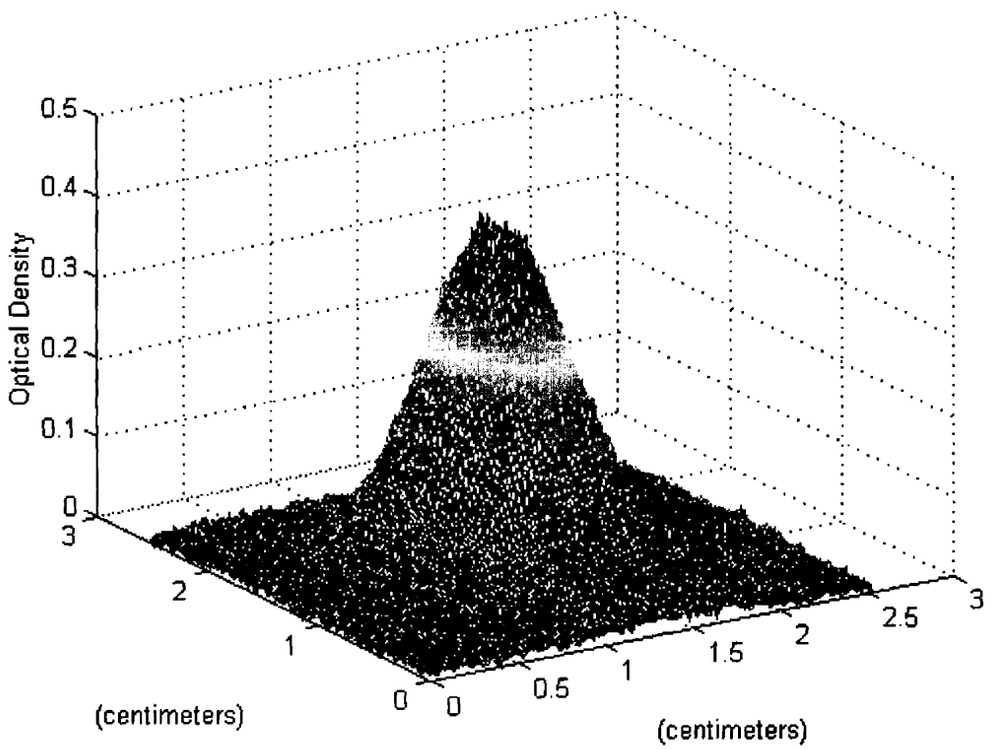

Figure 2-15. Net optical density of the film based on the raw scanner signal for 225 μA beam.

The beam edge was defined by setting the net optical density to zero for any pixel which fell below five percent of the peak optical density value. Figure 2-16 is a plot of the OD after having been truncated at the 5% level to define the beam edge. Dose to the film was determined by multiplying the OD value of each pixel by the constant, 191.2, determined in §2.5.1. By checking to see that the dose was kept in the range 0-100 Gy at all points in the film, the linear dependency of dose on current density was ensured. Figure 2-17 illustrates the resulting dose deposition on the film. Uncertainty in the dose measurement is ±9.6%.

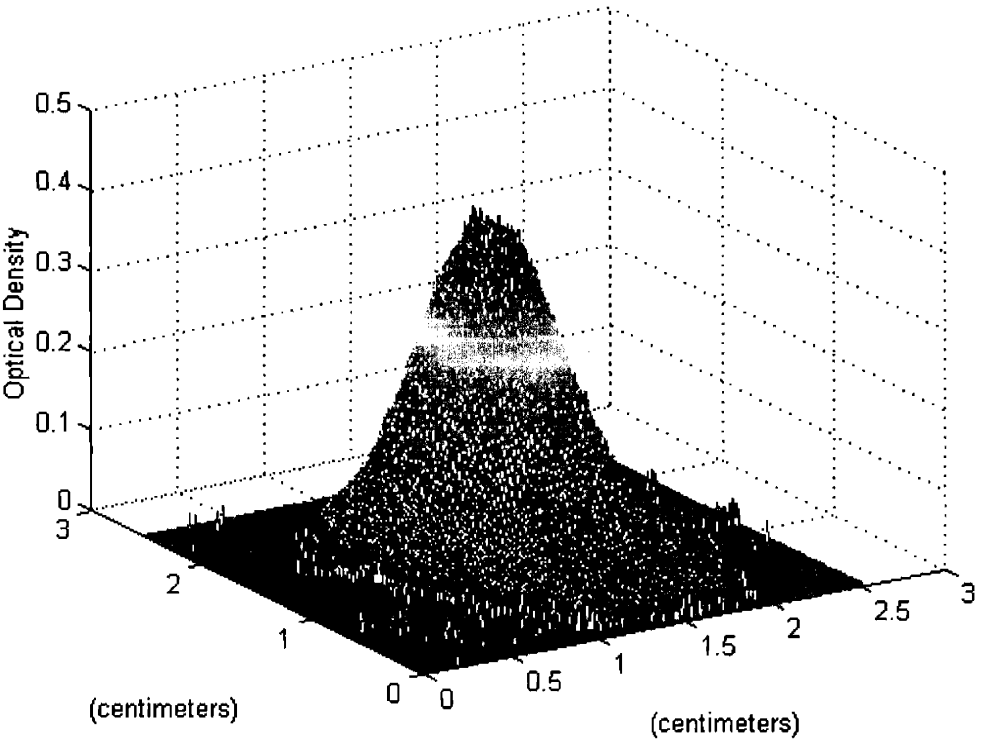

Figure 2-16. Plot of the optical density after truncating values on the periphery to define the beam edge.

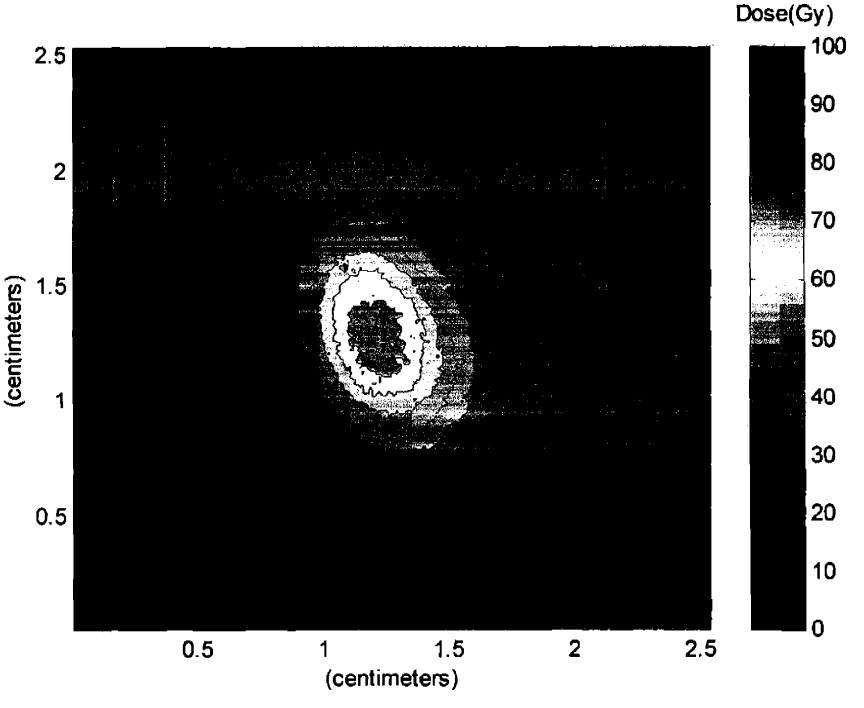

Figure 2-17. Plot of dose deposition used to check that the film has been delivered between 0 and 100 Gy.

Having determined that dose deposition was in the linear range, current density was then calculated from the optical density. Since all pixels having an OD value of 0.0 were assumed not to contribute to the beam, the current density was calculated by first dividing the pixel OD by the sum of all the nonzero OD pixels. This value is multiplied by the measured current and divided by the pixel area (7.168444×10^{-5} cm^2 for 300 dpi scan) to obtain a current density. This process also allowed for calculation of the total beam area which was simply the number of nonzero pixels multiplied by the pixel area. In this case the beam measured 2.55 cm^2. The resulting current density is plotted in Figure 2-18.

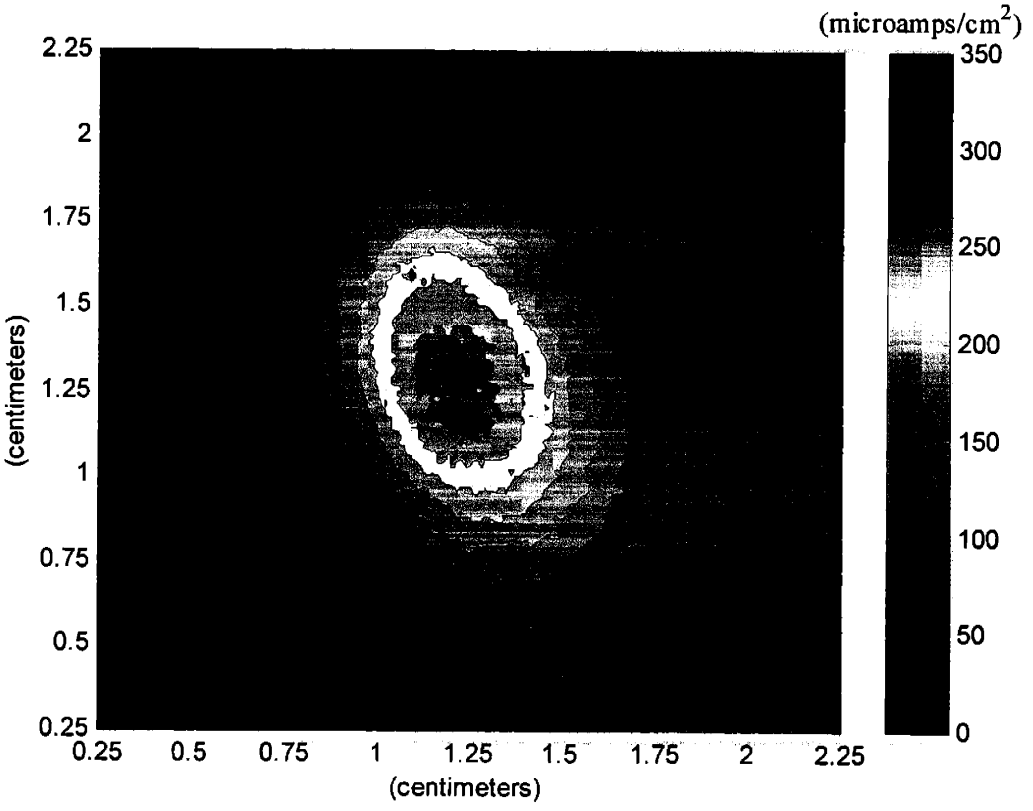

Figure 2-18. Current density of the 225 μA beam determined from the change in optical density of radiochromic film.

Plots of current density and dose are shown in Figures 2-19 and 2-20 for the two other beams measured in this experiment. Total beam currents were 240 and 200 μA respectively.

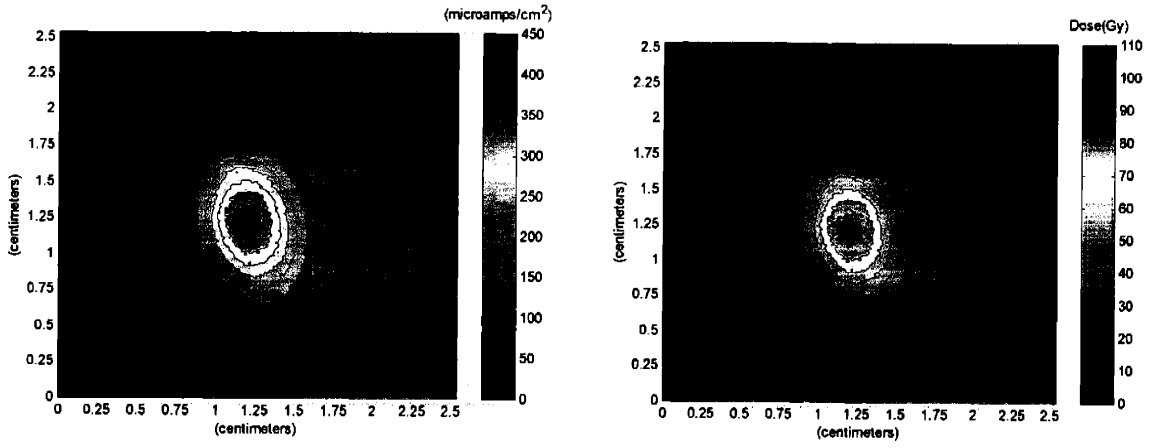

Figure 2-19. Current density and dose plots for 240 μA beam.

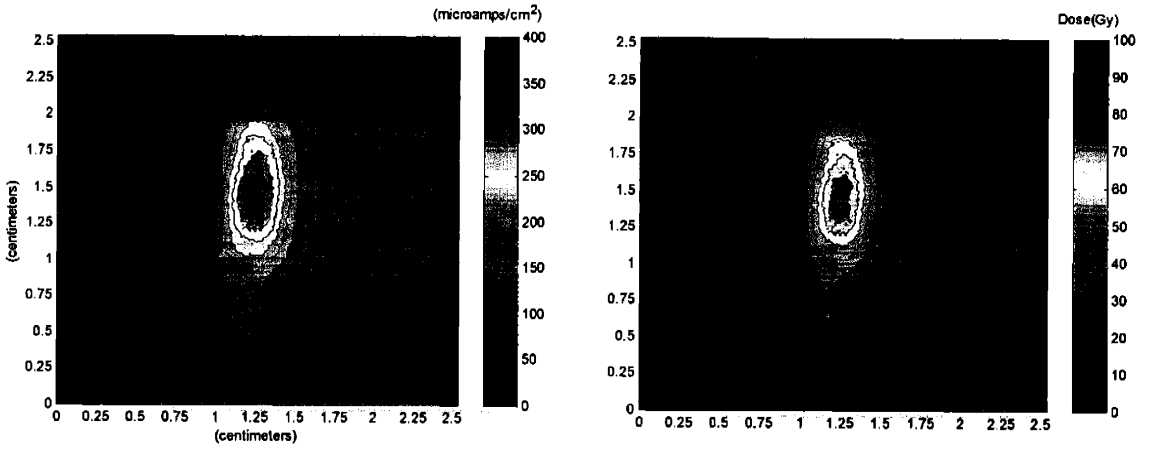

Figure 2-20. Current density and dose plots for 200 μA beam

2.5.2.3 Conclusions

Current densities in beams of hundreds of microamps or more can be measured with the technique discussed in this chapter. Each measurement can be tailored within certain limits to fit various time requirements. For the experiments involving the 225, 240, and 200 μA beams, respectively, all irradiation times were set at 30 seconds; decay times were 1650, 600, and 600 seconds; film irradiation times were 3000, 285, and 336 seconds. Total measurement times therefore were 78.0, 15.25, and 16.1 minutes. The definition of irradiation time requires further explanation.

From Equation 2.13 it is apparent that calculation of the current density can be determined from absolute dose through multiplying by a constant which depends only on the irradiation times and dose deposition per particle. As a check of the values calculated with the procedure described in §2.5.2.2, which does not rely on knowledge of dose, current densities were evaluated without use of the total measured current. Current densities based on absolute dose were found to differ from previous values by 50%, 45%, and 60% in the respective beams. The magnitude of the difference was constant over the entire beam. When total beam current was reconstructed by taking the sum of the current density x area for all pixels, total current levels were less than the value measured on the current integrator. This difference results from the fact that the transient portion of the target irradiation produces radioisotope which contributes some percentage of the film image. Raising the beam current from zero to the maximum value requires several tens of seconds. Termination of the irradiation takes less than a second. At high currents significant radioisotope production could occur during the startup period. Once maximum current is achieved, however, variations in current produce a negligible transient effect. The fraction of the image due to the transient period was calculated using the total charge collected during the irradiation. Any charge over and above the value of (maximum current x 30 seconds) was due to beam during the startup period. The total number of decay particles resulting from irradiation in this transient period was divided by the total number of decay particles in order to get a percentage of the film image due to the transient period. For the three beams, the transient period contributed 31.3%, 28.9%, and 29.8% of the total dose. Once the current levels were adjusted to an average current value (total charge/total irradiation time), a second comparison of the measured current densities resulted in differences of 1.2%, 4.5%, and 10%.

Contribution from the transient startup was further tested in a separate experiment where current densities for beams of 290, 203, and 100 μA were evaluated. In these experiments transient contributions to the film image were 15.0%, 8.8%, and 9.0%. After the film from each run was checked to ensure that the maximum dose did not exceed 100 Gy, total current was calculated based solely on the dose deposited on the films. Total current measurements calculated in this manner yielded values of 236.3, 186.6, and 94.8 μA. Deviations from the values measured by the current integrator were 18.5%, 8.1%, and 5.2%.

It is apparent that the irradiation/decay times must allow for the production during the transient startup period. Times should be set so that at least 90% of the film image comes from the beam during the steady state period. In subsequent tests this was accomplished by extending the irradiation times from 30 seconds to either 60 seconds or 2 minutes. Comparison of the current density calculated with and without using the measured current provides a means by

which to confirm not only that irradiation times were properly set, but also to ensure that the dose delivered remained in the linear range of the film.

A prerequisite for this technique is that the maximum dose value be kept below 100 Gy to ensure that the response remains in the linear range. Once films have received enough dose to saturate, prediction of the current based on the change in OD will under-predict the total current. Equation 2.13, which was used to calculate appropriate irradiation times, was derived for a uniformly distributed beam. While this equation is accurate when checked on a pixel by pixel basis, it will under-predict the dose in the center region of the beam where the current density could be much higher than the area average. There are two possible remedies to this shortcoming. The first is simply to generate two or three images after a single target irradiation using decreasing numbers of particles for each film. While the current density measurement will not be affected by the total number of particles used to generate the film image, if one or two possess doses higher than 100 Gy, the third should be under 100 Gy. The second is to estimate the peaking factor of the beam based on a pure Gaussian shape as given in Equation 1.4. For most focused beams, this value will be between 1-4.

2.5.3 Repeatability in the Accelerator Settings

A major concern in the use of accelerators in neutron capture therapy is the ability to replicate ion beam characteristics over extended periods of time even after changes in filament current, stripping foils, or other beam optics. This is especially true for applications such as brachytherapy which require the beam to be transported down a long, thin tube before striking a target. Tuning the accelerator to find optimum conditions before every run can be extremely time consuming.

To investigate repeatability, six separate runs were conducted using varying accelerator settings. Three runs were conducted over a period of three days at accelerator settings commonly used for experiments. The currents achieved in each of the runs were 210, 215, and 200 μA. In these first runs, the beam was peaked and focused using the aluminum beam stop as described previously. Images were acquired on the films and scanned after 48 hours. After a period of about five weeks, the accelerator was operated at identical settings, and beam profiles were measured for comparison. While the second set of runs was conducted at optical settings identical to the first, no peaking or focusing was attempted. Since no peaking was attempted, currents achieved in the second set of runs were slightly lower than the first. Peak currents reached in the second runs were 192, 158, and 179 μA. Irradiations were conducted identically to the first runs, and films were scanned 48 hours later. This second set of runs was completed after

the accelerator had been opened to change a complete set of stripping foils. During this time a drop in the filament current from 130 A to less than 65 A had also occurred. A current level of 65 A indicated that the filament was approaching the level at which it required replacement. Replacement usually occurs once its current drops to around 50 A.

Because the current levels were slightly different in the second set of runs, current densities were normalized for comparison. Beam areas were also compared. Table 2-4 lists the currents and beam areas achieved in each of the runs, while the normalized current densities are plotted in Figures 2-21, 2-22, and 2-23. For the beams indicated in Figure 2-23, the peak current density was over 1.4 mA/cm^2. Based on the similarity in size, shape, and current density distribution it was shown that by returning to a particular setting, beam parameters can be replicated even after significant changes in the stripping foil and filament. Even without focusing and peaking of the current on the second set of runs, beam areas varied by 5.2%, 17.1%, and less than 1%, respectively. It can also be verified by comparing the widths of the contours in the figures that the variation in current density over the area of the beam was similar between the two runs at a particular setting.

Table 2-4. Summary of the six runs used to test repeatability of the accelerator settings.

Run	Current (μA)	% of Film Image Due to Transient	Beam Area
R-1a	210	2.2	2.67
R-1b	192	5.9	2.81
R-2a	215	5.8	1.29
R-2b	158	5.3	1.07
R-3a	200	6.2	0.40
R-3b	179	8.0	0.40

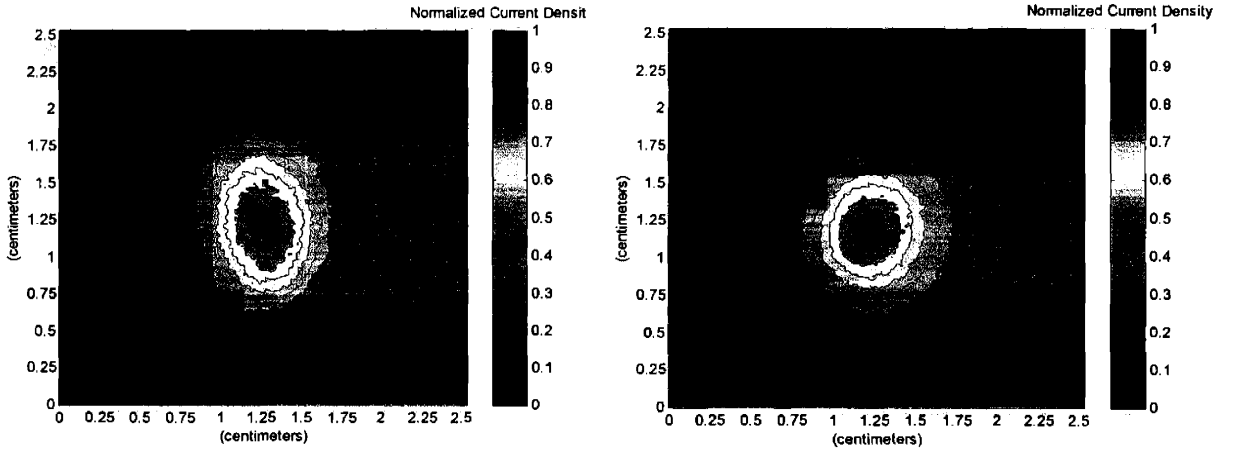

Figure 2-21. Two beams of approximately 200 μA measured 5 weeks apart to test beam repeatability. Acceleration electrode (10.69 kV), Focus electrode (2.06 kV).

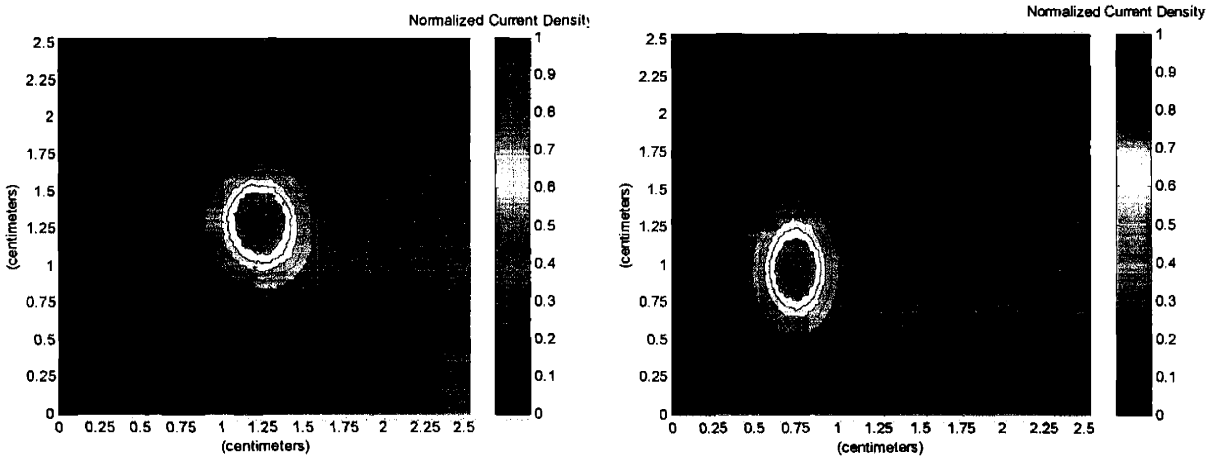

Figure 2-22. Two beams tested 5 weeks apart using electrode settings: Acceleration (7.8 kV), Focus (1.45 kV).

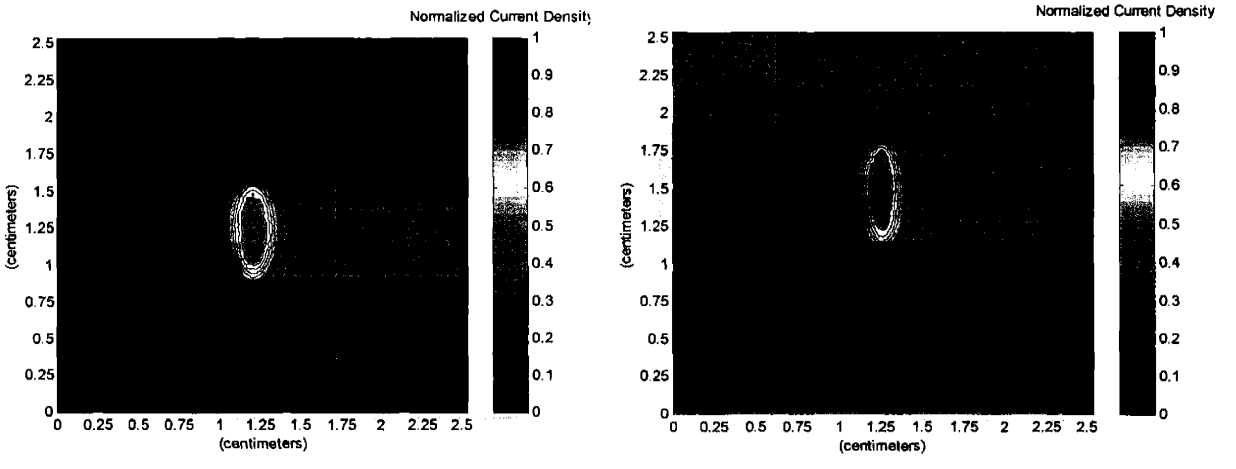

Figure 2-23. Beams having current densities in excess of 1.4 mA/cm^2 measured 5 weeks apart.

2.6 Future Work

Improvements and future work relating to this technique will focus on two areas: (1) development of a target for measurements of proton beams and (2) optimizing target thickness. For energies up to 4 MeV, ^{11}B is the best candidate target material for analyzing the current density of proton beams. Integration of experimental cross-section data[21] using Equation 2.8, yields a thick-target cross-section of 53 mbarns for boron irradiated with 4.0 MeV. Figure 2-24 plots the thick target cross-section for $^{11}B(p,n)^{11}C$ at energies between 3.1 and 4.1 MeV.

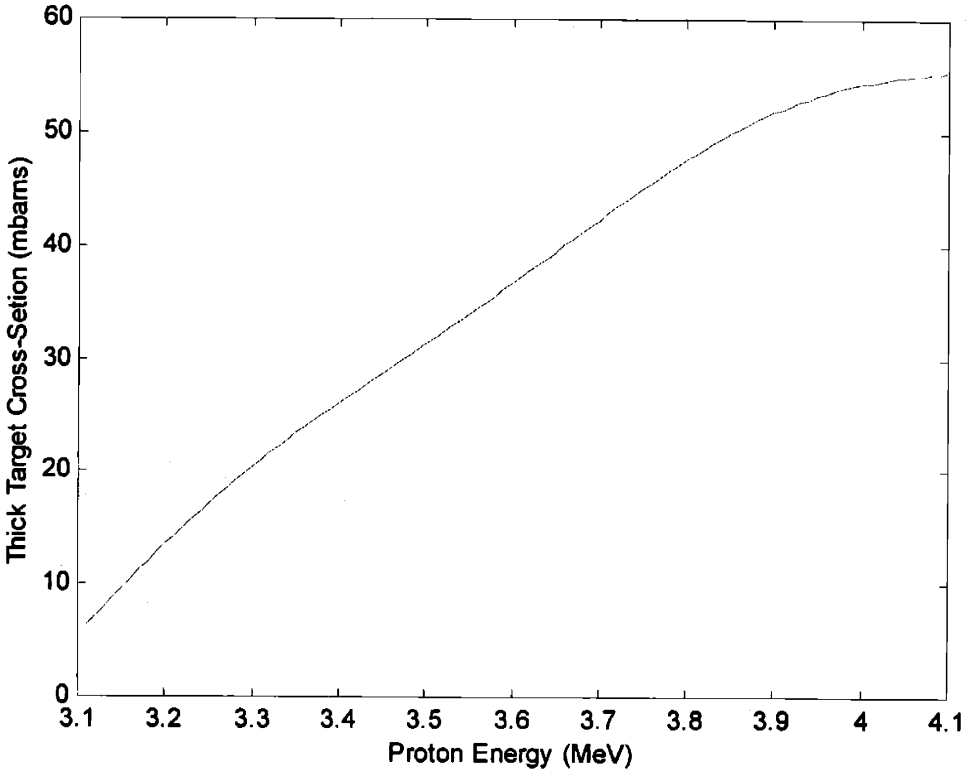

Figure 2-24. Thick target cross-section for boron irradiated with protons having energies of 3.1-4 MeV.

^{11}B makes up 80% of natural boron and has a density of 2.34 g/cm^3. Calculations based on Equation 2.12 incorporating differences in cross-section, density, half-life, and abundance indicate that to achieve equal film doses using 4.0 MeV protons on thick boron targets, all that is required is to increase film irradiation times by a factor of 2-3 over those used for 1.5 MeV deuterons on carbon. The major concern, however, in using protons or deuterons at energies above 1.5 MeV is range of the charged particles in the target and their effect on resolution.

The final step in optimizing current density measurements for use with either material requires minimizing the thickness of the target so that it can be used at any energy or current level. It was mentioned previously that for higher energies and especially for use with protons, consideration must be given as to the optimal target thickness. This is due to the fact that in thick targets, the charged particle slows from its maximum energy to zero energy within the target while at the same time creating reaction products. Ranges of charged particles with high energies (~ 4 MeV) could be as much as an order of magnitude greater than 1.5 MeV deuterons in carbon. If a large amount of radioisotope is produced deep in the target, scattering of the positrons will degrade the resolution of the technique. Also, at very high currents, excessively thick targets will unnecessarily increase the target temperature. While carbon is a reasonably good thermal conductor, boron possesses a low thermal conductivity comparable to stainless steel. A solution which alleviates both problems is simply to reduce the target to an overall thickness of around 1 μm. While standard machining cannot achieve such small dimensions, 1 μm layers can be created with carbon and boron using a variety of thin-film deposition techniques. One such method, electron beam sputtering, can provide ultra-thin (up to 1 μm) surface layers with good uniformity and adhesion. Details of this process will be described in the next chapter. By using thin layers, the overall resolution becomes insensitive to beam energy. Targets deposited in such a manner would also allow for either boron or carbon, or perhaps both materials, to be sputtered onto existing accelerator targets. Measurement of current density could then be accomplished using an existing target with the only modification being the deposition of the surface layer.

Reducing the target thickness, however, also lowers production of the needed radioisotope. This is also true for the energy deposited per decay. MCNP simulations of positron emission from a thick carbon target found that positrons emitted from the surface deposited 1852 MeV/g in the film, while positrons emitted from a distance into the target equal to the maximum range of the deuterons deposited 2645 MeV/g. Recalling that the dose deposited per decay from a thick carbon target was calculated to be 5.116×10^{-10} Gy, Figure 2-25 represents the fraction of thick target dose deposited per decay in thin carbon targets bombarded by 1.5 MeV deuterons. This figure incorporates the reduction in target atoms caused by decreasing the thickness, the increase in cross-section resulting from the higher average ion beam energy, and the variation of film dose deposited per decay. Comparisons are made based on equivalent target irradiation, decay, and film irradiation times.

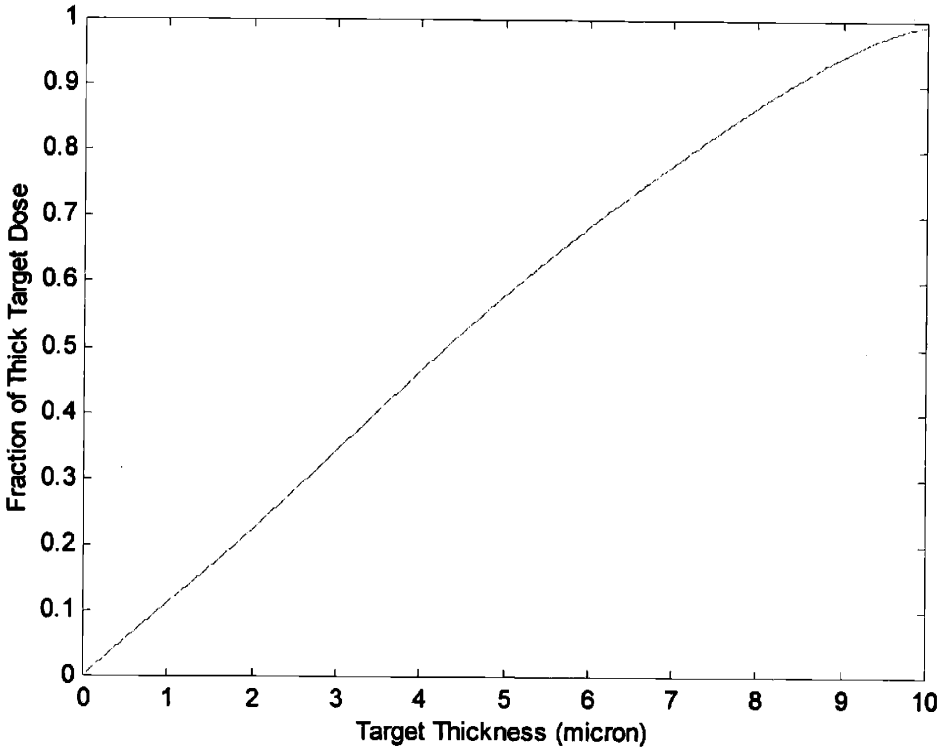

Figure 2-25. Fractional dose deposition per decay in thin targets. Comparisons are made assuming equal target irradiation (t), decay (t'), and film irradiation (T) times.

Reduction of the target thickness does not result in the need for seriously altering the experimental protocol established for thick targets. For 1.5 MeV deuterons on a 1.0 μm carbon target, the dose deposited in the film per decay is 11% of the thick target value. Slight variations in t, t', or T could be implemented to increase the delivered dose to the level needed for a measurement. The same argument holds also for a 1 μm boron target. Decreasing the target thickness to 1.0 μm with either material will alleviate thermal and resolution concerns which would otherwise be encountered with thick targets.

2.7 Conclusions

The ability to measure current density in ion beams is necessary for the development of accelerator targets capable of handling high heat loads. Determination of the current density allows the incident heat flux on a target to be calculated simply through multiplication by the beam energy. Accurate therapy planning is also facilitated through the knowledge of the beam size and current density. Typical methods currently available for beam profiling are limited to

low overall beam power and currents of around 100 μA. These methods have resolutions which are on the order of 0.5-2 mm.

This chapter has outlined the details and characteristics for using charged-particle reactions in combination with radiochromic film to measure current density in high power ion beams. For 1.5 MeV deuterons on a thick carbon target the technique has an overall resolution of 0.22±0.01 mm. Resolution was found to be limited by the isotropic emission of positrons as well as the inherent characteristics of the optical scanner. MD-55-2 radiochromic film was shown to exhibit linear response over the range of doses encountered in current density measurements. This technique was used to measure current density in beams exceeding 1.4 mA/cm^2. It was also used to demonstrate the repeatability of the LABA accelerator under different conditions. While the majority of derivations, simulations, and calculations were performed for 1.5 MeV deuterons on a thick carbon target, the equations and conclusions developed in this chapter can easily be adapted to other energies, particle types, or target thicknesses. Carbon is a satisfactory target for deuteron beams having energies >0.7 MeV. For beam energies of interest in neutron capture therapy (1-4 MeV) the most likely target material for use with protons is ^{11}B. Protons with energies above the $^{11}B(p,n)$ threshold, will have ranges of up to 120 μm. Isotopes produced deep (>10 μm) within a target will degrade the resolution of the technique as a result of scattering within the target material. Decreasing target thickness to around 1 μm results in resolution becoming insensitive to beam energy. It also alleviates any thermal limits which might be imposed by a thick target. Although the reduction in thickness will decrease the amount of produced radioisotope, successful measurements can be made simply by altering irradiation, decay, or film irradiation times.

2.8 References

1. M. Torikoshi, K. Noda, E. Takada, T. Kanai, S Yamada, H. Ogawa, K. Okumura, K. Narita, K. Ueda and M Mizobata, "Beam monitor system for high-energy beam transportation at HIMAC," Nuclear Instruments and Methods in Physics Research A, **435:** 326-338 (1999).

2. R.B. Fair, "A wide slit scanning method for measureing electron and ion beam profiles.," Journal of Physics E: Scientific Instruments, **4:** 35-36 (1971).

3. Annual Book of ASTM Standards ASTM standard E986-86, 1986.

4. M.D. Crapper, J.M. Lacey, S.D. Green and P.R Hadfield, "The measurement of the intensity profile of an electron gun using modulation techniques," Vacuum, **46:** pp. 23-25 (1995).

5. NTG Neue Technologien GmbH, "Rotating wire scanner Type DS 040 (Equipment Manual),"

6. NTG Neue Technologien GmbH, "Beam Profile Measuring System (Grid, Harp) Type DG070,"

7. S. K. Guharay, M. Hamabe and T. Kuroda, "A novel ion beam monitor using Kapton foils," Review of Scientific Instruments, **69:** 2182-2183 (1998).

8. General Electric, "Fuzed Quartz Properties and User's Guide: GE Type 214, 214LD, 124," 1995.

9. Star Tech Instruments, "BIP-5100 Beam Profiler," 2001.

10. M.L. Firouzbakht, D.J. Scholyer and A.P. Wolf, "Cross-section Measurements for the 13C(p,n)13N and 12C(d,n)13N nuclear reactions.," Radiochimica Acta, **55:** 1 (1991).

11. A. Niroomand-Rad, C.R. Blackwell, B.M. Coursey, K.P. Gall, J.M. Galvin, W.L. McLaughlin, A.S. Meigooni, R. Nath, J.E. Rodgers and C.G. Soares, "Radiochromic film dosimetry: Recommendations of AAPM Radiation Therapy Committee Task Group 55," Med Phys, **25:** 2093-2115 (1998).

12. M.A. Stevens, J.R Turner, R.P. Hugtenburg and P.H. Butler, "High-resolution dosimetry using radiochromic film and a document scanner.," Physics in Medicine and Biology, **41:** 2357-2365 (1996).

13. International Specialty Products, "GAFCHROMIC MD-55 Dosimetry Medium: Product Description," 2000.

14. W.L. McLaughlin, Y.D. Chen, C.G. Soares, A. Miller, G. Van Dyke and D.F. Lewis, "Sensitometry of the response of a new radiochromic film dosimter to gamma radiation and electron beams," Nuclear Instruments and Methods Physics Research A, **302:** 165-176 (1991).

15. W.L. McLaughlin, J.M. Puhl, Al-Sheikhly, A. Christou, A. Miller, A. Kovacs, L. Wojnarovits and D.F. Lewis, "Novel radiochromic films for clinical dosimetry," in *Proceedings of the 11th International Conference on Solid State Dosimetry II*, Budapest, A. Peto and G. Uchrin, pp. 1995.

16. M.C. Saylor, T.T. Tamargo, W.L. McLaughlin, H.M. Khan, D.F. Lewis and R.D. Schenfele, "A thin film recording medium for use in food irradiation," Radiat. Phys. Chem, **31:** 529-536 (1988).

17. J.F. Ziegler and J.P. Biersack, "Stopping and Range of Ions in Matter," Yorktown, NY, 2000) Computer Code

18. W.L. McLaughlin, C.G. Soares, J.A. Sayeg, E.C. McCullough, R.W. Kline, A. Wu and A.H. Maitz, "The use of a radiochromic detector for the determination of stereotactic radiosurgery dose characteristics," Medi cal Physics, **21:** 379-388 (1994).

19. J.F. Briesmeister, "MCNP - A general Monte Carlo N-Particle transport code, Version 4B," Los Alamos National Laboratory Report, LA-12625-M, 1997.

20. Eastman Kodak Co., "TL-5003 Kodak Digital Science Imaging Test Chart," 1995.

21. K. Ramavataram, R. Larue, V. Turcotte, C. St-Pierre and S. Ramavataram, "Study of the 11B(p,n)11C reaction below the giant dipole resonance in 12C.," Nuovo Cimento A, **58:** 342 (1980).

Chapter 3 Thermal and Mechanical Considerations of Target Design

A neutron-producing target subjected to an energetic beam of charged particles will develop a thermal profile which depends on various factors which can be separated into the general categories of beam, target, and cooling system. Within each of these categories, the specific parameters which determine the final temperature profile are: (1) beam energy and current density; (2) target material and dimensions; (3) cooling rates (heat transfer coefficients) achieved. While Chapter 2 focused on determining the beam current density, §§3.1- 3.3 of this chapter investigates the latter two areas as they pertain to target design.

As a result of the temperature profile generated in the target as well as the mechanical loads imposed by the vacuum and cooling system, substantial thermal and mechanical stresses could develop within the target. Section 3.4 will consider the interaction of thermal and mechanical stresses and the limits they impose on beam size and power for an NCT target.

By drawing on the conclusions from these sections, the goal of this chapter is to establish a process by which the thermal and mechanical performance of a neutron-producing target can be evaluated. Such an evaluation will allow a designer to optimize target dimensions, predict the required cooling parameters, and establish limits on the size and total power of a beam which can be safely handled by the target.

In order to fulfil these stated objectives, the current chapter will begin with a description of the deposition of heat as a function of depth (z) into the target. Once combined with the method described in Chapter 2 for determining the (r, ϕ) distribution of the beam, a complete (r,ϕ,z) dependent model of volumetric heat generation (q''') can be generated. Numerical predictions of temperature profiles resulting from beams of varying size and power will then be presented for beryllium and lithium targets. These simulations are designed to illustrate the relationship between, beam size, target dimension, cooling capacity, and their effect on the total power which can be placed on a target. The subsequent section will introduce a novel technique using liquid gallium metal to satisfy the target-cooling requirements. Experiments conducted with both water and liquid gallium metal will compare and contrast the ability of the two fluids to serve as the heat transfer fluid. These experiments are supplemented by computational fluid dynamics (CFD) simulations. In the final section, the interaction of thermal and mechanical stresses will be investigated and combined with target cooling in finite element simulations which illustrate the process of optimizing performance as measured by maximizing the amount of power which can be safely handled by a target.

3.1 Heat Deposition as a Function of Depth

When a temperature gradient is determined completely by conduction within a material and by boundary conditions applied to its surface, the volumetric heat generation, q''' (W/m^3), must be zero. When an energetic charged particle beam strikes a material, however, heat is not deposited solely on the surface. Depending on the energy of the beam, very little energy may be deposited on the surface while the remainder of the beam energy will be deposited as the charged particle slows through the target. This energy deposition may not occur at a uniform rate and can only be determined by calculating the stopping power (-dE/dz) of the charged particle in the material. With no volumetric heating and a temperature independent thermal conductivity, k (W/mK), the appropriate form of the 1-D, steady-state, general heat equation is

$$\frac{\partial}{\partial z}\left(k\frac{\partial T}{\partial z}\right)=0 \tag{3.1}$$

which has the general solution

$$T(z)=\frac{C_1}{k}z+C_2. \tag{3.2}$$

In this case the heat flux, q" (W/m^2) is constant and the temperature gradient is linear throughout the body. With volumetric heating, however, Equation 3.1 becomes

$$\frac{\partial}{\partial z}\left(k\frac{\partial T}{\partial z}\right)+q'''=0 \tag{3.3}$$

with the corresponding general solution

$$T(z)=-\frac{q'''}{k}z^2+C_1+C_2. \tag{3.4}$$

To illustrate the difference in the resulting temperature profile between volumetric heating and a uniform heat flux, Equations 3.2 and 3.4 can be solved for a 1-D target of thickness, t, having a constant thermal conductivity. At z= 0 the target is subjected to a heat source which either deposits all energy on the surface or deposits heat uniformly throughout the volume. For this example, the z-axis is collinear with the ion beam. In both cases the target is subject to the following boundary conditions:

$$T\big|_{z=t} = T_0;$$

$$-k\left.\frac{dT}{dz}\right|_{z=t} = q'' = q'''t.$$

With these boundary conditions, Equations 3.2 and 3.4 can be solved analytically.

$$T(z) = \frac{q''}{k}(t - z) + T_0 \tag{3.5}$$

$$T(z) = \frac{q'''}{2k}t^2\left(1 - \frac{z^2}{t^2}\right) + T_0 \tag{3.6}$$

Evaluation of the temperature difference between the hot and cold side of the target in each case indicates that a target with uniform heat generation will experience a temperature rise half as large as the uniform surface heat flux case. This temperature rise is linearly dependent on the target thickness and the magnitude of q" at (z= t). Using the one-dimensional calculation for a uniform 1.0 cm^2 beam with a total power of 1000 W deposited in a lithium target (k = 78 W/m K) which is 100 μm thick, the temperature increase is 25.6 °C for the surface heat flux case compared to 12.8 °C for uniform volumetric heat generation. Resulting temperature profiles are illustrated in Figure 3-1.

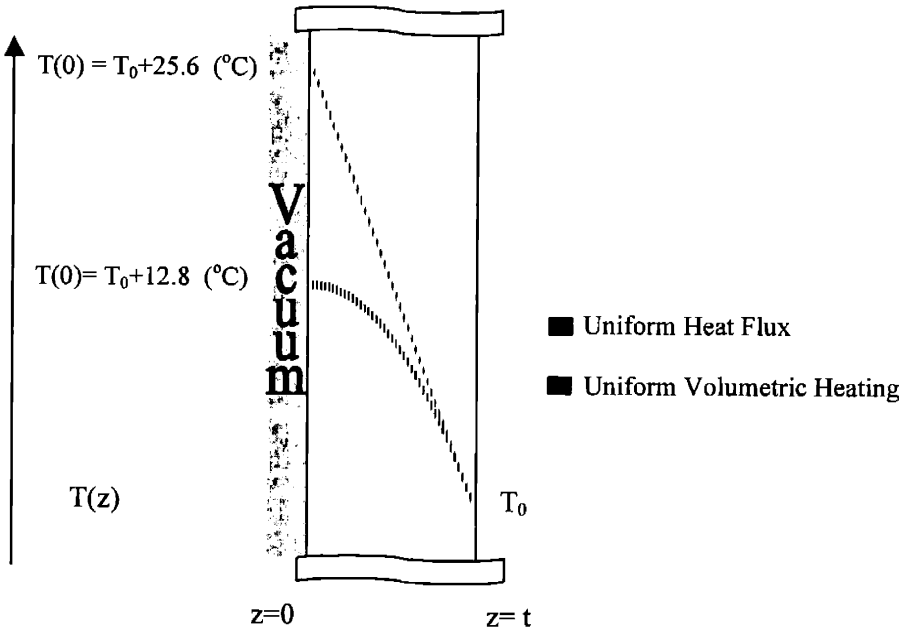

Figure 3-1. 1-D Temperature profile in a 100 μm thick lithium target subjected to a surface heat flux (q") and a uniform volumetric heating (q''') with a total power of 1000 W.

3.1.1 Heat Deposition in a Beryllium Target

Of the different reactions based on a beryllium target which have been proposed for use in neutron capture therapy, two reactions in particular have garnered the most attention based on their yield and energy spectrum.[1-4] Reactions using protons at 4.0 MeV and deuterons at 1.5 MeV on beryllium have been studied and used at LABA for both BNCT and BNCS. (Refer to Table 1-1 for yield and maximum neutron energy).

3.1.1.1 4.0 MeV $^{9}Be(p,n)^{9}B$

In order to determine the relationship between neutron production and heat generation, two quantities, the energy dependent neutron production cross-section, $\sigma(E)$, and charged particle energy at depth, E(z), must be determined. Protons striking the beryllium target with energy, E, are slowed and deposit heat through collisions with atomic electrons. The amount of energy lost per unit length, -dE/dz (stopping power), can be approximated by the Bethe-Bloch formula. As the proton travels a distance, dz, it loses a dE amount of energy. Subtracting this lost energy from the original energy results in a new energy, E-dE. At this new energy the stopping power is slightly different than at the previous energy and must be recalculated. Repeating these iterations until E=0 results in the calculation of particle range. Numerical simulations such as SRIM2000[5] process these calculations and also account for angular deflection, lattice damage, and backscatter.

SRIM was used to simulate the interaction of 10000 protons striking a beryllium target at 4.0 MeV. The total range of these protons was 160.43 μm with a lateral straggle of 2.89 μm. The resulting stopping power for the protons is plotted in Figure 3-2. Using the stopping power information, the energy of the particle along its trajectory can be determined in the following manner. Over a distance interval, dz, the total energy lost is calculated by integrating the stopping power curve. The resultant is then subtracted from the energy of the particle entering the interval. This is repeated in each successive dz interval until E(z) equals zero. The resulting curve of proton energy versus depth in target is plotted in Figure 3-3.

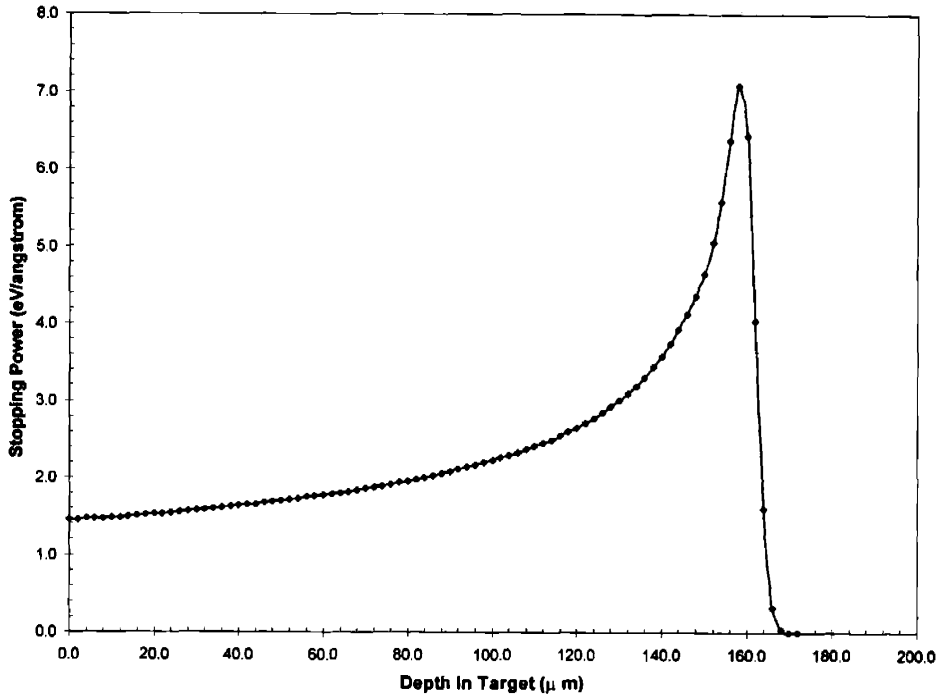

Figure 3-2. Stopping power versus depth in target for 4.0 MeV protons on beryllium.

Protons not only deposit heat but simultaneously generate neutrons as they travel through the target. The probability of producing a neutron per unit length of travel is quantified by the reaction cross section. The $^{9}Be(p,n)^{9}B$ reaction has a Q-value of -1.9 MeV and a threshold value of 2.059 MeV with rapid increase in the cross-section to around 100 mbarns at 2.5 MeV. A resonance at 2.57 MeV increases the cross-section to 164 mbarns. Beyond the threshold, the cross-section continues to increase with energy so that the cross-section is 278 mbarns at 4.01 MeV.[6] Using the energy dependent cross-section data, a piece-wise 4^{th}-order polynomial function

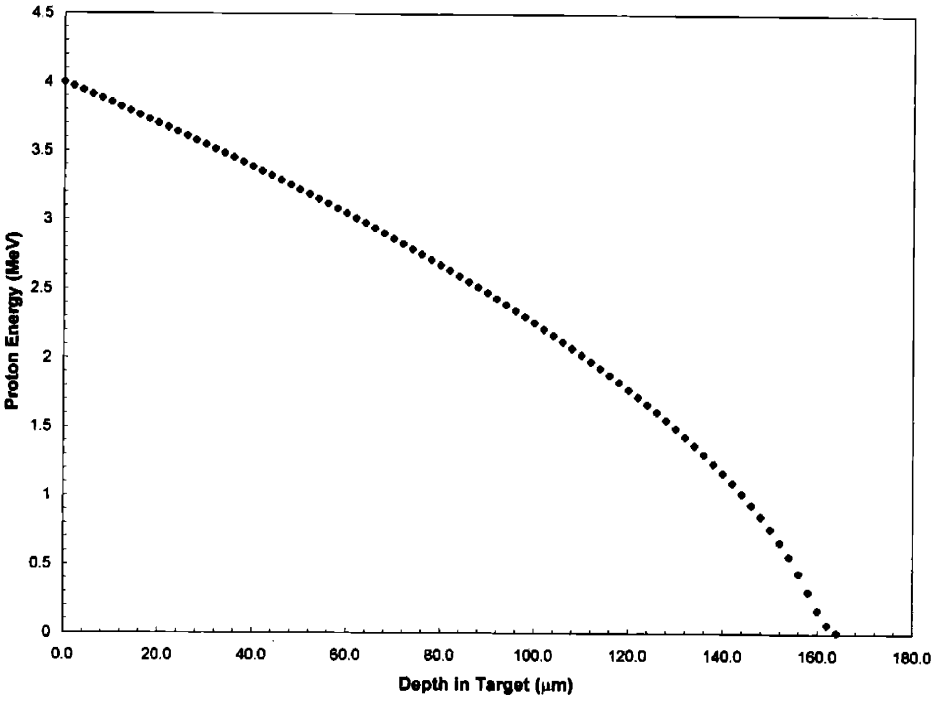

Figure 3-3 Energy as a function of depth in target for 4.0 MeV protons in beryllium. The slope of this curve is the stopping power (-dE/dz).

was generated to match the experimental values of $\sigma(E)$ over the energy range of 2.05-4 MeV. This function was then coupled with the E(z) data derived from the previous calculation in order to generate a curve of $\sigma(z)$. Figure 3-4 illustrates the neutron production cross-section versus depth in the beryllium target up to the point where $\sigma(z)$ becomes zero. Integration of this curve indicates half of the total neutrons produced come from the first 36 μm. Ninety percent come from the first 80 μm, and neutron production stops after 110 μm as illustrated in Figure 3-5.

The issue of non-uniform neutron production, raises the possibility that it might be more effective to reduce the beryllium thickness and raise the beam current to achieve lower target temperatures. The following derivation indicates, however, that this is not the case. Consider a 1-D target which has temperature independent thermal properties. It consists of a neutron producing layer of beryllium (k_b=200 W/m K) on top of a substrate layer such as copper (k_s=350 W/m K). A uniformly distributed beam of 10 kW of 4.0 MeV protons having a power density (q_0") of 10 MW/m^2 is incident on the target. This configuration is illustrated in Figure 3-6.

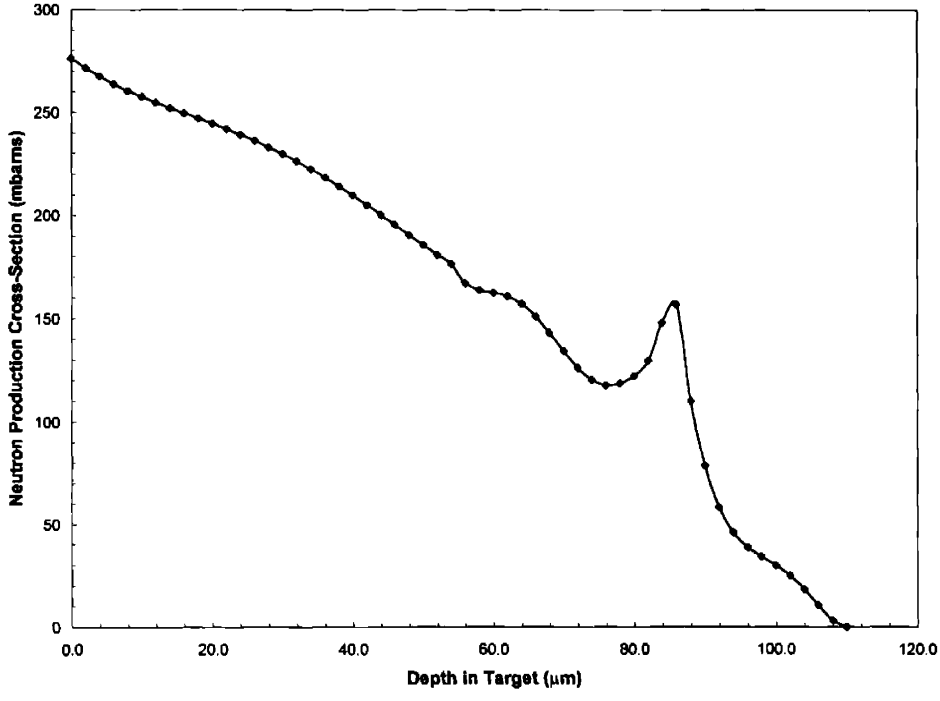

Figure 3-4. $^{9}Be(p,n)^{9}B$ neutron production cross-section at various depths in the target.

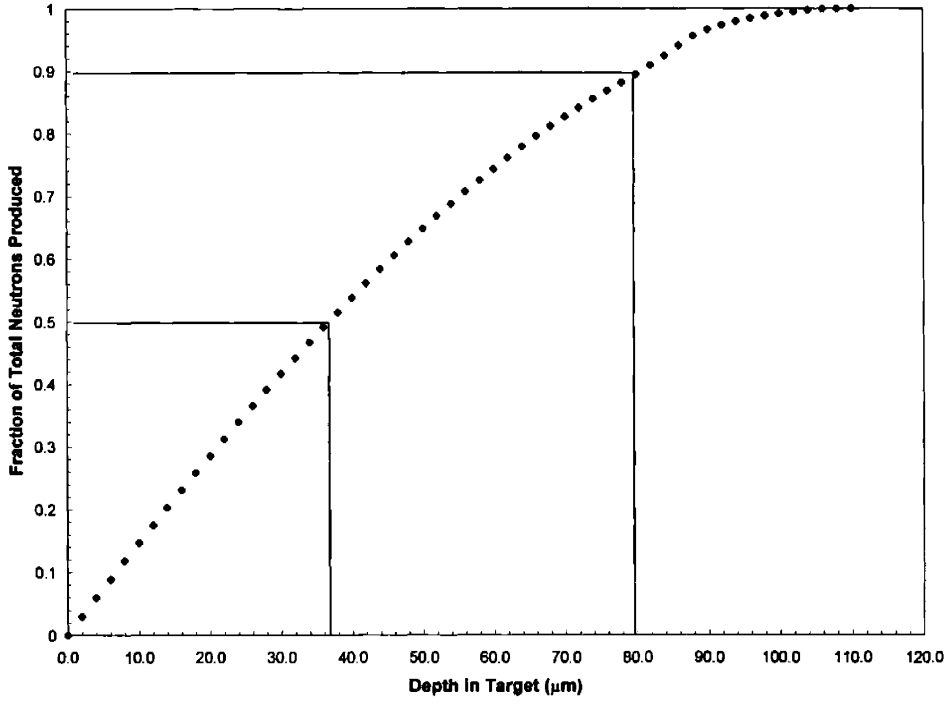

Figure 3-5. Percentage of total neutrons produced as protons travel to depth in beryllium.

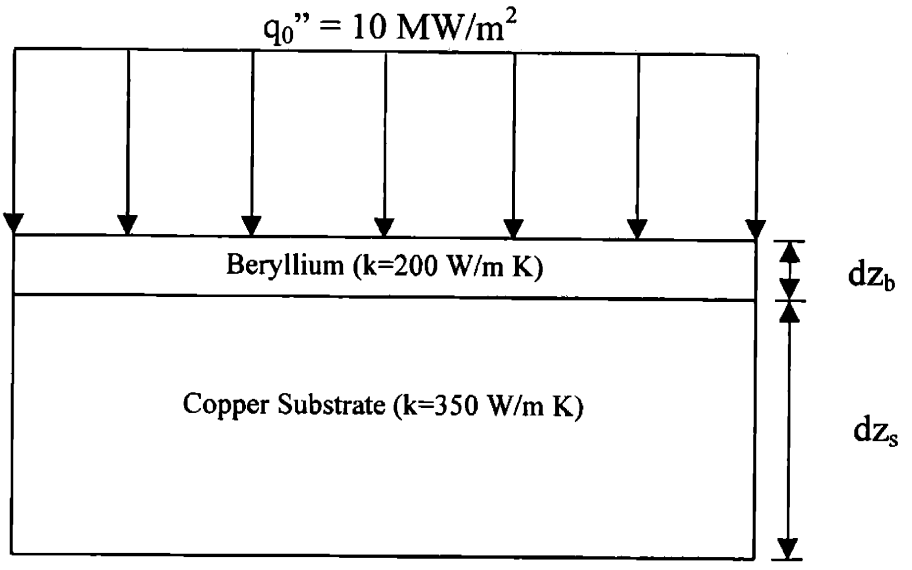

Figure 3-6. One-dimensional model of a beryllium target on copper substrate subjected to a uniform beam of 10 kW over 10 cm^2.

Energy deposited in the target, $E(dz_b)$, is considered uniformly deposited throughout the beryllium thickness so that Equation 3.6 is applicable. The nearly constant slope of Figure 3-3 illustrates that this is a reasonable approximation. As the beryllium thickness is varied from dz_b=0 μm up to a total thickness of 2000 μm, the overall thickness of the target/substrate layer is held constant at 2000 μm by making the substrate thickness equal to 2000-dz_b μm. In order to maintain constant neutron production, q_0" is increased by the amount $1/P_n(dz_b)$, where $P_n(dz_b)$ is the percentage of total possible neutrons generated by a beryllium target of thickness dz_b. For beryllium thicknesses less than 165 μm, heat which is not deposited in the beryllium is immediately absorbed at the target/substrate interface. Based on these assumptions, the temperature increase in the composite target, dT, can be calculated using Equations 3.5 and 3.6.

For dz_b< 165 μm range (including straggle) of 4.0 MeV protons:

Beryllium thickness: dz_b μm

Substrate thickness: dz_s=(2000-dz_b) μm

$$q''' = q_o'' \frac{\left(\frac{E(dz_b)}{4}\right)\left(\frac{1}{P(dz_b)}\right)}{dz_b} \tag{3.7}$$

$$dT = q_0'' \frac{\left(\frac{E(dz_b)}{4}\right)\left(\frac{1}{P(dz_b)}\right)dz_b}{2k_b} + \frac{q_0''\left(\frac{1}{P(dz_b)}\right)dz_s}{k_s} \tag{3.8}$$

For $dz_b > 165$ μm range of 4.0 MeV protons:

Beryllium thickness: dz_b μm

Substrate thickness: $dz_s=(2000-dz_b)$ μm

$$dT = q_0'' \frac{165\mu m}{2k_b} + q_0'' \frac{(dz_b - 165\mu m)}{k_b} + q_0'' \frac{dz_s}{k_s} \tag{3.9}$$

The resulting temperature rise in the composite beryllium/copper target is plotted in Figure 3-7.

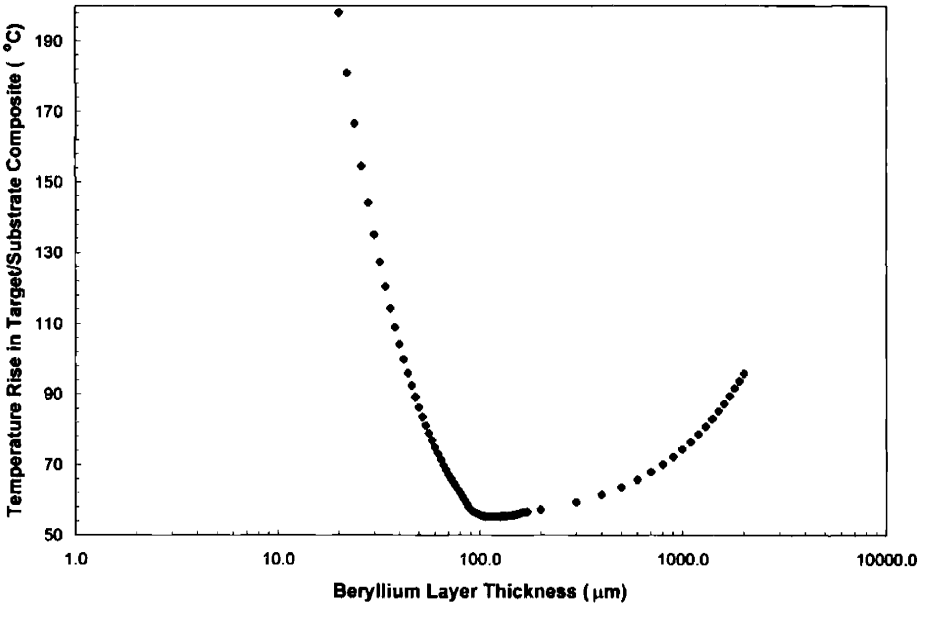

Figure 3-7. Temperature increase in a 1-D composite beryllium/copper target subjected to uniform beam of 4.0 MeV protons. All points represent equivalent neutron production, although increased beam current is required for beryllium thicknesses less than 110 μm.

From this 1-D estimation, some basic observations can be made about the relationship between the target/substrate composition and the overall temperature rise. The minimum temperature rise of 55.4 °C occurs with a beryllium thickness of 110 μm. If the entire 2000 μm thickness is composed of beryllium, the overall temperature rise will be about 95.9 °C. Reducing the beryllium thickness beyond 110 μm and concurrently increasing the beam current to maintain constant neutron production does not reduce the overall temperature rise even with a substrate such as copper which has a high thermal conductivity. In fact, Figure 3-7 illustrates that the overall temperature rise increases dramatically at reduced beryllium thicknesses because of the increased current needed to maintain neutron production.

3.1.1.2 1.5 MeV $^{9}Be(d,n)^{10}B$

Deuterons at 1.5 MeV have a much shorter range in beryllium than 4.0 MeV protons. The reaction is exothermic with a Q value of 4.36 MeV. Based on SRIM simulations of 10^4 particles, the range of deuterons in beryllium at this energy was calculated to be 21.29±0.35 μm. Compared to the other neutron producing reactions, little cross-section data exists for deuteron energies up to 1.5 MeV.[7, 8] Most of the data exists for deuterons at higher energies. Using the available data, however, calculation of $\sigma(z)$, $P(dz_b)$, and the overall temperature rise for a beryllium/copper composite was carried out using the procedure outlined in the above sections. Results of theses calculations are shown in Figures 3-8, 3-9, and 3-10.

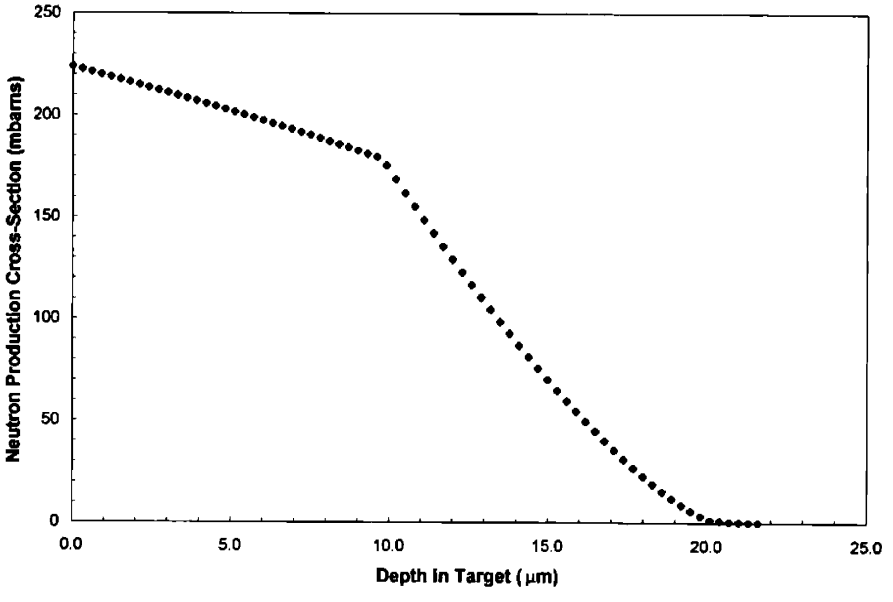

Figure 3-8. $^{9}Be(d,n)^{10}B$ neutron production cross-section for 1.5 MeV deuterons at various depths in a beryllium target.

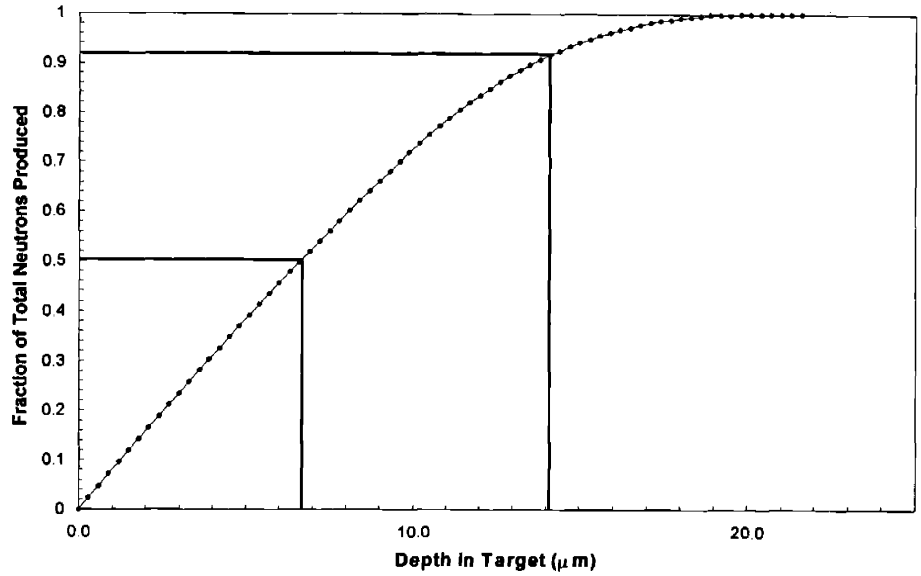

Figure 3-9. Percentage of total neutrons produced as deuterons travel to depth in beryllium.

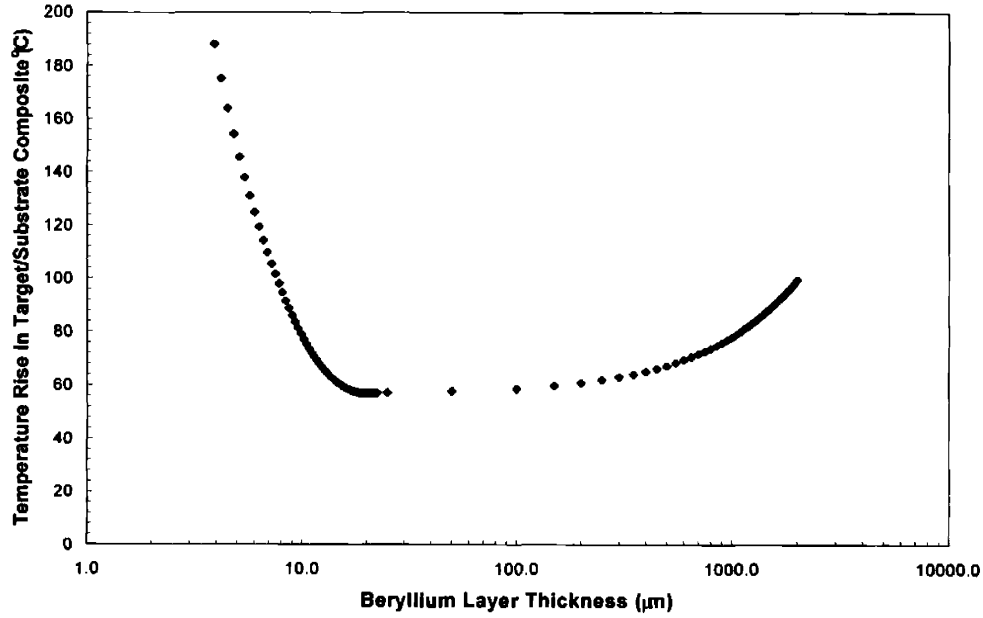

Figure 3-10. Temperature increase in a 1-D composite beryllium/copper target subjected to uniform beam of 1.5 MeV deuterons. All combinations represent equivalent neutron production, although increased beam current is required for beryllium thicknesses less than 21.6 μm.

A minimum temperature difference of 57.0 is found for a beryllium target thickness of 20.3 μm. Further reduction of the beryllium thickness below 20.3 μm does not result in lowering the overall temperature rise as long as neutron production is held constant. An all beryllium target with a thickness of 2000 μm will experience a temperature rise of 99.5 °C. This same

temperature rise can be achieved with an extremely thin, 7.65 μm, beryllium layer on top of a copper substrate, but would require 1.75 times the current to achieve equivalent neutron production.

3.1.2 Heat Deposition in a Lithium Target

As stated in previous chapters, the $^{7}Li(p,n)^{7}Be$ reaction is the most favorable neutron producing reaction in terms of yield and energy spectrum for use in Accelerator-based Neutron Capture Therapy. The reaction has been thoroughly studied and extensive cross-section data exist.[9,10] Unlike beryllium, lithium is poorly suited as a target material. The low thermal conductivity (78 W/m K), a melting temperature of 180.5 °C, poor mechanical strength, and explosive reactivity with water virtually ensures that a viable target cannot be composed of pure lithium.

The same calculation of $\sigma(z)$, $P(dz_L)$, and overall temperature increase was performed for a 1-D composite lithium/copper target subjected to 2.5 MeV protons. Results are illustrated in Figures 3-11,3-12, and 3-13.

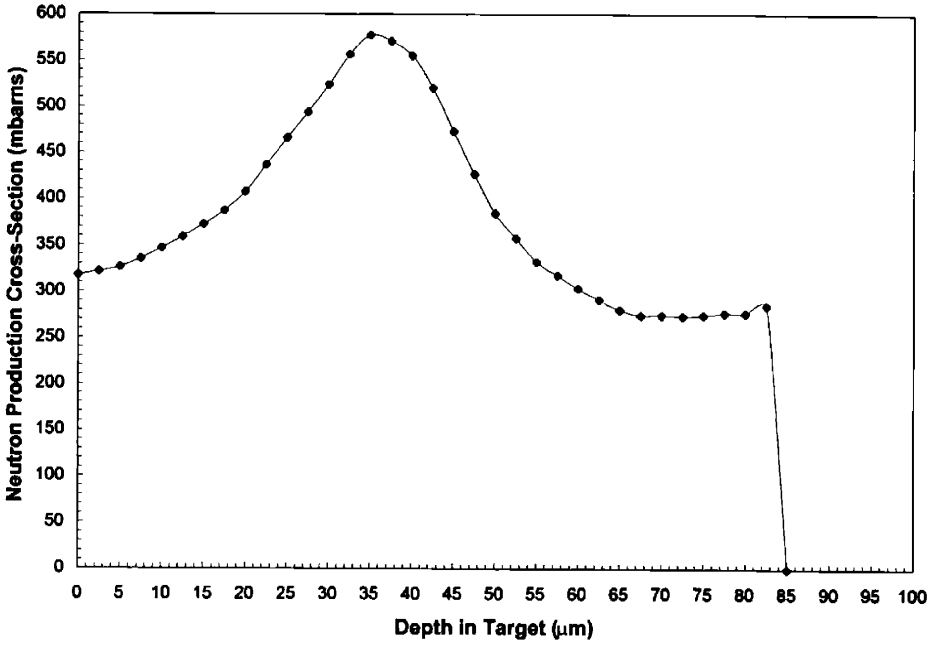

Figure 3-11. $^{7}Li(p,n)^{7}Be$ neutron production cross-section for 2.5 MeV protons at various depths in a lithium target.

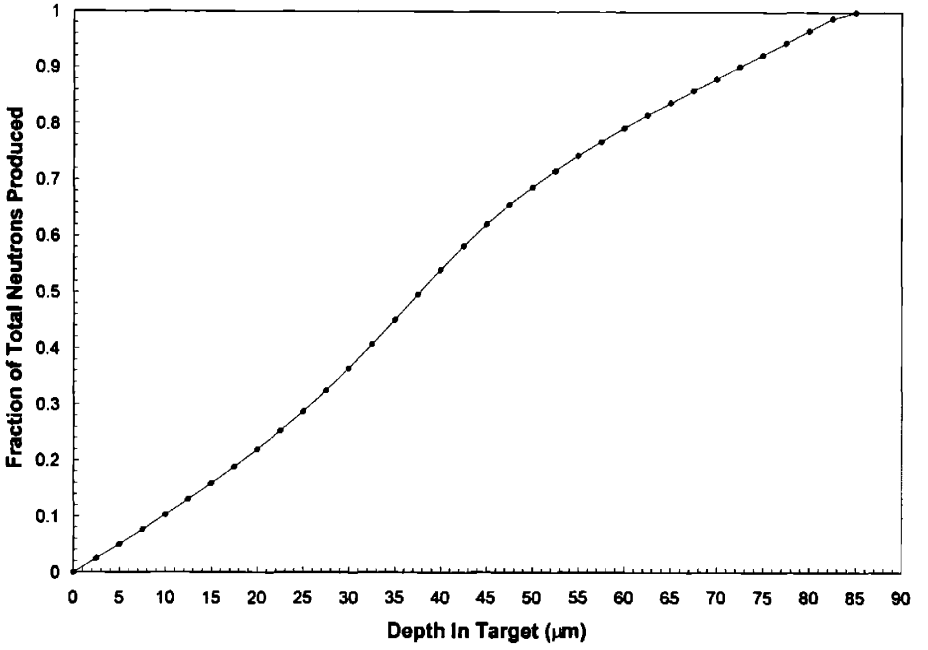

Figure 3-12. Percentage of total neutrons produced as 2.5 MeV protons travel to depth in lithium.

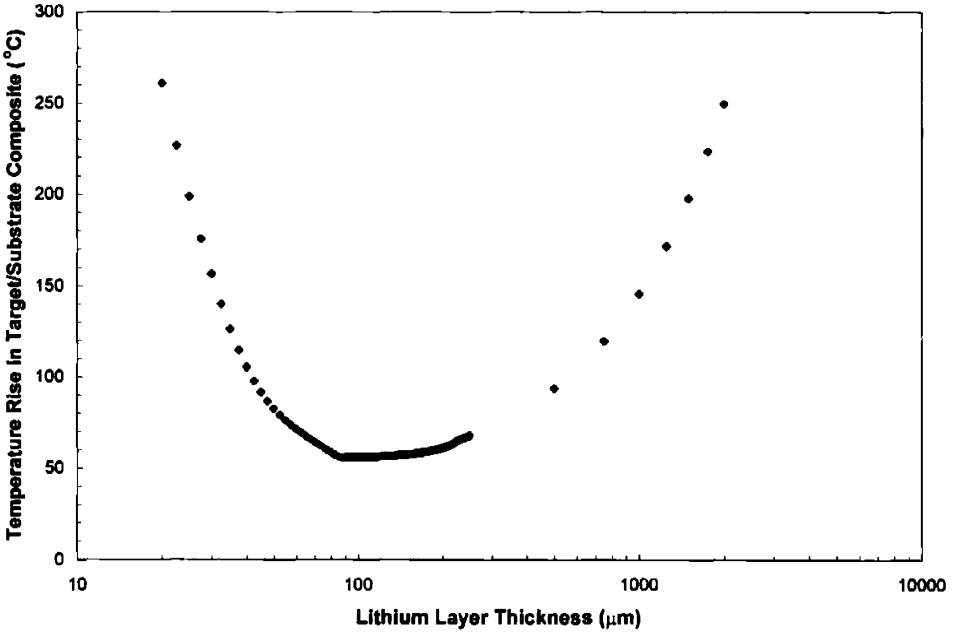

Figure 3-13. Temperature increase in a 1-D composite lithium/copper target subjected to uniform beam of 2.5 MeV protons. All combinations have equivalent neutron production but require increased beam current for lithium thicknesses less than 85 μm.

Despite the fact that the cross-section rises from slightly above 300 to nearly 600 mbarns at a target depth of 35 μm, Figure 3-11 illustrates that neutron production does not fall off as drastically with depth compared to beryllium targets. The cross-section remains over 250 mbarns throughout the target until only 5 μm from the point at which the proton energy falls below the 1.881 MeV threshold. The minimum temperature rise of 56.1 °C occurs for a lithium thickness of 85 μm. Although this may not seem like a large temperature increase, a brief example will illustrate the difficulty in designing a cooling strategy for a lithium target. In addition to the temperature rise in the target body, an increase will also be experienced between the bulk coolant temperature and the interface of any target. For a q_0'' of 10 MW/m^2 the temperature rise between the bulk coolant temperature and the target interface would be 100 °C even with a cooling scheme generating a heat transfer coefficient of 10^5 W/m^{2}K. Coupled with the 56.1 degree rise in the target body, a bulk coolant temperature of 25 °C would cause the front of the lithium target to exceed the 180.5 °C melting point.

3.1.3 Making the Transition between Analytic Calculations and Numeric Simulations

Before making the transition from the 1-D calculations of §3.1.1 and §3.1.2 to a numeric simulation, it was helpful to understand some general trends in the thermal behavior of targets based on the 4.0 MeV Be(p,n) and 2.5 MeV Li(p,n) reactions. Because of the large number of possible combinations of beam size, heat transfer coefficient, target material, and substrate thickness, these trends helped to narrow the range of parameters which were then studied using numeric simulations. Analytic calculations were carried out for a target of radius (R) and thickness (t) which was similar in structure to the one pictured in Figure 3-6. The target consisted of a neutron producing layer of either 110 μm of beryllium or 85 μm of lithium on top of a substrate. Dispersion-strengthened copper alloy, C15715-H04, which has a good combination of strength and thermal conductivity was used as the substrate material for both the beryllium and lithium-based targets. Heat removal from the substrate was accomplished by assuming a uniform heat transfer coefficient produced by water at 25 °C. Recognizing the fact that an ion beam has basically a Gaussian distribution, the heat source was modeled using the following equations.

$$q''(r) = q''_{max}\, exp(-\frac{r^2}{2\sigma^2_{beam}}) \tag{3.10}$$

$$Q = \int_0^{2\pi} d\theta \int_0^R q''(r) r dr \tag{3.11}$$

where,

q''_{max}: maximum value of heat flux at the center of the ion beam (W/m^2)

σ_{beam}: standard deviation of the beam distribution (m)

Q: total beam power on target (W)

R: maximum target radius exposed to ion beam (For these calculations R= 0.027 m)

These 1-D calculations were conducted along a line parallel to the direction of beam and neglected radial heat transfer. This condition is satisfied when $(t/\sigma_{beam})^2 \ll 1$.[11] Even when radial conduction is included, however, the highest temperatures in the target can be expected to occur in the center at r = 0 for targets which possess strong axisymmetry. Using Equations 3.10 and 3.11, q''_{max} values were calculated with standard deviations ranging from 0.1 to 1.51 cm to cover the spectrum from highly focused to defocused beams. Although the choice of 1.51 cm as the maximum value for σ_{beam} might seem arbitrary, it was selected to reflect the manner in which targets are mounted on the beamline. The R value in Equation 3.11 refers to the maximum radial location in a target which is exposed to the ion beam. The physical radius of the target, which for these calculations was 0.03 m, is usually slightly larger than the R value because the periphery of a target would be shielded from the ion beam by an aperture, Faraday cup, or mounting support. By limiting the standard deviation of the beam to a value of 1.51 cm, the fraction of the total beam power which would be lost on sections of the beamline other than the target is kept to below 15%. Given the target dimensions, beam distribution, and heat transfer coefficient, the theoretical beam power limit was determined either by the onset of critical heat flux (CHF) or a phase change in the target using the following assumptions. For C15715 copper, a minimum thickness of 1.04 mm is required to support a pressure differential of 0.10135 MPa (1 atm) with a fixed-edge target having a radius of 0.03 m. A slightly larger minimum thickness of 1.47 mm is required for a simply-supported target. Calculations used to determine the minimum thickness for substrate materials are presented in §3.2. For a given substrate thickness, the maximum allowable pressure on the cooled side of the target was used to evaluate a saturation temperature. Although there was no limit placed on the substrate thickness, no pressure value was allowed to exceed 1.0 MPa. The power at which CHF is reached, which is calculated with Equation 3.12, is difficult to quantify since no assumption was made regarding the nature of the cooling configuration. Equation 3.12 attempts to account for the fact that CHF in forced convection increases with fluid velocity, evidenced by the dependence on h in 3.12, as well as pressure. The 30 °C quantity is included so that calculated CHF values predicted by Equation 3.12

converge to the saturated pool boiling CHF values predicted by Zuber[12] when small values of h are used in Equation 3.12. In §§3.3 and 3.4 a CHF limit specifically for submerged jet impingement will be introduced. Besides the CHF limit, temperatures were not permitted to exceed the point at which a phase change would occur anywhere in the target. For a lithium target, this meant the beam side could not exceed 180.5 °C. In the beryllium target, the substrate melting temperature of 1083 °C, which would be a maximum at the interface between the target and the substrate, fixed the upper temperature limit. Given these two criteria, the theoretical beam power limits could be determined with the following equations.

CHF Limit

For a given bulk coolant temperature (T_∞) of 25 °C, heat transfer coefficient (h), and a saturation temperature (T_{sat}), the power at which CHF is reached is :

$$Q^{CHF} = \frac{(T_{sat} + 30 - T_\infty)h}{q''_{max}(1)} \tag{3.12}$$

T_{melt} Limit

In the case of a lithium-based target, the power limit imposed by the restriction on melting was found by

$$Q^{melt} = \left(\frac{T_{melt} - T_\infty}{\left(\frac{1}{h}\right) + \left(\frac{t_{sub}}{k_{sub}}\right) + \left(\frac{F_{np} t_{np}}{2k_{np}}\right)} \right) \left(\frac{1}{q''_{max}(1)} \right) \tag{3.13}$$

For the beryllium target, where melting of the substrate would limit power, Equation 3.13 was adjusted to

$$Q^{melt} = \left(\frac{T_{melt} - T_\infty}{\left(\frac{1}{h}\right) + \left(\frac{t_{sub}}{k_{sub}}\right)} \right) \left(\frac{1}{q''_{max}(1)} \right) \tag{3.14}$$

where,

Q^{CHF}: power limit imposed by CHF (W)

Q^{melt}: power limit imposed by phase change in the target (W)

$q''_{max}(1)$: peak heat flux in a 1 W beam for a given standard deviation (W/m^2)

h: heat transfer coefficient (W/m^2K)

t_{sub}: thickness of substrate (m)

k_{sub}: thermal conductivity of substrate (W/mK); averaged over range from 25 °C to T_{melt}

F_{np}: fraction of beam energy deposited in the neutron producing layer

t_{np}: thickness of neutron producing layer (m)

k_{np}: thermal conductivity of neutron producing layer (W/mK); averaged over range from 25 °C to T_{melt}

T_{melt}: temperature at which the first phase change occurs (°C)

Figures 3-14 (beryllium) and 3-15 (lithium) plot the ratio of the T_{melt}/CHF power limit for a variety of heat transfer coefficients and substrate thicknesses. In the regions where this ratio is less than unity, phase change of the target would likely determine the power limit. Likewise, CHF would determine the power limit for ratios greater than one. The dashed lines in both graphs indicate the point at which the limits imposed by the two constraints are equal.

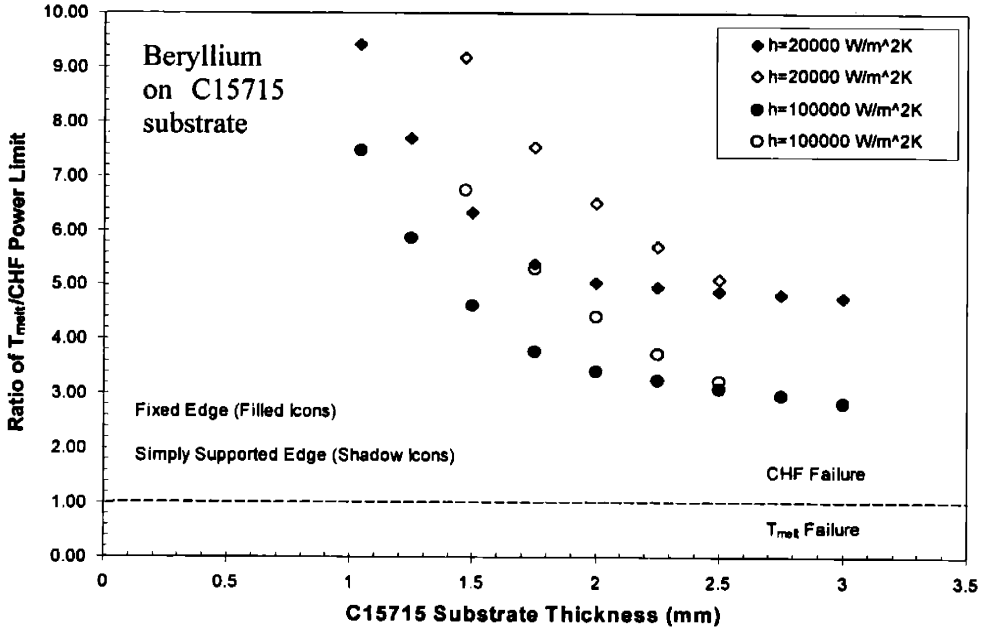

Figure 3-14. Ratio of the T_{melt}/CHF power limit versus substrate thickness for a target composed of 110 μm beryllium on a C15715 copper substrate. Heat transfer coefficients of 20000 W/m^2K and 100000 W/m^2K are indicated for both fixed and simply-supported edge conditions.

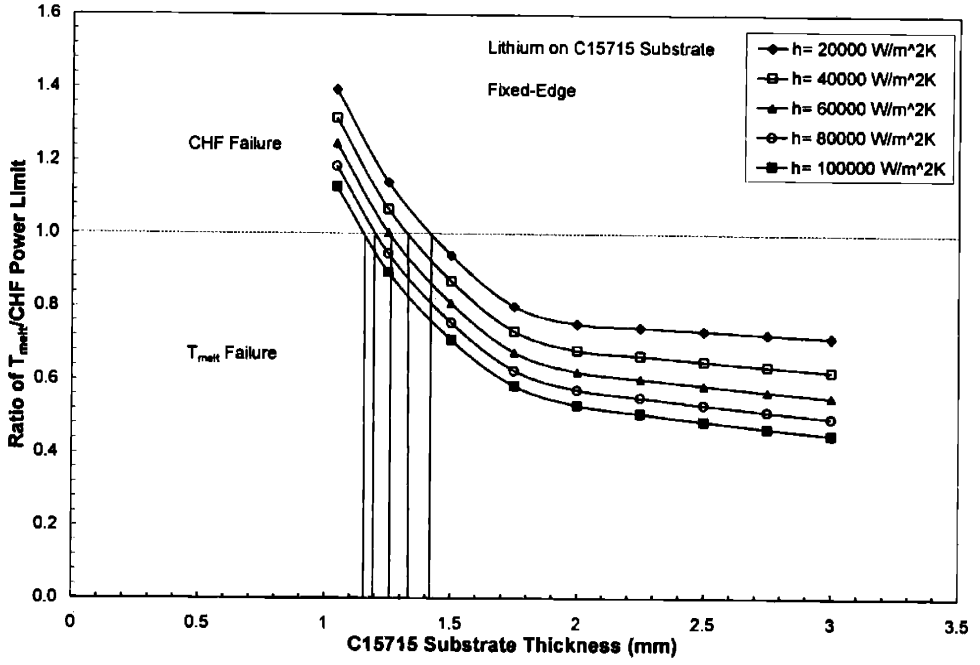

a)

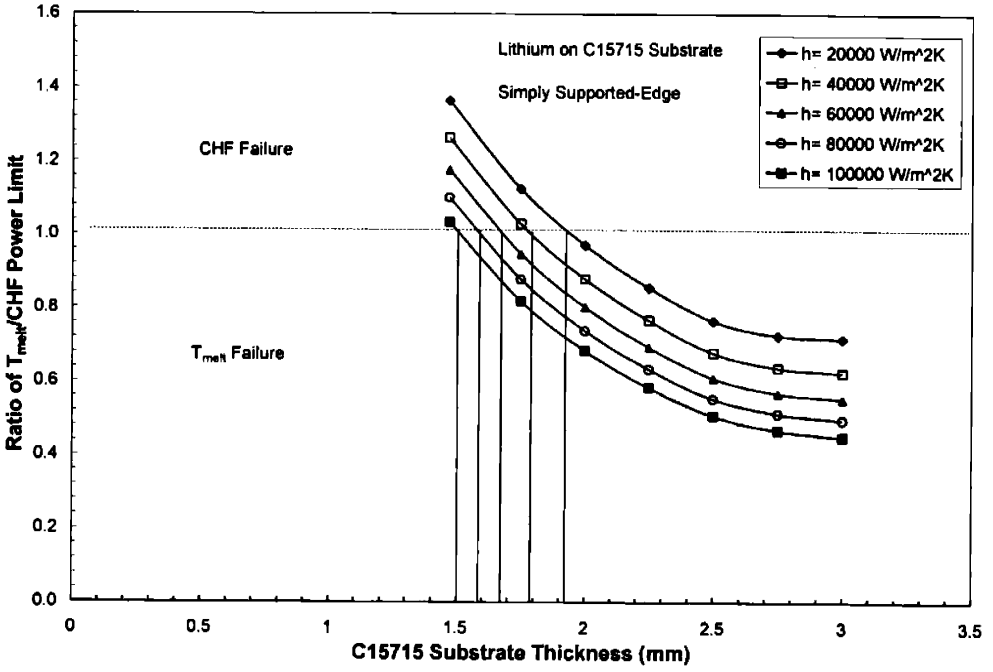

b)

Figure 3-15. a) Ratio of the T_{melt}/CHF power limit versus substrate thickness for a fixed-edge target composed of 85 μm lithium on a C15715 copper substrate. b) Ratio of the T_{melt}/CHF power limit versus substrate thickness for a simply-supported target composed of 85 μm lithium on a C15715 copper substrate.

From the standpoint of thermal hydraulics, these graphs indicate that the primary limiting factor for a beryllium-based target cooled with water would be the onset of CHF. Under all combinations of substrate thickness and heat transfer coefficient used in these calculations, CHF determined the ultimate power limit. This was true for both simply-supported and fixed-edge targets. In a lithium-based target, however, most combinations were limited by melting of the lithium as a result of its relatively low T_{melt} at 180.5 °C. At small substrate thicknesses, however, targets were found to suffer from CHF. All fixed-edge lithium targets below 1.15 mm suffered from CHF, while the simply-supported cases were subject to CHF for a substrate thickness below 1.51 mm. Above a substrate thickness of 1.42 mm (fixed-edge) and 1.95 mm (simply-supported) all targets were limited by the melting of the lithium. Within the region bounded by these dimensions failure depended on the combination of heat transfer coefficient and substrate thickness. Maximum power which could be achieved for a specific combination of heat transfer coefficient and substrate thickness was found to exist at the point where the T_{melt}/CHF ratio equaled 1. This is illustrated in Figure 3-16 which plots the maximum power for the lithium-based targets. Peaks in the curves correspond to the points indicated in Figure 3-15 where the power limit ratio had a value of 1.

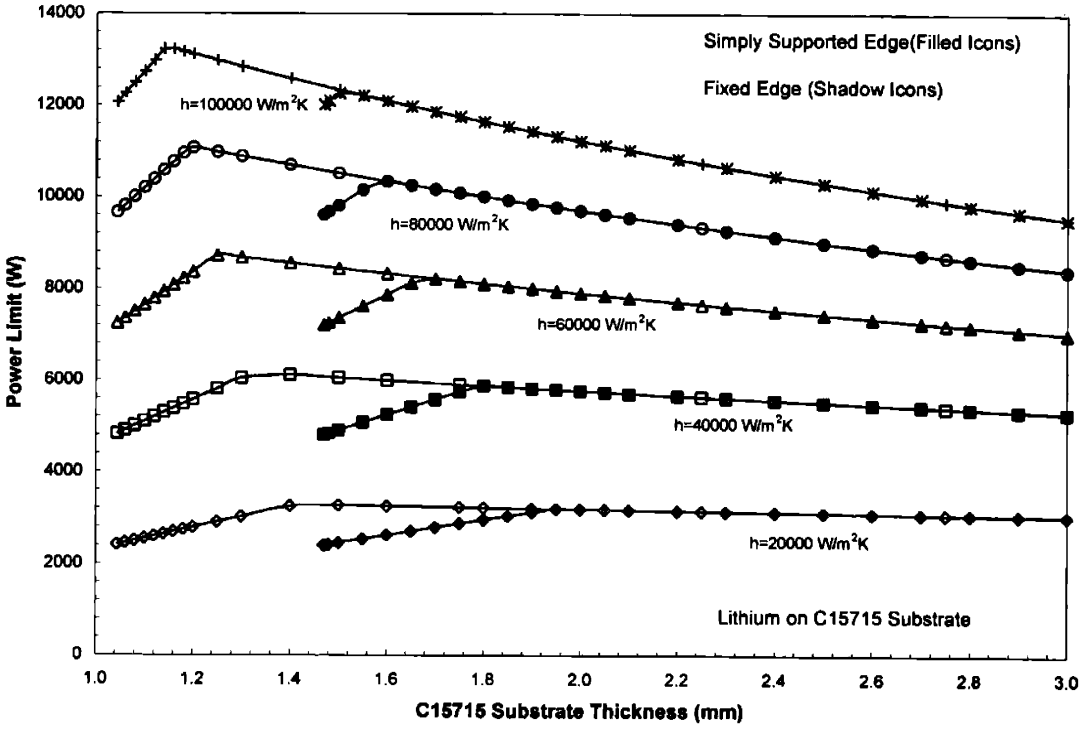

Figure 3-16. Power limit versus substrate thickness for a target composed of 85μm of lithium on a C15715 copper substrate. Fixed-edge and simply-supported edge conditions are depicted for various heat transfer coefficients.

Figure 3-16 also indicates that limits imposed by CHF reduce the maximum power to a greater extent than increased thickness, as evidenced by the increased slope of the curves to the left of the peaks.

The results of Figures 3-14 through 3-16 gave no indication of the role played by the distribution of beam power. In addition to target dimensions and heat transfer coefficient, beam power density was a crucial factor in determining the amount of power which could ultimately be handled by a target. Figure 3-17 illustrates the minimum σ_{beam} which allowed a power level of 10 kW to be achieved for fixed-edge beryllium and lithium targets.

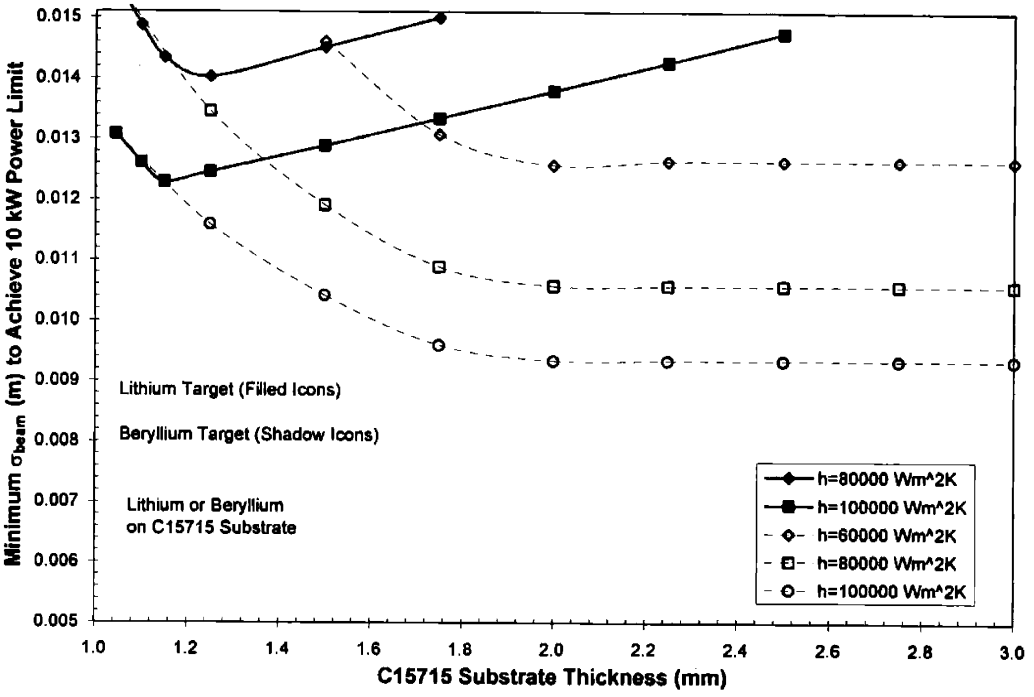

Figure 3-17. Plot of the smallest σ_{beam} (m) which permitted a maximum beam power of 10 kW for a fixed-edge beryllium and lithium target. With heat transfer coefficients lower than those illustrated, 10 kW could only be achieved with a σ_{beam} greater than the limiting value of 1.51 cm.

The influence of σ_{beam} is also illustrated in Figures 3-18 and 3-19 which plots the power limit for a given heat transfer coefficient. Each figure gives the results of fixed-edge targets at the substrate thickness found to allow the maximum power. For the lithium target, these thicknesses are indicated on Figure 3-15a. Maximum power for the beryllium target was achieved with a substrate thickness of 1.85 mm which could support the limiting pressure of 1 MPa.

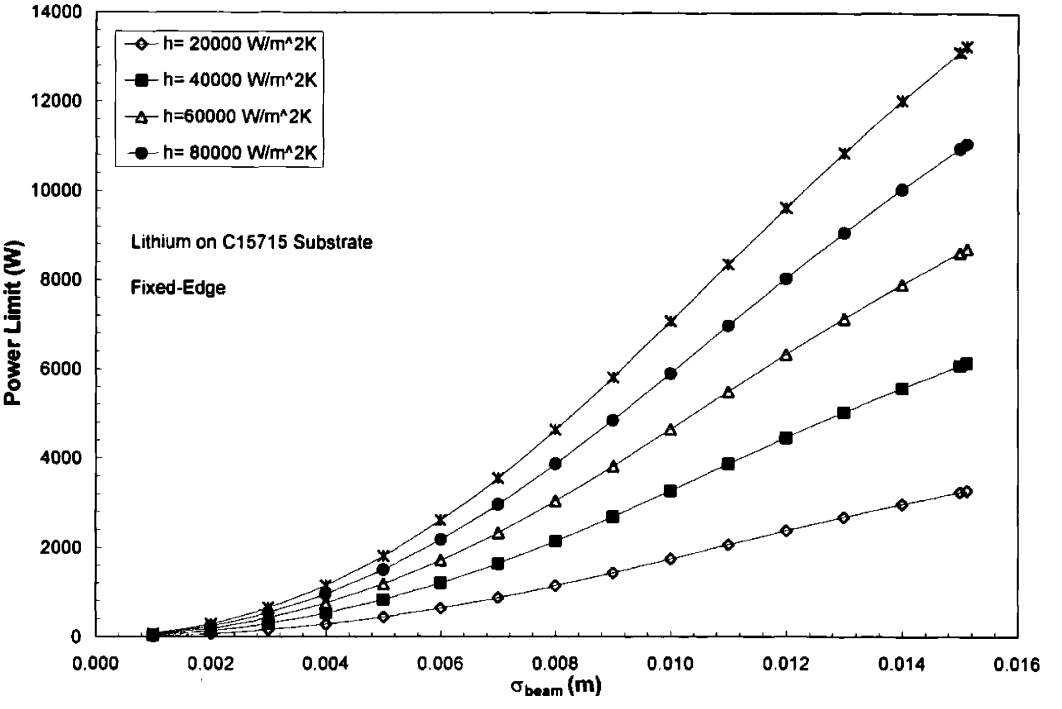

Figure 3-18. Maximum power versus beam standard deviation (m) in a fixed-edge lithium target on a C15715 copper substrate for heat transfer coefficients from 20000-100000 W/m^{2}K.

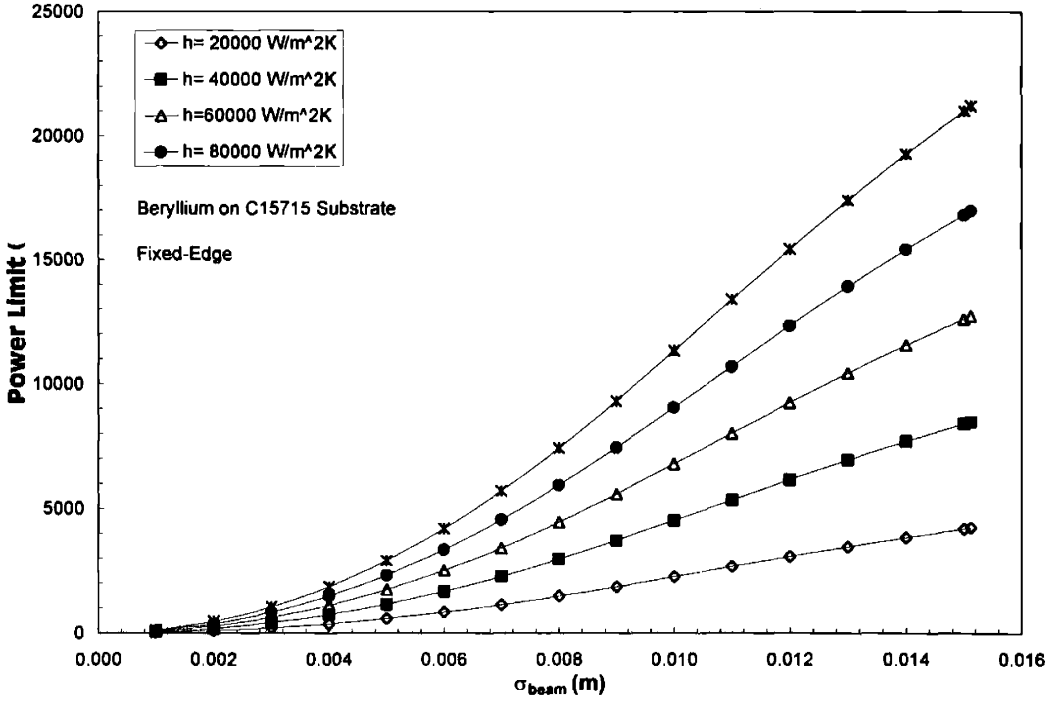

Figure 3-19. Maximum power versus beam standard deviation (m) in a fixed-edge beryllium target on a C15715 copper substrate for heat transfer coefficients from 20000-100000 W/m^{2}K.

Using these figures, the magnitude of the heat transfer needed to reach a certain power level given a specific beam distribution can readily be obtained.

While the results of the preceding calculations do not represent a final target design, they do illustrate several important interactions between materials, dimensions, heat transfer coefficient, and beam size. The most important conclusions can be summarized as follows:

(1) CHF is likely to determine maximum beam power for the beryllium-based targets for all combinations of substrate thicknesses and heat transfer coefficient.

(2) To offset the limitations imposed by CHF, power limits were increased by making the substrate thicker. This permitted higher pressurization of the coolant, raised the saturation temperature, and delayed the onset of CHF.

(3) Maximum power in lithium targets was found to occur at the point where the ratio of T_{melt}/CHF power limits equaled 1. For fixed-edge targets this occurred with substrate thicknesses between 1.15-1.42 mm. In simply-supported targets the range was 1.51-1.95 mm.

(4) The smallest σ_{beam} which allowed 10 kW in the lithium target was 0.0125 m. The value was 0.0093 m for the beryllium target. Both values were for fixed-edge targets.

3.2 Numerical Simulation of Target Temperature Profiles

The analytic solutions of §3.1 relied on assumptions which converted the general steady-state heat transfer equation into a 1-D, temperature independent version. In order to more accurately predict the thermal response of a target a numerical model was created which included the following refinements:

(1) q" uniform replaced by q"" (r,z)
(2) temperature independent thermal conductivity replaced by k(T)
(3) radiation and convective boundary conditions introduced
(4) limits on maximum temperatures as a result of critical heat flux or target phase change

Incorporation of these refinements was accomplished by generating a finite element model (FEM) of the target using the ADINA-T code. Once the model had been constructed, parameters could be changed with minimal effort and a new temperature profile generated. Temperature dependent materials were used throughout the simulations to account for any non-linearities introduced by variations in thermal conductivity. Appropriate boundary conditions were selected to reflect those which would exist in a target mounted on the end of an accelerator beam line.

3.2.1 Building the Finite Element Model

Most targets used in Accelerator-based Neutron Capture Therapy are symmetric about the axis of the beamline. Utilizing this axisymmetry, a 2-D finite element model of the target was created using ADINA-T. The portion of the target included in the simulation is shown in Figure 3-20.

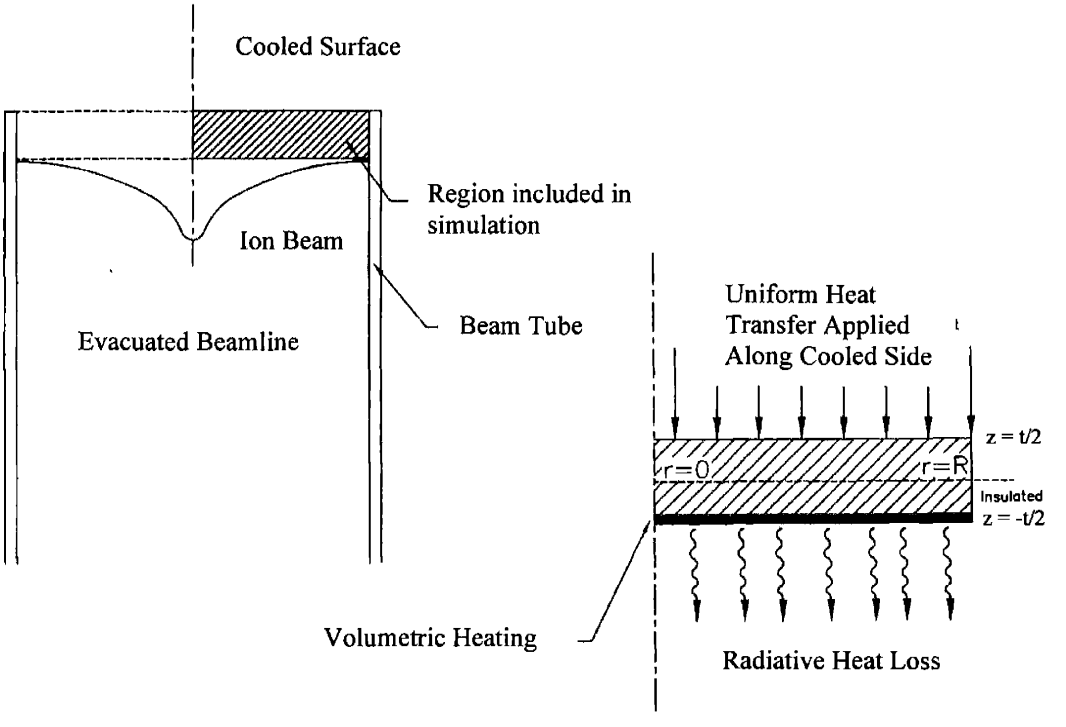

Figure 3-20. Illustration of the 2-D axisymmetric target simulated using ADINA-T. The highlighted region used in the model is symmetric about the z-axis which passes through the centerline of the target at r=0.

3.2.1.1 Target Dimensions

A three-layer, 2-D target was generated so that various material combinations could be tested. This three-layer target was used to model volumetric energy generation which varied in both radial and axial coordinates. Based on MRA optimization studies carried out at LABA,[13, 14] target diameters of 2-6 cm have been proposed. In this study, all targets had a diameter of 6 cm to allow for large variations in beam size.

Plate theory was used to evaluate the minimum thickness required to support a 0.10135 MPa (1 atm) pressure differential. Targets were modeled as a circular plate having a radius (R), thickness (t), Young's Modulus (E), and Poisson's ratio (v). The target, which was subjected to a

uniformly distributed pressure differential (P), was constrained at its edge (r = R) in order to maintain equilibrium. Edge constraint was modeled as being either simply-supported (w(R) = 0) or fixed (w(R) = 0; w'(R) = 0). Plates loaded in this manner experience a deflection (w) which varies with radial position. Minimum thickness was determined in each case by limiting the maximum deflection at the center to 10% of the total thickness (w(0) = 0.1t). Beyond the 10% deflection limit non-linear strains become important and plate theory is no longer valid. For most structural materials, the 10% deflection formulation is equivalent to using a safety factor of 2-3.

Regardless of the edge constraints, flexural rigidity (D) for circular plates is defined as

$$D = \frac{Et^3}{12(1-\nu^2)}. \tag{3.15}$$

Maximum deflection occurs at r = 0 and can be found using

$$w_{max} = \frac{P}{64D}\left(\frac{5+\nu}{1+\nu}\right)R^4 \quad \text{Simply-Supported Edge} \tag{3.16}$$

$$w_{max} = \frac{P}{64D}R^4 \quad \text{Fixed-edge.} \tag{3.17}$$

Setting $w_{max} = 0.1t$ and solving for t resulted in solutions for the minimum target thickness:

$$t_{min} = \left(\frac{15P(1-\nu)(5+\nu)}{8E}\right)^{0.25} R \quad \text{Simply-Supported Edge} \tag{3.18}$$

$$t_{min} = \left(\frac{15P(1-\nu^2)}{8E}\right)^{0.25} R \quad \text{Fixed-edge} \tag{3.19}$$

Table 3-1 summarizes the minimum target thickness and thermal resistance (t_{min}/k) calculated for various substrate materials. All properties were evaluated at 20 °C.[15] Quantities in the table are listed for plates having a radius of 0.01 m. Values of t_{min} and R_t in targets having radii greater than 0.01 m can be calculated by multiplying the value given in the table by the ratio of the radii. For example, $t_{min}(R=0.03\ m) = 3*t_{min}(R=0.01\ m)$. Minimum target thickness was determined only the substrate thickness. The target layer (110 μm of beryllium or 85 μm of lithium) was assumed to provide no structural support.

Table 3-1. Minimum target thickness (t_{min}) and thermal resistance (R_t) for circular plates (R=0.01m) needed to support a 0.1 0135 MPa pressure differential with simply-supported (SS) or fixed-edge (Fixed) constraints.

Material	E (GPa)	ν	k (W/m K)	t_{min} (SS) (mm)	t_{min} (Fixed) (mm)	R_t (SS) x (10^{-6}) (m^2 K/W)	R_t (Fixed) x (10^{-6}) (m^2 K/W)
Aluminum 6061	70	0.33	167	0.558	0.394	3.338	2.360
Aluminum 7075	71	0.33	124	0.556	0.393	4.500	3.180
C15715-H04	117	0.30	365	0.495	0.348	1.355	0.954
C18200-TH01	117	0.30	324	0.495	0.348	1.530	1.077
Beryllium (S-200F)	303	0.08	200	0.413	0.281	2.506	1.701
Tantalum	183	0.26	57	0.447	0.313	7.794	5.456
Moly TZM alloy	292	0.30	128	0.394	0.277	3.077	2.165
Magnesium M11311	44	0.29	78	0.635	0.446	8.115	5.700
Silicon Carbide	414	0.16	118	0.375	0.258	3.180	2.190
304 Stainless Steel	194	0.29	15	0.438	0.308	29.158	20.489
316 Stainless Steel	194	0.29	13	0.437	0.307	32.971	23.184
Tungsten	399	0.28	179	0.366	0.257	2.051	1.439

3.2.1.2 Boundary Conditions and Heat Inputs

Neutron producing targets used in NCT are attached to the end of an evacuated beam line and are housed in a moderator/reflector assembly (MRA). A charged-particle beam having a fixed energy and current density strike the target and deposit energy through collisions as the ions slow down. On the opposite side of the target, forced convection generates a heat transfer coefficient which could be uniform or have some spatial distribution. In order to model these interactions the following boundary conditions were applied to the 2-D model pictured in Figure 3-20. Along the centerline of the target (r=0) a symmetry boundary condition (dT/dr = 0) was imposed. A uniform convection boundary having a bulk coolant temperature of 25 °C, which is analogous to using an area-averaged heat transfer coefficient, was modeled along the cooled edge of the target ($0 \le r \le R$, $z = t/2$). The target edge at r= R was considered to be insulated. On the beam side of the target, which is located in vacuum, some radiation will occur. Along the line (0

$\leq r \leq R$, $z = -t/2$) a radiation boundary having an environmental temperature (T_{env}) of 25 °C was generated ($q'' = \sigma \varepsilon (T_s^4 - T_{env}^4)$).

As described in Chapter 2, efficient transport of ion beams makes it difficult to achieve a completely uniform current density. Although broad beams are possible they would still have Gaussian distributions albeit with large standard deviations. In these simulations beams having a range of standard deviations (σ_{beam}) were tested, while azimuthal asymmetry was not considered. Internal heat generation (q''') was modeled based on the total power on target using Equations 3.7, 3.10, and 3.11. SRIM-2000 was used to partition the fraction of $q'''(r)$ deposited in the top neutron-producing layer as well as the fraction deposited in the non-neutron producing layer.

3.2.2 Numerical Simulations for Lithium and Beryllium -Based Targets

The four materials highlighted in Table 3-1 were considered as candidate substrate materials for the 4 MeV $^9Be(p,n)^9B$ and 2.5 MeV $^6Li(p,n)^6Be$ reactions based on their low thermal resistances and the fact that they retain high yield strength at elevated temperatures. Power limits were set according to the following temperature-based conditions which are similar to those mentioned in §3.1.3.

1) Temperature of target and substrate material could not exceed T_{melt}.

2) Temperature at a position 3 mm from the edge could not exceed O-ring melting temperature of 260 °C. This is the position at which an O-ring contacts the target in order to make a vacuum seal on the beamline.

3) Critical heat flux calculated with Equation 3.12. Again this is just an estimate of CHF since so assumption is made about the nature of the cooling.

A couple of points should be kept in mind during the presentation of these results. The saturation temperature used in each simulation was based on the maximum pressure differential which could be supported for a given substrate thickness as determined by Equations 3.18 and 3.19. Saturation temperatures at a given pressure were determined from steam table data.[16] As a matter of taking into account the implementation of a target into a completed Accelerator-NCT system, the maximum allowable pressure differential was limited to 1.0 MPa (~145 psi). Lithium-based targets were the first to be considered using the numerical simulations. Beam standard deviations of 2-15.1 mm and heat transfer coefficients of 20000-100000 W/m^2K were simulated. For each substrate material, the process for determining the power limit required determining the point at which the T_{melt}/CHF ratio equaled one. Figure 3-21 illustrates how the ratio varies depending on substrate thickness for a lithium target on a C15715 substrate.

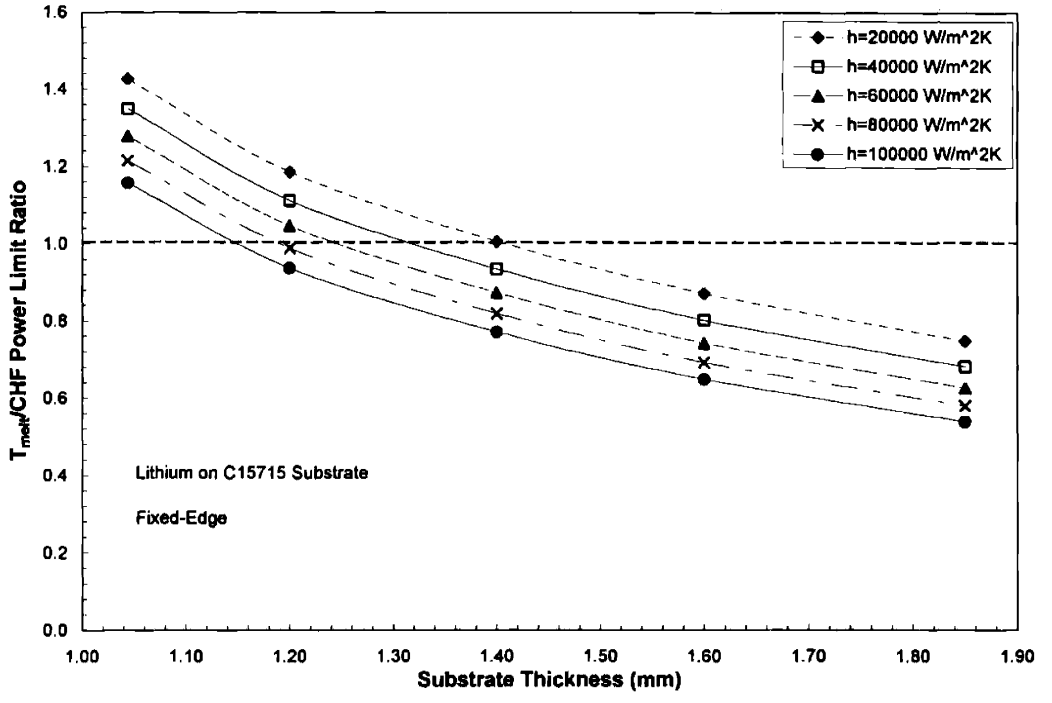

a)

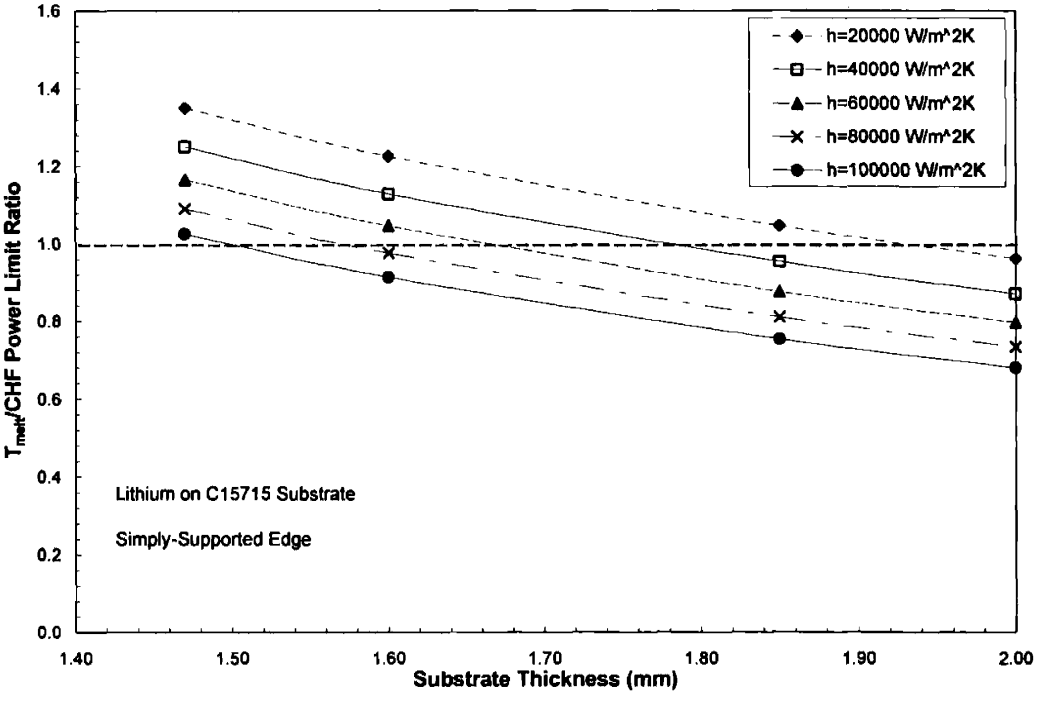

b)

Figure 3-21. T_{melt}/CHF ratio for (a) fixed-edge and (b) simply-supported lithium target on a C15715 substrate of varying thickness.

Regardless of substrate material, the maximum power which could be achieved occurred at the point where the T_{melt}/CHF equaled one. The only two exceptions, however, occurred when the C15715 and C18200 substrates were simulated using a heat transfer coefficient of 20000 W/m^{2}K. With an h of 20000 W/m^{2}K, heat flow due to radial conduction was significant compared to the axial conduction even in beams having large standard deviations. Figure 3-22 illustrates this fact by plotting the radial and axial heat flow in a target subjected to a broad beam, σ_{beam} = 15.1 mm, at a total power of 3500 W with heat transfer coefficients of 20000 and 100000 W/m^{2}K. The simulation results found the axial heat flux at r= 0 on the cooled side of the target was actually less for h=20000 W/m^{2}K than for h=100000 W/m^{2}K because of the increased radial heat transfer in the former case.

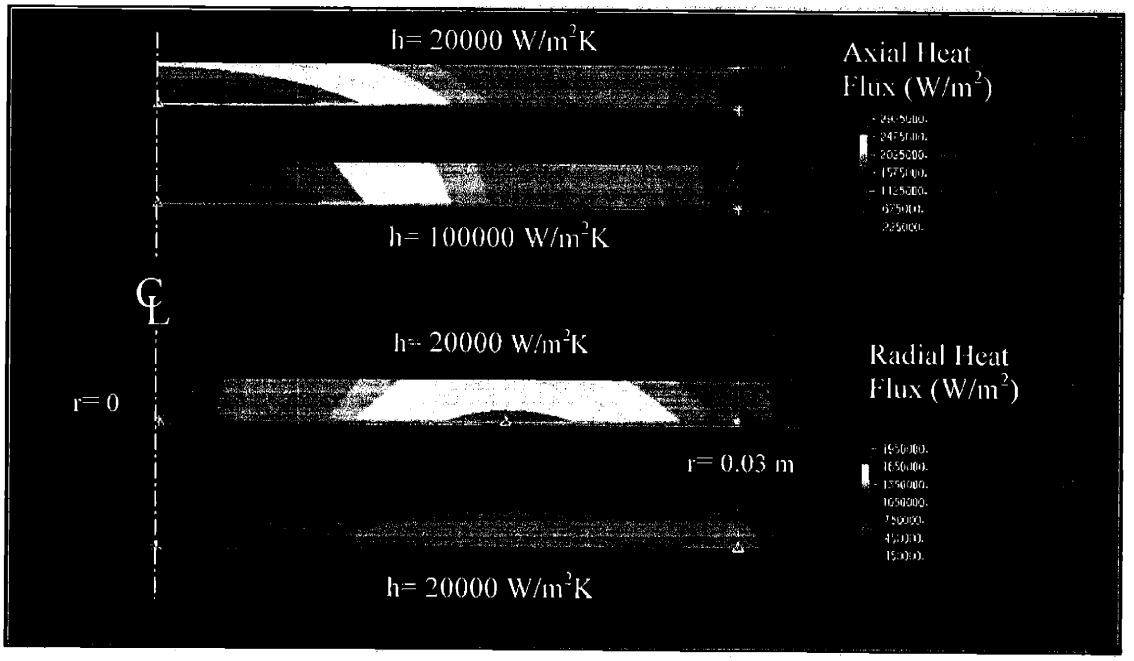

Figure 3-22. Plot of the axial and radial heat flux in a lithium target subjected to a beam of 3500 W having a σ_{beam} of 15.1 mm. Heat transfer coefficients of 20000 and 100000 W/m^{2}K were used for the simulations. In this figure axial heat flux is directed from the bottom towards the top of the section is positive. Radial heat flux away from r= 0 toward r= 0.03 m is positive.

Other than the combination of h=20000 W/m^{2}K with the copper alloy substrates, the largest total powers on target were found to occur for substrate thicknesses within 0.3 mm of the minimum thicknesses required to support a 0.10135 MPa differential. Table 3-2 lists the maximum power and substrate thickness at which this power was achieved for fixed-edge lithium targets using four different substrate materials. Even for substrates such as beryllium and tungsten which can support higher pressure differentials at reduced thickness, the copper alloys permitted higher total power.

Table 3-2. Thicknesses of various substrate materials required to achieve maximum power for a given heat transfer coefficient. Values listed are for fixed-edge targets.

Heat Transfer	C15715 Substrate		C18200 Substrate		Tungsten Substrate		Beryllium Substrate	
(W/m^2K)	(mm)	(W)	(mm)	(W)	(mm)	(W)	(mm)	(W)
20000	4.320	4117	4.320	4114	0.982	3572	1.076	3343
40000	1.318	6728	1.320	6724	0.904	5960	0.985	5860
60000	1.246	9258	1.248	9250	0.845	8212	0.916	8052
80000	1.191	11618	1.190	11590	0.801	10224	0.861	10020
100000	1.148	13680	1.140	13584	0.771	12020	0.843	11701

Because simply-supported targets required a greater thickness to support a given pressure differential, the maximum power which could be achieved was less than the fixed-edge cases. For the C15715 and C18200 copper alloys, simply-supported targets required substrates which were 0.35-0.47 mm greater than the values of Table 3-2 and could achieve power levels 1.5-5.5% less than the fixed-edge cases depending on the assumed heat transfer coefficient. At h=20000 W/m^2K the fixed-edge and simply-supported cases reached a maximum at the same substrate thickness.

Power limits for simply-supported beryllium substrates reached a maximum at thicknesses which were 0.31-0.40 mm greater than those listed in Table 3-2. For heat transfer coefficients of $60000<h<100000$ W/m^2K, maximum power occurred at the minimum thickness of 1.24 mm which could support the 0.10135 MPa differential. Power levels of the simply-supported beryllium substrate targets were 7.6-18.1% lower than the fixed-edge cases depending on the assumed heat transfer coefficient. Using simply-supported tungsten substrates, power levels were 6.7-16.6% less than the fixed-edge cases. For heat transfer coefficients of $80000<h<100000$ W/m^2K, maximum power occurred at the minimum thickness which could support the 0.10135 MPa differential. Simply-supported tungsten substrates required 0.22-0.32 mm greater thicknesses than the fixed-edge cases.

In addition to target dimensions and the heat transfer coefficient, power density as reflected by σ_{beam}, was an important factor in determining the maximum power which could be placed on a target. Figure 3-23 plots the maximum power for a given σ_{beam} which can be achieved with fixed-edge substrates of C15715, beryllium, and tungsten. All data in the figure are taken at substrate thicknesses listed in Table 3-2 except for the case of h=20000 W/m^2K which was taken at the point where the T_{melt}/CHF ratio was one.

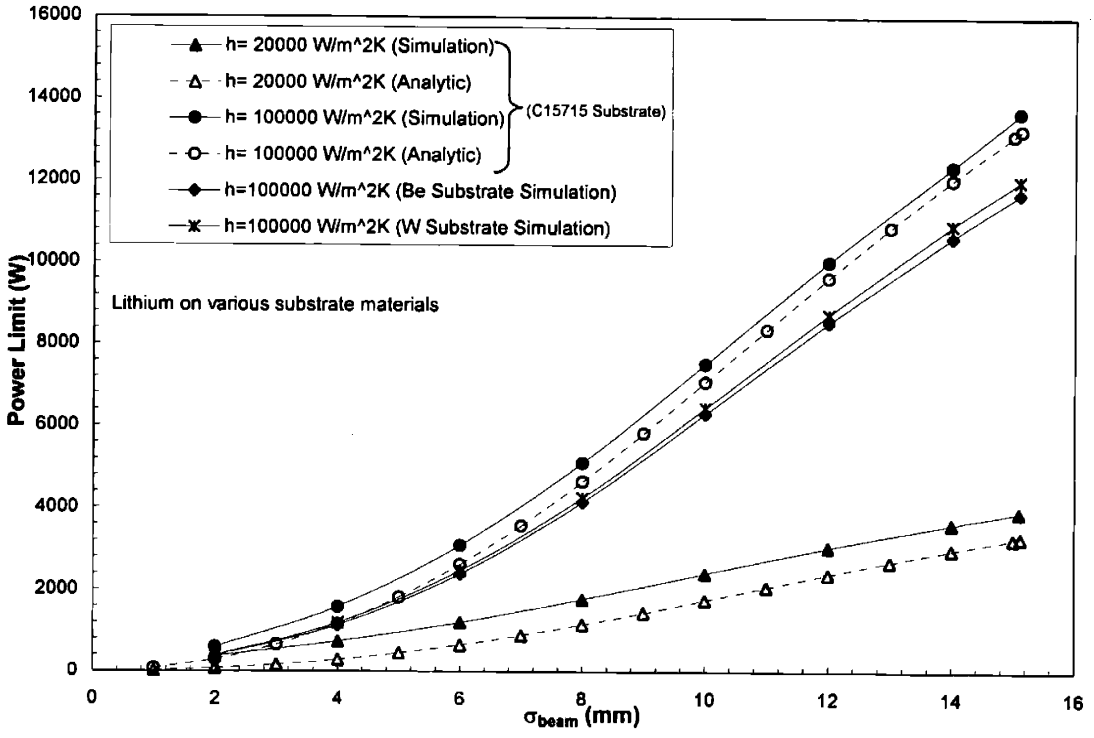

Figure 3-23. Plot of the maximum power which can be achieved for a given beam standard deviation. All data points were taken at the substrate thickness where the T_{melt}/CHF ratio was unity. Analytically derived values from §3.1.3 are shown for the C15715 substrate for comparison.

At small standard deviations the absolute power limits achieved by using the different substrate materials are relatively constant with the copper alloys being able to handle about 200 W more than the tungsten or beryllium targets. As σ_{beam} increases, the discrepancy between power limits increases to the point that at the maximum σ_{beam} value of 15.1 mm, copper alloys can support 1600-2000 W more than the tungsten and beryllium substrates. The dashed lines of Figure 3-23 represent the analytic solutions calculated in §3.1.3 for the C15715 substrate. Comparison of the analytic to the full numeric simulation data found that the solutions agreed the most (within 3%) for broad beams and high heat transfer coefficients. Analytic and numeric results for highly focused beams and low heat transfer coefficients differed by 413% due to the fact that radial conduction was most prevalent in these cases.

Because the melting point of lithium is low it was possible to narrow the range of substrate thicknesses by finding the point at which the power limit imposed by T_{melt} and CHF failure were equal. At this point the power which could be placed on the target was maximized. Such was not the case with the beryllium targets because any phase change of the target materials would occur at power levels much higher than can be achieved before the onset of CHF. For all beryllium-

based targets, power limits increased with substrate thickness. From the point of minimum thickness (1.04 mm, fixed; 1.47 mm, simply-supported) up to the thickness which could support the limiting pressure of 1.0 MPa (1.85 mm, fixed; 2.61 mm, simply-supported), power limits increased with thickness in a nearly linear fashion. Further increase in substrate thickness raised the power level, although at a reduced rate, as a result of greater radial conduction. Taken by themselves, these curves would seem to indicate that power limits could be raised to extremely large values simply by making the substrate very thick. Use of the O-ring melt limit imposed no restrictions on the beryllium target dimensions because even in the case of a broad beam, the temperature at the edge of the target was well below the 260 °C failure point. Useful information from the numerical simulations could be derived, however, if an additional failure criteria based on thermal stress was assumed. While §3.4 will present the interactions of thermal stress in much greater detail, the results presented here are used merely to show that the thermal performance alone is not sufficient to determine a useful range of substrate thicknesses for beryllium targets. Figures 3-24 a,b plot the power limits of a 110 μm beryllium target on a C15715 copper alloy substrate using an σ_{beam} of 2 mm, while Figures 3-25 a,b utilize a beam having σ_{beam} of 15.1 mm. These curves show that power limits imposed by the yielding of the substrate, in fact, decrease with thickness for a given heat transfer coefficient. In these figures, the intersection of the black and red lines corresponding to the same heat transfer coefficient would indicate the magnitude of the maximum achievable power and the substrate thickness at which it is achieved.

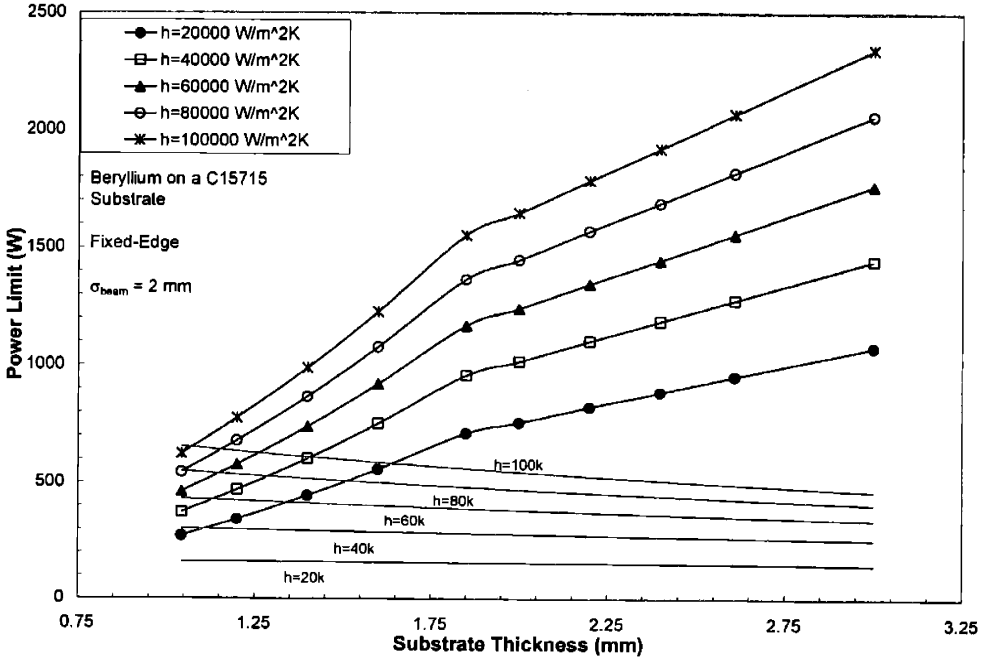

3-24 a)

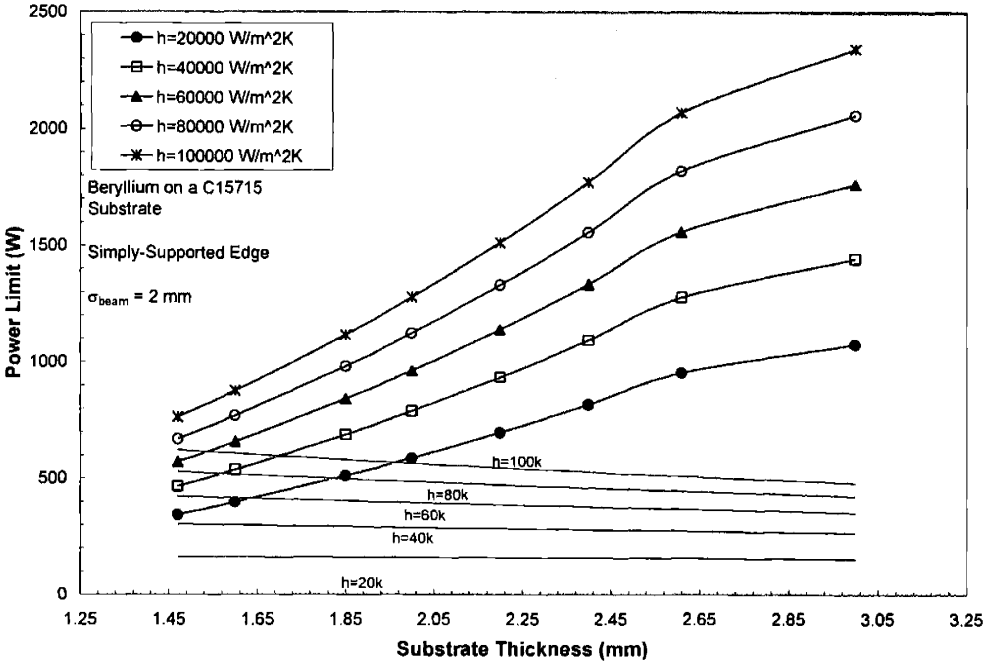

3-24 b)

Figure 3-24. Power limits imposed by the onset of CHF (black) and estimates of the limits imposed by thermal stress (red) for fixed (a) and simply-supported (b) beryllium targets on a C15715 substrate. Both plots are data from a simulation using σ_{beam} = 2 mm.

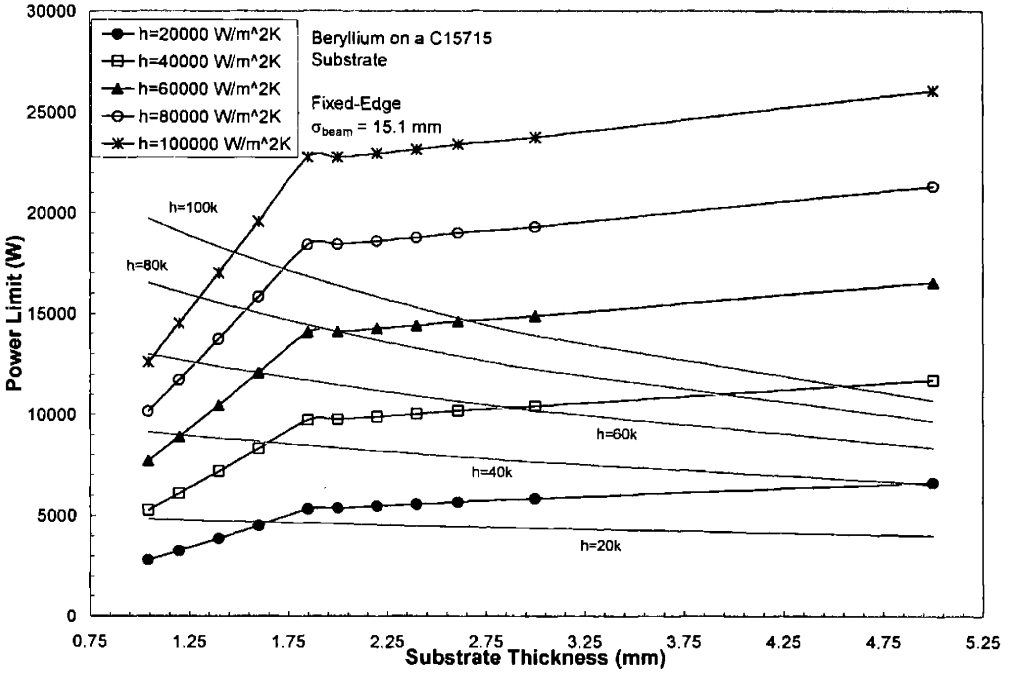

3-25 a)

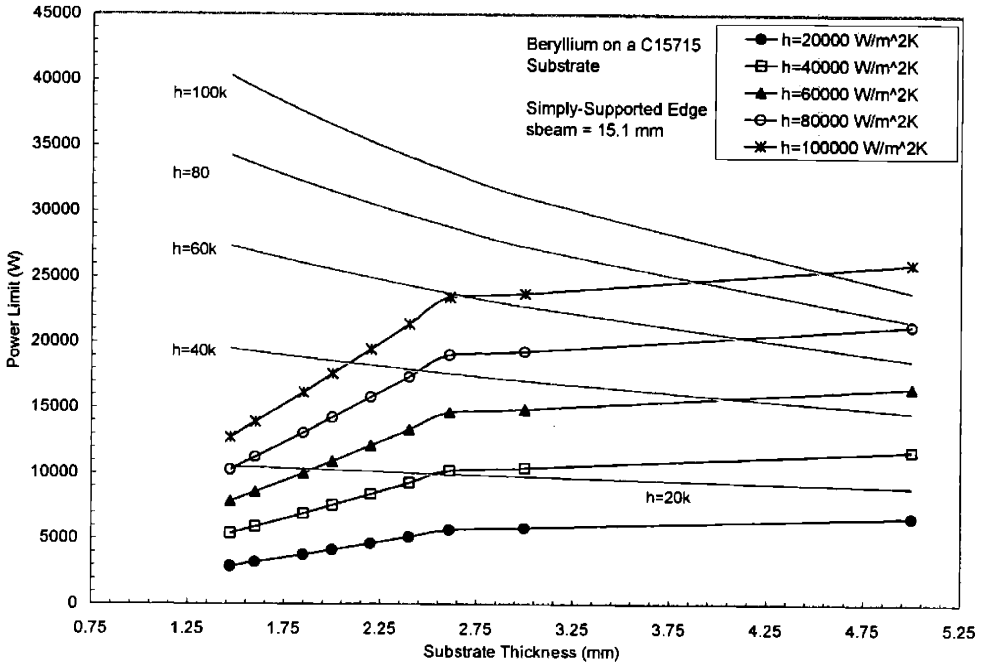

3-25 b)

Figure 3-25. Power limits imposed by the onset of CHF (black) and estimates of the limits imposed by thermal stress (red) for fixed (a) and simply-supported (b) beryllium targets on a C15715 substrate. Both plots are data from a simulation using σ_{beam} = 15.1 mm.

This data illustrates that substrate thicknesses in fixed-edge targets will likely be limited to within 0.1 mm of the minimum value. For h<80000 W/m^{2}K, the thermal stress curves are always less than the CHF limit curves and give the maximum power at a thickness of 1.04 mm. For the simply-supported targets in Figure 3-24 thermal stress limits are less than the CHF limits for all heat transfer coefficients. At higher σ_{beam} values, the intersection of the CHF and thermal stress curves move away from the point of minimum thickness but still fall within a relatively narrow band. In the fixed-edge cases of Figure 3-25 curves intersect in a region between 1.45 and 1.65 mm, whereas the simply-supported targets begin to reach maximums at thicknesses in excess of 4.5 mm.

3.2.3 Conclusions Based on Numerical Simulations

From these numerical simulations it was possible to identify certain trends in the behavior of both lithium and beryllium-based targets. Regardless of the substrate material, lithium targets were able to achieve maximum total power at substrate thicknesses which were typically no more than 0.5 mm higher than the minimum thickness which is necessary to support a 0.10135 MPa

pressure differential. Increased thickness was required because of the need to pressurize the coolant to delay the onset of CHF. This was true for both fixed and simply-supported targets. Under the combination of h=100000 W/m^2K and the C15715 fixed-edge substrate, the maximum power density which would allow a total power of 10 kW on target required a beam having a standard deviation of 12 mm which results in a q" at the center of the ion beam of 12 MW/m^2. The data of Table 3-2 indicate that a minimum heat transfer coefficient of 70000 W/m^2K is required to reach the 10 kW power level.

Dimensions for beryllium targets could not be defined in the same manner based only on thermal considerations since the onset of CHF was shown to occur well before any phase change in the target. Approximations of the power limits imposed by thermal stress indicated that substrate thicknesses would likely be close to the minimum values required to support a 0.10135 MPa pressure differential. The only cases in which thermal stresses did not seem to impose a limit were the simply-supported targets subjected to a broad beam.

Throughout previous discussions the nature and origin of the heat transfer coefficient has not been detailed. Clearly it is advantageous to have the highest possible h to support high beam power. It is also evident from the numerical studies that regardless of the magnitude of the heat transfer coefficient, thin targets will suffer from CHF. Raising the pressure on the back side of the target will raise the saturation temperature and delay CHF, but there is a tradeoff to be made. Targets must still be capable of supporting vacuum even if pressure is increased and thickness is decreased. Thermal stresses as well as pressure generating by the flow of the coolant will further add to the problem. If it were possible to enhance the magnitude of the heat transfer coefficient while eliminating the possibility of CHF, targets could be constructed with very small thicknesses without regards to the target/coolant interface temperature. Cooling using liquid gallium metal has a number of advantages which make it an attractive alternative to conventional water cooling. At present little data exists on the capabilities of liquid gallium cooling. In the following section some of the first experimental data regarding the cooling capabilities of submerged jet impingement cooling using liquid gallium metal is presented.

3.3 Submerged Jet Impingement Using Liquid Gallium Metal

Liquid jet impingement has been extensively studied for a wide variety of applications including metal forming processes, thermal management of circuits, and turbine blade cooling. Jet impingement is an attractive cooling configuration because high heat transfer coefficients (10^4-10^5 W/m^{2}K) are readily achieved, implementation is relatively simple, and the region of maximum heat transfer can be directly aimed at the area of highest heat flux. This makes jet impingement ideal for cooling targets subjected to localized heat loads generated by ion-beams. Since targets in NCT applications are located within a completely flooded assembly which is inserted into a moderator/reflector assembly, submerged jet impingement as opposed to free jet impingement is considered in this section. Throughout these discussions it is assumed that jets are fully turbulent (Re>4000) since laminar jets would have little use in the high heat flux conditions encountered in NCT. More specifically, the cooling configuration discussed in this section is an axisymmetric submerged jet as opposed to a planar jet. Axisymmetric submerged jet impingement (see Figure 1-8) differs from free jet impingement in that the jet is introduced through a region of static fluid before striking the target.

A submerged jet can be described in terms of three distinct hydrodynamic regions which are indicated in Figure 1-8. Far away from the target the free-jet region is characterized by increasing levels of turbulence and mixing due to the shear of the jet by the ambient fluid. As the distance from the jet exit to the target is increased this mixing tends to displace the potential core of the jet. This displacement eventually reaches the jet centerline unless the nozzle to target spacing is less than 6-8 nozzle diameters.[17] As the jet approaches the target plate its velocity is decelerated in the axial direction and accelerated radially.

The impingement region defines an area which extends approximately 2 nozzle diameters from the target plate in the axial (z) direction and 1.6 to 3 nozzle diameters in the radial direction.[18] Within this region, the stagnation zone extends out to about 0.8 nozzle diameters from the centerline and is characterized by a nearly uniform heat transfer coefficient.[19] Before giving further background about jet impingement cooling, it is necessary to introduce nomenclature which will be used throughout this section. As much as possible, variables and symbols from previous sections are maintained in this section for clarity.

c_p: specific heat at constant pressure (J/kg °C)

d: nozzle diameter (m)

ε: dissipation rate of turbulent kinetic energy (m^2/s^3)

h_o: stagnation point heat transfer coefficient (W/m^2K)

$\bar{h}$: area-averaged heat transfer coefficient (W/m^2K)

K: turbulent kinetic energy (m^2/s^2)

k: thermal conductivity (W/mK)

μ: molecular viscosity (kg/m s)

μ_T: turbulent viscosity (kg/m s)

Nu_o: stagnation point Nusselt number (= hd/k)

$\overline{Nu}$: average Nusselt number (=$\bar{h}$ d/k)

Pe: Peclet number (= RePr)

Pr: Prandtl number ($\mu c_p/k$)

ρ: density (kg/m^3)

Re: jet Reynolds number ($=V_j d/\nu$)

r/d: non-dimensional radial distance from jet center

s/d: non-dimensional nozzle-nozzle spacing for jet arrays

V_j: jet velocity (m/s)

ν: kinematic viscosity (m^2/s)

ν_T: turbulent kinematic viscosity (m^2/s)

z/d: non-dimensional axial distance from jet to target

3.3.1 Single Submerged Jet Impingement (Pr > 1)

Heat transfer using single submerged jets has been studied by a number investigators under different configurations.[20-24] In these studies the maximum heat transfer coefficient, h_o, was found to occur in the stagnation region with local heat transfer values decreasing at large r/d. A number of correlations exist for the stagnation Nusselt number for turbulent submerged jets. For jets with Pr>1 in the range of 5000<Re<36000 the correlation $Nu_o=1.02\ Re^{0.5}\ Pr^{0.368}$ was proposed by Sun et al.[17] Gabour and Lienhard [25] suggest a correlation, $Nu_o = 0.278\ Re^{0.633}\ Pr^{1/3}$, which is more strongly dependent on Reynolds number for 25000<Re<85000.

Beyond the stagnation region local h values tend to fall off with r/d as a result of the increasing thickness of the laminar wall-jet boundary layer. When z/d spacing is less than about 6, however, local h values recover to a secondary maximum at an r/d of $\approx$ 1.9 as a result of increased turbulent kinetic energy in this region. The magnitude of this maximum is less than h_o for z/d greater than unity. At a z/d less than unity any improvement in h is overshadowed by increased flow resistance resulting in the need for extremely large system pressures.[21] Nozzle-to-

target spacing not only affects the radial variation in h but Nu_o as well. The stagnation Nusselt number tends to rise as z/d spacing is increased from 1 to between 4-5 in submerged jets. Beyond a z/d of 5, Nu_o decreases linearly with spacing. Unlike the correlations given previously, Garimella and Rice included z/d as an additional parameter in their correlations. For $1<z/d<5$ they suggest $Nu_o = 0.492\ Re^{0.585}\ Pr^{0.4}\ (z/d)^{0.024}$.[22]

Since h generally decreases with r/d, use of a heat transfer coefficient based only on the stagnation point Nusselt number will overpredict the cooling capacity unless the heated area is 1-2 times the area of the jet. Area-averaged Nusselt numbers are a more representative means of predicting the heat transfer over areas much greater than that of the jet. The study of confined and submerged jets by Garimella and Rice[22] mentioned previously proposed correlations for both Nu_o and $\overline{Nu}$ over the range of $4000 < Re < 23000$. Comparison of the correlations indicates that the ratio of $\overline{Nu}/Nu_o$ approaches unity as Reynolds number increases. At a z/d of 4, the ratio is 0.64 for Re = 4000 and increases to 0.78 at Re = 23000. This comparison is applicable over an area extending out to an r/d value of 3-4.

The results of §3.2 illustrated that the pressure of the cooling system affected the onset of critical heat flux. Impinging jets have an added advantage over other types of cooling configurations in that the dynamic pressure created from the combined axial deceleration and radial acceleration raises the pressure in the stagnation region beyond the ambient system pressure. Outside the stagnation region the pressure falls off in a Gaussian fashion to the point where the ambient pressure level is reached at an r/d of 1. The pressure in the stagnation region is given by

$$P_{stag} \approx P_{sys} + \frac{1}{2}\rho V_j^2 \tag{3.20}$$

At this point it is helpful to understand orders of magnitude for both the heat transfer coefficient and dynamic pressure generated by jets of a given diameter and velocity. Heat transfer coefficients using the previously mentioned correlations are given over a range of Reynolds numbers in Figure 3-26. This graph plots h_o values calculated for 3 different nozzle diameters at a z/d spacing of 4. For each curve Pr = 6 and $\nu = 10^{-6}\ m^2/s$ which are typical for water jets. Figure 3-27 illustrates the rapid increase in dynamic pressure required to achieve high heat transfer coefficients for different diameter nozzles.

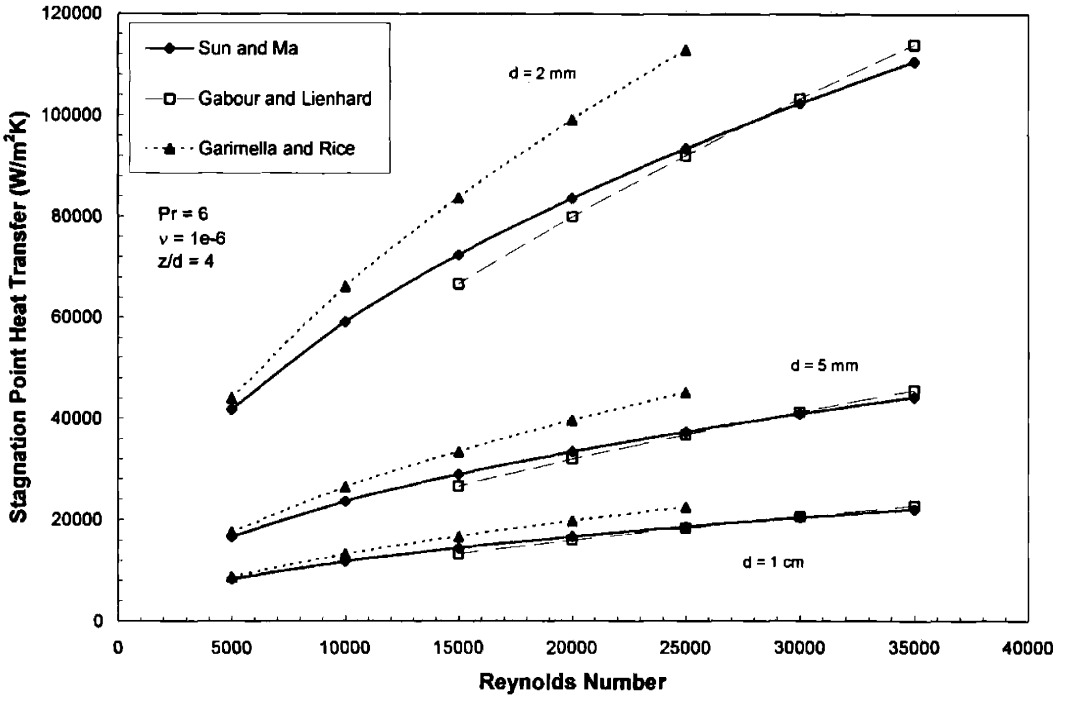

Figure 3-26. Stagnation point heat transfer coefficients as a function of Reynolds numbers for three different diameter nozzles at a constant z/d of 4.

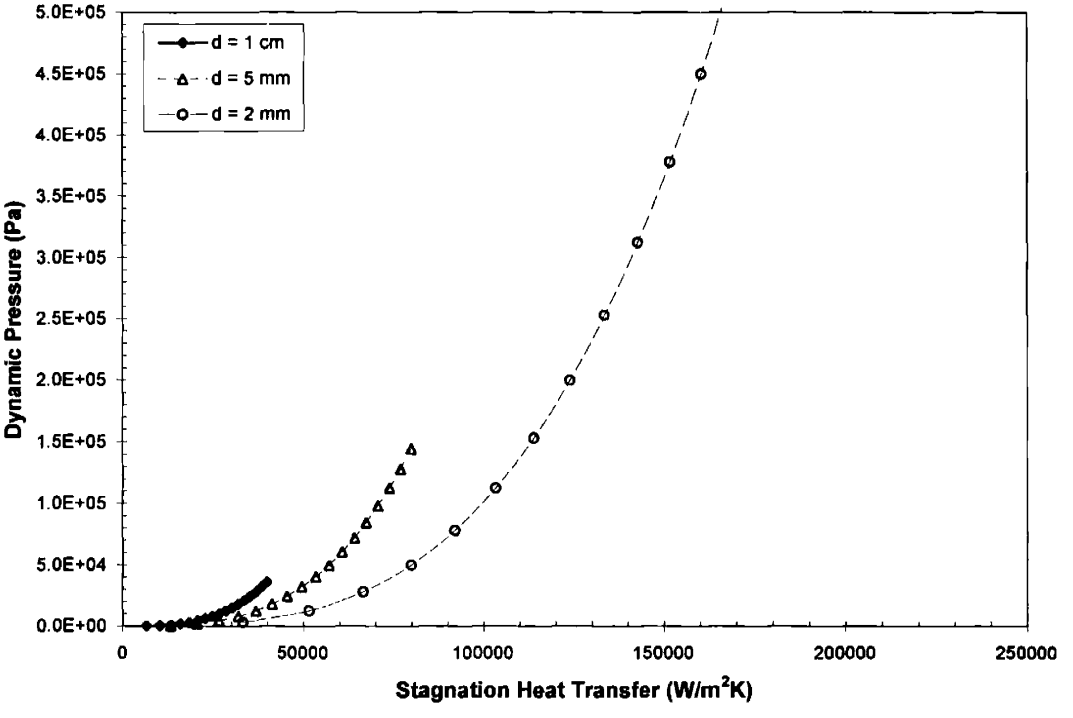

Figure 3-27. Plot of the dynamic pressure generated by nozzles of various size at a given heat transfer coefficient.

3.3.2 Submerged Jet Arrays

In an NCT target, which could have an area of tens of cm^2, reduction of the heat transfer coefficient outside the stagnation region poses a problem for single jet configurations. Reduction in dynamic pressure is also a concern since at high heat flux levels the possibility of CHF failure is likely to exist at large r/d. By using an arrangement of several nozzles in an array, a number of the shortcomings of a single nozzle system can be overcome. By placing nozzles close together, the region associated with a single jet is reduced and the heat transfer coefficient remains at a value nearer to that of the stagnation point. Secondary stagnation zones of increased heat transfer and dynamic pressure are also set up where the individual jets collide and are accelerated away from the solid surface. In addition to the parameters mentioned in the previous correlations, the use of arrays introduces an additional parameter, s/d, which represents the nozzle-to-nozzle spacing. Based on the correlation of Pan and Webb,[26] $\overline{Nu} = 0.225 Re^{2/3} Pr^{1/3} e^{-0.095(s/d)}$, the ratio of $\overline{Nu}/Nu_o$ for an array is 0.65 at a Reynolds number of 5000. At higher Reynolds numbers (Re = 20000) the ratio for arrays has risen to 0.94. These comparisons used an s/d array spacing of 4.

3.3.3 Liquid Metal as a Heat Transfer Fluid

Many different types of liquid metals have been used or proposed as the cooling medium for a number of industrial processes. In the nuclear industry liquid metals have been used in fast-breeder reactors such as SUPERPHENIX and EBR-II, which used sodium, and EBR-I, which used a sodium-potassium eutectic. Regardless of the application, liquid metals are attractive primarily because they can operate at very high temperatures and have a thermal conductivity much higher than traditional coolants such as water or oil. Because of this high thermal conductivity, heat transfer correlations for liquid metals ($Pr \ll 1$) take-on a slightly different form from the $C_i Re^a Pr^b$ correlations developed for higher Prandtl number fluids. Correlations for liquid metal forced convection are usually given in the form $C_1 + C_2 Pe^a$ to account for the significant heat transfer even when the flow goes to zero.[27, 28]

One disadvantage encountered in some systems is that operating temperature must be kept high to maintain the metal in the liquid state. Traditional liquid metal coolants such as lithium, sodium, and lead-bismuth alloys have melting points of 180.5, 97.8, and 125 ℃ respectively.[29] Liquid gallium has been studied on a very limited basis as a heat transfer fluid. Beside cesium and mercury, gallium has the lowest melting point (29.78 °C) of any pure metal. As a cooling fluid it has a high thermal conductivity, low molecular and kinematic viscosity, and has the highest liquid range (29.78-2205 ℃) of any metal with the exception of tin. Table 3-3 compares many of the relevant heat transfer properties of gallium and water.

Table 3-3. Various properties relating to heat transfer for gallium and water

Properties at 30 °C	Gallium	Water
Density (kg/m^3)	6096	995.7
Melting point (°C)	29.8	0.0
Boiling Point (°C)	2205	100.0
Thermal conductivity (W/m K)	30.6	0.62
Specific Heat (J/kg K)	408	4180
Molecular viscosity (kg m/s)	1.97e-3	0.798e-3
Kinematic viscosity (m^2/s)	3.2e-7	0.801e-6
Vapor Pressure at 100 °C (torr)	10^{-11}	760
Pr	0.026	5.42

One of the primary obstacles in using gallium as a heat transfer fluid is its rapid attack of most structural metals. Any of the typical heat transfer structural materials such as copper, aluminum, platinum, zirconium, nickel, silver, and gold form solid solutions with gallium even at low temperatures. A few metals such as tantalum, tungsten, beryllium, and high chromium stainless steels offer good resistance to gallium although these materials suffer significant corrosion at temperatures above 300-600 °C depending on the material. The best resistance to attack by liquid gallium comes from non-metal oxides such as BeO, Al_2O_3, ceramics, and certain forms of graphite. These materials have been found to resist attack by liquid gallium at temperatures in excess of 1000 °C.[30] The density of gallium increases upon melting from ~5900 to ~6100 kg/m^3, and its volume expands upon freezing. It also has a strong tendency to supercool for long periods of time without solidification. Studies regarding the toxicity of gallium and its nitrates indicate that it has a comparable toxicity to aluminum although an acute dose of 72 mg per kilogram of body weight produced nephritis in rats.[29]

Because of its low melting point, high thermal conductivity, and low kinematic viscosity, gallium appeared to be a suitable candidate for use in NCT. No experimental correlations exist for liquid metal submerged impinging jets, and very limited data exist for free surface liquid metal jets. Two correlations which have been proposed for free surface liquid metal jets were based on experiments in which a single turbulent jet impinged normally upon and subsequently melted a metal target plate. Sato et al[31] proposed: $Nu = 0.0152\ Re^{0.92}\ Pr^{0.8}$, while Green et al[32] suggested a correlation based on Peclet number: $Nu = 0.47\ Pe^{0.5}$.

For cases in which no phase change of the substrate occurs literature suggests that laminar jet correlations could be used.[33] Analytic derivation of the Nusselt number for a laminar jet

having Pr<<1 gave the correlation: $Nu = 1.08Pe^{0.5}$.[34] Comparing the heat transfer coefficient predicted for gallium at 30 °C using the laminar correlation to that predicted by a turbulent water jet at 20 °C (Re= 20000; d= 5 mm) results in an h_{ga}/h_{H20} ratio of 5.6:1. These calculations suggest that water would require a velocity of 60.7 m/s to match the convection generated by the gallium jet at 1.28 m/s. In order to test the practicality and efficacy of a gallium-based system, however, it was apparent that a small-scale test was required to compare the heat transfer of gallium and water.

3.3.4 Small Scale Tests of Liquid Gallium Submerged Jets

The results of §3.2, which used water as the working fluid, indicated that CHF failure would be a significant limiting factor in NCT target development. In order to remove high heat fluxes, water jets rely on the dramatic increase of dynamic pressure to raise the saturation temperature to the point where large temperature gradients can exist at the target/coolant interface without initiating CHF. Beyond the stagnation region, however, reduced pressure and decreased heat transfer make the onset of CHF likely, especially if single jets are used which have an area smaller than the beam. To avoid CHF at large r/d positions, pressurizing the system to several atmospheres is possible but this places additional mechanical stress on the target. If gallium jets were capable of generating heat transfer coefficients comparable to or greater than water, the onset of CHF would be avoided completely without the need to raise the system pressure.

3.3.4.1 Experimental Set Up for the Gallium/Water Tests

Small-scale tests were conducted to investigate the ability to design, build, and experiment with a system using liquid gallium at low powers and flowrates. Experiments were designed to measure and compare the heat removal of a single submerged jet using both water and gallium. Experiments using a beryllium target heated by a low power ion beam were carried out first with water and then with gallium to ensure that beam conditions were the same for both fluids. The following description details the experimental set up and procedure utilized with gallium. Procedures in the water experiments were the same with the obvious exception that water was used as the cooling fluid rather than gallium.

Figure 3-28 gives a schematic representation of the assembly which was constructed in the accelerator vault at the LABA facilities. A 7-gallon polypropylene reservoir was mounted on a movable cart and fitted with brackets to hold a small 12 VDC mechanical gear pump and a 250 ml bottle which served as the gallium reservoir. Before beginning the experiment, the reservoir was filled with water and heated to between 40-50 °C by a 500 W immersion heater. In order to

keep the gallium supply completely immersed in the water the 250 ml bottle was positioned so that the entirety of its volume, with the exception of the top of the sealing cap, was below the waterline. Likewise, the pumping head was kept submersed in the water during the experiments with the electric connections and motor above the waterline. The water reservoir along with the immersion heater, pump, and 250 ml gallium reservoir are shown in the photo of Figure 3-29.

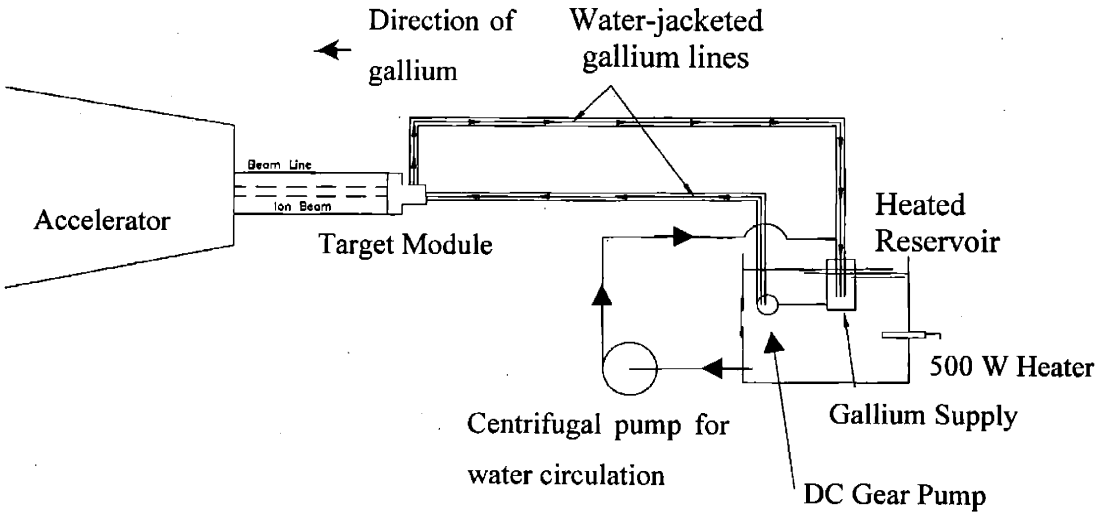

Figure 3-28. Small-scale assembly used to test the heat removal of water and gallium jets from a beryllium target heated by a 1.5 MeV proton beam.

Because of the small size of the pump and the weight of the liquid metal, the gallium level had to be kept above the pumping head so that gravity alone would maintain a net positive suction head (NPSH) on the pump inlet. Upon discharge from the pump, gallium traveled to the target system through a water-jacketed stainless steel tube, which can also be seen in Figure 3-29. The jacketing tube was constructed by encasing a 1.27 cm (½") OD 316 stainless steel tube within a 1.59 cm (5/8") OD polypropylene outer tube. This configuration allowed heated water to be passed in the outer annular region of the jacket in counterflow path while gallium passed through the inner stainless steel tube. This flow configuration served both to keep the gallium warm as it passed to and from the target as well as serving as a simple counterflow heat exchanger. Heated water was drawn from the water reservoir and circulated in the jacket by a 1/3 hp centrifugal pump.

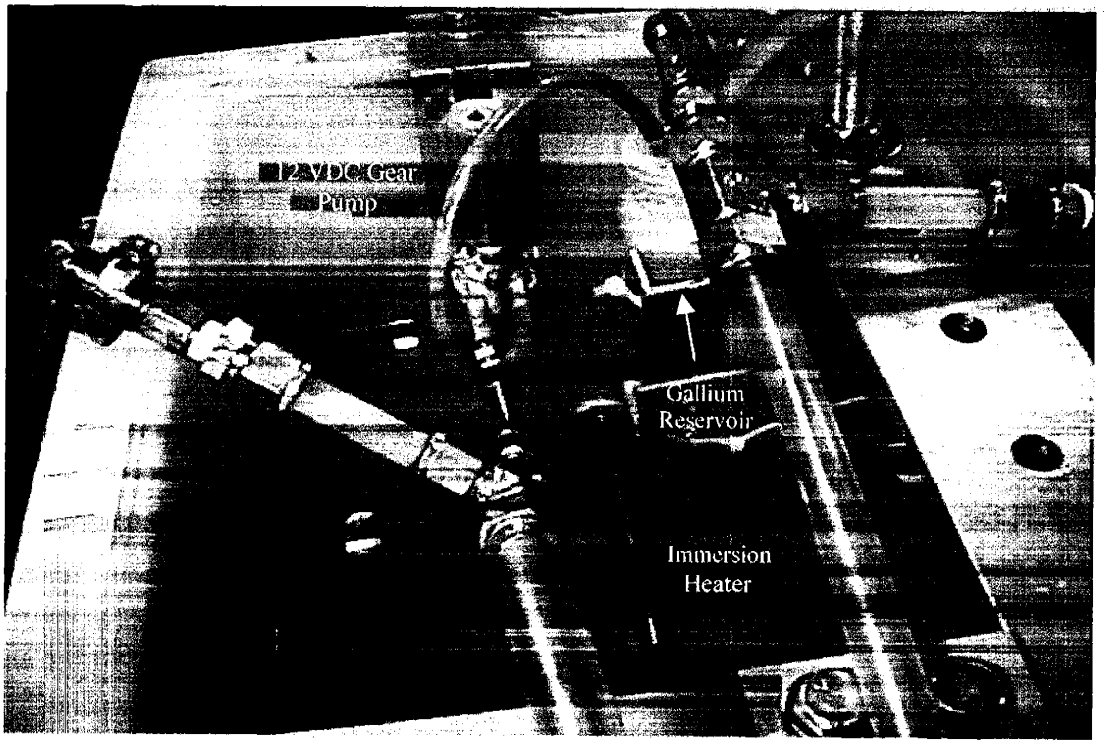

Figure 3-29. Photograph of the polypropylene heated water tank along with the gear pump, immersion heater, and gallium reservoir positioned within the tank.

Gallium was loaded into the system by first melting a 200 ml sample contained in a plastic bottle using a hot water bath. After the gallium was completely melted it was slowly poured into the 250 ml container which was positioned in the heated reservoir. This pouring technique helped remove the scale which tended to form on top of the liquid surface. After transferring the metal to the 250 ml bottle its cap was replaced. In this cap three holes were drilled that were just large enough to allow 6.35 mm (¼") OD tubing to pass. Two of these holes served as an inlet and outlet for the gallium line while the third allowed a blanketing supply of dry nitrogen to be positioned above the gallium. Use of dry nitrogen was intended to displace as much oxygen and moisture as possible to slow oxidation and scale formation. Flexible polyvinyl tubing, which is shown in Figure 3-29, was used to connect the gallium reservoir and pumping head with the jacketed cooling line.

The target module constructed for these experiments is illustrated in the schematic of Figure 3-30a. A straight edged nozzle (d = 3.91 mm) was formed out of 316 SS tubing which had an OD of 6.35 mm. A 304 SS KF-50 blank flange stub was tapped on the back side to allow the insertion of a SWAGELOK fitting. The nozzle was passed through this fitting and positioned with its edge at a z/d of 1.75 from the target surface. Nozzle-to-target spacing was measured to an accuracy of ±0.1 mm using a micrometer. An angular cut was made in the stub so that the

spent fluid would travel away from the target in an annular fashion before exiting, thereby minimizing crossflow. The target plate was constructed from a 2.54 mm thick beryllium plate having a diameter of 4.445 cm which was brazed into a modified 304 SS KF-50 flange. Brazing of the target was performed by Brush Wellman.

a)

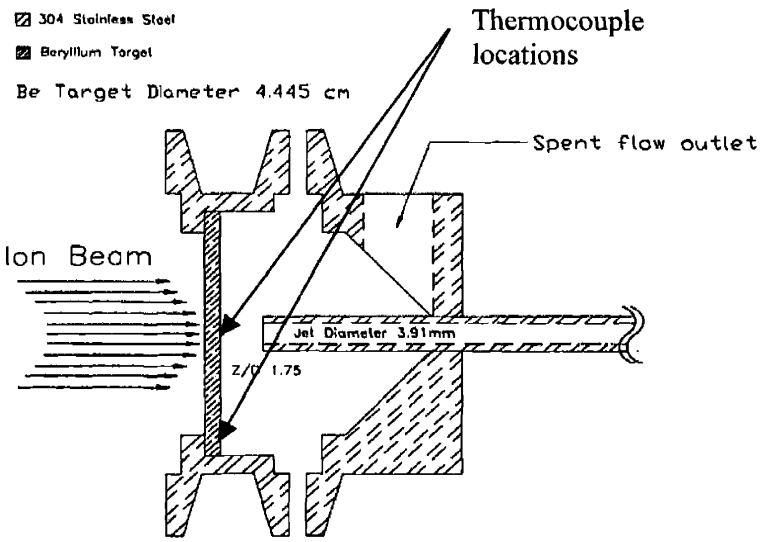

b)

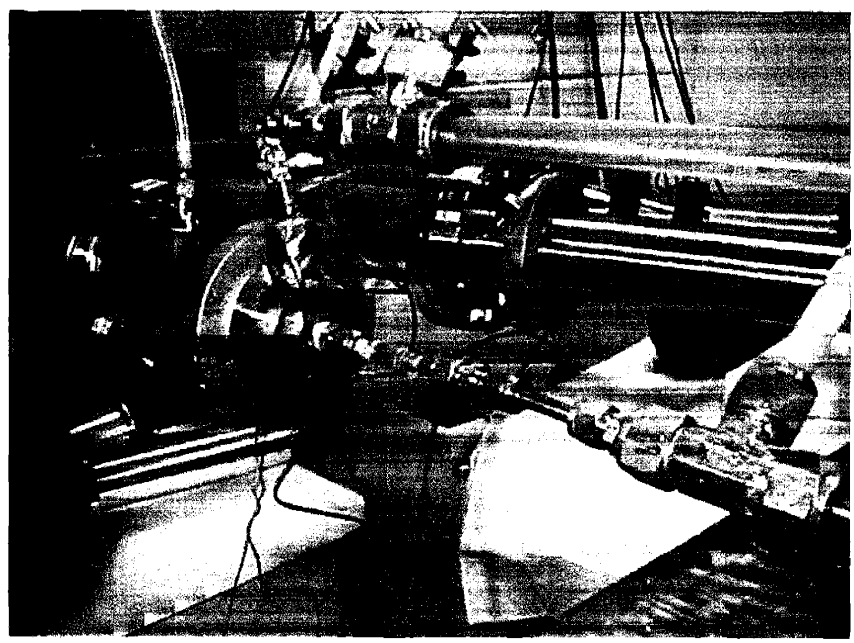

Figure 3-30. a) Schematic of the target assembly constructed by brazing a beryllium disk (d= 4.445 cm; t= 2.54 mm) into a modified KF-50 flange. b) Photograph of the target assembly positioned on the accelerator beam line. Thermocouple leads as well as the jacketed cooling line are visible.

A 1.5 MeV proton beam served as the heating source for these experiments. Temperature measurements of the target were made with K- type thermocouples which had a stainless-steel sheath diameter of 1.0 mm and a resolution of ±0.1 °C. Thermocouples were affixed to the cooled side of the target directly underneath the jet and at the edge of the target at an r/d of 5.2. These were joined to the target by passing them through two small holes drilled into the stainless steel body of the flange and were affixed by a thin layer of thermally conducting epoxy. Care was taken to make the epoxy mound as small as possible to avoid disturbing the flow field of the jet. Inlet and outlet temperatures of the coolant were also measured by K-type thermocouples attached to the stainless steel cooling line immediately prior and after the target assembly. Insulation was used on these thermocouple connections to minimize heat exchange with the surrounding air. A picture of the target assembly mounted on the end of the beamline is given in Figure 3-30b.

Flowrate measurement was accomplished by collecting the flow from the system into a graduated cylinder for a given period of time. This technique is recommended by Omega Engineering (Stamford, CT) for field calibration of direct reading flowmeters.[35] Three separate measurements were conducted before temperature readings were taken. Average flowrate and uncertainty were calculated from these readings. As an added check on the consistency of the flowrate, the current drawn by the pump was monitored throughout the experiment to ensure that the large deviations in pumping power did not occur. Error analysis on the measured volumes and times found that the greatest flowrate error was 0.061 L/min, which represented an uncertainty of 8.7%.

After the system had been loaded with gallium and flowrates had been measured, the vault was sealed and the accelerator, which had already been tuned, was brought up to the appropriate terminal voltage. Beams of increasing power were placed on the target and temperatures were measured. After each increase in beam power, the temperature variations were monitored until a steady-state had been achieved at which time temperature recordings were made.

Tests were conducted over three separate days using water flowrates of 0.55, 0.70, and 1.75 L/min. For the test at 0.70 L/min the cooling water was kept at 25 °C. All other water tests were conducted using jet temperatures of 45-50 °C. Two gallium tests were performed at flowrates 0.29 and 0.46 L/min with inlet temperatures of 50-55 °C. All experiments were conducted at a z/d ratio of 1.75. Accelerator optical settings were set to identical levels for all tests and produced a peak heat flux of 3250±203 W/m^2 per Watt of beam power. Experiments described in Chapter 2 indicated that beam size and shape is repeatable given the same optical settings. Temperature at the target center was peaked to ensure that the beam was located directly beneath the stagnation

area of the jet. The third experiment with gallium was terminated when the pump overheated and the motor failed. Tests at other z/d spacings had also been planned but were not performed for the same reason. Pump failure was a major factor in limiting the amount of time that could be devoted to each gallium run. In the first two gallium experiments, pumps failed after about 15 minutes of operation. Failure of the third pump occurred after 2 minutes of operation and did not allow for a third gallium experiment. During normal operation, current drawn by the motor remained within 0.1 amp of the initial current. Each pump failure was preceded by a spike in the current followed by an immediate drop to zero.

3.3.4.2 Results and Discussion of the Small-Scale Tests

Figure 3-31a plots the difference (dT) between the stagnation point (T_o) and the jet inlet temperature (T_{in}) versus beam power for the three water tests. Figure 3-31b plots the corresponding data collected in the gallium experiments. Jet velocities achieved in each experiment are listed in the legend. Calculation and comparison of h_o achieved in the experiments was accomplished by performing a least squares linear regression on each set of data. This regression resulted in the slope of dT versus power. Since h= q"/dT, h_o could be calculated using h_o= C/X, where C = 3250±203 W/m^2 per Watt of beam power and X is the slope of the regression which has units of W/K. The slopes of the regressed lines along with calculated h_o are presented in Table 3-4. Comparison of the stagnation point heat transfer produced by gallium and water indicates that even at jet velocities lower by factors of 2-4, gallium generates a greater heat transfer coefficient than water. With only two data points it is difficult to assess, but the data also seems to suggest that the stagnation point Nusselt number for submerged gallium jets increases more rapidly with Reynolds number than is the case with water jets.

Table 3-4. Regression data and stagnation point heat transfer coefficients from gallium and water jets.

Jet Type and Velocity	Slope (W/K)	h_o (W/m^{2}K)
Gallium V_j = 0.40 m/s	0.1948	16690 ± 1258
Gallium V_j = 0.64 m/s	0.0866	37544 ± 2784
Water V_j = 0.76 m/s	0.2314	14050 ± 901
Water V_j = 0.97 m/s	0.1889	17212 ± 1212
Water V_j = 2.43 m/s	0.1002	32448 ± 3645

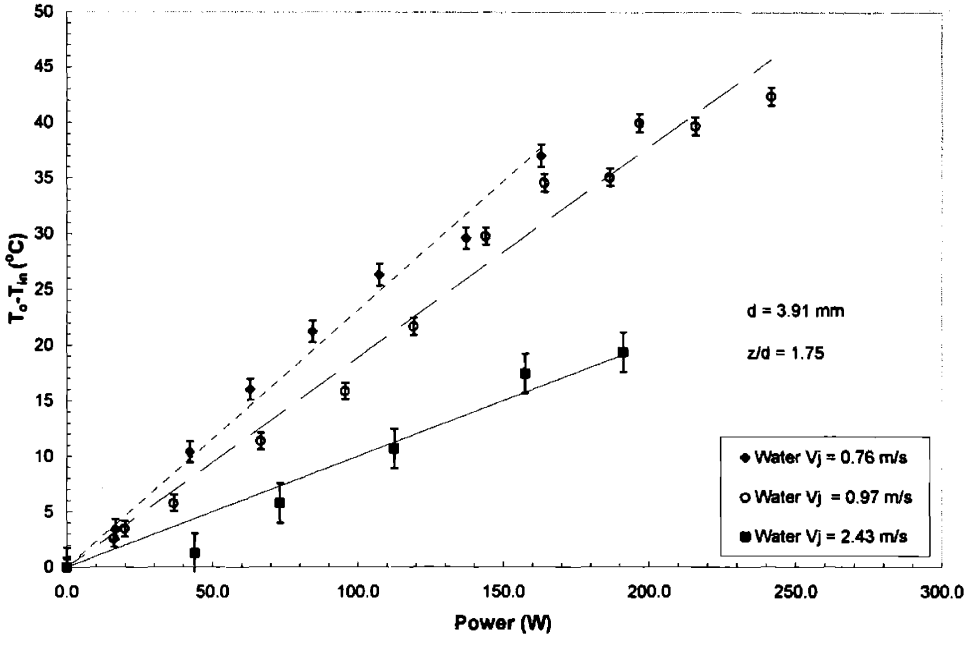

a)

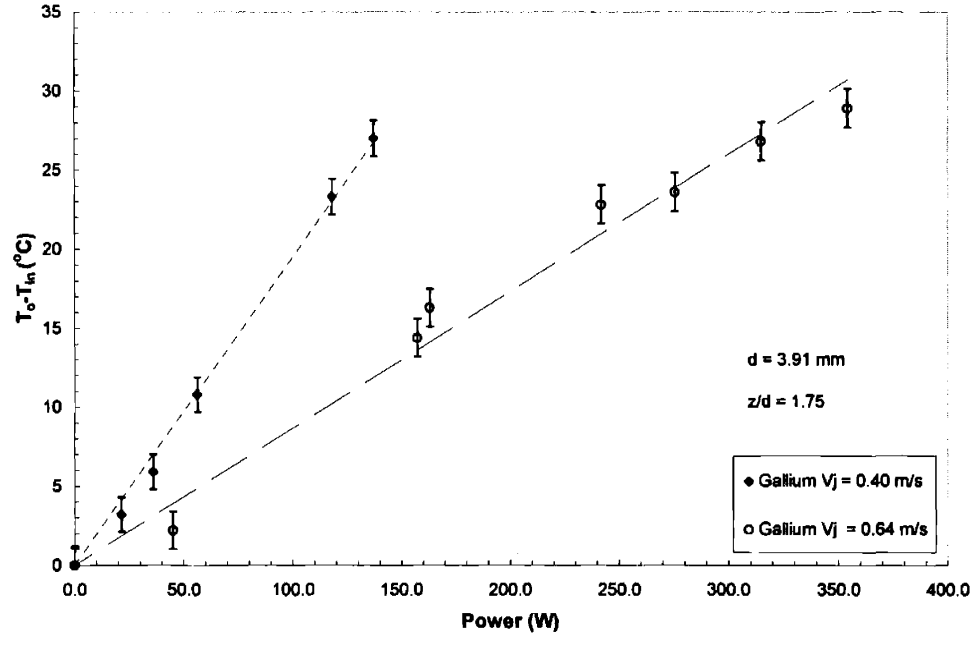

b)

Figure 3-31. a) Temperature difference (dT) between stagnation point (T_o) and inlet (T_{in}) for water jets. b) Temperature difference (dT) between stagnation point (T_o) and inlet (T_{in}) for gallium jets.

The data collected from the thermocouple placed at the target edge, r/d= 5.2, suggests that the heat transfer at large distances away from the stagnation point is poorer in gallium than in water jets. Results of the difference in temperature between the target periphery and the jet inlet is illustrated in Figure 3-32. Both gallium jets exhibit larger increases in temperature at the edge of the target compared to water jets at equal beam power. This can be attributed partly to the lower flowrates and the fact that the specific heat of gallium is 10 times lower than water. Even after accounting for the differences in specific heat and flowrate using a first law energy balance, however, gallium still exhibits a larger temperature rise at the target extremity which suggests that the local heat transfer of gallium jets at large r/d declines more rapidly from the stagnation point value than water jets.

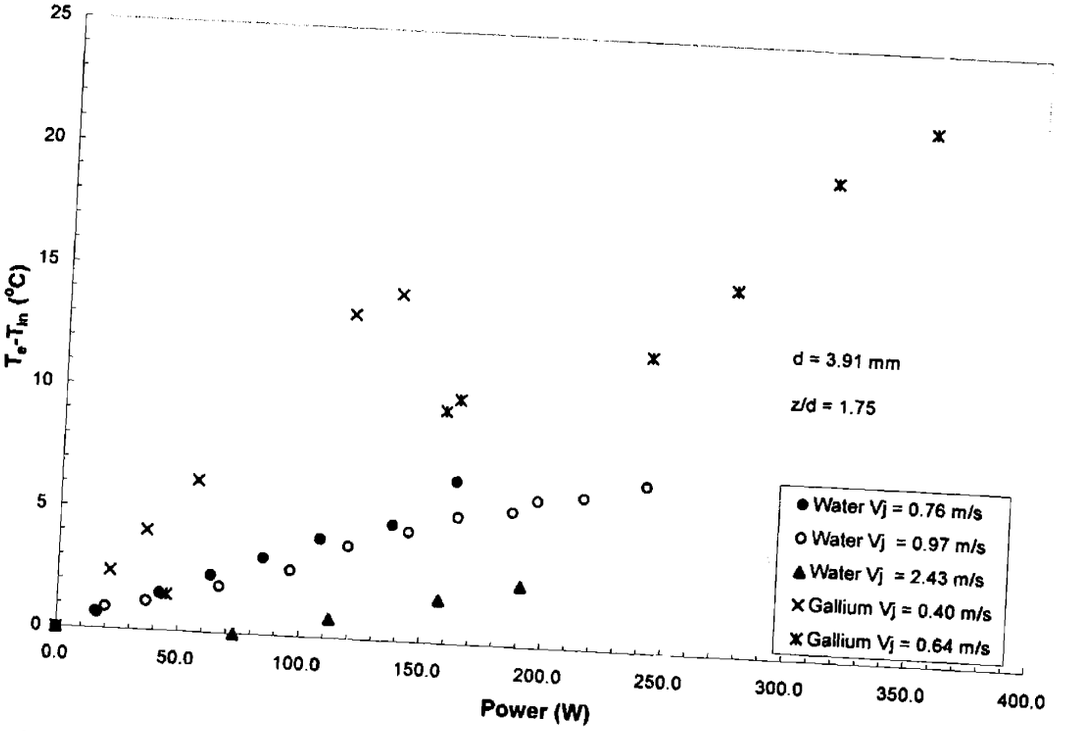

Figure 3-32. Plot of the temperature difference (T_e-T_{in}) between the target edge (r/d = 5.2) and the jet inlet for gallium and water jets.

Besides the results involving heat transfer, other conclusions from a practical engineering standpoint could be drawn from these small-scale experiments. A primary concern was the scale and oxidation which tended to form on the gallium during the experiment. During each of the runs using gallium a significant amount of scale was observed in the 250 ml bottle even with the presence of dry nitrogen. A separate test using argon as the blanketing gas did not prevent scale formation. The likely cause of the scale formation was the significant amount of water vapor in

the vicinity of the gallium reservoir throughout the experiment. Under static conditions direct contact of gallium with steam should not have produced a large amount of scale since the oxide layer formed on the surface protects the underlying gallium from further oxidation.[30] When the gallium was flowing, however, the continual agitation of the surface tended to break up the oxide and provided an exposed liquid surface which led to further oxidation. Although these tests indicated that gallium could be successfully circulated with a positive displacement pump, a larger pump would certainly be required in further experiments. Disassembly of the Teflon pumping heads indicated that chipping of the gears had occurred. As the experiment progressed, solid oxide particles had certainly been drawn into the pumping head resulting in chipping of the gears. Larger particles which could not pass through the gears would have led to the seizing of the motor and its subsequent failure. From the standpoint of material compatibility, 316 and 304 stainless steel, beryllium, and the polymers used in the tubing did not appear to suffer any detrimental interactions with the gallium. For the low powers encountered in this test, the simple counter flow path of the gallium and the heating water was sufficient to remove the heat from the gallium. Jet inlet temperature increases of 2-3 degrees over the course of the experiment indicated that the thermal mass of the water reservoir was sufficient to absorb most of the power removed from the target. At higher power levels, however, the heat transfer from the gallium to the water reservoir as well as the thermal mass of the heat sink would have to be increased.

3.3.5 Numerical Simulations of Water and Gallium Jets Using the K-ε RNG Method

Based on the promising results of the small-scale tests, fluid dynamic simulations were conducted to supplement the information gained during the experiments. It was also hoped that the simulations would give further insight into the variation of the local heat transfer from gallium jets. The K-ε RNG model was used in the ADINA-F code to model both water and liquid gallium jets. A brief introduction into K-ε theory is presented before the discussion of the simulation results.

The incompressible Navier-Stokes equations govern the behavior of turbulent fluids.

$$\frac{\partial V}{\partial t} + (V \cdot \nabla)V = -\frac{1}{\rho}\nabla P + \nu \nabla^2 V \qquad (3.21)$$

$$\nabla \cdot V = 0 \qquad (3.22)$$

Direct numerical simulation of these equations is possible but is limited by computer resources, because the velocities, timescales, and energies involved in turbulent flow vary by many orders of magnitude. These scales can be divided into three groups[36]:

(1) Large-scale eddies

In this range turbulent kinetic energy (K) is generated as a result of shear. The largest eddies have a length-scale which is on the order of the boundary layer thickness. The length scale in this range is on the order of $K^{3/2}/\varepsilon$.

(2) Inertial subrange

Turbulent kinetic energy is neither created or dissipated in this region. Turbulent kinetic energy as a function of eddy size is governed by Kolmogoroff's -5/3 power law.

(3) Viscous dissipation range

Turbulent kinetic energy is dissipated in this range as a result of viscosity. This dissipation occurs at a rate ε. Length scales in this region scale as $(\nu^3/\varepsilon)^{1/4}$.

From the length scale of the very smallest eddies it is apparent that a mesh for direct integration would require a spacing on the order of $\nu^{3/4}$. Two dimensional simulations would therefore need $\nu^{-6/4}$ integration points and 3-D simulations, $\nu^{-9/4}$ points. In order to reduce the computing power required for direct simulation, time averaging of the Navier-Stokes equations have been used to eliminate the small-scale variations. In turbulent flow the instantaneous velocity in a given direction is given by

$$v = U + u \tag{3.23}$$

where,

U: mean velocity (m/s)

u: fluctuating velocity component (m/s)

If this two-component velocity is substituted into the Navier-Stokes equations and averaged according to the conditions: $\langle U \rangle = U$; $\langle u \rangle = 0$, the Reynolds Averaged Navier-Stokes equations emerge. The averaging process, however, introduces a term which still involves the fluctuating velocity component and prevents closure of the equation. Various closure models have been

proposed which allow calculation of this new term, $-\partial_i\langle u_i u_j\rangle$, which is given the name Reynolds stress. This term is not technically a stress, but since it has behaves as such, $-\langle u_i u_j\rangle$ is modeled using an equation which is very similar to the shear stress formula for viscous laminar flow.

$$-\langle u_i u_j\rangle \sim \nu_T(\partial_j U_i + \partial_i U_j) \tag{3.24}$$

where,

ν_T: turbulent kinematic viscosity

The standard K-ε model developed by Jones and Launder is still the basis for most numerical simulations of turbulent flow.[36] Closure of the Reyonlds Averaged Navier-Stokes equations is accomplished by formulating a system of differential equations in terms of the turbulent kinetic energy, $K= \frac{1}{2}\langle u\rangle^2$ (m^2/s), and the rate of turbulent energy dissipation, ε (m^2/s^2), which can be solved to give ν_T. The standard model of Jones and Launder was expanded by Yakhot and Orszag who applied perturbation theory and dynamic scaling to the standard K-ε model.[37] Their solution method, known as the Renormalization Group or K-ε RNG model, can be utilized in ADINA-F to model turbulent flow. The RNG model was found to be more accurate than the standard method for recirculating flows which are encountered in jet-impingement.[38] Both the standard K-ε and K-ε RNG models introduce constants which are not derived analytically but are proposed based on experimental data. These constants are listed in Table 3-5.

Table 3-5. Numerical constants used in the standard and RNG K-ε models.[36, 39]

	Standard Model	RNG Model
C_μ	0.09	0.085
C_1	1.44	1.42
C_2	1.92	1.68
σ_k	1.0	0.7179
σ_e	1.3	0.7179

A sixth constant, σ_T (turbulent Prandtl number), is also required when the conservation of energy equation is used in the K-ε formulation to model heat transfer. While the other constants remain unchanged throughout all regions of the simulation, experimental evidence suggests that σ_T varies depending on the configuration of the flow.[40]

3.3.5.1 Building the Numerical Model for Simulations of Single Submerged Jets

The target illustrated in Figure 3-30a, which was used for the small scale gallium and water experiments, was highly axisymmetric. Based on this symmetry, a 2-D model was generated in ADINA-F which was symmetric about the z-axis. Figure 3-33 illustrates the portion of the target used in the small-scale experiments which was modeled in the numeric simulations.

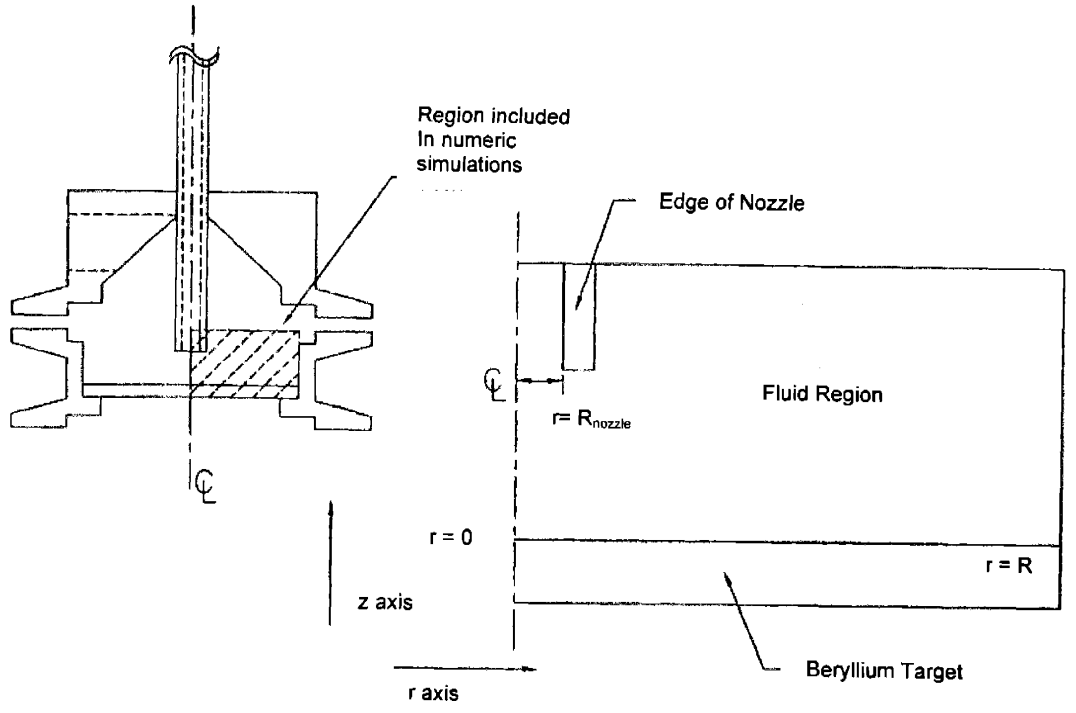

Figure 3-33. Large scale view of target and close-up of the region simulated using the K-ε RNG model. Since the model is axisymmetric, only the region from r=0 out to the wall at r = R is modeled.

In terms of specifying the boundary conditions for the simulation, the traction/velocity and heat flux/temperature boundaries were relatively straightforward. Either a velocity or traction (pressure) boundary had to be specified on all nodes along the periphery of the model. Likewise, either a heat flux or temperature had to be specified on all nodes located at the model boundary. The boundaries listed below were used in the model.

Traction/Velocity

1. Velocity profile of the fluid located within the nozzle region was determined by iterating the equations of fully developed internal flow which follow the logarithmic law.

$$\frac{V_j(r_n)}{u_*} = \frac{1}{\kappa} ln(\frac{(R_{nozzle} - r_n)u_*}{\nu}) + 5.0 \tag{3.25}$$

$$\frac{1}{\pi R_{nozzle}^2} \int_0^{R_{nozzle}} [V_j(r_n)] 2\pi r_n dr_n = \frac{Q}{A_{nozzle}} = V_j^{mean} \tag{3.26}$$

where,

Q: coolant flowrate (m^3/sec)

r_n: radial distance from nozzle wall toward centerline of jet

u_*: friction velocity (m/s)

κ: Von Karman's constant = 0.41

Definition of the velocity profile was carried out separately from the ADINA-F program in the following manner. Since u_* in Equation 3.25 cannot be solved analytically, a centerline velocity had to be assumed. By fixing a centerline velocity, u_* could then be solved through iteration. With this value of u_*, $V_j(r_n)$ was integrated using Equation 3.26 to determine a mean jet velocity. This was repeated until the mean jet velocity determined through integration of the velocity profile matched the experimentally measured jet velocity calculated by dividing the flowrate by the nozzle area.

2. $\partial V/\partial r = 0$ (symmetry condition) at r = 0.

3. No-slip condition for nodes at nozzle boundaries, target surface, and along wall at r = R.

4. Normal traction of 0.10135 MPa along top of fluid region.

Heat Flux/Temperature

1. Jet inlet temperature prescribed for fluid within the nozzle region.

2. $\partial T/\partial r = 0$, $\partial q''/\partial r = 0$ at r = 0.

3. Along the front side of the beryllium target the heat flux was modeled with a Gaussian distribution a standard deviation of 7 mm and a peak of 3251 W/m^2 per Watt of beam power.

4. q"= 0 (insulated) at all other boundary nodes

The only remaining boundary conditions which needed to be specified were those used for turbulent kinetic energy and dissipation rate. Careful selection of these boundary conditions, especially at fluid/solid interfaces, was critical for the proper execution of the simulation. At the inlet region within the nozzle, K and ε were related to the mean jet velocity using[41]

$$K = 0.003(V_j)^2 \qquad \varepsilon = \frac{C_\mu^{0.75} K^{3/2}}{0.05d} \tag{3.27}$$

At the boundary corresponding to the top of the fluid the gradients of K and ε were set to zero. Near no-slip boundaries the behavior of the K-ε model is known to become unreliable because of suppressed turbulent mixing in the boundary layer.[36] In applications such as jet impingement, however, this near-wall region is critical in the heat transfer process. Several studies have shown that the K-ε model without modification overpredicts the turbulent kinetic energy in the stagnation region which can result in an overestimation of Nu_o by as much as 300%.[42] In order to improve the behavior of the model in these regions, wall-functions can be introduced to replace the normal K and ε equations. Standard wall-function equations for K and ε are utilized in the ADINA-F code and have the following form

$$K = \frac{u_*^2}{\sqrt{C_\mu}} \qquad \varepsilon = \frac{u_*^3}{\kappa z_p} \tag{3.28}$$

where,

z_p: is the axial distance from the wall where the functions are applied. The variable is given the subscript "p" because it is at this point that the normal equations for K and ε are "patched" with the wall function equations.

At solid/fluid interfaces such as the nozzle boundaries and the wall at r = R the standard wall-functions needed no further modification. This was not the case, however, at the solid/fluid interface in the stagnation region.

Initial simulations with water jets using only the standard wall-functions resulted in h_o values of 2-3 x 10^5 W/m^2K at jet velocities similar to those encountered in the small-scale experiments. A quick comparison with h_o values calculated with previously mentioned correlations indicated that the simulation had severely overestimated the heat transfer. This overestimation was found to result from the position at which the wall-functions were applied in the stagnation region of

the impinging jet and the inability of the wall functions to balance the production and dissipation of turbulent kinetic energy in the stagnation zone. Wall-functions are based on the assumption that the patching between the modified K-ε equations and those of the general model occur in a region where the logarithmic velocity profile of Equation 3.25 still holds. Wall-functions, furthermore, have been calibrated for flows which are parallel to boundaries and are free of large pressure gradients.[43] This defines a region $40 < z^+ < 100$ in which the patching can take place. (The non-dimensionlized distance from the target surface is used $z^+ = z\ u_*/\nu$.) In jet impingement, however, the flow is not entirely parallel to the surface and large pressure gradients do exist in the stagnation region. Additionally, the viscous boundary layer, which lies in the region between the wall and the logarithmic boundary layer, is extremely thin in jet impingement. For these reasons, application of the standard wall function was occurring at a z^+ outside the applicable range. The resulting artificial increase in turbulence and a near singularity in the dissipation rate are typical symptoms of the stagnation point anomaly. To avoid this problem, non-equilibrium wall-functions were imposed in the viscous boundary layer by using constraint equations on K and ε. Non-equilibrium wall functions force K to zero at the wall and avoid the dissipation singularity and are given by[44]

$$K = \left(\frac{z}{z_{vis}}\right)^2 K_p \qquad \varepsilon = \frac{2\nu K}{z^2} \tag{3.29}$$

where,

z^0: dimensionless constant = 11.225

K_p: turbulent kinetic energy at location of patching

z_{vis}: viscous sub-layer thickness

$$z_{vis} = \frac{\mu z^0}{\rho C_\mu^{1/4} K_p^{1/2}} \tag{3.30}$$

In addition to the boundary conditions applied in the model, one other modification regarding the turbulent Prandtl number, σ_t, was required. Unlike other constants introduced in the K-ε model, the value of σ_t has been shown to vary depending on the nature of the flow and the distance from a solid interface.[40] This dependence on the distance from the wall tends to increase σ_t especially for fluids with $Pr \ll 1$. For fluids having $Pr > 1$, σ_t values range from 0.8-

0.9.[36] For water jet simulations a σ_T of 0.9 was used in the boundary layer and a σ_T of 0.85 throughout the rest of the model. In low Prandtl number fluids, however, σ_T can be >>1 especially near the wall.[39] An extended prediction algorithm developed by Weigand et. al. was used to calculate the turbulent Prandtl number in the simulations of the gallium jets.[40]

3.3.5.2 Results of the Numerical Simulations for Water and Gallium Jets

Simulations of both water and gallium jets were carried out at velocities, z/d spacing, and inlet temperatures which matched the conditions used in the small-scale experiments described in §3.3.4. Since the simulations with water could be benchmarked not only against the small-scale experiments but also against data in the literature, they were conducted first. Figures 3-34 a,b,c plot the experimental and simulations results for the three water tests. Comparison of the simulated stagnation point temperatures for the water jets found that maximum deviations from the experimental results were 9.6%, 5.8%, and 8.0% respectively. Simulated temperatures at a radial position of r/d = 5.2 agreed within 12.3%, 6.2%, and 3.7%. Outlet temperatures differed by a maximum of 1.2%, 1.2%, and 2.8%. In addition to the temperature comparisons which indicated good agreement between the numerical model and experiments, additional comparisons involving the heat transfer coefficients were made. Table 3-6 lists the simulated and experimental h_o values from the three water jets (V_j = 0.76; 0.97; 2.43 m/s) having Reynolds numbers of 4950, 6300, and 16000 along with the predicted h_o from four different correlations in literature.[17, 22, 25, 45]

Table 3-6. Comparison of simulated stagnation point heat transfer coefficient to experiment and various correlations. Number in parentheses is the percent difference between the experiment or correlation value.

Simulated h_o (W/m^2K)	Experimental h_o (W/m^2K)	Garimella & Rice (W/m^2K)	Lee & Lee (W/m^2K)	Sun & Ma (W/m^2K)	Gabour & Lienhard (W/m^2K)
14479	14050 (2.9)	16104 (11.2)	17268 (19.3)	18722 (29.3)	16891 (16.7)
17879	17212 (3.7)	18560 (3.8)	19838 (11.0)	21601 (20.8)	19694 (10.2)
33420	32448 (2.9)	33636 (0.7)	35434 (6.0)	35858 (7.3)	37662 (12.7)

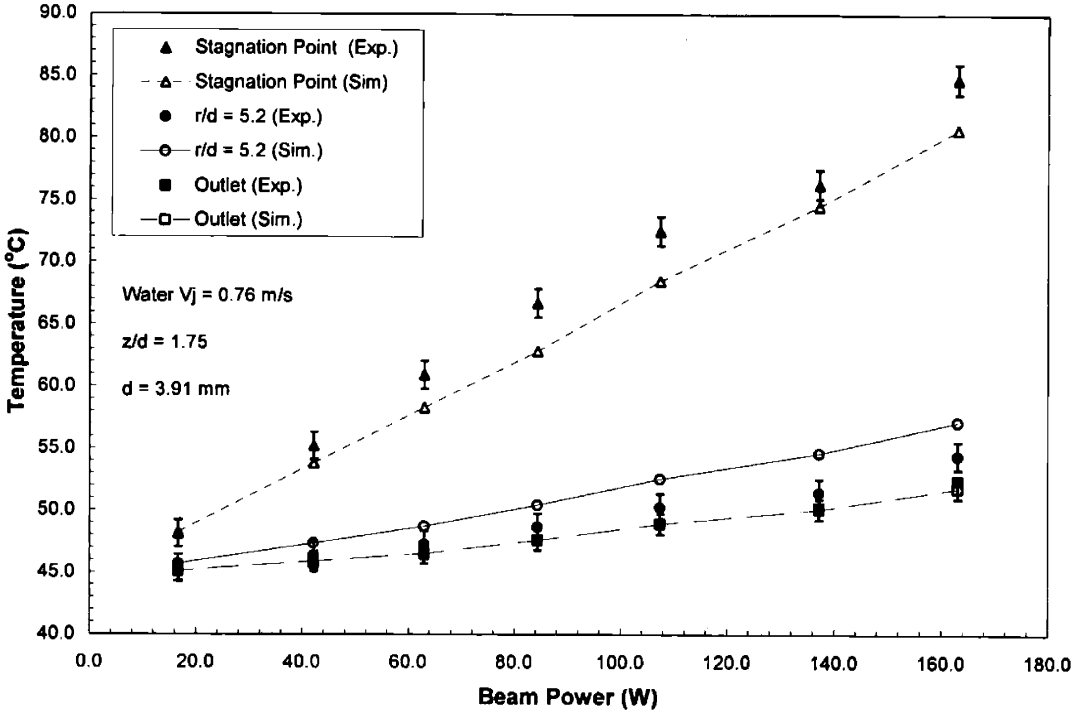
Stagnation Point (Exp.)
Stagnation Point (Sim)
r/d = 5.2 (Exp.)
r/d = 5.2 (Sim.)
Outlet (Exp.)
Outlet (Sim.)
Water Vj = 0.76 m/s
z/d = 1.75
d = 3.91 mm
Temperature (°C)
Beam Power (W)
90.0
85.0
80.0
75.0
70.0
65.0
60.0
55.0
50.0
45.0
40.0
0.0
20.0
40.0
60.0
80.0
100.0
120.0
140.0
160.0
180.0

a)

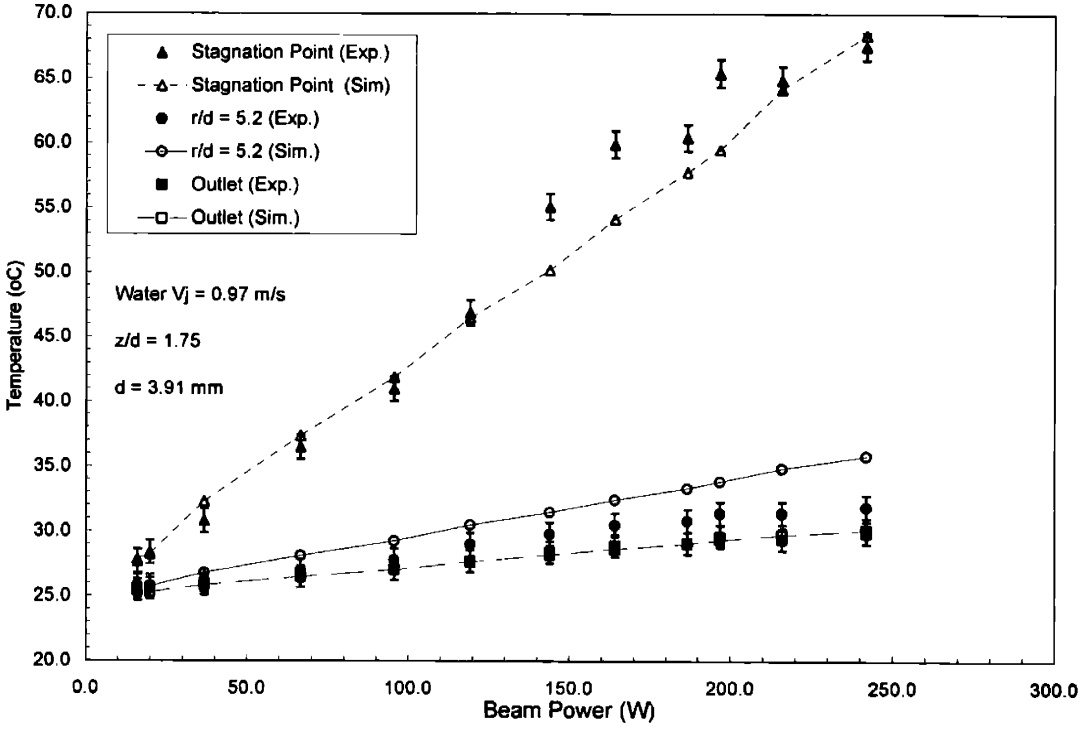
Stagnation Point (Exp.)
Stagnation Point (Sim)
r/d = 5.2 (Exp.)
r/d = 5.2 (Sim.)
Outlet (Exp.)
Outlet (Sim.)
Water Vj = 0.97 m/s
z/d = 1.75
d = 3.91 mm
Temperature (oC)
Beam Power (W)
70.0
65.0
60.0
55.0
50.0
45.0
40.0
35.0
30.0
25.0
20.0
0.0
50.0
100.0
150.0
200.0
250.0
300.0

b)

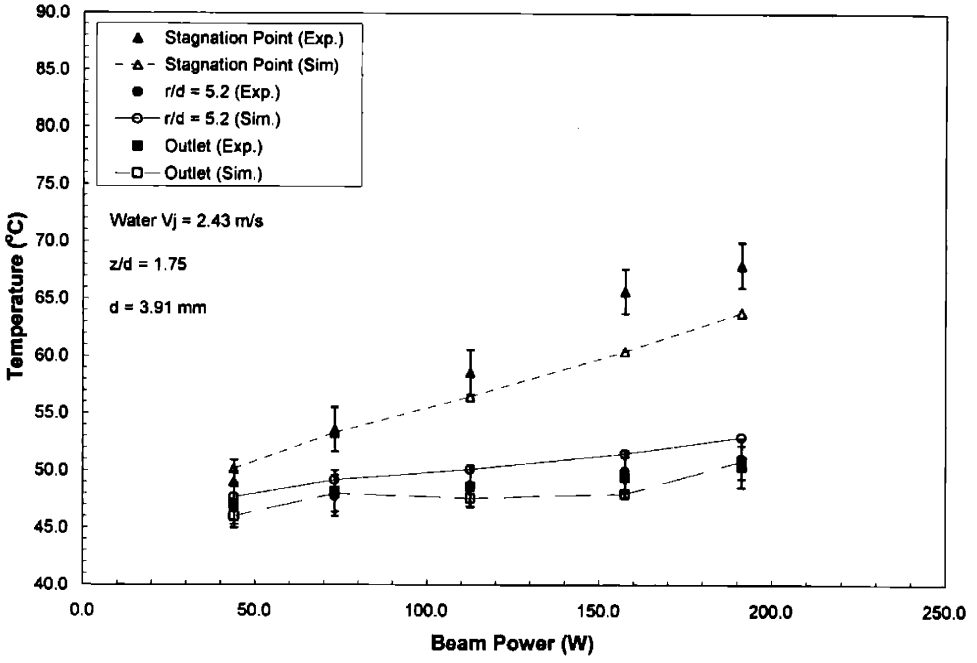

c)

Figure 3-34. Experimental and simulation data for the small-scale test of the water jet (a) V_j = 0.76 m/s; (b) V_j = 0.97 m/s; (c) V_j = 2.43 m/s.

A final check on the accuracy of the simulations and the robustness of the wall functions was made using the position and magnitude of the secondary maxima in the local heat transfer coefficient. The local value of the heat transfer for each of the water experiments is pictured in Figure 3-35. This data indicates that a secondary maximum in the local heat transfer arises at an r/d position of 1.7-1.9 as jet velocity increases. In the simulation (V_j = 2.43 m/s; Re = 16000; z/d = 1.75; d = 3.91 mm), the secondary maximum exhibited a peak heat transfer coefficient which was 76% of the stagnation value. Garimella and Rice experimentally measured the magnitude of this secondary peak to have a value $0.79h_o$ at an r/d of 2 for the jet conditions (Re = 13000; z/d = 2; d = 3.2mm). Lee and Lee measured the secondary peak to be $0.75h_o$ at an r/d of 1.8 (Re = 15000; z/d = 2; d = 25 mm). The development of this secondary peak is associated with increased turbulent kinetic energy. As z/d spacing increases, the magnitude of the secondary peak is reduced and the r/d position at which it occurs moves away from the jet axis. The consistency of the secondary peak in this simulation with those of experimental data indicate that the wall-functions and turbulence modeling of the jets has performed correctly. Turbulent kinetic energy for the simulated jet is pictured in Figure 3-36. Only the fluid region is depicted in this figure for clarity. This figure illustrates that the wall-functions were indeed successful in limiting K in the stagnation region. Without wall-function corrections the highest K values would have been located within r/d< 0.5.

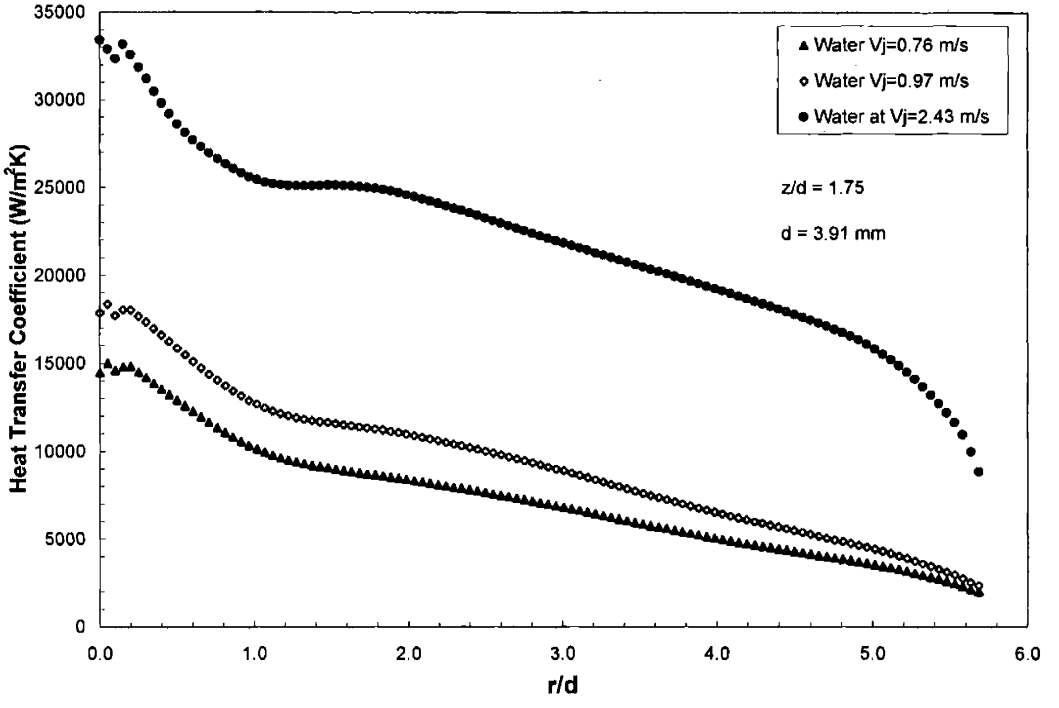

Figure 3-35. Local heat transfer coefficient versus r/d position from the simulations of the three water jets used in the small-scale experiments.

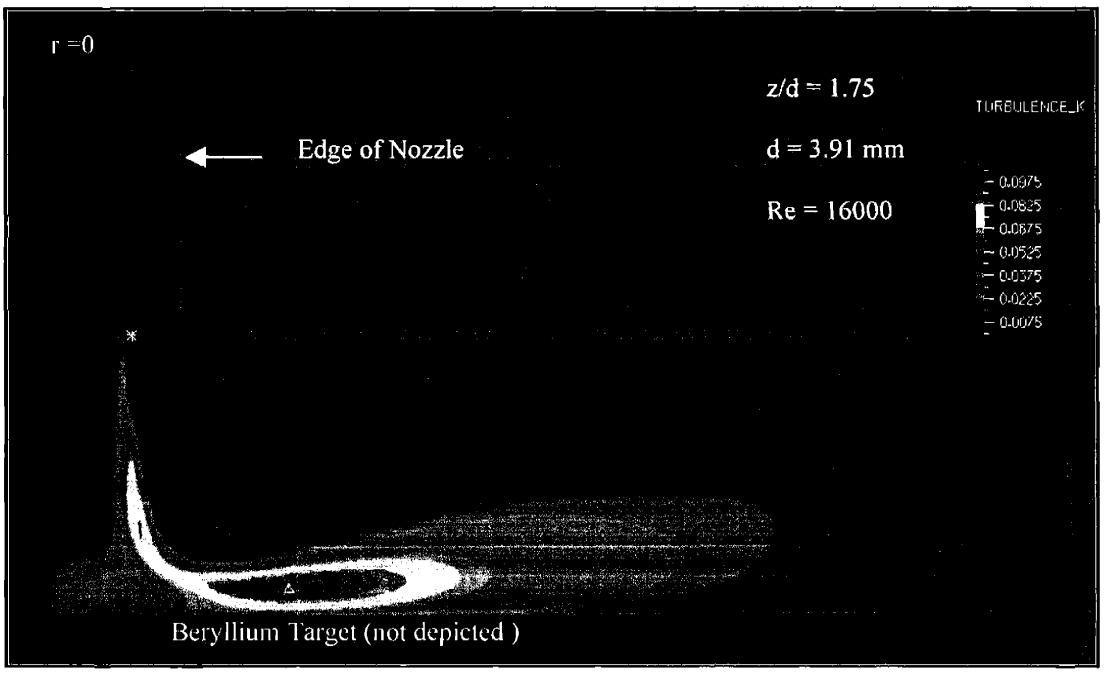

Figure 3-36. Turbulent kinetic energy (m^2/s^2) from simulation of water jet (V_j = 2.43 m/s; Re = 16000; z/d = 1.75; d = 3.91). View is axisymmetric about the jet centerline at r= 0.

While simulations of the water jets could be compared to data from literature as well as the small-scale experiments, only the data from the small-scale tests could be used for comparisons with the simulated gallium jets. Initial simulations of the gallium experiments resulted in h_o values of 86362 W/m^2K and 120500 W/m^2K for the 0.40 and 0.64 m/s jets respectively. Even with the utilization of the appropriate non-equilibrium wall functions and turbulent Prandtl number corrections, the simulated h_o values were 5.2 and 3.2 times greater than the experimentally measured values. These values, however, were close to the predicted h_o values of 100716 and 124430 W/m^2K using the laminar jet correlation mentioned earlier. Examination of the turbulent kinetic energy in the stagnation region did not indicate any artificial buildup which could possibly account for the erroneously high heat transfer values. Surface wetting was investigated as the cause of the discrepancy between the experimental and simulated h_o values. Although surface wetting will be discussed in detail in §3.3.6.5, a brief description is helpful in understanding the origin of the high stagnation heat transfer found in the simulations and the manner in which corrections were made to account for the effect.

The degree to which a fluid wets a surface is quantified by the contact angle, θ_c, between the fluid and the surface. Contact angles near zero reflect a strongly wetting fluid while increasing angles are representative of non-wetting. Sessile drop tests of the contact angle between water and various metal surfaces have yielded a wide range of θ_c between 0 and 90 degrees.[46] Gallium, on the other hand, has been measured to have a contact angle in excess of 120-150° for most surfaces.[47, 48] The non-wetting of a surface by a liquid metal can dramatically reduce the heat transfer by effectively raising the thermal contact resistance between the fluid and the surface. Early studies using liquid metals, in fact, recommended reducing the heat transfer coefficient predicted from correlations by a factor of two to account for non-wetting.[29] One way to improve the wetting of a fluid is to increase its temperature. In gallium, however, the temperature at which wetting begins to improve is quite high. Temperatures at which the gallium contact angle decreases have been found to be 600 °C or above.[47,49] Since non-wetting has the effect of increasing the thermal resistance of the viscous boundary layer, corrections were made by adjusting the thermal conductivity of the fluid in the viscous boundary layer. The thermal conductivity of the fluid within the boundary layer was decreased until the simulated and experimental temperatures at the highest beam power agreed to within 5%. Plots of the local heat transfer coefficient with and without the wetting correction are shown in Figure 3-37. Plots of the simulated data (with wetting correction) and the experimental data from the small-scale experiments using gallium jets are given in Figures 3-38 a,b.

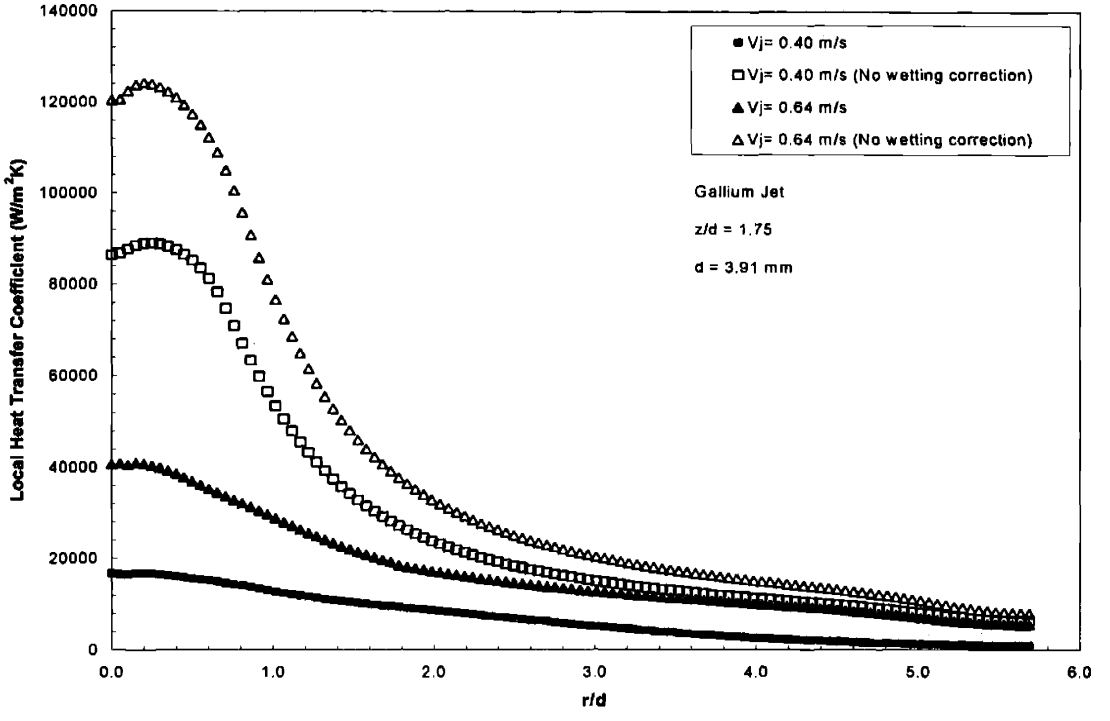

Figure 3-37. Local heat transfer coefficients for the simulated gallium jets which reflect the reduction in h due to the non-wetting of the solid surface.

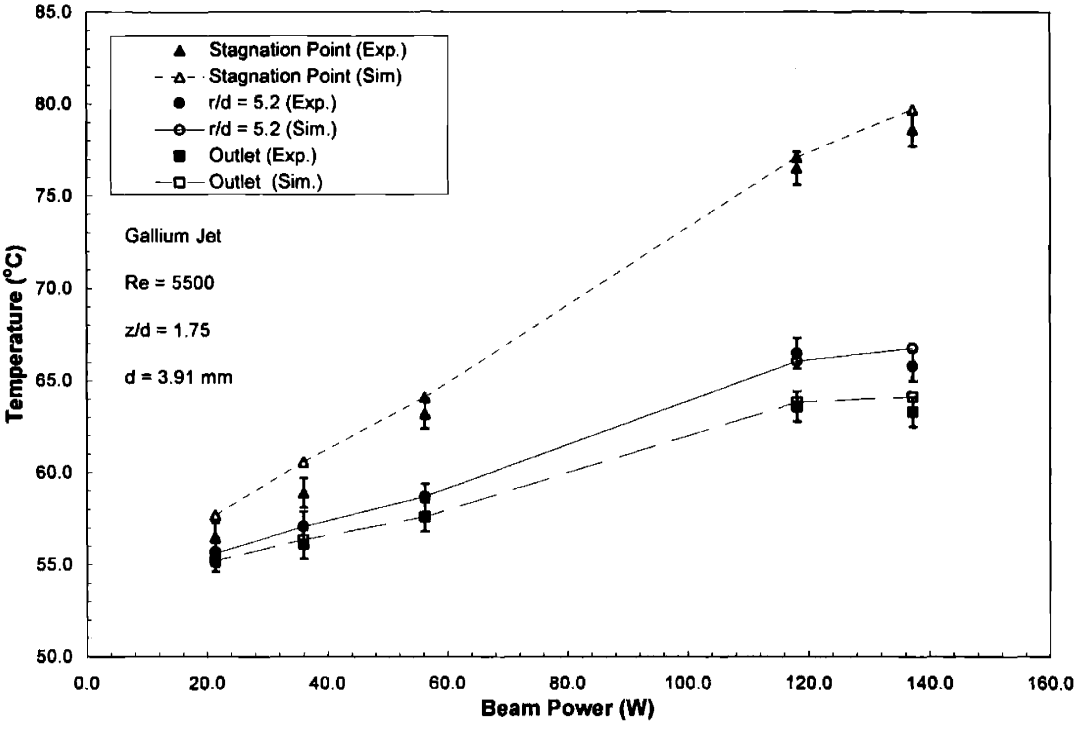

3-38. a)

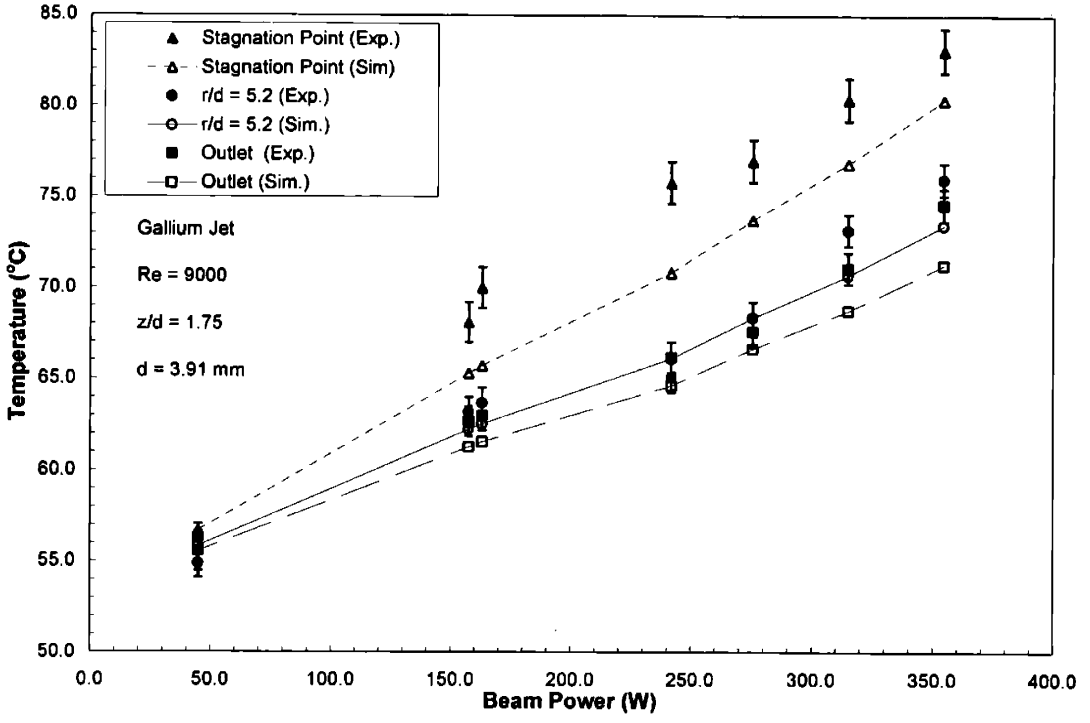

3-38. b)

Figure 3-38. a) Experimental and simulation (with wetting correction) temperature values at stagnation point, r/d= 5.2, and outlet for gallium jet (a) V_j= 0.40 m/s; Re= 5500; z/d= 1.75; d=3.91 mm (b) V_j= 0.64 m/s; Re= 9000; z/d= 1.75; d=3.91 mm.

Using the numerical simulations in conjunction with experimental heat transfer data allows for a qualitative measure of the effect of non-wetting. Figure 3-39 plots the ratio of $\bar{h}_{non-corrected} : \bar{h}_{corrected}$ as a function of r/d. This graph was created by area averaging the local values of h found in the original (no wetting correction) and corrected gallium simulations. The ratio can be considered the factor of reduction due to non-wetting. Recall that Lyon proposed a constant reduction factor of 2 in early liquid metal studies. At an r/d= 0 the factor of reduction pertains to h_o and was found to be 5.15 and 2.96 for the 0.4 m/s and 0.64 m/s jets respectively. Figure 3-39 indicates that the reduction in $\bar{h}$ out to an r/d of about 1 is relatively constant for both jets. Beyond an r/d of 1, reduction in the low velocity jet (V_j= 0.4 m/s) drops to 3.32 before rising to 3.82 at large r/d values. Reduction in $\bar{h}$ for the higher velocity jet (V_j= 0.64 m/s) decreases continually beyond r/d = 1 to a minimum value of 1.81. The results of this figure illustrate that the effect of wetting is not constant for all r/d associated with a single jet. Rather than being a constant value the amount of reduction varies depending on the velocity of the jet and the area over which the heat transfer is considered. It appears that wetting is reduced at higher jet velocity.

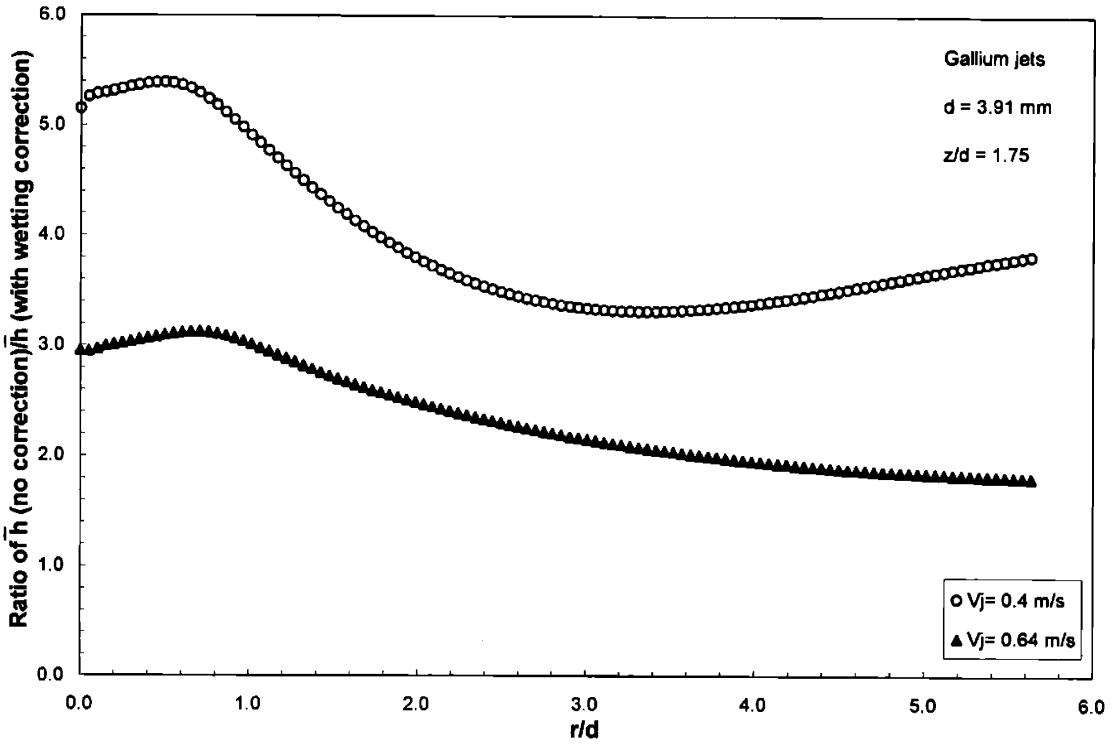

Figure 3-39. Plot of the factor by which the area-averaged heat transfer coefficient is reduced as a result of the non-wetting of the gallium. The value plotted at a specific r/d was calculated by averaging over a circular area of radius r.

A final comparison between the water and gallium (with wetting correction) jets is warranted. In Figures 3-40 a,b the local and area-averaged heat transfer is plotted versus r/d for the gallium and water jets. The three water jets had Reynolds numbers of 4950, 6300, and 16000, while the two gallium jets had Reynolds numbers of 5500 and 9000. The respective h_o values from the simulations were 14479, 17879, 33420, 16755, and 40722 W/m^{2}K. Considering the lower velocities first, the data suggests that gallium and water jets of equivalent Reynolds number generate nearly equal stagnation point heat transfer coefficients. Because of the low kinematic viscosity of the gallium, however, generating equal Reynolds numbers required water jets of twice the velocity of a gallium jet. While the h_o values of the water jets increased with roughly an $Re^{0.6}$ dependence, the small-scale and simulation results of the gallium indicate that the stagnation heat transfer increased at a greater rate in the gallium jets. Improved wetting of the surface by the gallium at higher jet velocity would account for this accelerated increase in h_o.

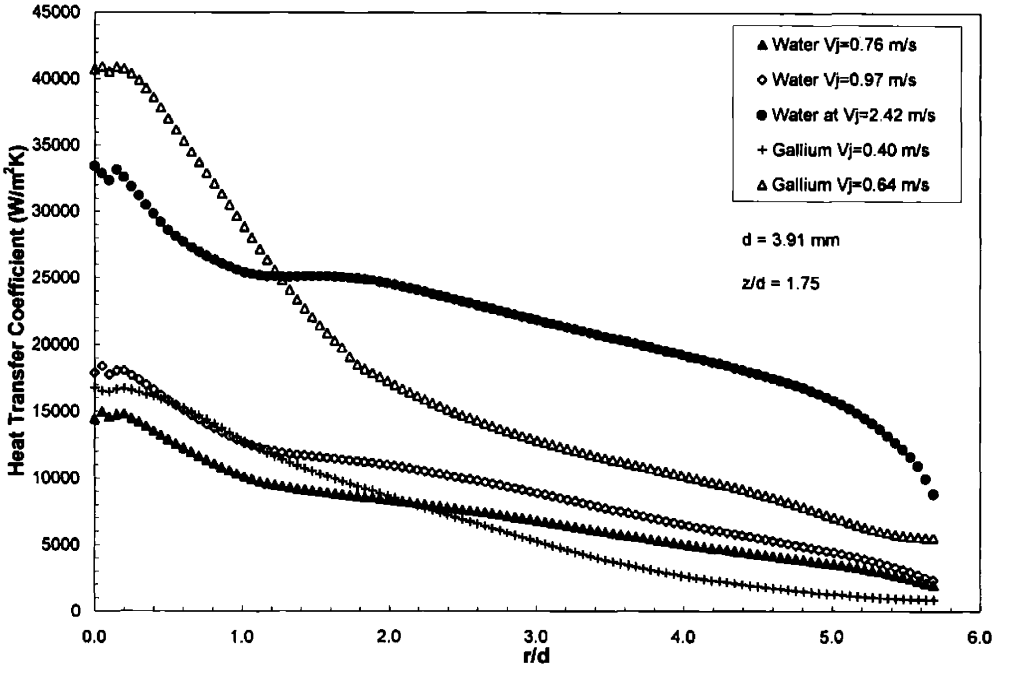

a)

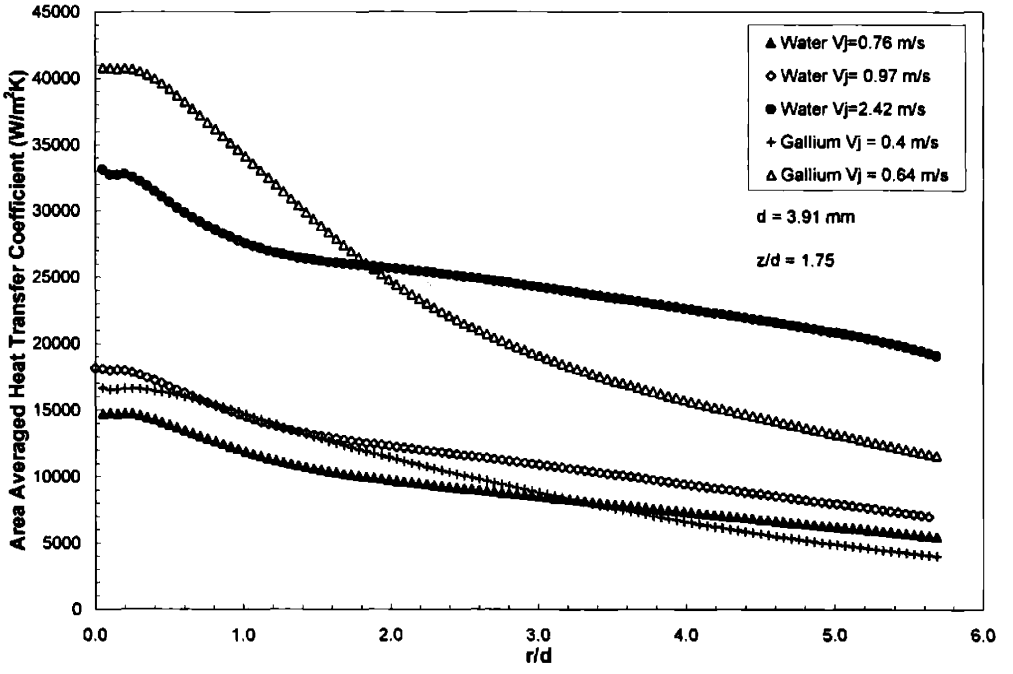

b)

Figure 3-40. a) Local heat transfer coefficient (W/m^2K) for gallium and water jets calculated using the K-ε RNG turbulence model. b) Area averaged heat transfer coefficient (W/m^2K) which is applicable over a circular area centered at r=0 and having a radius r.

Despite the superiority of h_o in the gallium jets, the area-averaged heat transfer tended to be inferior to the water jets at large r/d. This is not unexpected, since the increased velocity of the water jets translates to higher levels of turbulent kinetic energy at r/d values away from the centerline. Comparison of the gallium jet (V_j= 0.40 m/s) to the water jet (V_j= 0.76 m/s) found that the local heat transfer former exceeded that of the latter out to an r/d of 2.2, while $\bar{h}$ was superior out to an r/d of 3.3. With a slight increase in the water jet velocity from 0.76 to 0.97 m/s, both the local and area-averaged heat transfer coefficients from the gallium jet were less than those of the water jets. As the velocity and Reynolds number of the gallium jet was increased, however, a jet velocity of nearly a factor or 4 was required in order to approach equivalent heat transfer. Comparison of the V_j= 0.64 m/s (Re= 9000) gallium jet to the V_j= 2.43 m/s (Re= 16000) water jet found that the local heat transfer of the gallium jet exceeded that of water out to an r/d of 1.3, while $\bar{h}$ was superior out to an r/d of 1.9.

The K-ε RNG simulations have supported the experimental data which indicate that submerged gallium jets provide increased heat transfer over water even at reduced flowrates. By matching the simulation and experimental data from the gallium jets it was possible to make a quantitative measure of the wetting effect. The degree to which gallium wets a surface was shown to improve with increasing jet velocities. It was also shown that the reduction in heat transfer caused by the non-wetting effect varies with r/d. Finally, comparison between the water and gallium jet simulations indicated that the rate of increase in h_o with Reynolds number is greater for the gallium jets than with water. Consideration was also given to the fact that at large r/d values, higher velocity water jets have greater turbulent kinetic energy. If large heated areas are associated with a single jet, the area-averaged heat transfer of a water jet could surpass that of a gallium jet at large r/d.

3.3.6 Large Scale Tests of Heat Transfer from Gallium and Water Jet Arrays

Based on the results indicating improved heat transfer of gallium over water at low Reynolds numbers, a large scale test was constructed to compare the heat transfer of the fluids at power levels and flowrates more indicative of NCT. As with the small-scale tests, experiments were conducted first with water and then with gallium under identical conditions in order to compare the heat transfer. A schematic of the setups used for the water and gallium tests are shown in Figure 3-41 a,b.

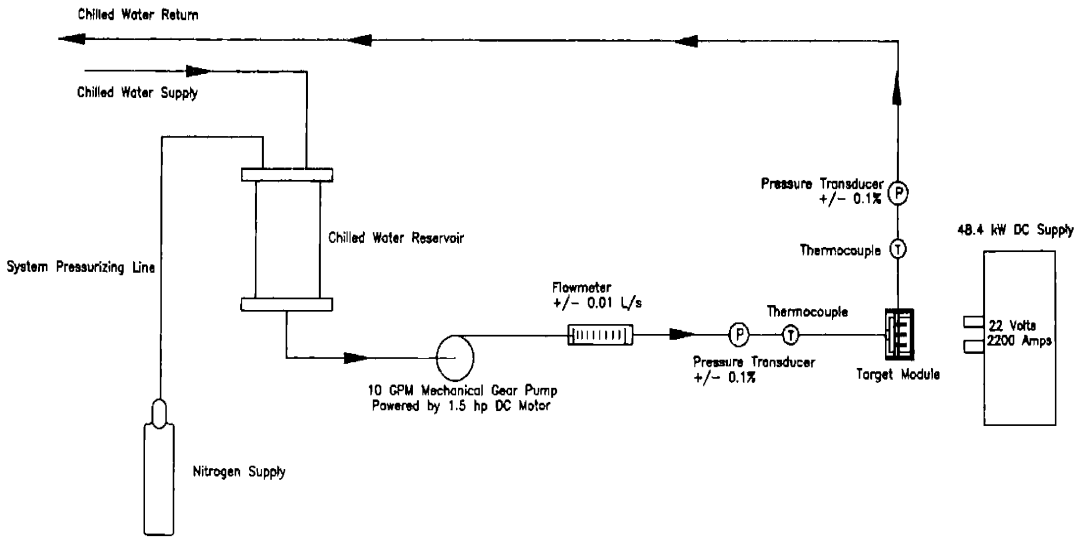

a)

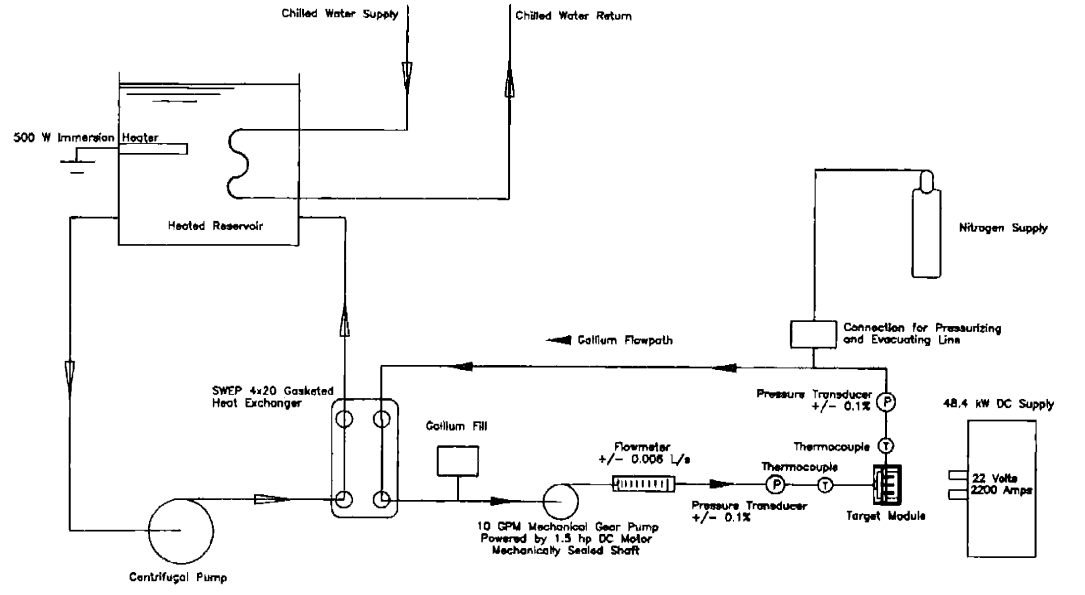

b)

Figure 3-41. a) Cooling loop for the large-scale heat transfer experiments using water jets. b) Cooling loop used to test gallium jets in the large-scale heat transfer experiments.

3.3.6.1 Flow System for Water Experiments

The flow system pictured in Figure 3-41a used contaminant-free building-supplied chilled water (16-19 °C). Water was introduced into a reservoir constructed from a 304 SS ASA flange having a internal volume capacity of 4.4 L in order to eliminate any fluctuations in the flowrate of the building supply. Fluid was drawn from the bottom of the reservoir into the inlet of a 316 SS mechanical gear pump capable of a maximum flowrate of 0.631 L/s (10 GPM) at 1750 rpm and a maximum system pressure of 0.69 MPa (100 psi). Power was supplied to the pump by a 1.5 hp DC electric motor, which was controlled through a rectifying circuit coupled to a Variac running off a standard 120 V outlet. This arrangement allowed for control of the coolant flowrate through variation of the voltage supplied to the pump. Upon exiting the pump, coolant entered a variable area flowmeter (±0.01 L/s) before entering the target assembly. Directly before entering the target assembly, pressure and temperature were measured with a pressure transducer (±0.1%) and K-type thermocouple immersed in the fluid by means of a high-pressure feed-through. Spent fluid was collected from the target from an exit at the top of the assembly where a second pressure transducer and thermocouple were located. All piping used in the system with the exception of the nozzles in the target module was composed of 1.59 cm (5/8") O.D. 316 SS tubing coupled with Swagelok fittings.

3.3.6.2 Flow System for Gallium Experiments

Experiments with gallium as the working fluid required minor changes to the system illustrated in Figure 3-41a primarily because of material compatibility and the need to have a completely sealed gallium loop. The resulting system, pictured in Figure 3-41b, consisted of a primary gallium loop, a secondary heated water loop, and a tertiary chilled water loop. The primary gallium cooling loop was composed of 1.59 cm (5/8") OD 316 SS tubing connected with Swagelok fittings. Pumping of the fluid was accomplished with a mechanically-sealed DC gear pump constructed of 316 SS having the same operating parameters as the original pump used in the water experiments. Initial tests attempted to use the original pump, which had a packing-sleeve seal, but proved unsuccessful with gallium. Interaction between the packing sleeve material and gallium caused rapid scaling and the evolution of a dark sludge which degraded the pumping capacity. The second pump which had a mechanically-sealed drive shaft eliminated these problems. The flowmeter used in the water experiments was replaced with a positive-displacement flowmeter (±0.006 L/sec) which had wetted materials of Teflon and ceramics. Temperature and pressure measurements were made with the same instruments used in the water tests. While those tests had relied upon the chilled water supply to regulate the jet temperature,

the gallium tests required a heat exchanger. Upon exiting the target system, gallium was piped into a SWEP MINEX 4x20 plate/gasket type heat exchanger. The heat exchanger pictured in Figure 3-42 was composed of 20 316 SS plates which separated the primary gallium loop from the secondary heated water loop and served as heat exchange surfaces. Sealing of the plates was accomplished with nitrile gaskets.

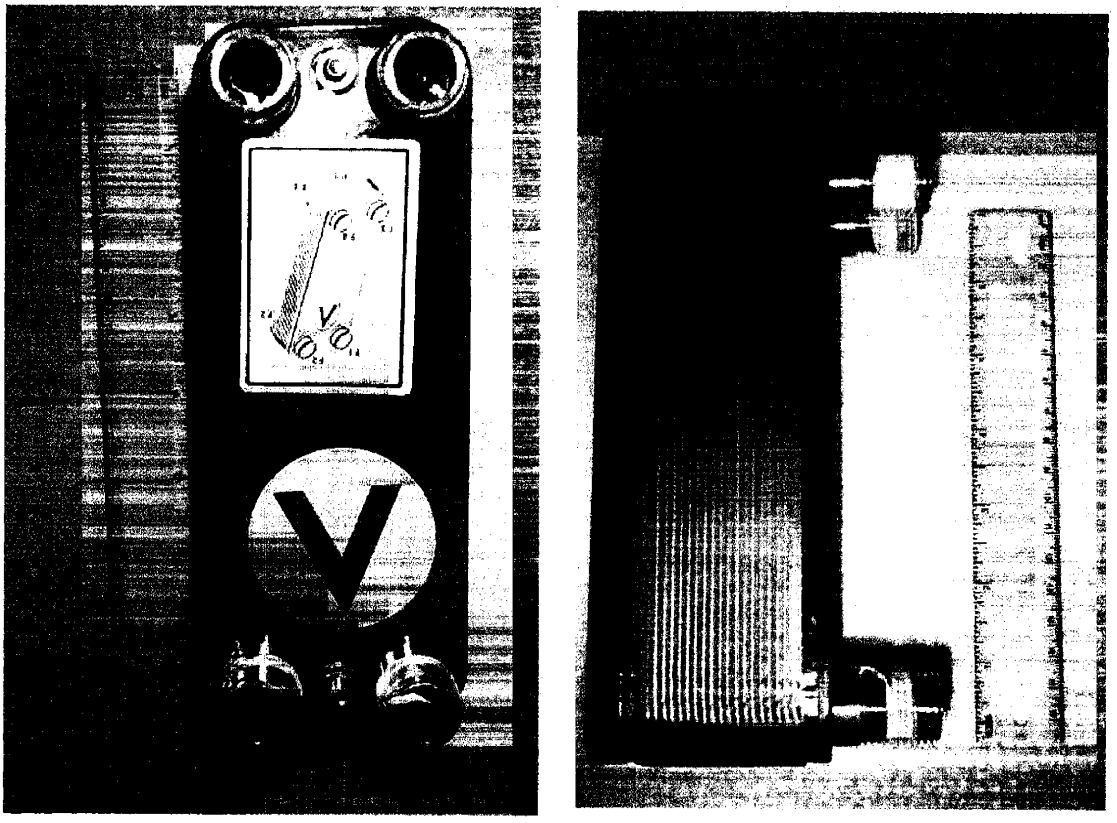

Figure 3-42. SWEP MINEX 4x20 plate/gasket type heat exchanger used in the gallium experiments.

Water used in the secondary loop was contained in a 34-gallon polyethylene tank fitted with a 500 W immersion heater. Control of the gallium jet temperature, which was kept between 34-53 °C during the experiments, was accomplished by monitoring the temperature of the water in the reservoir and adjusting the power supplied to the heater. A 1/3 hp centrifugal pump circulated the water in the secondary loop from the reservoir, through the heat exchanger, and finally back to the reservoir. Although the thermal mass of the water in the secondary loop limited the temperature increase of the gallium, some additional heat removal was necessary at high powers. Removal of heat from the reservoir was achieved by circulating building supplied chilled water through a tertiary loop consisting of coiled copper tubing located in the reservoir.

3.3.6.3 Target Module

The modular target assembly illustrated in Figure 3-43 consisted of an electrical resistance heater and a 3x3 nozzle array housed in a Teflon body. Fluid entering the back of the module was distributed into a plenum before encountering a 1 cm thick nozzle plate. Nine square-edged nozzles having an ID of 3.02 mm and an overall length of 3.81 cm were machined out of 6.35 mm OD (1/4") 304 stainless steel tubing.

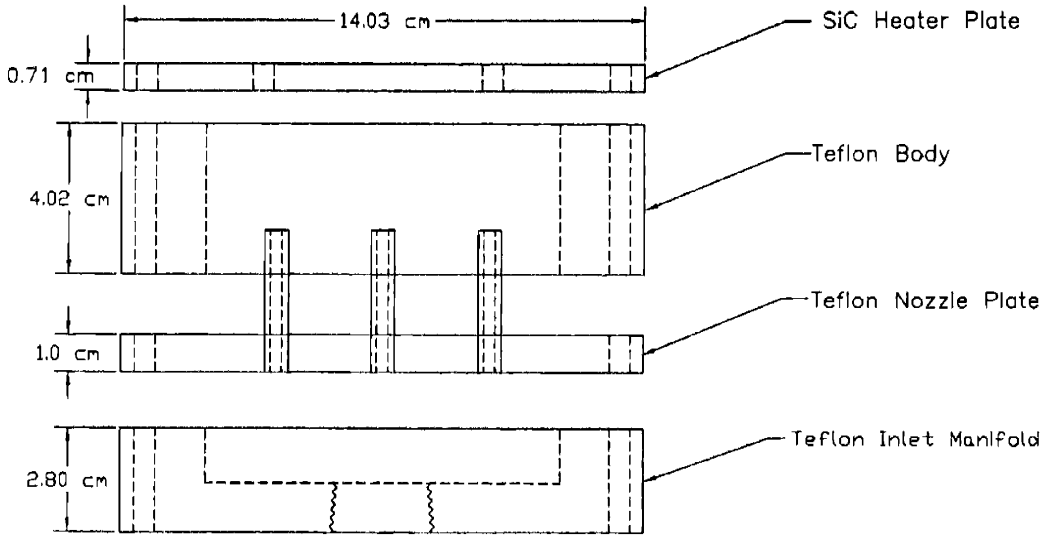

Figure 3-43. Schematic of the target module consisting of a Teflon manifold, nozzle plate, body, and a silicon carbide heating plate.

The nozzles were threaded into the nozzle plate in a non-uniform array and positioned in the target body at a nozzle-to-target (z/d) spacing of 4. Figure 3-44 illustrates the arrangement of the nozzles as well as their positioning within the target body. Verification of the spacing was made using a precision caliper to an accuracy of ±0.1 mm. Previous studies of single submerged jets found heat transfer increased with z/d up to a maximum at a z/d of 5-6.[17,45] Garrett et al., however, found that the maximum Nusselt number for jet arrays occurred at a smaller z/d of 4.[24] The non-uniform array having an s/d of 4.6 in one dimension and 9.5 in the other was required for two reasons. (1) Rectangular dimensions having a L/W ratio of 2:1 were needed to achieve the proper resistance in the heating element; (2) nine jets were determined to give the proper balance between covering a large area ≈ 29 cm^2 while still generating high jet velocities.

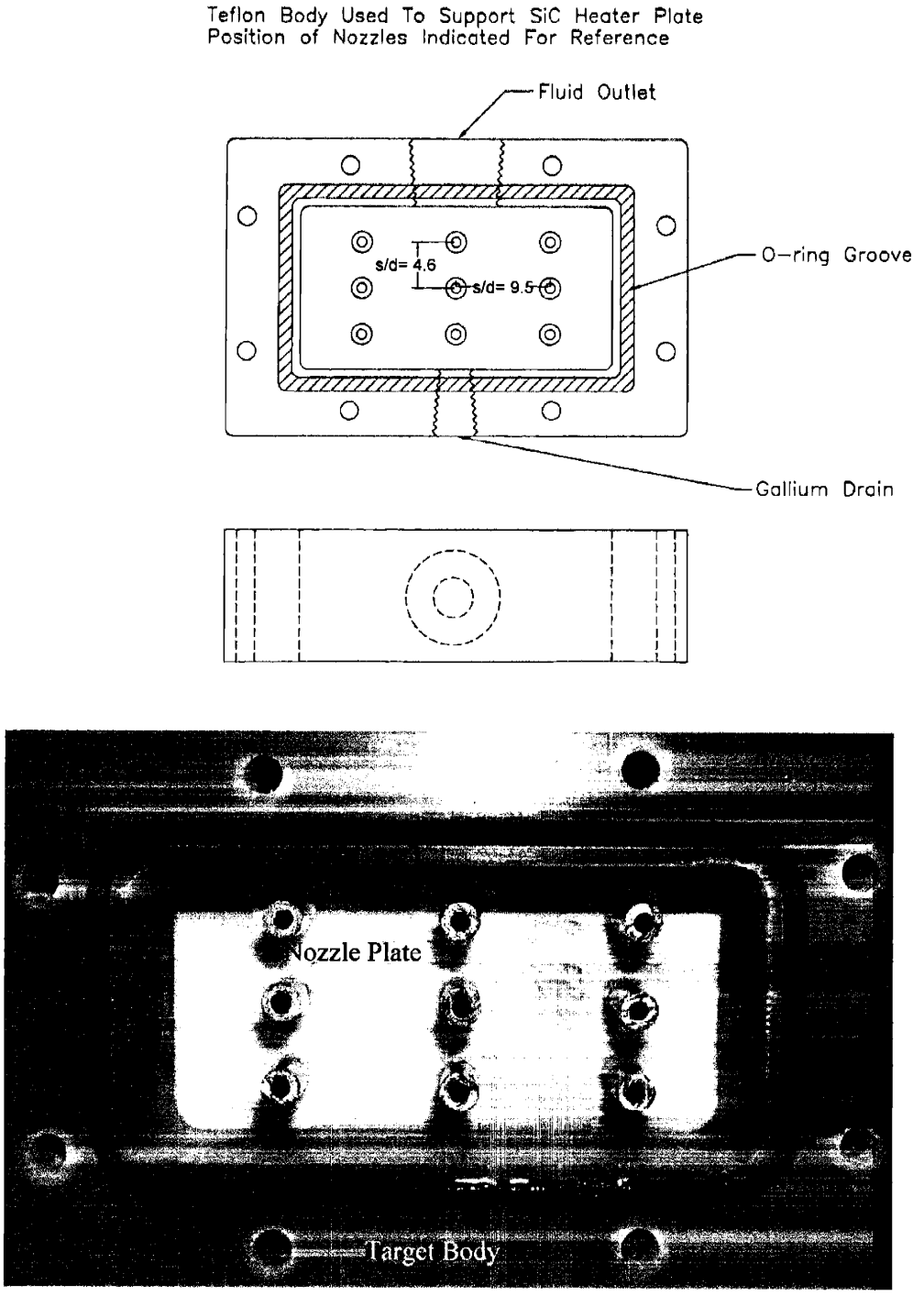

Figure 3-44. Schematic and photograph of the target body showing the orientation of the nozzles threaded into the nozzle plate. The photograph shows an early design of the body constructed with phenolic. Because of cracking in the target body, phenolic was replaced by Teflon.

Jets issuing from these nozzles were kept fully submerged by draining the fluid through a single large opening at the top of the target body. Early tests using a dual exit configuration from the sides of the target body indicated the possibility that the top row of jets might not remain fully submerged.

A uniform heat flux was generated by passing high current from a low impedance 48 kW (2200 A at 22 V) DC electrical power supply through a thin layer of copper deposited on a silicon carbide substrate. In order to use a resistance heater which was cooled by a conducting fluid, a design which electrically isolated the heating element from the gallium while maintaining high thermal conductivity was required. Silicon carbide is a strong yet brittle material which has a rare combination of high impedance (10^6 Ω-cm at 20 °C) and high thermal conductivity (125.6 W/m^2 K at 20 °C).[50] The heating element pictured in Figure 3-45 was composed of a uniform 1.0 μm copper layer deposited by electron beam evaporation onto a 7.1 mm-thick Hexoloy SA silicon carbide substrate. Plate thickness, stated by the manufacturer at 7.112 ±0.381 mm, was verified to within ±0.05 mm using precision calipers.

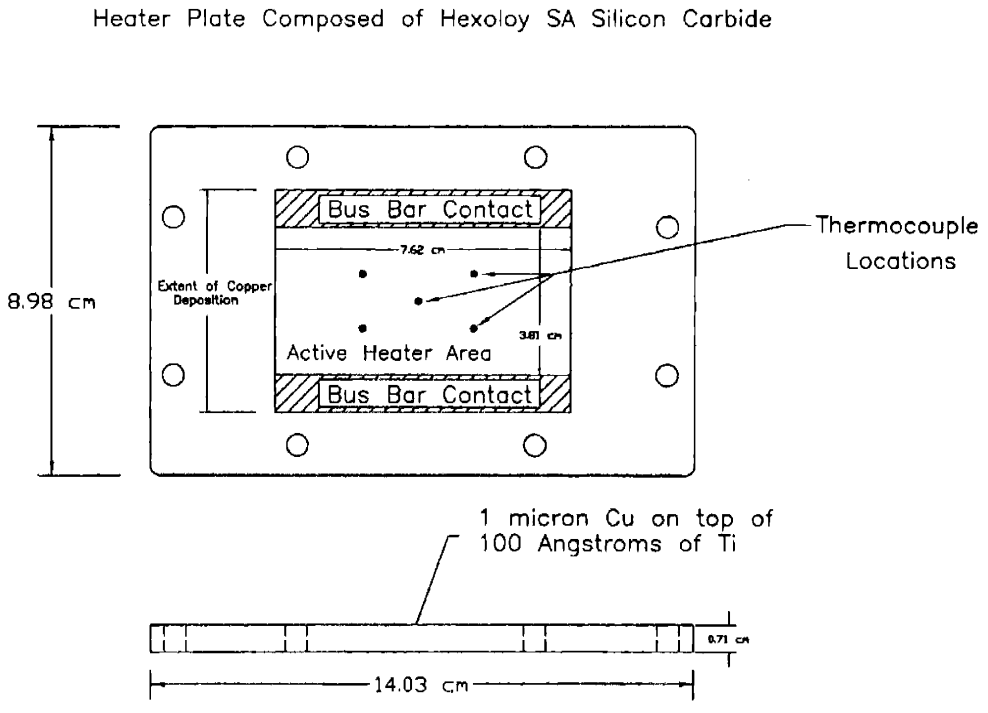

Figure 3-45. Heater plate composed of a 1-micron copper layer deposited by electron beam evaporation onto a Hexaloy SA silicon carbide plate.

Several methods exist for depositing a thin layer of material onto a surface. Air plasma spraying (APS), vacuum plasma spraying (VPS), and high-velocity oxygen fuel spraying (HVOF) have been used by other groups to manufacture heating elements.[44] One of the largest uncertainties in these processes, however, was the uniformity of the deposited layer. Oh et al. found that the thickness of deposited layers could vary by as much as 25 μm. Not only did the spraying process generate layers of varying thickness, but because the layers were porous, the thermal conductivity of the sprayed material was reduced from that of the bulk material.

Electron beam evaporation provides a means by which extremely thin, uniform layers of material can be deposited on a substrate. E-beam evaporation uses a focused beam of particles to vaporize a sample held in a crucible. This vapor travels in vacuum toward the substrate where it condenses and forms a coating. By controlling the focus and energy of the beam, deposition rates from 0.1 nm per second to over 150 μm per minute can be achieved.[51] Coatings produced in this manner preserve the microstructure and retain the properties of the bulk material. Since the material is deposited on a molecular basis, bonding to the surface is strong and thermal contact resistance is negligible. Heating elements used in this experiment were coated using the TEMESCAL E-beam evaporator at the M.I.T Microsystems Technology Laboratory. Coating was conducted under a vacuum of 10^{-7} Torr at a deposition rate of 5-10 Å per second. Deposition, which required 10-15 minutes per plate, consisted of first laying down 100 Å of titanium followed by 1 μm layer of copper over a rectangular area measuring 7.62 cm x 5.72 cm. The titanium layer, which was used as a bonding material, contributed little thermal resistance and was neglected in subsequent calculations. Uncertainty in the copper layer thickness was ± 0.03 μm.

Current from the power supply was carried through four large-bore copper cables attached to fixed aluminum supports on opposite sides of the target module. On each of the fixed supports four 2.54 cm-wide, sharp-edged copper braids were clamped to the supports with an aluminum plate. By using four leads on each side of the module, excessive heating of the braids was avoided even at currents of several hundred amps. These braids were pressed onto the heating element by 6.35 mm-thick aluminum bus bars which had been milled flat. Both the bus bars and braids were clamped onto the target module with a 1.27 cm-thick plexiglass plate. The assembly is pictured in Figure 3-46. Sharp edges of the braids ensured the dimensions of the heated area could be kept constant between each experiment. By positioning these braids on the top and bottom 0.95 cm of the copper, the total heated area, 7.62 cm wide by 3.81 cm long (29.032 cm^2), had an impedance (~0.01 Ω) which matched the that of the power supply. This area was verified through measurement after each experiment with an uncertainty of ±0.011 cm^2.

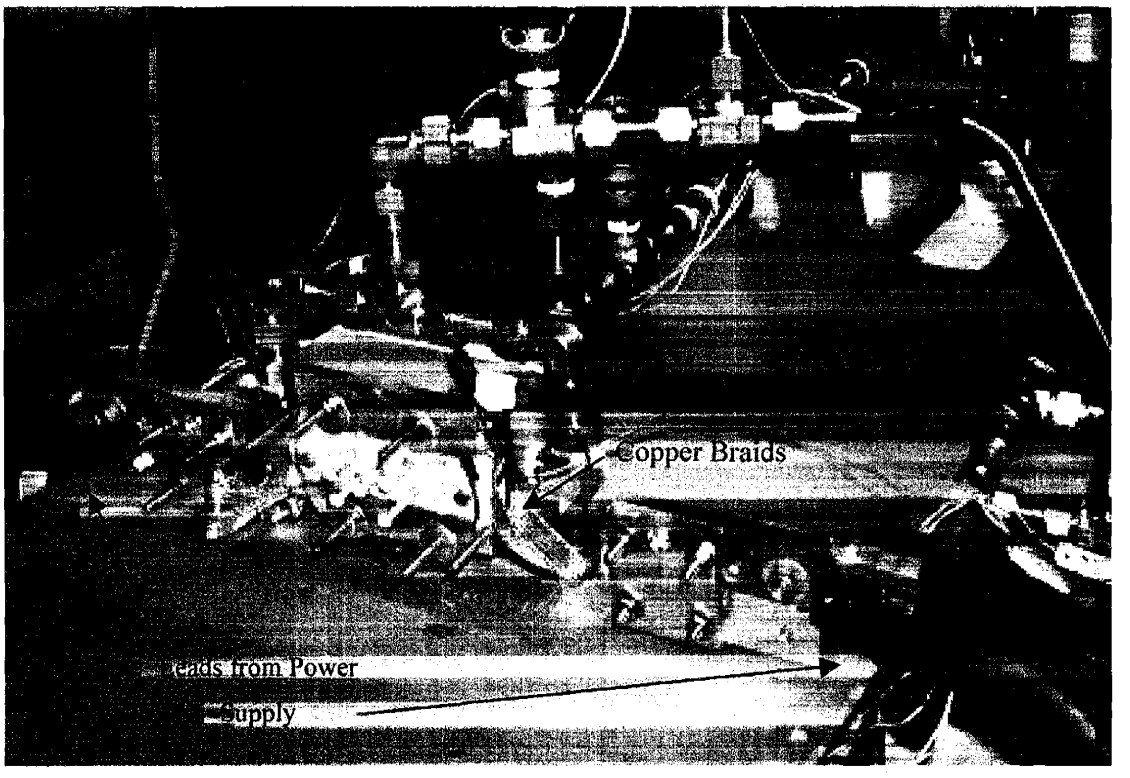

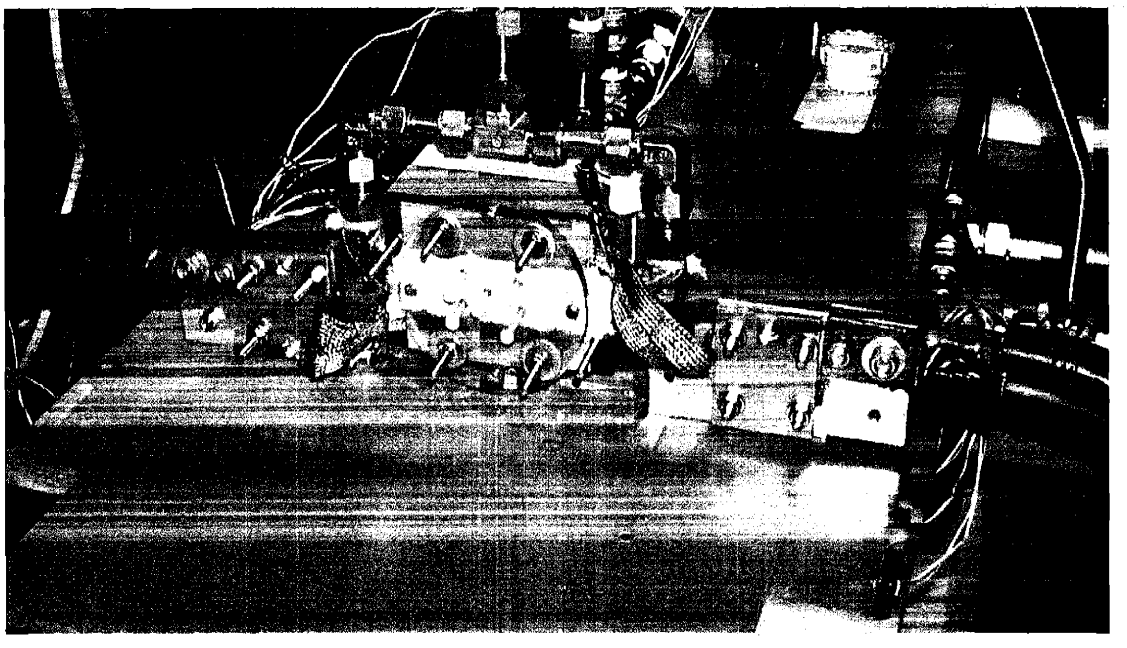

Figure 3-46. Photographs of the target assembly which illustrate how power was supplied to the heating element. The edge of the heating element (gray material) located under the plexiglass disk can be seen. Insulation was placed between the plexiglass and the heating element to reduce heat loss to the air.

High temperature insulation was placed between the plexiglass and the heating element to minimize natural convection losses. Even without the insulation, numerical simulations which included the effects of natural convection from the front and sides of the heating element, indicated that the front side temperature would be lower than the measured values by only ~0.1 °C per kW. From these simulations conduction losses through the copper braids and aluminum bus bars were estimated to be no more than 3.3 % of the total power. Radiation losses were estimated at 0.17 % at 10 kW assuming the copper to be a perfect black body. Losses due to convection, radiation, and conduction into the bus bars were minimal compared to the heat transfer due to the impinging jets. Temperature of the heating element was monitored by five K-type thermocouples fixed to the copper using high temperature ceramic epoxy. Intimate contact between the thermocouple and the copper surface was checked with a digital multimeter before each experiment. To avoid delamination of the thermocouple contacts, small nylon screws were threaded through the plexiglass plate and gently tightened down on the epoxy beads. Conduction losses through the epoxy and nylon were minimal.

3.3.6.4 Experimental Procedure and Control

Because the small-scale experiments with gallium had shown evidence of scaling, special care was taken to ensure that minimal contact between gallium and the outside atmosphere occurred before the tests. No contact between the atmosphere and the gallium occurred during the tests. For 24 hours prior to the experiment the entire primary loop was sealed and evacuated by a roughing pump which maintained a vacuum of 10^{-2}-10^{-3} Torr in the system. Shortly before the start of an experiment a 1.0 L volume of gallium metal contained in a sealed polyethylene bottle was melted in heated water bath. Liquid gallium was then poured through a funnel into a machined Teflon cylinder which was connected to the primary loop immediately prior to the inlet of the pump. With the system still under vacuum, the pump was slowly rotated by hand and a valve on the Teflon cylinder was opened so that gallium was drawn by the pressure differential into the system. Filling of the system was monitored by checking the thermocouples located at various positions throughout the loop. A small reservoir capped with a 1.27 cm thick plexiglass plate was connected to the highest point in the system and allowed visual inspection of the filling process. Filling was complete once the gallium level in the filling cylinder and visual port reached a constant level. At this point, the system was pressurized to 0.2 MPa (30 psi) with dry nitrogen.

Baseline readings were made at the start of each experiment to verify flowrate, temperature uniformity, system pressure, and heater power. Measurements were collected from various instruments with an Hewlett Packard 34901A 20-ch. multiplexer which sampled at 2-second

intervals and immediately transferred the readings to a PC via an RS-232 connection. These readings were displayed in real time on the PC in a scrolling readout. Experimental measurements were based on 30-second averages from each instrument taken after the temperatures had reached steady-state.

Current from the power supply was monitored through a 50 mV shunt, and the voltage drop in the resistance heater was read from clip leads on the copper braids. Total power generated by the resistance heater, Q_h (W), was the product of these two values. Uncertainties in the total heater power ranged from ±0.5% at low power to no more than ±0.7% at high power. Heat flux was calculated by dividing Q_h by the active heater area, A_h. Maximum uncertainty in heat flux was ±0.8 %. Temperature measurement of the heater surface was made by averaging the five thermocouple readings. These thermocouples were positioned in an area away from the edges of the heating element to avoid the large thermal gradients. By locating the thermocouples in the center portion of the heating element, the temperature measurement of the heater surface reflected the thermal resistance imposed by the SiC substrate and the convective cooling of the jets under essentially 1-D heat flow. Determination of the area average heat transfer coefficient was accomplished by building a 3-D model (Figure 3-47) of the heating element with the ADINA-T code using temperature dependent properties. In order to determine a heat transfer coefficient,

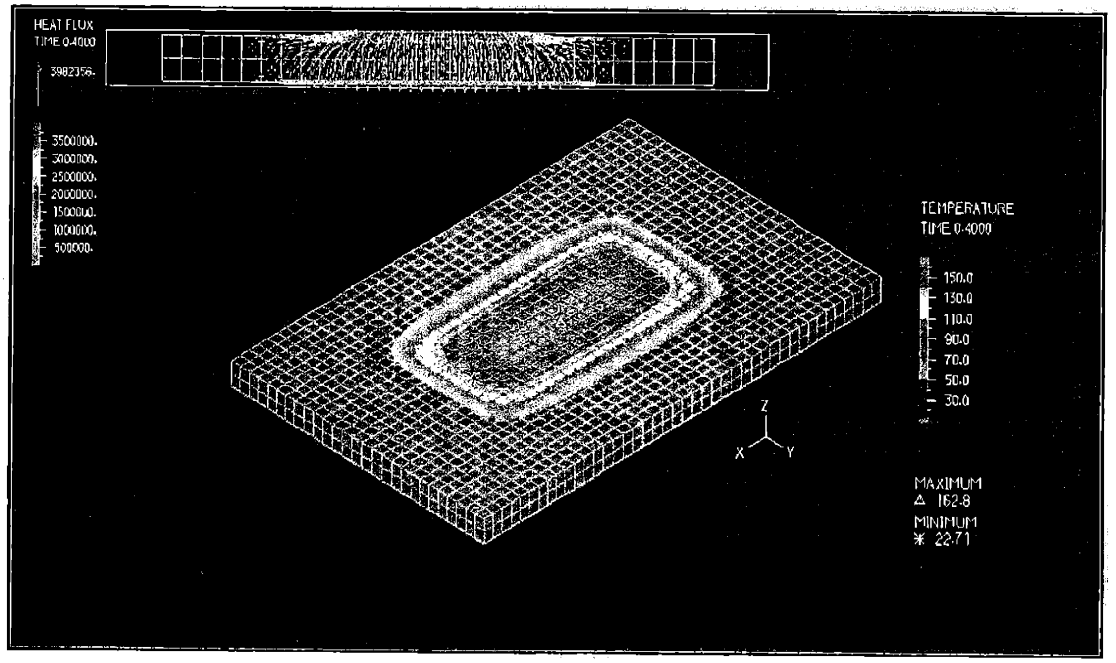

Figure 3-47. Simulation of the 3-D SiC heating element subjected to a 5 kW heat load and cooled by an area-averaged heat transfer coefficient of 60000 W/m^{2}K at a bulk temperature of 20 °C. This figure includes a plot of the temperature as well as a cross-section showing the 1-D nature of the heat flow. The cut was made perpendicular to the x-axis through the center of the target.

the h used in the simulation was varied until the average of temperatures from the simulation, which corresponded to the location of each of the thermocouples, matched the experimentally derived average of all five thermocouples. $\overline{Nu}$ could then be calculated according to $\overline{Nu} = \frac{\bar{h}d}{k}$.

3.3.6.5 Results and Discussion

While this study was not concerned with developing a Nusselt number correlation for an array of water jets, it was important to illustrate that the procedures used in this experiment produced results consistent with those in literature. Jet velocities in the water tests ranged from 2.5-6.2 m/s and produced Reynolds numbers of 7250-33800. Power levels generated by the heating element ranged from 1-11 kW. A plot of the area-averaged Nusselt number calculated with the experimental data along with $\overline{Nu}$ values predicted by the correlations is given in Figure 3-48. All fluid properties used in the correlations were evaluated at the film temperature, T_{film}, which is the average of the coolant/target interface (T_{int}) and jet inlet (T_{in}) temperatures.

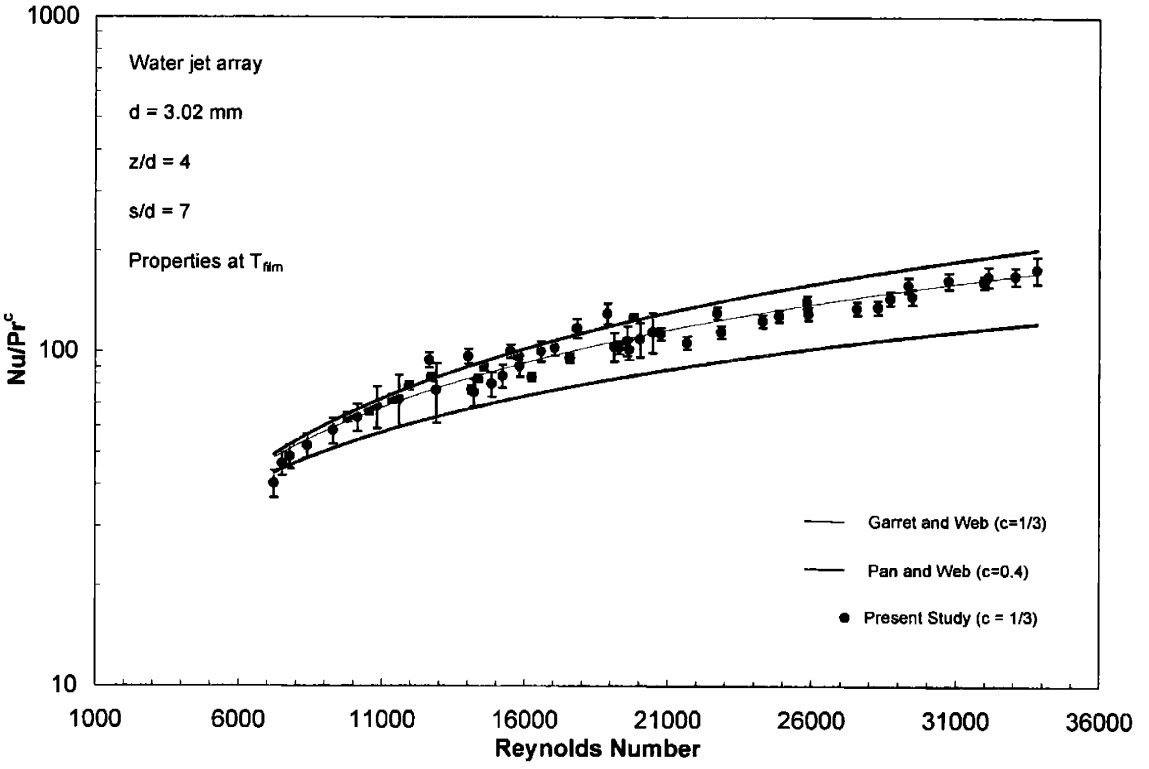

Figure 3-48. Plot of the experimental water jet data along with the predictions of Garrett &Webb and Pan &Webb. Average Nusselt number data is normalized by Pr^c for sake of comparison.

Calculations of $\overline{Nu}$ based on the experimental water jet data gave values which were 1.3-20.5% lower than predicted using the correlation of Garrett and Webb[24] with an average difference of 10.5%. Compared to the Pan and Webb[26] data, which was derived for arrays of free surface jets, $\overline{Nu}$ values from the current experiment were 1.4-48.7% higher with an average difference of 28.7%. As expected, the heat transfer coefficients measured in this experiment, which involved submerged jets, were higher than the free jet data of Pan and Webb. When compared under similar flow conditions, submerged jet impingement produces heat transfer coefficients 25-30% higher than free surface jets.[52] The two correlations used to predict $\overline{Nu}$ required a single s/d spacing. In this study, however, jets were arrayed in a non-uniform pattern illustrated in Figure 3-44. It would not be accurate to characterize the spacing in this array with either an s/d of 4.6 or 9.5. Instead, an s/d of 7 was chosen as the appropriate median value for use in the correlations.

A least squares regression of the water jet data from the current experiment found $\overline{Nu}$ varied according to

$$\overline{Nu} = 0.032 Re^{0.82} Pr^{1/3} \tag{3.31}$$

Maximum deviation from the experimental data using this correlation was 28.1% with an average deviation of 6.6%. The Reynolds number dependence of $\overline{Nu}$ from this experiment is consistent with values found in previous studies. Garrett and Webb found an increase in the exponent from 0.7 to 0.97 as s/d was increased from 4.8 to 12.[24] A study of air jet arrays by Obot and Trabold found the exponent to be between 0.72-0.82 depending on crossflow conditions and suggested a fixed value of 0.8.[53] Likewise, Kercher and Tabakoff found that the exponent varied from 0.6 to 0.95 as s/d spacing was increased from 3-12.[54]

Having illustrated that the experimental procedure using water jets produced results consistent with previous studies, gallium jets having velocities of 1.9-3.6 m/s ($18150<Re<39000$) were studied and area-averaged Nusselt numbers were calculated. Values of $\overline{Nu}$ from the gallium jet experiments are plotted along with the predictions of the laminar correlation proposed by Liu as well as the turbulent jet correlations of Sato et. al. and Green et. al. These three correlations which can be used with liquid metal jets were given in §3.3.3. Although none of these three correlations were derived for arrays, but rather for single jets, they are presented for comparison because of the limited amount of data pertaining to liquid metal jets. While the laminar correlation and that of Green predict Nu_o, the correlations of Sato give $\overline{Nu}$. Before plotting the

data it is important to note that the latter two correlations were based on experiments in which phase change occurred in the target plate. Also, the Reynolds range for which those experiments took place were higher than present study. Sato et. al. considered the range 41000<Re<490000 while Green et. al. studied the range 44000<Re<209000.

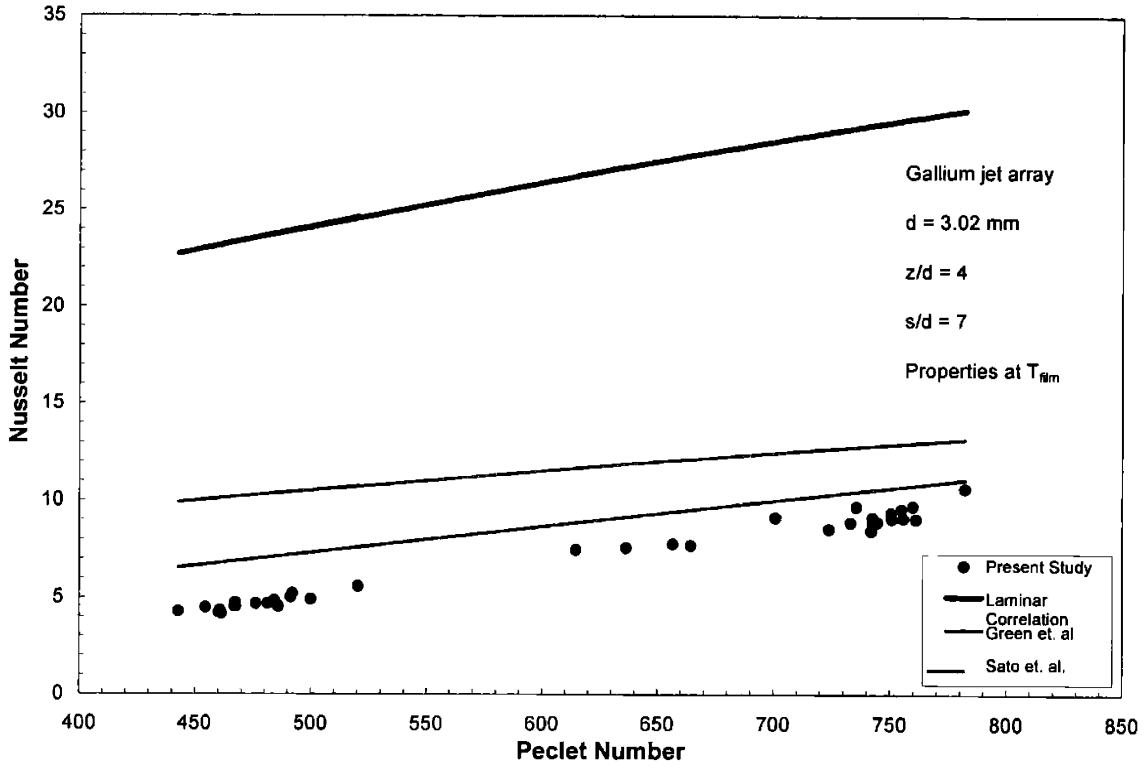

Figure 3-49. Nusselt number versus Peclet number for the current study as well as the laminar correlation (Pr<<1) and the turbulent liquid metal jet correlations of Green et. al. and Sato et. al.

Several correlations of the form C_1Pe^m with m values ranging from 0.5-1.0 were initially examined with limited success. At higher values of m, however, the proposed correlations predicted the experimental data with a greater degree of accuracy. Table 3-7 quantifies the predictive ability of the correlations with various combinations of C_1 and m, while the curves themselves are presented graphically in Figure 3-50. Despite the differences between the studies of Green and Sato, which used single jets of tin, Wood's metal, and stainless steel, and involved a phase change of the target, the Peclet exponent found in the current study indicates a stronger dependence of $\overline{Nu}$ on jet velocity. Considering the other gallium properties (density, specific heat, thermal conductivity) which affect the Peclet number ($\rho V_j d c_p/k$), they were found to vary by less than 10% during the course of the experiment.

Table 3-7. Minimum, maximum, and average deviations between experimental and predicted $\overline{Nu}$ values using various C_1 and m coefficients.

Correlation Coefficients	Minimum Deviation	Maximum Deviation	Average Deviation
C_1= 0.293 m= 0.500	2.1%	51.1%	22.6%
C_1= 5.87e-2 m= 0.750	0.4%	40.4%	16.8%
C_1= 1.17e-2 m= 1.000	0.7%	29.7%	11.3%
C_1= 3.91e-4 m= 1.523	0.0%	8.6%	3.3%

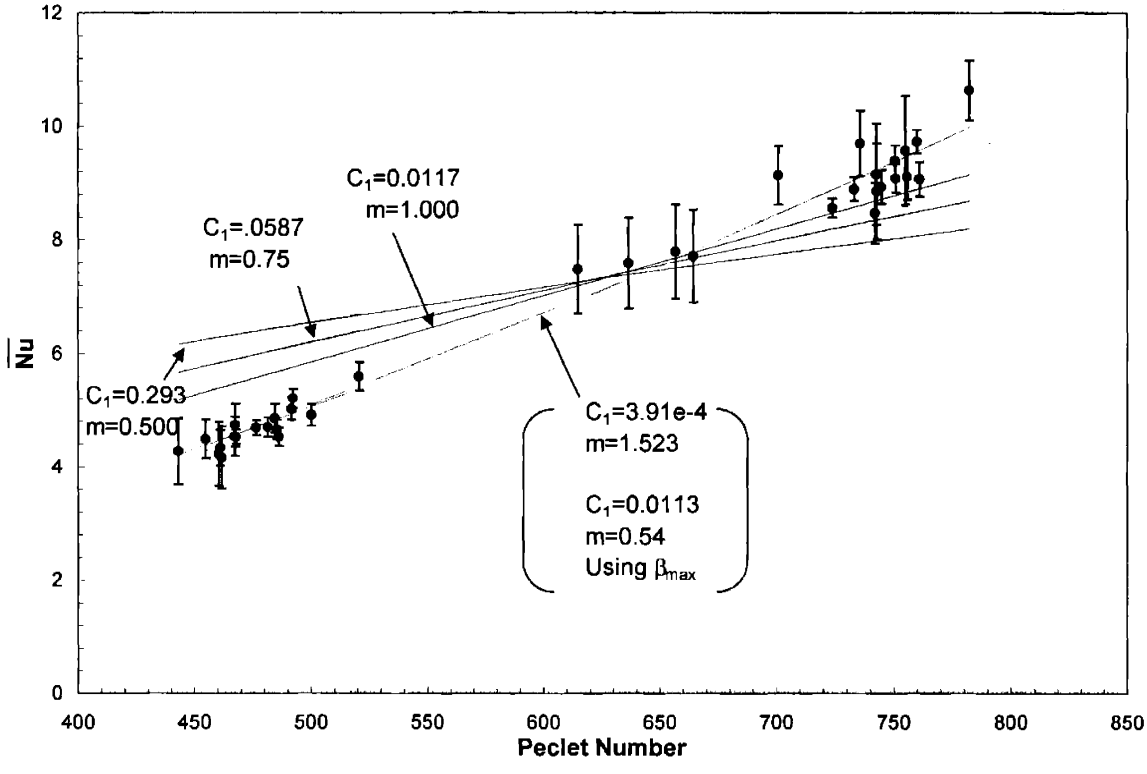

Figure 3-50. Plot of the experimental $\overline{Nu}$ data along with predicted values from correlations in the form C_1Pe^m. A least-squares fit to the data led to a correlation of the form $\overline{Nu} = 0.000391Pe^{1.523}$. The large Peclet number exponent was attributed to improved surface wetting at increased jet velocity.

Surface wetting and the spreading ratio of gallium were examined in attempt to understand the growth of $\overline{Nu}$. The ability of a liquid metal to wet a surface and the extent to which it spreads out over the surface are separate but not independent phenomena which affect heat transfer. Surface wetting, quantified in terms of the contact angle, θ_c, affects the extent to which a liquid spreads over the surface which, in turn, impacts the heat transfer between the liquid and solid surface.[55] The inability of liquid metals to wet most surfaces was recognized early on as a

limitation on the performance as a heat transfer fluid. As mentioned earlier, to account for the lack of wetting by some liquid metals, it was recommended that the forced convection correlations be reduced by a factor of 2.[29] Figure 3-39, however, illustrated that the reduction factor caused by non-wetting is not constant. Although no studies have quantified the nature of this effect in liquid metal jets, several studies have attempted to quantify the effects of wetting and spreading of molten metal droplets as they relate to heat transfer.[56-58] While these studies considered single droplets as opposed to jets, they found that heat transfer increased with $\sim \beta^2_{max}$ as a result of decreased thermal contact resistance. The flattening or spreading ratio, β_{max}, is defined as the ratio of the maximum diameter of liquid after impact to the initial drop diameter. In the following discussion, the quantity β^2_{max} is proposed as an additional parameter to be used to correlate $\overline{Nu}$.

Although several models have been proposed to predict β_{max}, a great deal of the physics of wetting is still not understood.[56] The Kurabayashi-Yang (KY) equation was found to provide the best agreement between an analytic expression and experimental values of β_{max} for liquid drops impacting a surface.[59] This equation, which must be solved numerically, relates β_{max} to the impact Weber number (We) and Reynolds number. In its original form, however, it only utilized energy and surface tension effects but neglected surface wetting. Healy et. al. expanded the equation to account for surface wetting effects by multiplying the resulting β_{max} from the KY equation with the correction factor of $(45/\theta_c)^{0.241}$. The modified KY equation is given by

$$\frac{We}{2} = \frac{3}{2}\beta_{max}^2\left[1 + \frac{3We}{Re}\left(\beta_{max}^2 \ln\beta_{max} - \frac{\beta_{max}^2 - 1}{2}\right)\left(\frac{\mu_o}{\mu_{wall}}\right)^{0.14}\right] - 6 \qquad (3.32)$$

where,

We: Weber number ($= \rho V^2 d/\sigma$) All properties except μ_{wall} taken at jet temperature.

β_{max}: maximum spreading ratio (d'/d)

d': diameter after spreading

d: initial diameter

μ_o: initial fluid viscosity

μ_{wall}: fluid viscosity at wall temperature

σ: fluid surface tension (Nm)

Figure 3-51 plots β_{max} as a function of Reynolds number for gallium using a diameter of 3.02 mm which corresponds to the jet diameter used in the experiment. Gallium properties were evaluated at an initial temperature of 50 °C, except for μ_{wall} which was calculated at 80 °C. A contact angle of 150° was assumed since gallium has been experimentally measured by Hida et. al. to have large contact angles between 140-150° for a variety of substrates.[48] While SiC was not used in the experiment by Hida et. al., a separate study with a SiC substrate and liquid aluminum, which has a slightly higher surface tension than gallium, measured contact angles of ~160°.[60] Temperature dependent values of surface tension for gallium was evaluated using $\sigma(T) = 0.7239 - 0.000068\,(T(^{\circ}C) - 29.8)$.[61]

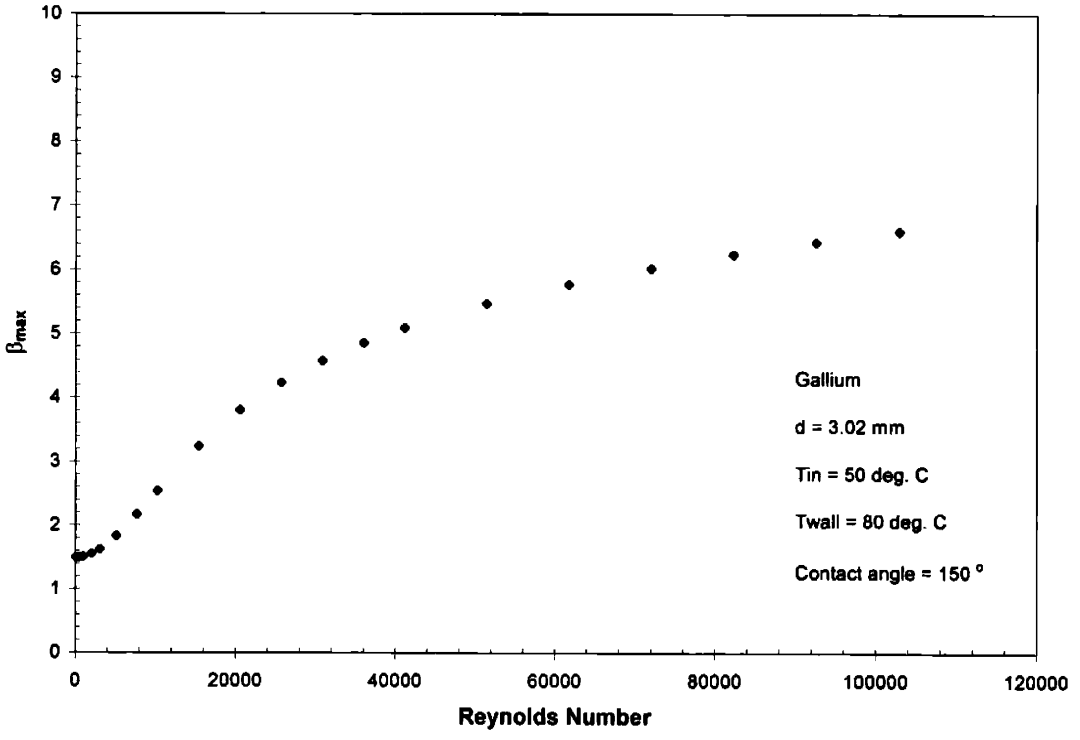

Figure 3-51. Variation of β_{max} with Reynolds number for a gallium droplet (d= 3.02 mm) assuming a contact angle of 150 °.

As seen in Figure 3-51 the maximum slope in the β_{max} curve occurs between $5000 < Re < \sim 40000$. Beyond Re= 40000 β_{max} continues to grow although at a reduced rate. Since β_{max} tends to affect the contact resistance, it would be expected that this resistance would reach a constant value at high Reynolds number. Aziz et. al reported such a behavior with molten tin by measuring no decrease in thermal contact resistance beyond a Reynolds number of 26000.[57]

Equation 3.32 was used to obtain β^2_{max} values for gallium under conditions existing in the experiment. By introducing the β^2_{max} parameter and using a least squares fit for C_1 and m, the predictive ability of the correlation was improved. The new correlation given by

$$\overline{Nu} = 0.0113\ \beta^2_{max}\ Pe^{0.54} \tag{3.33}$$

predicted $\overline{Nu}$ values which differed from the experimental values by an average of 4.8% with a maximum deviation of 12.2% over the 39 experimental data points. Since $\overline{Nu}$ depends on β^2_{max}, the behavior of the spreading factor is extremely important if this correlation is used at higher Reynolds numbers. The β^2_{max} value found with Equation 3.32 continues to increase with Reynolds numbers, contrary to experimental evidence. Although this evidence is limited, it is likely that β^2_{max} will reach a fixed value at Reynolds numbers between 3-5x10^4.[62] Since the highest Reynolds number investigated in this study was 39000, a conservative estimate would be to fix β^2_{max} for Reynolds numbers above 40000. According to Figure 3-51, the β^2_{max} value above a Reynolds number of 40000 would be ~25.

A final comparison of data collected in this experiment illustrates the improvement of gallium over water jets. The experimentally measured values of $\bar{h}$ for the water and jet arrays is presented in Figure 3-52. This figure illustrates that gallium jet arrays provide superior heat transfer compared to water jets for Re>13500. Because of the low kinematic viscosity of gallium, water jets require velocities 2-2.5 times that of gallium to achieve equal Reynolds numbers. Despite this inequity in jet velocities, gallium arrays exhibit enhanced heat transfer over water jets. At a Reynolds number of 18000, $\overline{Nu}$ for the gallium jet array is 19% higher than for water jets. This improvement increases to 50% at Re = 25000 and 80% at Re = 35000. Figure 3-52, however, does indicate that at reduced Reynolds numbers the array-averaged heat transfer for gallium would fall below that of water jets for Re<13500. This effect was previously illustrated at the end of §3.3.5.2 from the results of the numerical simulations of single jets. By placing jets in an array, however, the area-averaged heat transfer from gallium is maintained above that of water. This will be true for all s/d less than 7 as long as Re>13500.

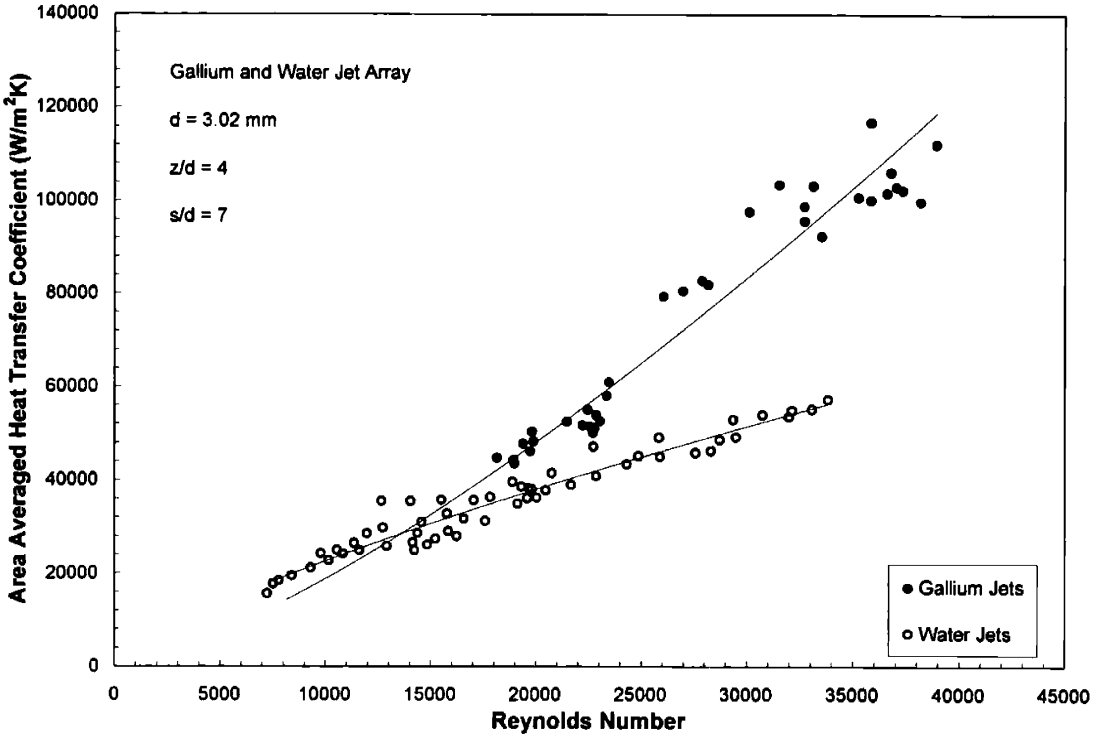

Figure 3-52. Experimentally measured $\bar{h}$ values for gallium and water jet arrays. The solid lines represent $\bar{h}$ values predicted by the correlations given in Equations 3.31 and 3.33.

3.4 Combining Mechanical and Thermal Considerations

Up to this point there has been only cursory examination of the mechanical and structural considerations of an accelerator target. In this final section of the chapter, the conclusions regarding heat deposition and cooling with an array of submerged impinging jets are coupled with the structural implications of the mechanical and thermal stresses. While it would be impossible to present optimized targets for all possible parameter combinations, the goal is to develop a procedure for determining the dimensions of beryllium and lithium-based targets. Before describing the process it is necessary to list certain assumptions regarding different parameters affecting target design. These parameters include:

1. Neutron producing target material and charged particle reaction

   -As has been the case throughout this chapter, the 4 MeV (p,n) reaction is used with the beryllium target, while the 2.5 MeV (p,n) reaction is used with the lithium target.

2. Substrate material

   -Beryllium targets can be constructed out of pure metal or with the neutron-producing layer located on a substrate of different material. Beryllium targets with and without substrates are considered.

   -C15715 copper alloy is used as the substrate for lithium because of its high thermal conductivity and mechanical strength.

3. Target diameter

   -Fixed at 6 cm based on moderator dimensions given in Table 1-2.

4. Coolant

   -Water having an inlet temperature of 20 °C and gallium at an inlet temperature of 35 °C are used.

5. Heat transfer coefficient

   -Assumed to be uniform over the cooled surface as a result of using a jet-array. Jet velocities required to achieve a given heat transfer coefficient calculated with Equations 3.31 and 3.33.

6. Total pressure loading on target

   -Total pressure on target is a combination of the system pressure and dynamic pressure of the jet. In the case of water, system pressure is assumed to be at the minimum value which ensures that the target/coolant interface temperature is less than the saturation temperature.

7. Edge constraints

   -Fixed and simply-supported edges are both considered.

8. Beam size

   -Broad beams allow higher total powers to be placed on target. Highly defocused beams, however, result in part of the current being lost on non-neutron producing materials.

   As a limit on beam size, σ_{beam} is set at 12 mm. This assumption places 95% of the total accelerator output on the 6 cm diameter target.

9. Target thickness

   -Primary parameter which is varied in order to achieve maximum possible power on target.

3.4.1 Mechanical and Thermal Stress in Cylindrical Plates

Stress in an accelerator target will arise because of the pressure loading of the cooling system as well as thermal gradients due to heating by the ion beam. Because a target will be subjected to significant thermal and mechanical loads, proper material selection as well as a design which mitigates stress are crucial. Equation 1.7, which indicates that thermal stress is proportional to ~$E\alpha\Delta T$, gives some indication of the desired properties in a target material. Suitable target materials should have a small elastic modulus, low coefficient of thermal expansion, and a high thermal conductivity. Target materials must also retain their strength at high temperature since they support a pressure differential imposed by the cooling system and the beam line vacuum. In many cases, however, attempts to alleviate either the thermal or mechanical stress has the effect of increasing the other. For example, target thickness can be reduced to lower the thermal resistance. While this will decrease thermal stress by lowering the overall target temperature, it will increase the mechanical stress. Likewise, increases in jet velocity will lower the thermal stress by improving heat transfer, but the mechanical stress will increase as a result of higher dynamic pressures. The following analytic description of mechanical and thermal stresses in a target, modeled as a thin circular plate, will help illustrate these interactions. A detailed derivation of the mechanical stress in a thin cylindrical disk can be found in Kelkar et. al.[63] Calculation of the thermal stress follows a methodology prescribed by Lienhard and Napolitano,[11] with the exception that the cold side temperature is allowed to vary with position rather than being fixed.

3.4.1.1 Derivation of Thermal and Mechanical Stress Based on Plate Theory

A target having a radius, R, and a thickness, t, is centered such that the middle of the target is located at (r,z) = 0,0. The hot edge of the target is located at z = -t/2 and is subjected to a Gaussian heat flux ($q''(r=0) = q_{max}''$; st. dev. = σ_{beam}). The opposite side of the target at z = t/2 is subjected to a uniform pressure, P, in the -z direction and a uniform heat transfer coefficient h, at a bulk temperature, T_∞. The sides of the target are insulated, and the temperature across the target is assumed to vary linearly from the hot to cold side. The material is assumed to be unstressed at a temperature, T_o. A cross-section of the target plate is illustrated in Figure 3-53.

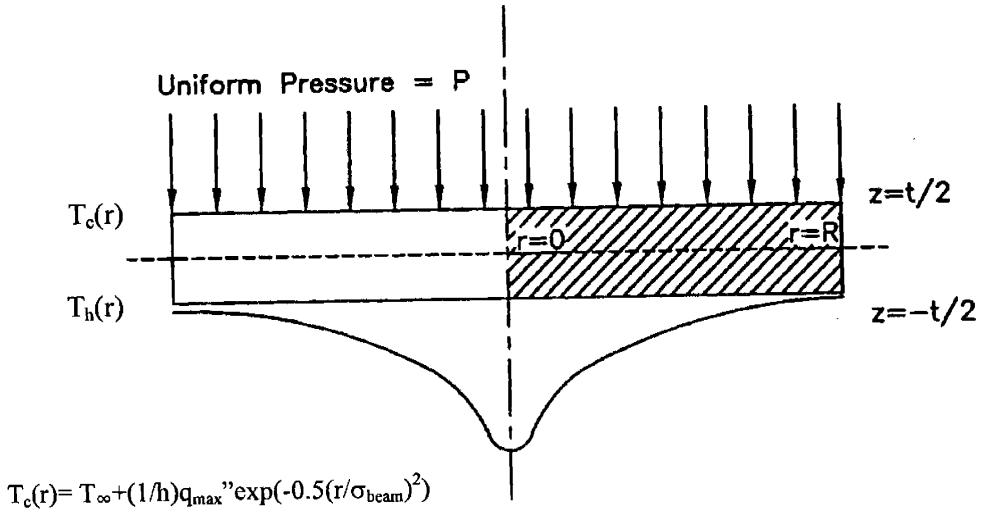

Figure 3-53. Cross-section of target disk used to derive the analytic expressions for thermal and mechanical stress.

In general (using cylindrical coordinates), a plate can be subjected to in-plane membrane forces (per unit length) N_r, N_θ, $N_{r\theta}$, and out-of-plane shearing forces (per unit length) $N_{\theta z}$, N_{rz}. In addition to the membrane forces and shears, bending moments (per unit length) M_r, M_θ, $M_{r\theta}$ arise because the edge of the plate is either fixed or simply-supported. When loads are axisymmetric, such as the thermal and mechanical loads in this case, $N_{\theta z}$, $N_{r\theta}$, and $M_{r\theta}$ are zero. The resulting radial and azimuthal stress can be written in terms of the membrane forces and bending moments given by Equation 3.34.

$$\sigma_{rr} = \frac{N_r}{t} + \frac{12M_r z}{t^3}$$

$$\sigma_{\theta\theta} = \frac{N_\theta}{t} + \frac{12M_\theta z}{t^3} \qquad (3.34)$$

For a uniform pressure load applied at z =t/2, which results in small deflections (<0.1t), the membrane forces N_r and N_θ are zero, and stresses are caused only by the bending moments M_r and M_θ. These moments can be calculated from the deflections in the -z direction, w(r), as indicated in Equation 3.35. Depending on whether the edges are simply-supported or fixed, resulting deflections are given by Equations 3.36 and 3.37.

$$M_r = -D\left(\frac{d^2w}{dr^2} + \frac{\nu}{r}\frac{dw}{dr}\right)$$

$$M_\theta = -D\left(\nu\frac{d^2w}{dr^2} + \frac{1}{r}\frac{dw}{dr}\right) \qquad (3.35)$$

$$w(r) = \frac{P}{64D}\left(\frac{5+\nu}{1+\nu}R^4 - \frac{6+2\nu}{1+\nu}R^2r^2 + r^4\right) \quad \text{(Simply-supported)} \qquad (3.36)$$

$$w(r) = \frac{P}{64D}\left(R^2 - r^2\right)^2 \quad \text{(Fixed-Edge)} \qquad (3.37)$$

Taking the first and second derivatives of 3.36 or 3.37 followed by substitution into 3.35 and then 3.34 gives expressions for the radial and azimuthal stresses from an axisymmetric pressure load.

$$\sigma_{rr} = \frac{3P}{4}\frac{z}{t^3}(3+\nu)(R^2 - r^2)$$

(Simply-supported) (3.38)

$$\sigma_{\theta\theta} = \frac{3P}{4}\frac{z}{t^3}\left(R^2(3+\nu) - r^2(3\nu+1)\right)$$

$$\sigma_{rr} = \frac{3P}{4}\frac{z}{t^3}\left(R^2(1+\nu) - r^2(3+\nu)\right)$$

$$\sigma_{\theta\theta} = \frac{3P}{4}\frac{z}{t^3}\left(R^2(1+\nu) - r^2(3\nu+1)\right) \qquad \text{(Fixed-edge)} \qquad (3.39)$$

Unlike the stresses from a pressure load, which arise only from the bending moments, thermal expansions generate both in-plane membrane forces and bending moments. Expressions for the bending moments and membrane forces caused by thermal expansion can be found in (Johns)[64] for simply-supported plates and (Napolitano)[65] and (Goodier)[66] for fixed-edge plates. Integration of the expressions for the membrane forces and bending moments followed by substitution into Equation 3.34 results in expressions for the radial and azimuthal stresses. For clarity σ_{beam} is represented by σ in the following equations.

(Simply-supported)

$$\sigma_{rr} = [E\alpha(T(0,z) - T_o)]\left[\left(\frac{\sigma}{R}\right)^2\left(1 - e^{-\left(\frac{R^2}{2\sigma^2}\right)}\right) - \left(\frac{\sigma}{r}\right)^2\left(1 - e^{-\left(\frac{r^2}{2\sigma^2}\right)}\right)\right]$$

$$\sigma_{\theta\theta} = [E\alpha(T(0,z) - T_o)]\left[\left(\frac{\sigma}{R}\right)^2\left(1 - e^{-\left(\frac{R^2}{2\sigma^2}\right)}\right) + \left(\frac{\sigma}{r}\right)^2\left(1 - e^{-\left(\frac{r^2}{2\sigma^2}\right)}\right) - e^{-\left(\frac{r^2}{2\sigma^2}\right)}\right] \qquad (3.40)$$

(Fixed-edge)

$$\sigma_{rr} = -[E\alpha(T(0,z) - T_o)]\left[\left(\frac{1+\nu}{1-\nu}\right)\left(\frac{\sigma}{R}\right)^2\left(1 - e^{-\left(\frac{R^2}{2\sigma^2}\right)}\right) + \left(\frac{\sigma}{r}\right)^2\left(1 - e^{-\left(\frac{r^2}{2\sigma^2}\right)}\right)\right]$$

$$\sigma_{\theta\theta} = -[E\alpha(T(0,z) - T_o)]\left[\left(\frac{1+\nu}{1-\nu}\right)\left(\frac{\sigma}{R}\right)^2\left(1 - e^{-\left(\frac{R^2}{2\sigma^2}\right)}\right) - \left(\frac{\sigma}{r}\right)^2\left(1 - e^{-\left(\frac{r^2}{2\sigma^2}\right)}\right) + e^{-\left(\frac{r^2}{2\sigma^2}\right)}\right] \qquad (3.41)$$

where,

σ_{rr}: radial stress

$\sigma_{\theta\theta}$: azimuthal stress

E: Young's Modulus

α: coefficient of thermal expansion

T_o: temperature at which target is unstressed (assumed to be 25 °C)

ν: Poisson's Ratio

R: target radius

3.4.1.2 Failure Criteria

Any discussion of mechanics would be incomplete without a criterion in which calculated stresses can be used to predict when failure might occur. For ductile materials two popular failure theories are Tresca's yield theory (Maximum Shear Stress Theory) and distortion energy (Von Mises') theory. Experimental verification indicates only slight differences in the two with most favoring the predictions of Von Mises' theory, which states that yielding will occur when the energy density associated with the shear stresses reach a critical value, σ_E.[67] Distortion energy theory was selected for use in this study. The effective (Von Mises) stress, σ_E, is determined from the principal stresses σ_1, σ_2, σ_3 and is given by

$$\sigma_E = \frac{1}{\sqrt{2}}\sqrt{(\sigma_1-\sigma_2)^2+(\sigma_2-\sigma_3)^2+(\sigma_3-\sigma_1)^2}\,. \tag{3.42}$$

In cylindrical coordinates for the case where σ_Z is zero, the Von Mises stress is given by

$$\sigma_E = \sqrt{(\sigma_{rr})^2+(\sigma_{\theta\theta})^2-\sigma_{rr}\sigma_{\theta\theta}}\,. \tag{3.43}$$

Implementation of Von Mises theory requires the calculation of an equivalent stress σ_E which is then compared to σ_y in order to determine a safety factor according to

$$\text{Safety Factor} = \sigma_y / \sigma_E \tag{3.44}$$

Normally σ_y is given as the stress which produces an offset of 0.2%.

It might be assumed that an additional criterion is needed to determine failure in beryllium, which is normally considered a non-ductile material. As a result of manufacturing processes used for beryllium products, however, this is not necessarily the case. Beryllium which is formed through casting is brittle, difficult to machine, and has poor mechanical properties.[68] For this reason, nearly all beryllium products are produced through a powder metallurgy (PM) process, which results in reasonably good ductility. Improved ductility comes from the random orientation of the beryllium grains produced in the PM process.[69] Because of improved ductility, yield strength can be used as the primary design criterion.[70] The PM process involves creation of a powder either through grinding or melting followed by atomization and solidification. Powder is then pressed and heated so that the final density is >99% of the theoretical bulk density. In vacuum hot pressing, the powder is heated to 1025-1125 °C at pressures on the order of 8.3 MPa.[69] The most common structural grades of beryllium, which are produced through vacuum hot pressing, possess minimum tensile elongations of 1-3% at room temperature. S-200F beryllium, which was used to create the target for the small-scale heat removal experiments, is the most common structural grade for components made from hot pressed block.[68] All beryllium properties listed in this chapter refer to the S-200F grade.

3.4.2 Using Analytic Predictions of Stress and Failure In An All-Beryllium Target

Using Equations 3.38-3.41 the stresses which are induced in a target upon heating can be calculated given the magnitude and radial distribution of heat flux, heat transfer coefficient, bulk coolant temperature, and pressure. It is helpful to first look at the mechanical and thermal stresses separately. Figure 3-54 illustrates the radial and azimuthal components of the mechanical stress generated in an all-beryllium target having a radius of 3 cm and a thickness of 1.25 mm when subjected to a pressure differential of 0.10135 MPa. From Equations 3.38 and 3.39 it is evident that the maximum stresses will occur at the hot and cold sides and will be zero along the target centerline. Since the mechanical stresses on the hot and cold faces are equal in magnitude but opposite in sign, only the values for the hot edge are plotted. Radial variations in the stresses described for the heated face, therefore, would also hold along the cooled face but with tensile stresses becoming compressive and vice versa. On the heated face, the mechanical stresses are generally tensile. For a simply-supported edge all mechanical stresses are tensile with maximum values occurring at the center and decreasing with radius. While radial stress falls to zero at the edge, azimuthal stress at the edge approaches a value which is $(2-2\nu)/(3+\nu)$ times greater than the azimuthal stress at the center. For equivalent radii, thickness, and pressure, a fixed-edge

target experiences less deflection and stress at the center than a simply-supported target. At an r value slightly greater than 0.5R, the radial stress along the hot face transitions from tensile to compressive and reaches a maximum at the target edge. This maximum is twice the magnitude and opposite in sign from the radial stress at the center.

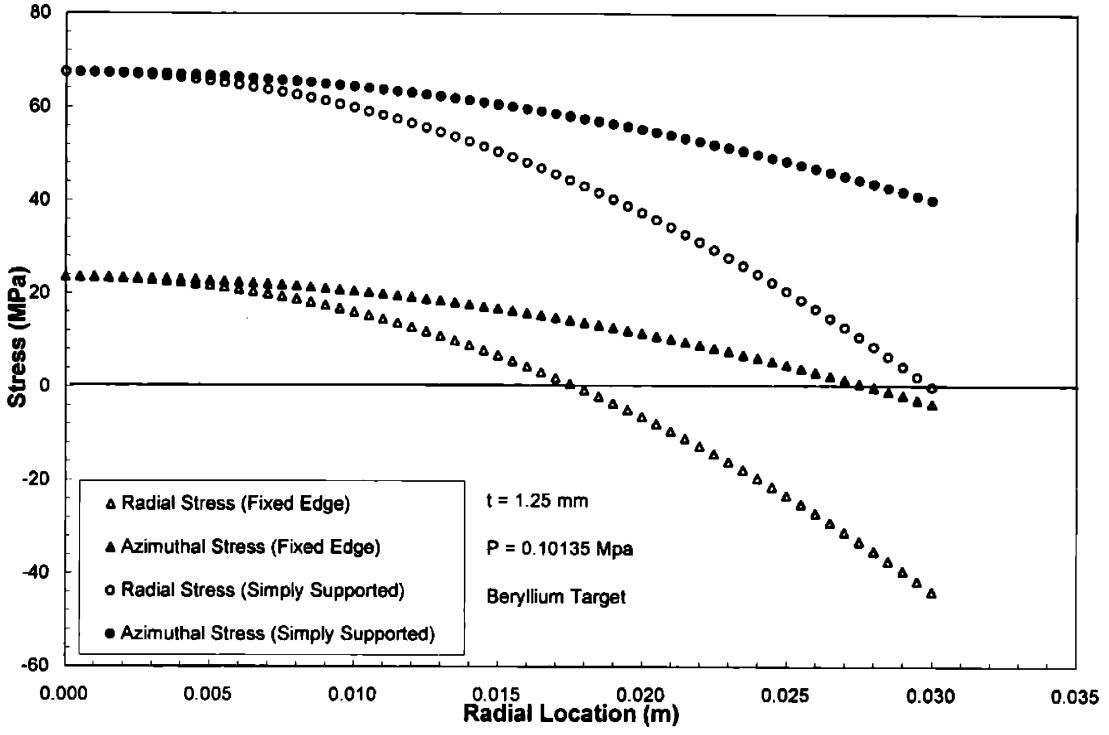

Figure 3-54. Radial and azimuthal stress along the hot face of an all beryllium target having a thickness of 1.25 mm. Positive stresses are tensile and negative stresses are compressive. Stresses along the cold face would have equal magnitude but opposite signs.

Two different heating conditions are considered to illustrate thermal stresses calculated with Equations 3.40 and 3.41. Both cases utilize a target thickness of 1.25 mm, a radius of 3 cm, and a heat transfer coefficient of 10^5 W/m^{2}K at a bulk temperature of 35 °C. The first case considers a highly focused beam (σ_{beam}= 2 mm; total power on target 100 W), while the second case uses a broad beam (σ_{beam}= 12 mm; total power on target 2 kW). These cases are plotted in Figures 3-55 and 3-56. From Figure 3-55 it is evident that the stresses for a highly focused beam are nearly identical for fixed and simply-supported edges. In the limit of $\sigma_{beam} \rightarrow 0$, Equations 3.40 and 3.41 reduce to equivalent expressions indicating that edge constraints are not important for a highly localized beam. Stresses on both the hot and cold side of the target are compressive at the center, but quickly fall at increased r values. For both edge constraints there is a tensile extremum in the azimuthal stress corresponding to the beam edge.

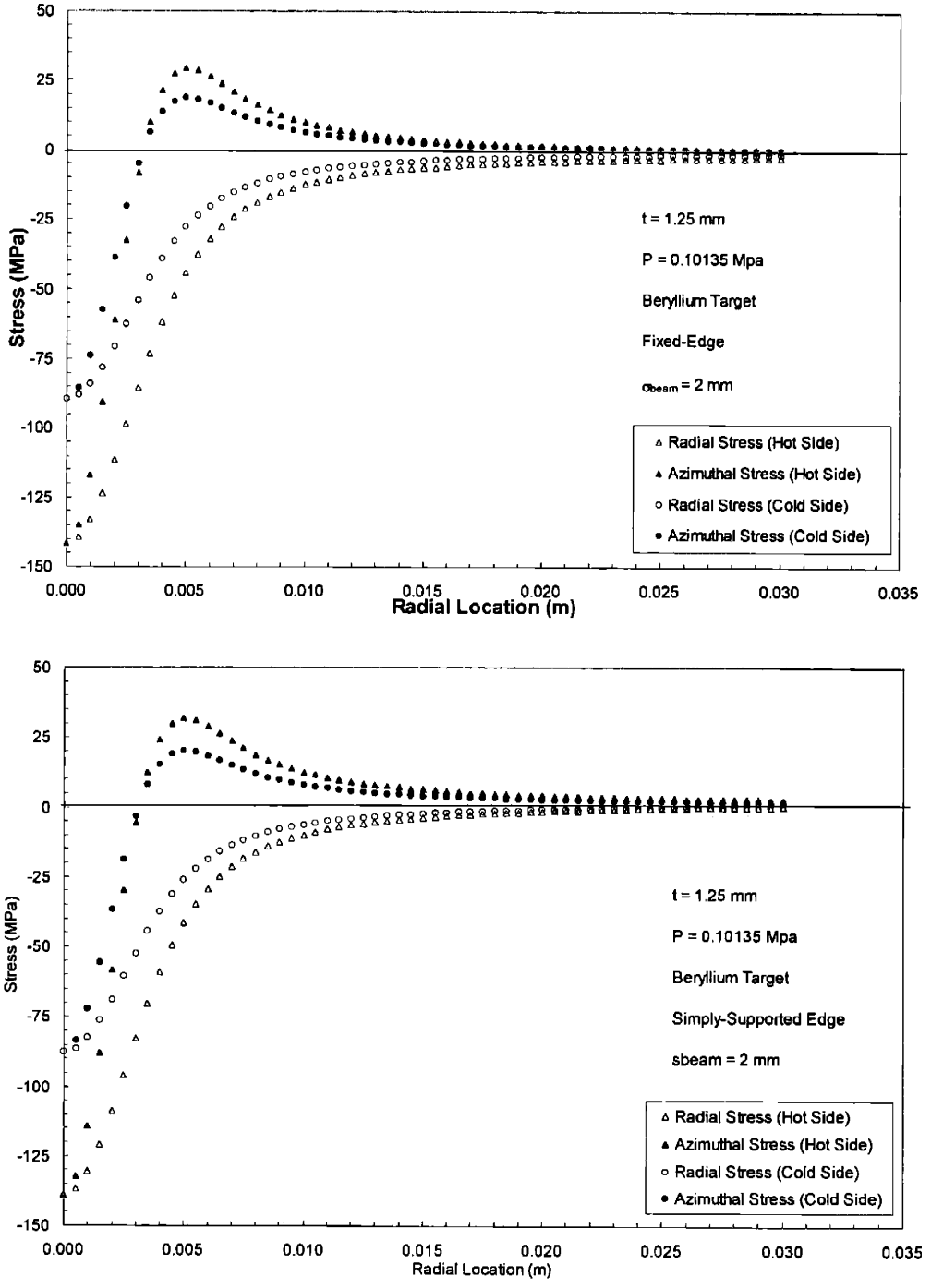

Figure 3-55. Thermal stress for a 1.25 mm thick beryllium target subjected to a highly focused 100 W beam (σ_{beam}= 2 mm). Stresses in a fixed-edge target are illustrated in the top graph, while the bottom graph plots the stresses for a simply-supported target under the same heating and cooling conditions. The graphs, which are nearly identical, indicate that edge constraints are unimportant for highly focused beams.

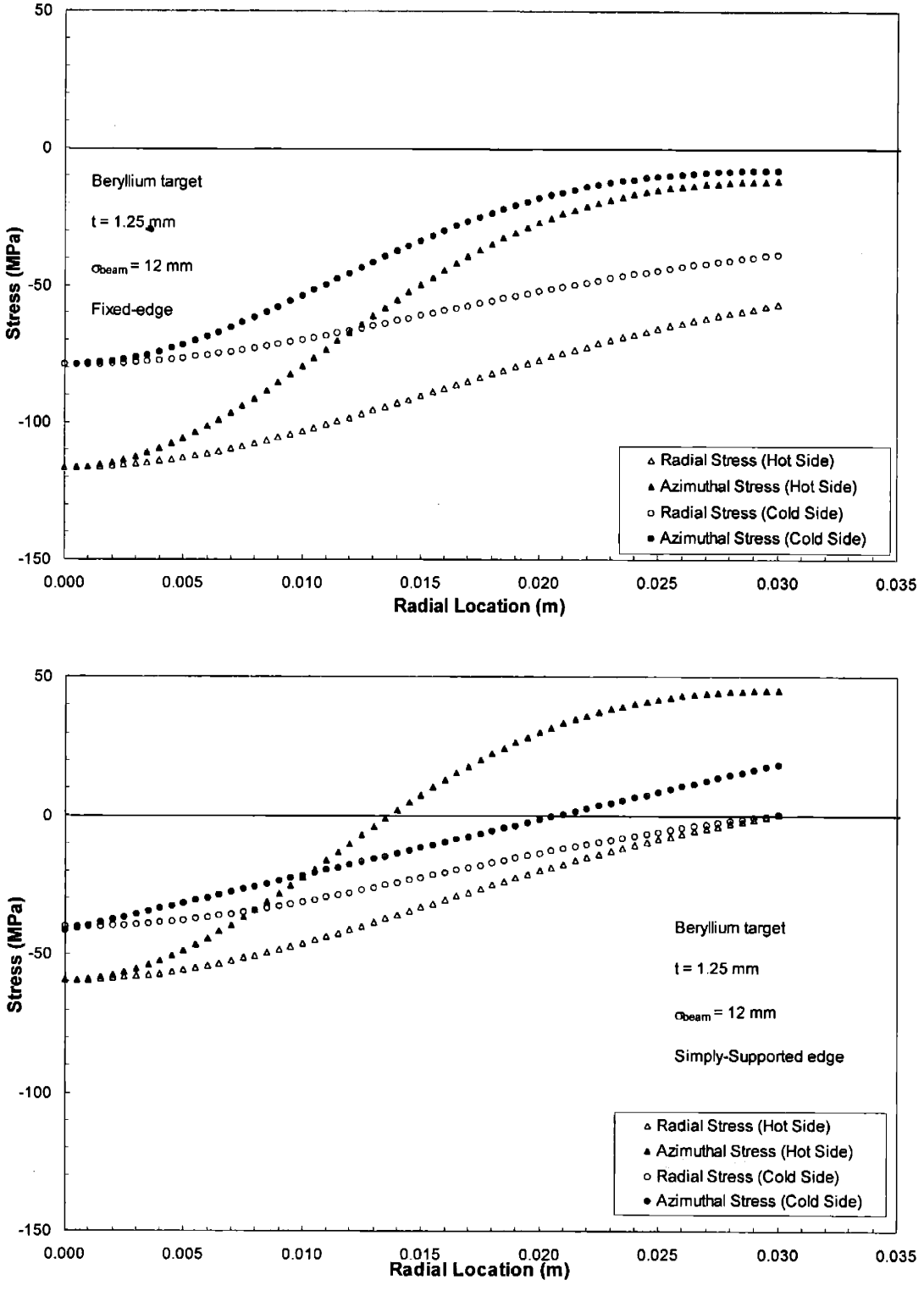

Figure 3-56. Thermal stress for a 1.25 mm thick beryllium target subjected to a broad 2 kW beam (σ_{beam}= 12 mm). Stresses in a fixed-edge target are illustrated in the top graph, while the bottom graph plots the stresses for a simply-supported target under identical conditions.

Figure 3-56, which plots thermal stresses generated by a broad beam, begins to illustrate some of the differences between fixed and simply-supported targets. Most noticeable is the fact that the maximum compressive stresses at the center of the simply-supported target are nearly a factor of 2 less than for a fixed-edge. Because the edge is not allowed to expand laterally, membrane forces generate compressive radial and azimuthal stresses throughout a fixed-edge target. With edges free to expand laterally, compressive stresses are reduced for simply-supported edges. From Equation 3.40 it is apparent that radial thermal stresses in simply supported targets are zero at the outer edge. Azimuthal stresses which are compressive at the center of the target become tensile toward the edge and can have magnitudes close to those at the center.

Having examined separately the mechanical and thermal components, it is apparent that there are certain locations in the target, such as the center and edges of the hot and cooled faces, which are likely to exhibit large total stresses. In situations where both thermal and mechanical stresses are compressive or tensile they would compound each other and generate a high total stress. To illustrate this point, Figures 3-57 and 3-58 plot the effective stresses (Equation 3.43) at certain locations in an all-beryllium target under the following conditions:

Heat transfer coefficient: 10^5 W/m^{2}K
Coolant temperature: 35 °C
Pressure: 0.10135 MPa
Beam standard deviation: 12 mm
Total beam power: 3 kW

Looking first at Figure 3-57, which plots the total stresses in a simply-supported target, it is apparent that optimizing the target thickness involves balancing the stresses at the center and edge of the hot side with those at the center of the cold face. This figure also illustrates how increasing or decreasing target thickness affects the stresses in certain regions. Thin targets would likely fail at the center of the cold face where the mechanical and thermal stresses are both compressive. Even at the center of the hot face, where the highest temperatures exist, stresses are quite low since the tensile mechanical stresses counter balance the thermal stresses. Increasing the target thickness reduces the mechanical stress and emphasizes the thermal stress. At increased thickness the stresses at the edge of the target tend to be large because the radial components of the thermal and mechanical stresses are both tensile. For very thick targets, thermal stresses at the center of the target would dominate and cause of failure. It is clear from this graph that for broad beams the stresses at the edge of the cold side remain small and would not affect the optimization process.

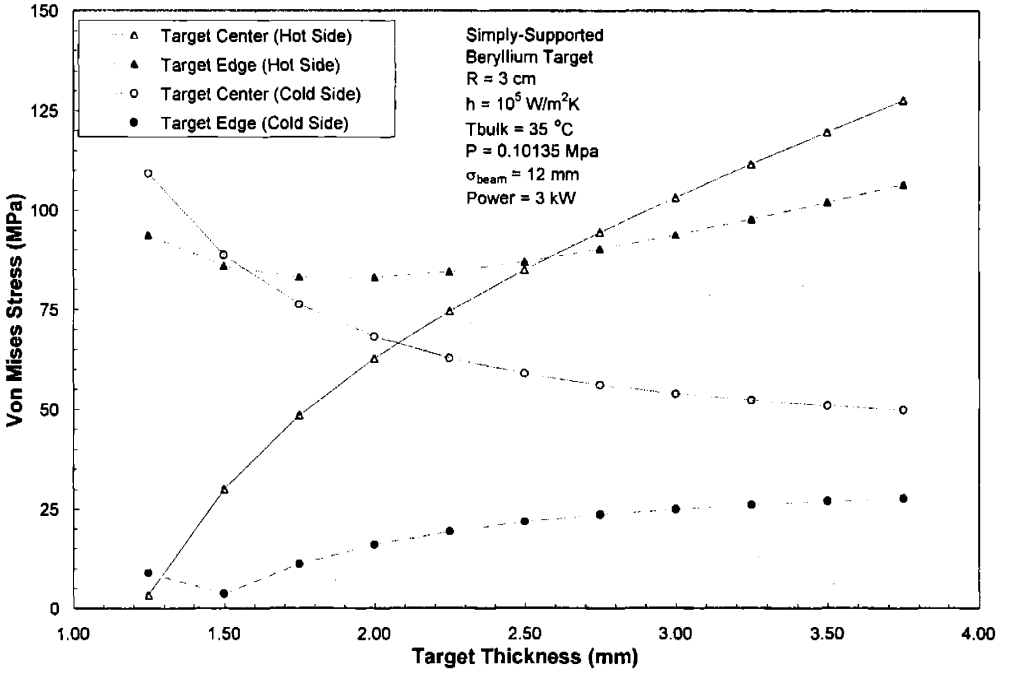

Figure 3-57. Plot of the effective stresses in a simply-supported target (R= 3 cm) at varying thicknesses when subjected to a 3 kW beam having a standard deviation of 12 mm and a pressure differential of 0.10135 MPa. A heat transfer coefficient of 10^5 W/m^{2}K at a bulk temperature of 35 °C was used.

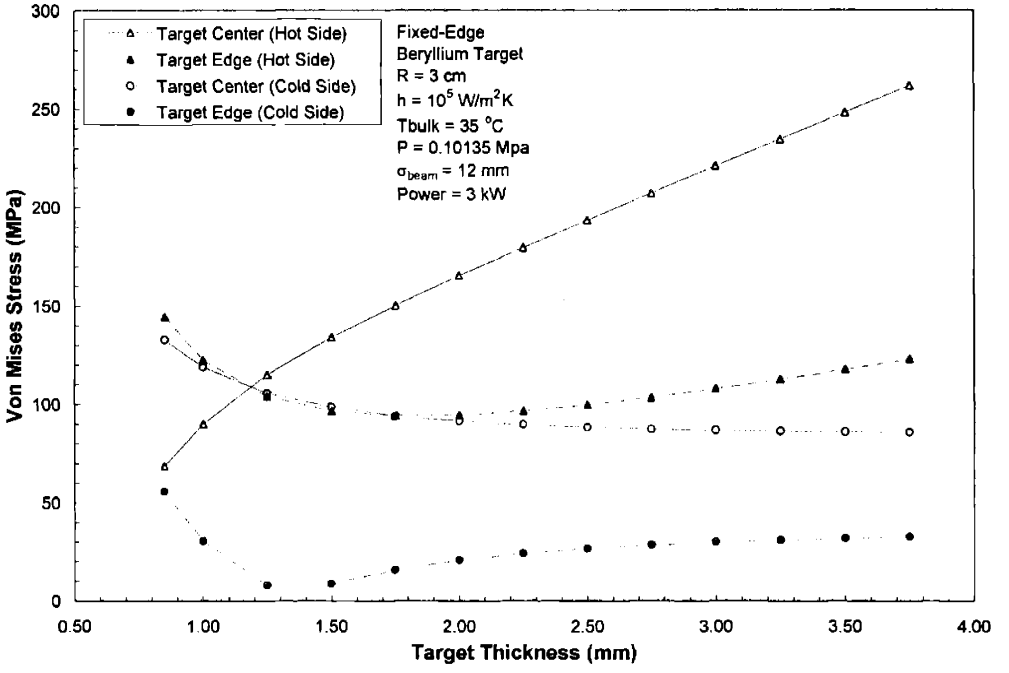

Figure 3-58. Plot of the effective stresses in a fixed-edge target (R= 3 cm) at varying thicknesses when subjected to a 3 kW beam having a standard deviation of 12 mm and a pressure differential of 0.10135 MPa. A heat transfer coefficient of 10^5 W/m^{2}K at a bulk temperature of 35 °C was used.

The most noticeable difference between Figures 3-57 and 3-58 is that the stresses in a fixed-edge target tend to be higher than those of the simply-supported target. At small thicknesses the highest stresses are located at the center of the cold face and the edge of the hot face where all mechanical and thermal stresses are compressive. As thickness is increased, the stress at the center of the hot face grows quickly because of the increased membrane forces resulting from a lack of lateral expansion. As was the case in the simply-supported target, optimization would involve balancing the stresses at the center and edge of the hot side with those of the center of the cold face. Stress at the edge of the cold face would not be important.

From the preceding discussion of how the mechanical and thermal stresses interact, it should be apparent that for a given set of conditions optimizing the target thickness to allow maximum power requires the balancing of stresses on the hot and cold face. In general, if the target is too thin, failure will occur on the cold face of the target well below the point at which failure would occur on the hot side. If the target is too thick, the opposite would be true, and failure would occur first on the hot face. The following examples illustrate the optimization of a target of thickness (t) and radius (R) of 3 cm composed completely of beryllium and constrained at the edge either by a simple-support or a fixed-edge. The target is centered at (r,z)=(0,0). As indicated in Figure 3-53 a Gaussian-shaped heat flux, having a standard deviation σ_{beam} of 12 mm is imposed on the vacuum side and a uniform heat transfer coefficient of 10^5 W/m^{2}K at a bulk temperature of 35 °C is imposed on the cooled side. Gallium is assumed as the cooling fluid. At a given power, q''_{max} can be determined using Equations 3.10 and 3.11. The temperature field given by the following equations retains the same radial variation as the heat source and assumes heat flow only in the axial direction. These profiles were used with Equations 3.40 and 3.41 to calculate thermal stress. Properties such as thermal conductivity, coefficient of thermal expansion, and Young's modulus were calculated at the average plate temperature.

$$T_c(r)= T_\infty+(1/h)q''_{max}\exp(-0.5(r/\sigma_{beam})^2) \quad \text{(Cold Side)}$$

$$T_h(r)= T_c+(t/k)q''_{max}\exp(-0.5(r/\sigma_{beam})^2) \quad \text{(Hot Side)}$$

$$T(r,z)= T_c(r)+(t/2-z)(1/k)q''_{max}\exp(-0.5(r/\sigma_{beam})^2) \quad \text{(Arbitrary (r,z) location)}$$

In order to prescribe a uniform pressure along the cooled face certain assumptions had to be made about the arrangement of the nozzles since the uniform heat transfer coefficient is the product of a jet array. The experiments of §3.3 used a rectilinear array with an average s/d of 7 to cool a rectangular-shaped heat source. In order to efficiently cover the entire surface of the circular target, this rectilinear arrangement was translated into an axisymmetric array with an

equivalent s/d spacing. This conversion has little effect on the area average heat transfer coefficient.[26] Equation 3.33 was used to calculate a gallium jet velocity of 3.2 m/s required to achieve an h of 10^5 W/m^{2}K. Radial distribution of the pressure underneath a single jet was determined using the following equation.[71]

$$P(r) = P_{\infty} + 0.5\rho V_j^{\,2} \exp\left[-\left(\frac{1.288r}{d}\right)^2\right] \tag{3.45}$$

At an r/d location halfway between the jet nozzles, the pressure increases to a value which is ~80 % of the stagnation value.[44] An illustration of the nozzle arrangement and pressure variation is shown in Figure 3-59. Using the axisymmetric pressure distribution illustrated in Figure 3-59, an equivalent uniform pressure was calculated by requiring that the sum of the moments about the target edge were equal for both a variable and uniform pressure. By solving for $P_{uniform}$ in Equation 3.46, a uniform pressure was found which produced deflections equivalent to those from a varying distribution.

$$\int_0^R 2\pi r P_{vary}(r)\cdot(R-r)dr = \int_0^R 2\pi r P_{uniform}\cdot(R-r)dr \tag{3.46}$$

For gallium at 3.2 m/s and a system pressure of 0.10135 MPa, the equivalent uniform pressure across the target was calculated to be 0.107698 MPa. This pressure was then used to calculate mechanical stresses. After combining the total stresses resulting from the mechanical and thermal loads, Equations 3.43 and 3.44 were used to determine the power at which failure would occur. Temperature dependent values of yield strength[68] were calculated at the local r position. The power limit was set at the point at which the safety factor reached unity. Figures 3-60 a,b,c plot the Von Mises and yield point stress for a simply supported target having a thickness of 1.0, 1.18, and 1.35 mm.

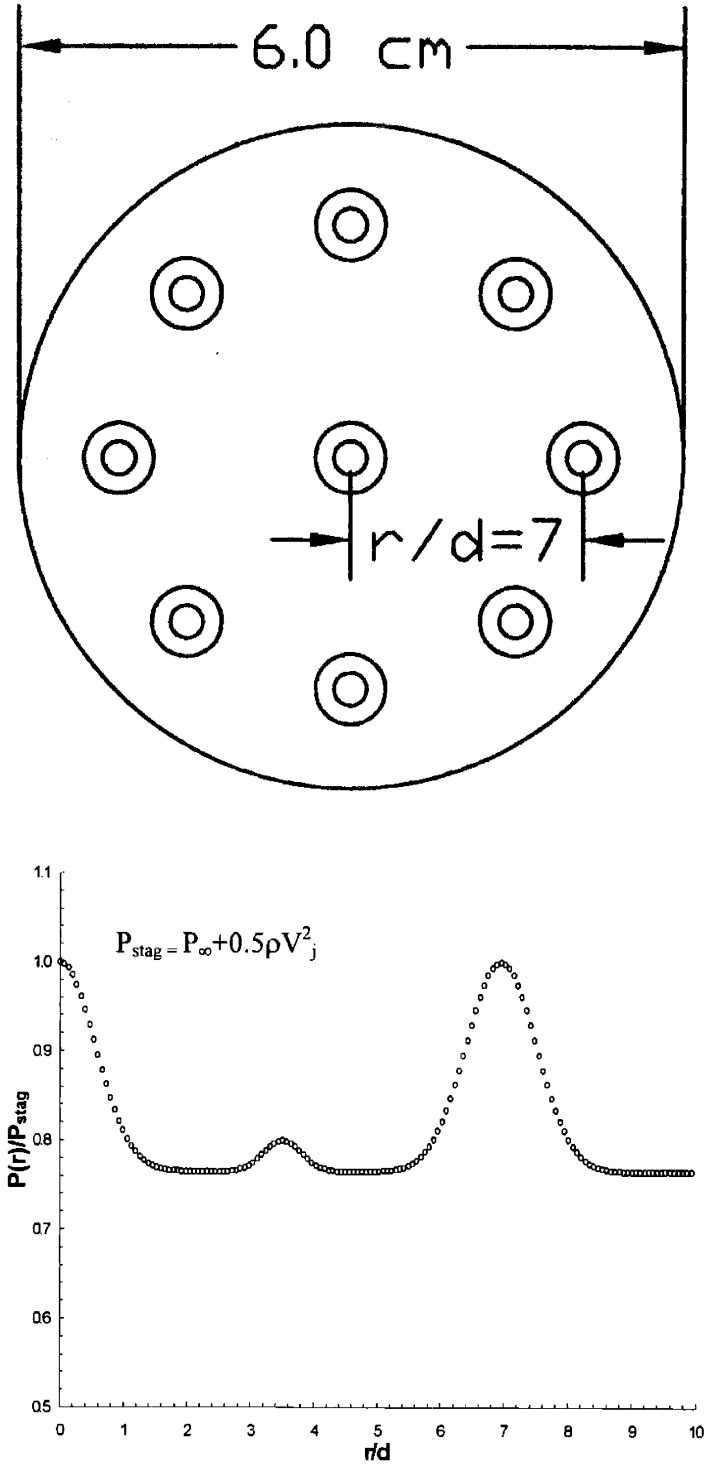

Figure 3-59. Illustration of nozzle orientation and axisymmetric pressure distribution assumed in the analytic stress calculations.

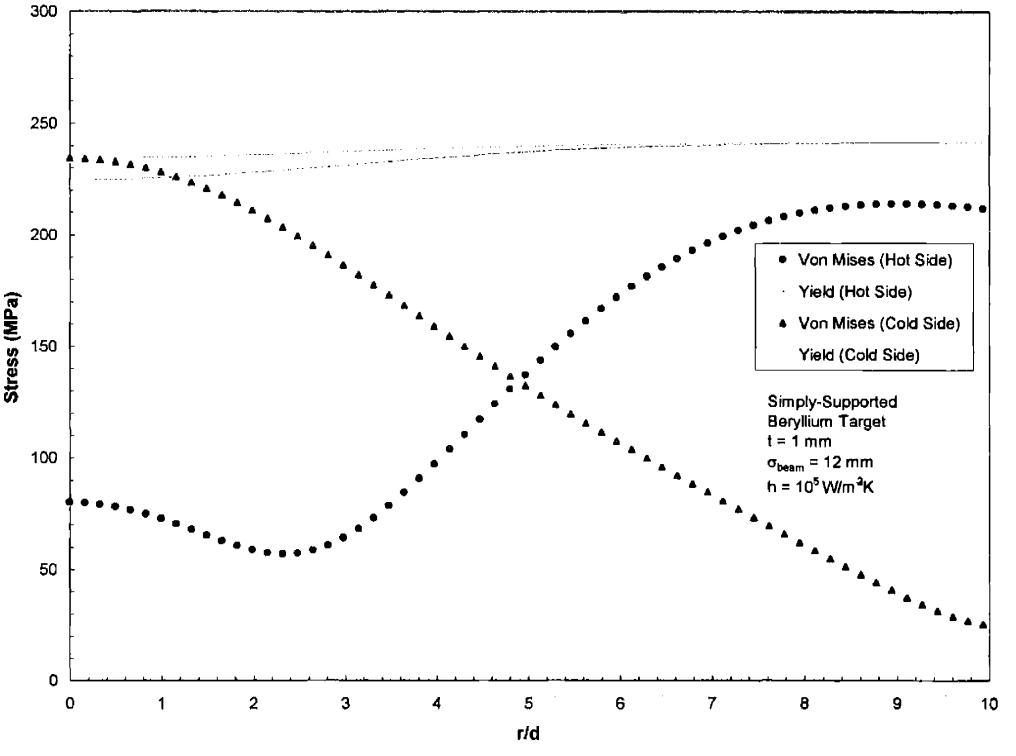
Stress (MPa)
r/d
Von Mises (Hot Side)
Yield (Hot Side)
Von Mises (Cold Side)
Yield (Cold Side)
Simply-Supported
Beryllium Target
t = 1 mm
σbeam = 12 mm
h = 10^5 W/m^2K

a)

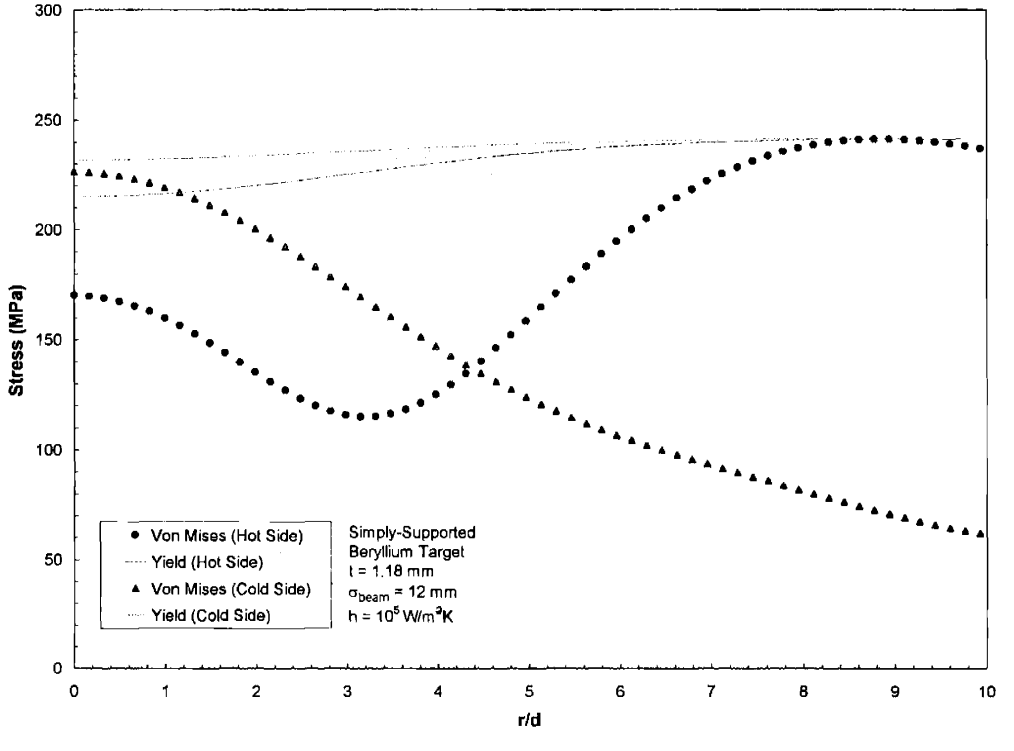
Stress (MPa)
r/d
Von Mises (Hot Side)
Yield (Hot Side)
Von Mises (Cold Side)
Yield (Cold Side)
Simply-Supported
Beryllium Target
t = 1.18 mm
σbeam = 12 mm
h = 10^5 W/m^2K

b)

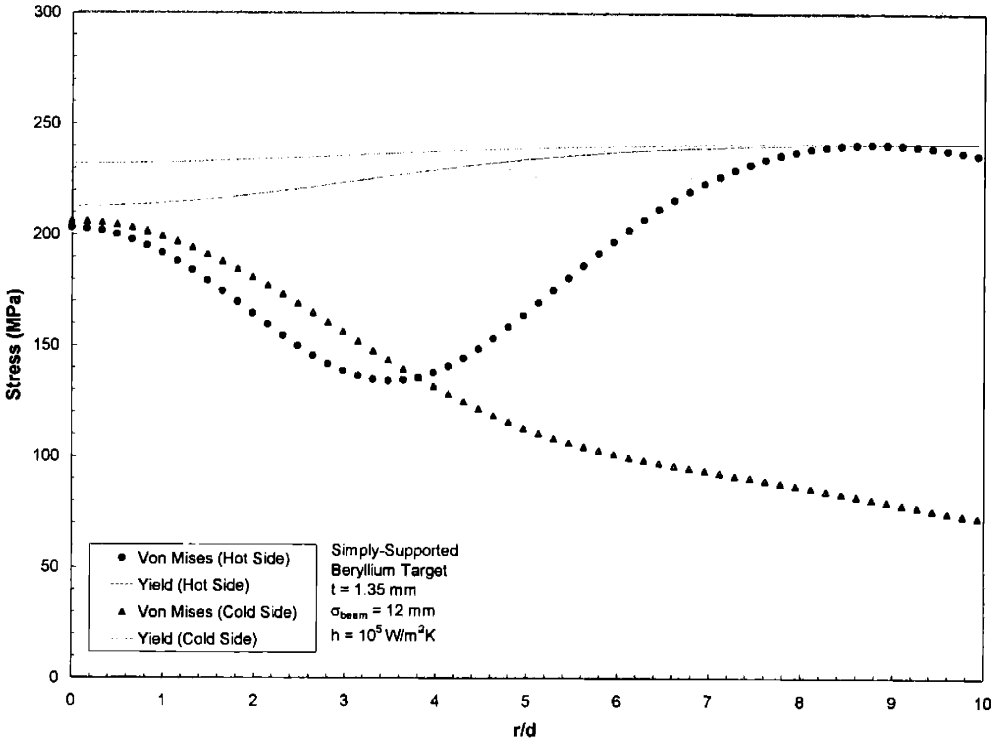

c)

Figure 3-60. a) Von Mises and yield point stress for a 1.0 mm simply-supported target subjected to a 7.4 kW beam having a standard deviation of 12 mm. b) Von Mises and yield point stress for a 1.18 mm simply-supported target subjected to a 8.83 kW beam having a standard deviation of 12 mm. c) Von Mises and yield point stress for a 1.35 mm simply-supported target subjected to a 8.74 kW beam having a standard deviation of 12 mm.

The graphs are plotted for power levels of 7.4 kW, 8.83 kW, and 8.74 kW, respectively which caused the targets to fail. Figure 3-61 gives the optimized fixed-edge case which had a thickness of 0.91 mm and failed at a power of 5.75 kW. These four graphs illustrate that a target which is properly optimized reaches failure on both the hot and cold side at a nearly simultaneous power level. In Figure 3-60a the 1.0 mm target is too thin and fails at the center of the cold side well before failure would occur at the edge of the hot side. The result is a maximum power which is 1.4 kW less than the optimized 1.18 mm target. At a thickness of 1.35 mm the target fails on the hot edge at a power level which is 104 W less than the optimized case. Making a target thicker than the optimized case does not lower the maximum power to the same extent as making the target too thin. For example, at a thickness of 1.5 mm the maximum power is 8.28 kW, and at 1.75 mm the maximum power is 7.39 kW.

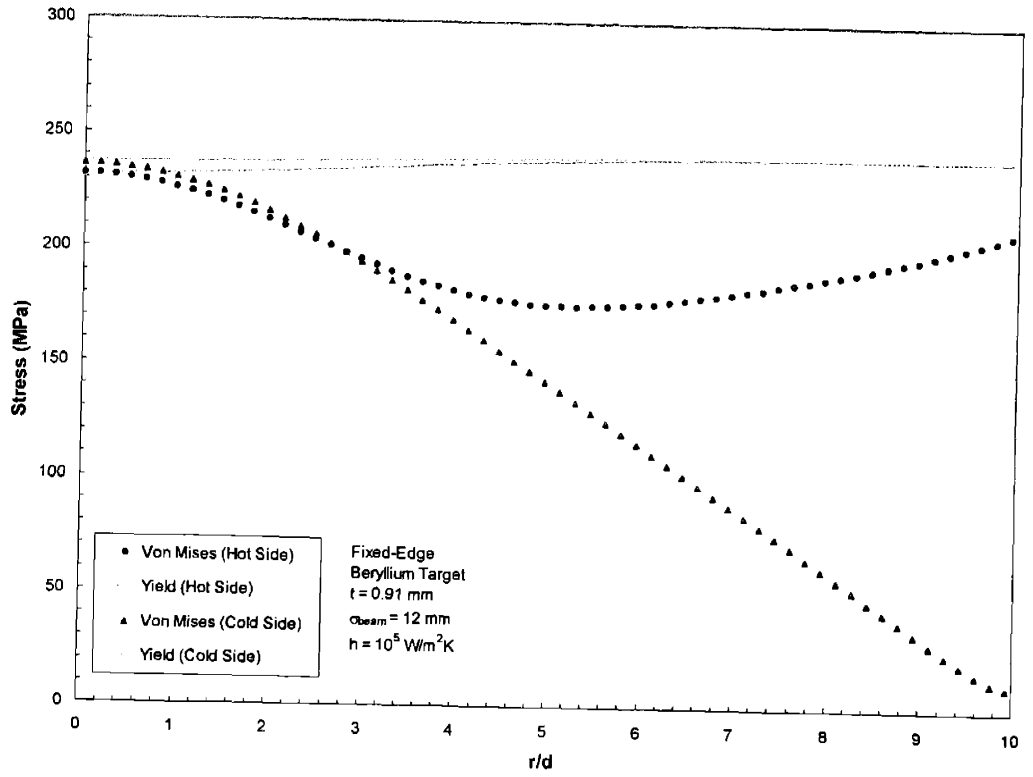

Figure 3-61. Von Mises and yield point stress for a 0.91 mm fixed-edge target subjected to a 5.75 kW beam having a standard deviation of 12 mm.

Figure 3-61 plots stresses in a 0.91 mm fixed-edge target generated by a 5.75 kW beam. As expected the optimized thickness for the fixed-edge case is less than a simply-supported edge because of the smaller amounts of deflection from the pressure loading. The most outstanding difference, however, is that the fixed-edge target could achieve a maximum power which was over 3 kW less than the simply-supported target under similar cooling conditions. Because the edges are not allowed to expand the membrane forces in the fixed-edge target limit the amount of power which can be achieved for broad beams. With a heat transfer coefficient of 10^5 W/m^{2}K it was found that for any beam having a standard deviation >4.7 mm a simply-supported beryllium target could achieve a higher maximum power. For a heat transfer coefficient of 20000 W/m^{2}K simply-supported targets can achieve higher power for beams having a standard deviation >2.5 mm.

3.4.3 Fully Temperature Dependent Simulations of Stress in Targets

To improve the accuracy of the optimization process, fully-temperature dependent numerical simulations were carried out for both beryllium and lithium-based targets. These simulations were carried out in a two step process. A temperature field was first determined using the ADINA-T module as in §3.2 for a given heating and cooling condition. The resulting temperature profile was then mapped onto an identical target model in the ADINA module, which included the mechanical loading and edge supports, and stresses were evaluated. The stresses calculated by ADINA, therefore, reflected both the stresses induced temperature gradients and mechanical loads and accounted for temperature dependent variations in properties. In building these models, a minor change was made in the simply-supported cases which more closely approximates how a real target would be mounted onto the end of a beamline. Rather than applying a simply supported boundary condition, contact between a support and the edge of the target was explicitly modeled. The 6 cm diameter target was modeled so that the outer 3 mm rested on the beamline support. This dimension was deemed sufficient to allow for an O-ring seal. Figure 3-62 illustrates this type of edge constraint with and without a target deflection.

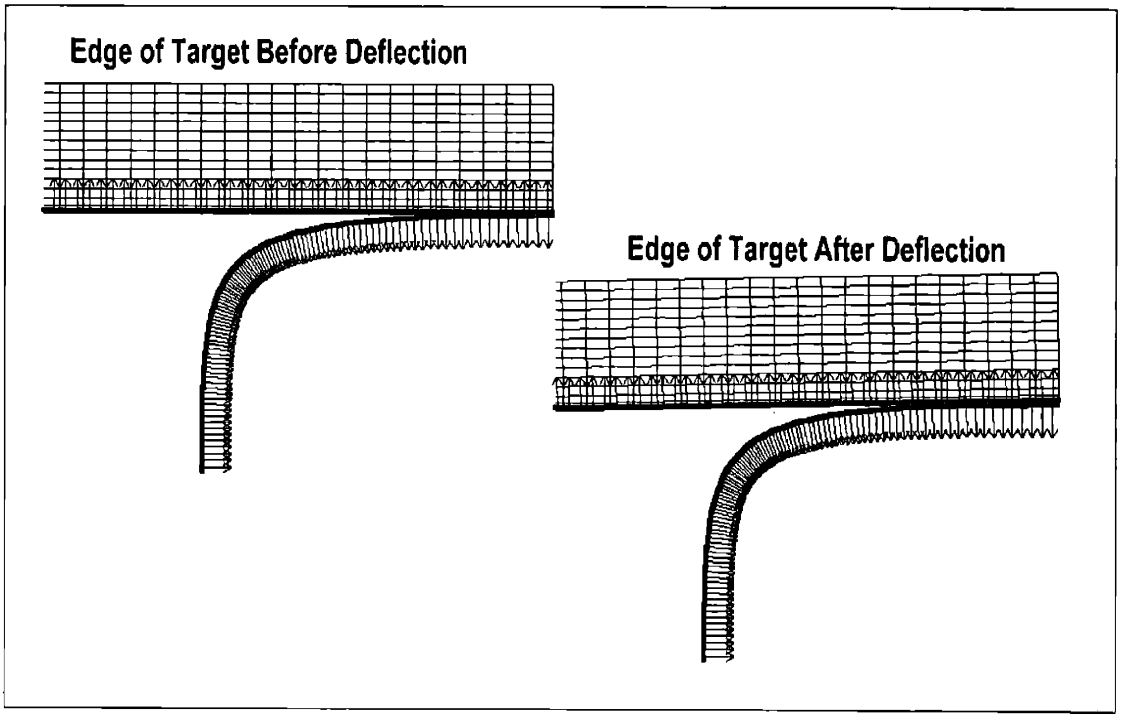

Figure 3-62. Illustration showing the explicitly modeled contact between the edge of a target and a supporting surface. This type of edge-constraint more accurately models the response of a target which is mounted on a beamline.

Simulations were carried out using both gallium at a jet temperature of 35 °C and water at a jet temperature of 20 °C. Experiments described in §3.3 have shown that it would be inequitable to assume equal heat transfer coefficients for each of the fluids. A more equitable assumption would be to assume equal Reynolds numbers or equal pumping power. In these simulations heat transfer coefficients for each of the fluids were based on jet Reynolds numbers of 35000 and film temperatures of 50 °C. Using Equations 3.31 and 3.33 the respective heat transfer coefficients for water and gallium are respectively calculated to be 55210 W/m^2K and 103167 W/m^2K. The simulations used values of 55000 and 10^5 W/m^2K. Pressure variation with radial distance was modeled as illustrated in Figure 3-59. System pressure in all gallium cases was 0.10135 MPa. System pressure in the water simulations was assigned the minimum value which ensured the local target temperature was less than the saturation temperature. Although boiling would increase the local heat transfer coefficient, disruption of the flow at increased r/d caused by the boiling could lead to burnout.[44] Although most of the following cases involve optimizations using beams that have a standard deviation of 12 mm, a brief discussion is included at the end of most of the following cases which concerns uniform beams. To achieve an essentially uniform beam profile requires rastering the beam at a high frequency (kHz) over the target. If the period of the rastering is much less than the thermal time constant of the target then the beam distribution can be treated as essentially uniform. For a beryllium target having a radius of 0.03 m and a thickness of 1 mm, subjected to a heat transfer coefficient of 10^5 W/m^2K over an area A_s, the thermal time constant is given by $\tau=mc_p/hA_s$= (5.23e-3 kg•1825 $Jkg^{-1}C^{-1}$)/(10^5 W/m^2K•2.827e-3 m^2) = 0.034 sec. Since the thermal time constant is nearly 30 times longer than the period of a 1 kHz raster, the uniform beam approximation seems reasonable. Because of the rastering process, however, time varying stresses in the target will cause fatigue. While these transient stresses are not considered, steady-state stresses resulting from a uniform beam are presented in some of the following cases for comparison with the Gaussian-shaped beams.

3.4.3.1 All Beryllium Target

In the case of an all beryllium target cooled with gallium, the analytic calculations gave an excellent first order approximation (1.18 mm) of the target thickness needed to achieve high beam power. They also correctly predicted that the target would reach the yield stress near the edge on the beam side. Numerical simulations found that a maximum power of 7.85 kW could be achieved at a thickness of 1.16 mm, and that target failure occurred near the edge of the hot face. Von Mises stresses and deflections in the target resulting from the 7.85 kW heat load are pictured in Figure 3-63a. Analytic and numerical values of temperatures and stresses are presented

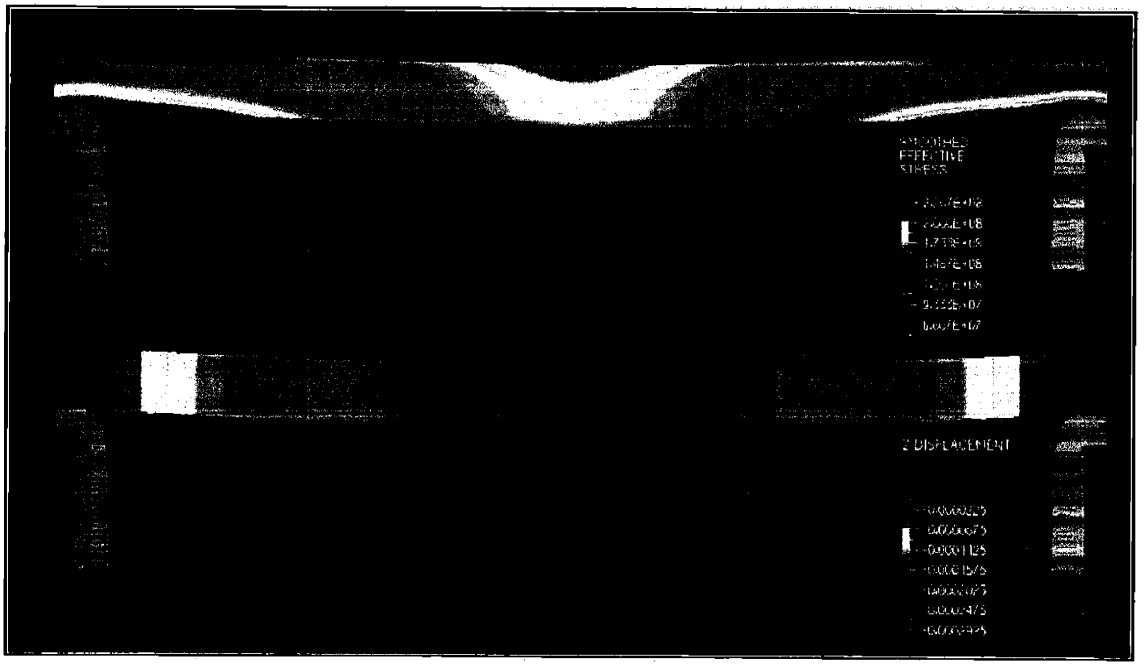

a)

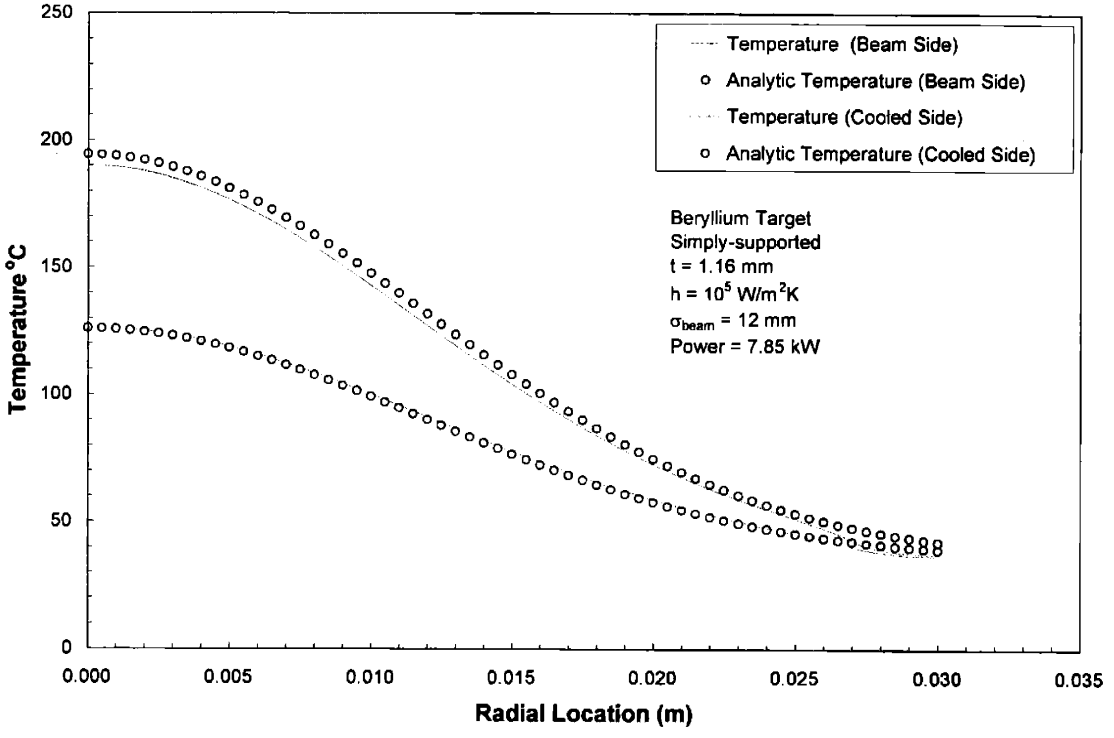
Temperature (Beam Side)
Analytic Temperature (Beam Side)
Temperature (Cooled Side)
Analytic Temperature (Cooled Side)
Beryllium Target
Simply-supported
t = 1.16 mm
h = 10^5 W/m^2K
σbeam = 12 mm
Power = 7.85 kW
Temperature °C
Radial Location (m)
250
200
150
100
50
0
0.000
0.005
0.010
0.015
0.020
0.025
0.030
0.035

b)

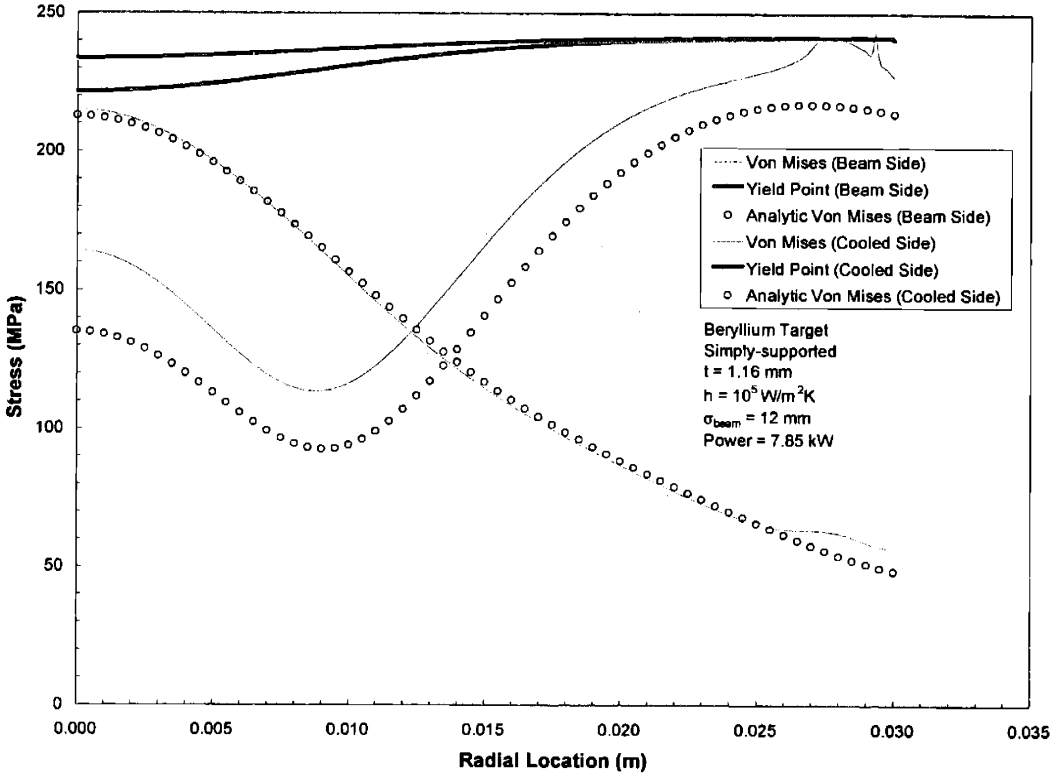

c)

Figure 3-63. a) Von Mises stress and deflection of a 1.16 mm beryllium target subjected to a 7.85 kW beam with a standard deviation of 12 mm. The target is cooled by a gallium jet at 35°C which generates a heat transfer coefficient of 10^5 W/m^{2}K. The ratio of thickness to radius is not to scale. Axial dimensions have been stretched by a factor of 3 in order to better illustrate the results. Numerical and analytic results of the b) temperature and c) effective stress in a 1.16 mm thick beryllium target subjected to a 7.85 kW beam with a standard deviation of 12 mm. The target is cooled by a gallium jet at 35°C which generates a heat transfer coefficient of 10^5 W/m^{2}K.

graphically in Figures 3-63 b,c. The fact that the analytic predictions gave a maximum power of 8.83 kW was the result of underpredicting the stresses along the heated face. Underprediction of the stresses in the analytic calculations comes from the inability to account for the temperature variations in thermal conductivity, Young's Modulus, and thermal expansion as well as the non-linear strains from large deflections which were larger than 10% of the target thickness. The spike in the Von Mises stress on the hot side of the target was a numerical artifact of the contact modeling between the target and the support. The maximum stress on the heated face occurred at a radial distance of 2.76 cm.

Optimal thickness using water jets was found to be 1.82 mm. At this thickness the beryllium target was able to sustain a beam load of 5.28 kW before yielding. In order to keep the temperature along the cooled side of the target below the saturation point, a system pressure of

210 kPa was required. Analytic and numerical results for the water-cooled target are shown in Figure 3-64 a,b. Increasing the thickness for a target cooled with a lower heat transfer coefficient seems counterintuitive. This increase, however, reduces the compressive stresses on the cooled side of the target and the azimuthal stresses which are tensile at the edge of the beam side. From Figure 3-57 it is apparent that the stress reduction on the hot edge is reversed if the target is made too thick. Greater radial conduction is also a result of increased thickness. A comparison of Figures 3-63b and 3-64a indicate that the temperatures at failure in both the gallium and water case are nearly identical. They differ by a maximum of 11.5 degrees on the beam side and 12 degrees on the cooled side.

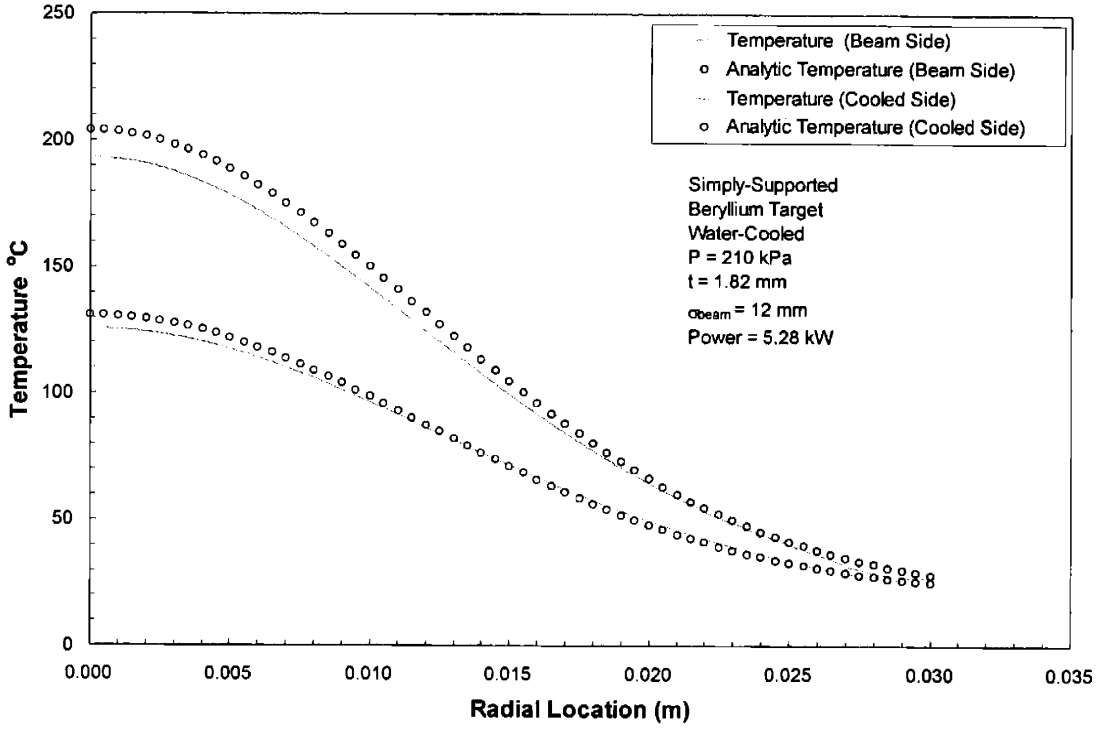

a)

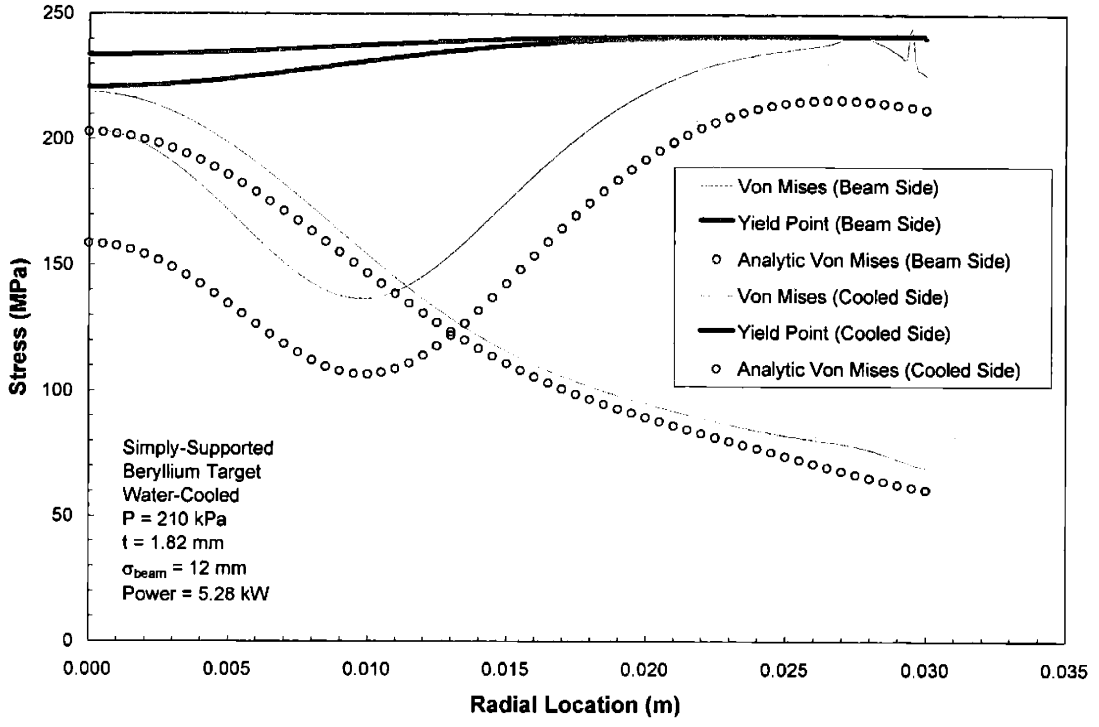

b)

Figure 3-64. Numerical and analytic results of the a)temperature and b)effective stress in a 1.82 mm thick beryllium target subjected to a 5.28 kW beam with a standard deviation of 12 mm. The target is cooled by a water jet at 20 °C which generates a heat transfer coefficient of 55000W/m^{2}K. A system pressure of 210 kPa was required to ensure that the temperature along the cooled surface was below T_{sat}.

In the case of a uniform beam, a maximum power of 9.74 kW was achieved on a 1.43 mm thick target using gallium, and 7.83 kW was achieved on a 1.82 mm target using water. The 24 and 48% increase in maximum over the distributed beam cases are somewhat surprising since the thermal stresses predicted by Equation 3.40 for a simply-supported target go to zero. The reason for the marginal increase is that significant stresses still exist at the target edges since the beam cannot extend over the entire target. Mounting the target on a beamline prohibits a small amount of the target periphery from seeing the beam and generates large tensile azimuthal stresses. Compounding this fact is that the azimuthal component of mechanical stress is also tensile at the target edge. Stresses resulting from a uniform beam and gallium jet cooling are shown in Figure 3-65.

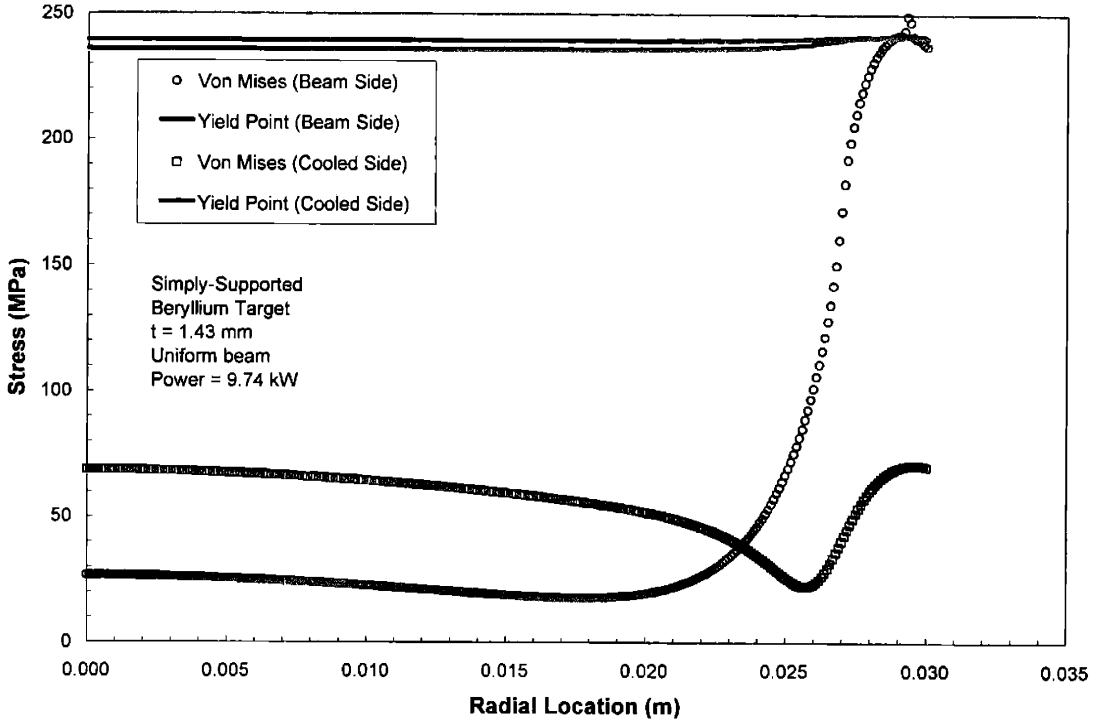

Figure 3-65. Stresses resulting from a uniform 9.74 kW beam on a 1.43 mm thick beryllium target cooled by a gallium jet ($h=10^5$ W/m^{2}K) at 35 °C.

In contrast to the distributed case, no increased system pressure was required with water when the uniform beam was tested. A 0.10135 MPa system pressure combined with the dynamic pressure from the jet were enough to keep the saturation temperature above the wall temperature at all locations along the cooled face up to the point at which yielding occurred.

3.4.3.2 Beryllium on a Substrate

A 110 μm thick beryllium window which is 6 cm in diameter is not sufficient to support a 0.10135 MPa pressure differential. Placing a thin layer of beryllium on a strong yet thermally conductive substrate, such as the copper alloys (C15715, C18200) mentioned in §3.2, has several advantages. One obvious advantage is that these copper alloys have a thermal conductivity which is ~30% higher than beryllium. A second and more subtle benefit is that their coefficients of thermal expansion (16-19 E-06 K^{-1}) are higher than that of beryllium (10-15 E-06 K^{-1}) as are their yield strengths at elevated temperature (300-500 MPa). Because the copper will expand to a greater degree than the beryllium when subjected to a heat load, tensile stresses in the beryllium generated from the unequal expansion helps to offset the thermal stresses which are generally compressive. The high yield stress of the copper alloys makes it almost certain that failure will

occur in the beryllium long before failure in the substrate. C15715 was used to investigate the performance of a beryllium target/copper substrate combination.

The first set of iterations for optimizing target thickness was conducted by fixing the beryllium thickness at 110 μm and varying the substrate thickness. For a 1.59 mm substrate using an h of 10^5 W/m^{2}K at 35 °C, the maximum power achieved for a distributed beam (σ_{beam} = 12 mm) was 8.46 kW. Figure 3-66, which plots the Von Mises stresses in the target at the onset of yielding, illustrates that failure does, in fact, occur in the beryllium. Stresses in the copper substrate remained much lower than the yield stress at all power levels. At the location of the hottest temperature in the center of the target the yield stress of the copper substrate is 348 MPa.

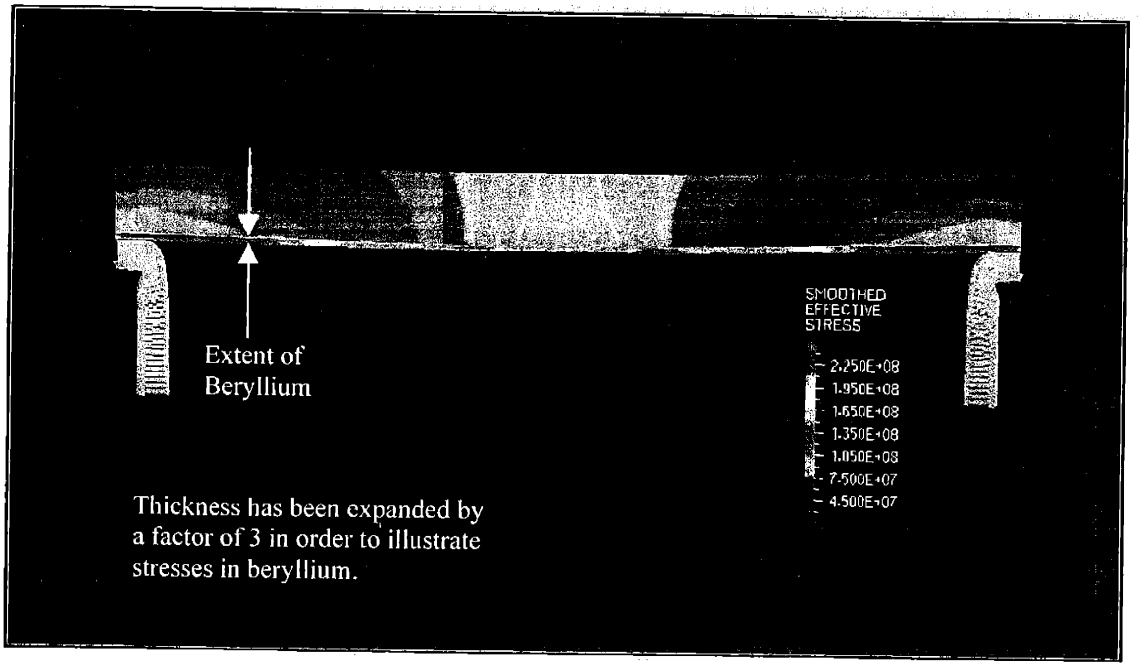

Figure 3-66. Von Mises stress (Pa) in the beryllium target/copper substrate target at a power of 8.46 kW. This target had a beryllium thickness of 110 μm and a substrate thickness of 1.59 mm.

At the edge of the target tensile stresses were generated by three different sources:

(1) thermal stresses at the point where the beam is terminated by the support

(2) mechanical stresses from the pressure loading

(3) stresses created by increased thermal expansion of the overlying copper substrate

With the beryllium layer fixed at 110 μm, there is insufficient material at the edges to withstand the combined stresses which are all tensile at this point. As a result, the stresses at the edge and center of the hot side are not properly matched and the resulting power limit is lower than could be achieved by varying the beryllium thickness. This is illustrated in Figure 3-67.

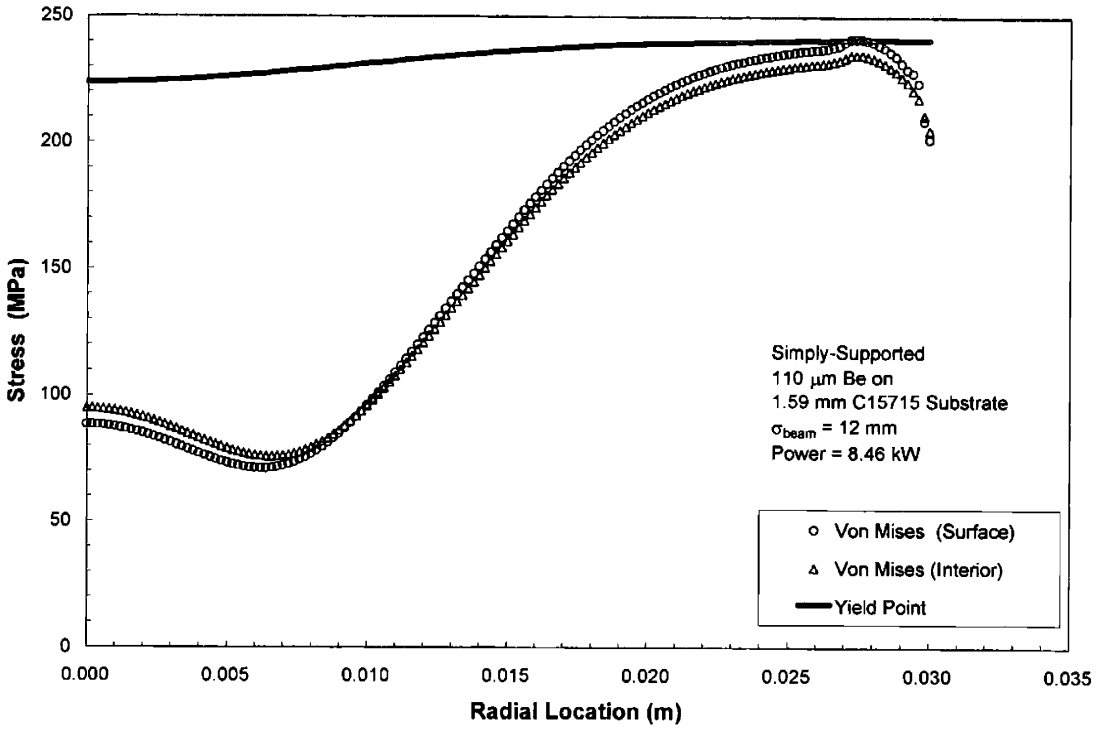

Figure 3-67. Von Mises stress and yield point for a 110 μm thick beryllium target on a 1.59 mm copper substrate. The trace labeled "surface" was taken along the hot surface, while "interior" plot was taken at a depth of 55 μm from the hot surface. Because of the axial dependence of heat deposition, maximum stresses at the center of the target do not occur on the heated face in this case.

By varying both the beryllium and substrate thickness, stresses at the center and edge of the target could be properly matched. A beryllium thickness of 500 μm combined with a substrate thickness of 750 μm increased the maximum power by 12.3 % from 8.46 kW to 9.3 kW. Figure 3-68 illustrates the properly matched stresses at the center and edge of the target resulting from the increase in beryllium thickness. As noted in the figure, interior and surface traces are included because the maximum stresses at the center occur at a small depth into the target. In the case of the 500 μm beryllium target the maximum stresses at the center occurred at 125 μm into the target. When water was used as the cooling fluid, a maximum power of 6.12 kW was achieved with a beryllium thickness of 750 μm and a substrate thickness of 1.25 mm. A system pressure of 300 kPa was required. Unlike the all-beryllium case, the optimal target thickness for the distributed beam also applied for the uniform beam. The 500 μm thick beryllium target achieved a maximum power of 11.7 kW when cooled with gallium. The 750 μm thick target achieved a power of 9.8 kW with water with a system pressure of 0.10135 MPa, which was sufficient to ensure that the target/coolant interface did not exceed T_{sat}.

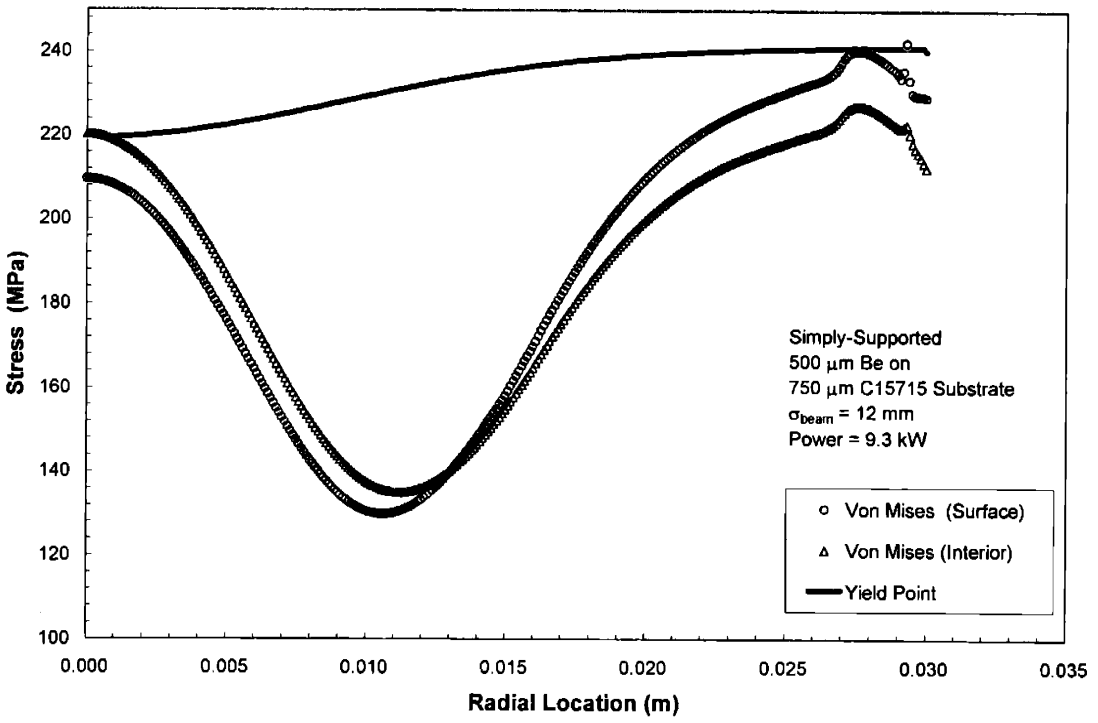

Figure 3-68. Von Mises stress and yield point for a 500 μm thick beryllium target on a 0.75 mm copper substrate at a power of 9.3 kW. Because of the axial dependence of heat deposition maximum stresses at the center of the target do not occur on the heated face in this case. The "interior" trace was taken at a depth of 125 μm into the target.

3.4.3.3 Lithium Targets

Lithium is poorly suited to act as a target material because of its poor mechanical strength, low thermal conductivity, and explosive reactivity with moisture. §3.2 has already shown, however, that lithium can be a viable target material when used in conjunction with a strong, thermally conductive substrate. Copper alloys such as C15715 and C18200 both have high thermal conductivity (>345 W/mK) and high yield stress (>375 MPa) at the lithium melting point. Over the range of 0-180.5 °C, C15715 has a slightly higher thermal conductivity than C18200. For the (p,n) reaction at 2.5 MeV, no more than 85 μm of lithium is needed. Beyond 85 μm the charged-particle energy falls below the reaction threshold resulting in heat deposition without neutron production. Figure 3-16 illustrated that beam powers of several kilowatts could be placed on a lithium target if the substrate were kept between 1-2 mm. This figure also illustrated that maximum power levels increased with decreasing substrate thickness up to the point at which critical heat flux became the limiting factor. With gallium as a coolant, however, critical heat flux is no longer a concern and it is possible to make targets as thin as possible while still maintaining structural integrity.

The fact that lithium has such a low melting point (180.5 °C) greatly simplifies the optimization process. Using the Equations presented in §3.4.1, stresses were calculated for a solid copper plate having a radius of 3 cm and a thickness of 1 mm when subjected to beams of varying sizes. A heat transfer coefficient of 10^5 W/m^{2}K at a bulk temperature of 35 °C was applied. The purpose of the study was to show that even under conditions which raised the hot side of the copper up to the melting point of lithium, effective stresses were well below the yield point. Allowing the copper surface to reach 180.5 °C is actually a conservative estimate since a deposited lithium layer would have melted before this point. Figure 3-69 plots the maximum Von Mises stress for both fixed and simply-supported C15715 targets subjected to beams of varying size and power. This figure illustrates that regardless of beam size, the lithium melting point rather than yielding of the copper substrate is the likely limiting factor for lithium-based targets.

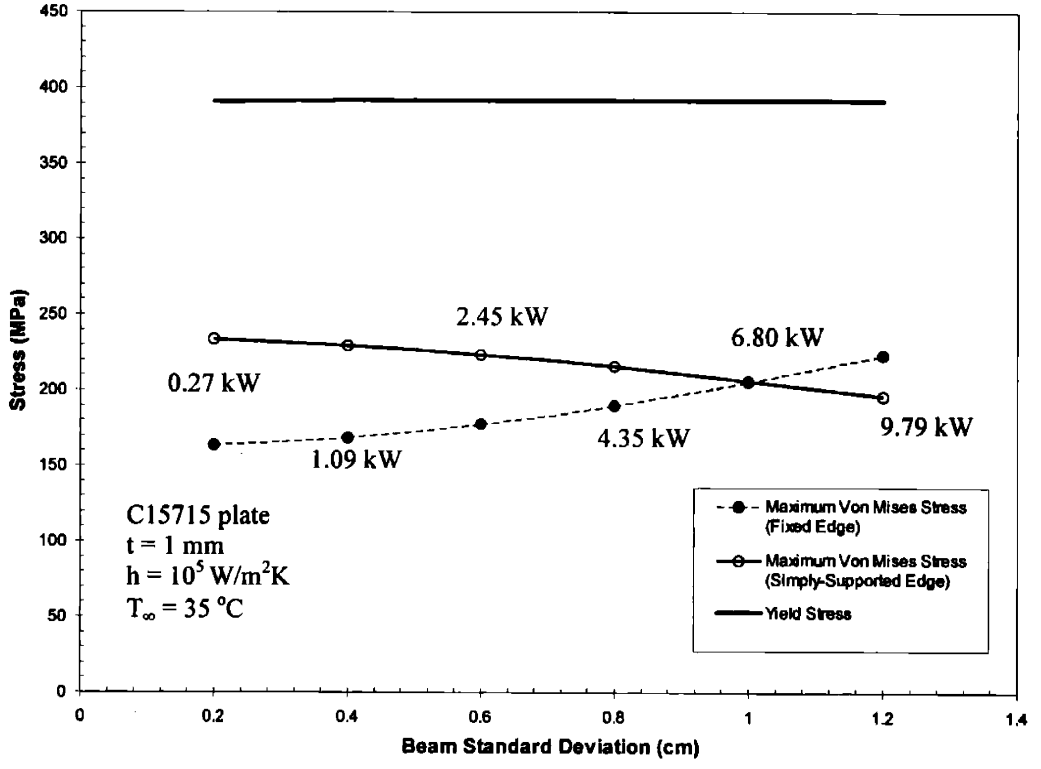

Figure 3-69. Maximum Von Mises stress in a 1 mm thick C15715 copper plate having a 3 cm radius when subjected to beams of various sizes. For a given beam standard deviation power was increased until the front surface of the copper reached the melting point of lithium. Stresses were calculated at the power level indicated.

Numerical simulations for a beam having a standard deviation of 12 mm, which included the 85 μm lithium layer, confirmed that the melting of lithium rather than the resulting stresses would limit the power. With gallium cooling, a target composed of 85 μm lithium on a 0.865 mm

substrate achieved a maximum power of 10 kW before the lithium melting point was reached. Maximum stresses occurred along the cooled edge of the target. Stresses and deflections are plotted in Figures 3-70 a,b.

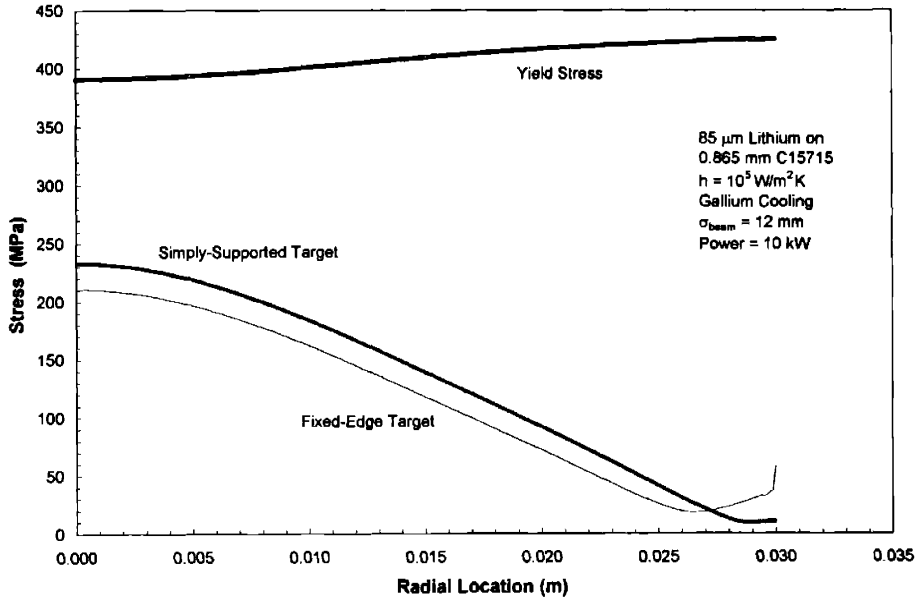

a)

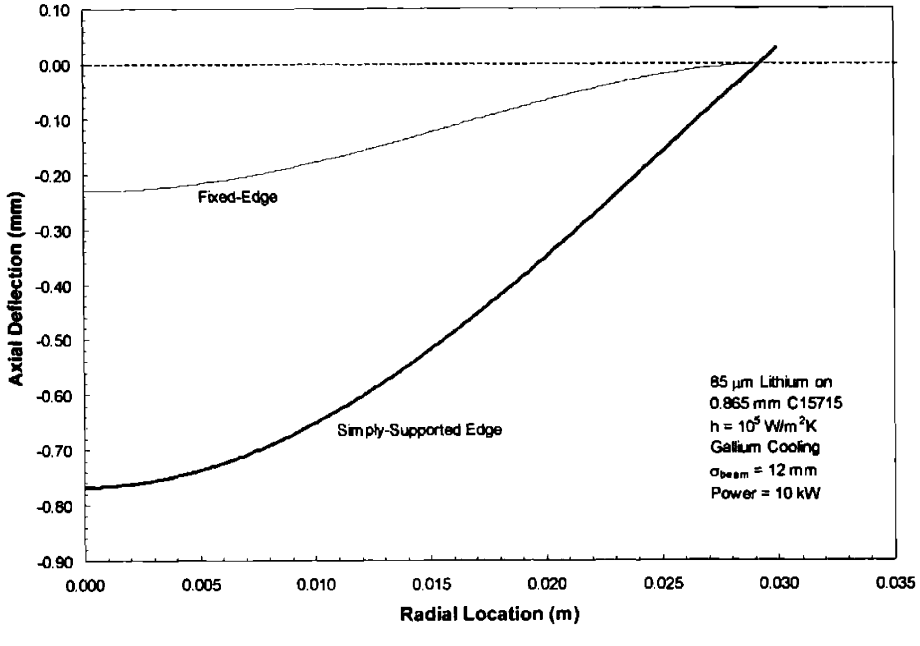

b)

Figure 3-70a) Von Mises and yield stress and b) axial deflection for a fixed-edge and simply-supported target composed of 85 μm lithium on a 0.865 mm thick C15715 copper substrate. The target is subjected to a beam power of 10 kW.

At such small substrate thicknesses, deflections in both the fixed-edge and simply-supported targets are already large. At 0.865 mm the simply-supported target experiences a deflection which is 84 % of the target thickness. Reducing the thickness of the substrate below 0.865 mm sharply increases the deflection but results in only marginal increases in maximum beam power. A substrate thickness of 0.765 mm increases the maximum power to 10.2 kW, but increases the deflection to 37% and 101% of the target thickness for fixed and simply-supported conditions, respectively. At a substrate thickness of 0.665 mm, the power limit is 10.4 kW with deflections of 60% and 195% of the target thickness.

Water cooling achieved a maximum power of 6.8 kW with a substrate thickness of 1.17 mm and a system pressure of 500 kPa. Tests using a uniformly distributed beam provided a marked increase over the σ_{beam} =12 mm case. With gallium cooling on the 0.865 mm substrate, 23.2 kW could be achieved on both fixed-edge and simply supported targets. A beam power of 17 kW was achieved using the water cooling on the 1.17 mm target with a system pressure of 500 kPa.

3.4.3.4 Hemispherical Beryllium Targets

From the results of the all beryllium and combined beryllium/copper targets it is apparent that achieving 10 kW total power is difficult even with thin targets cooled by heat transfer coefficients of 10^5 W/m^2K. For the distributed beam case (σ_{beam}=12 mm) the maximum power which could be placed on a beryllium/copper target was 9.3 kW. The ability for these targets to handle high heat loads is hindered because on one hand, they must be kept thin to minimize compressive stresses along the hot face, but they also must be thick enough to withstand the compressive stresses at the center of the cooled face and tensile stresses at the periphery. In addition to the fact that targets must be kept thin, diameters of the targets must be kept relatively large to allow for sufficient defocusing of the beam. Targets having large aspect ratios are particularly susceptible to the bending moments caused by the mechanical and thermal loading. For circular plates, bending moments generate stresses which increase linearly with axial distance away from the mid-plane with maximum resulting stresses located at the target surface. Targets are better capable of withstanding in-plane stresses which are distributed over the entire cross-sectional area. For this reason it is advantageous to adjust the design of the target so that the primary stresses in the target are in-plane stresses.

The vast majority of accelerator NCT targets which are in use presently, including those used and tested at LABA, have been conventional cylindrical disks. A thin hemispherical target possesses a number of advantages over a simple circular disk. By orienting the target so that its curvature points inward toward the vacuum, the pressure from the cooling system places the

majority of the structure in tension. In essence, the target acts like the hemispherical cap of a pressure vessel when placed on the end of the beam line. Prefabricated beryllium targets, similar to the one illustrated in Figure 3-71, are available from companies such as Brush-Wellman[72] and K-TEK International.[73]

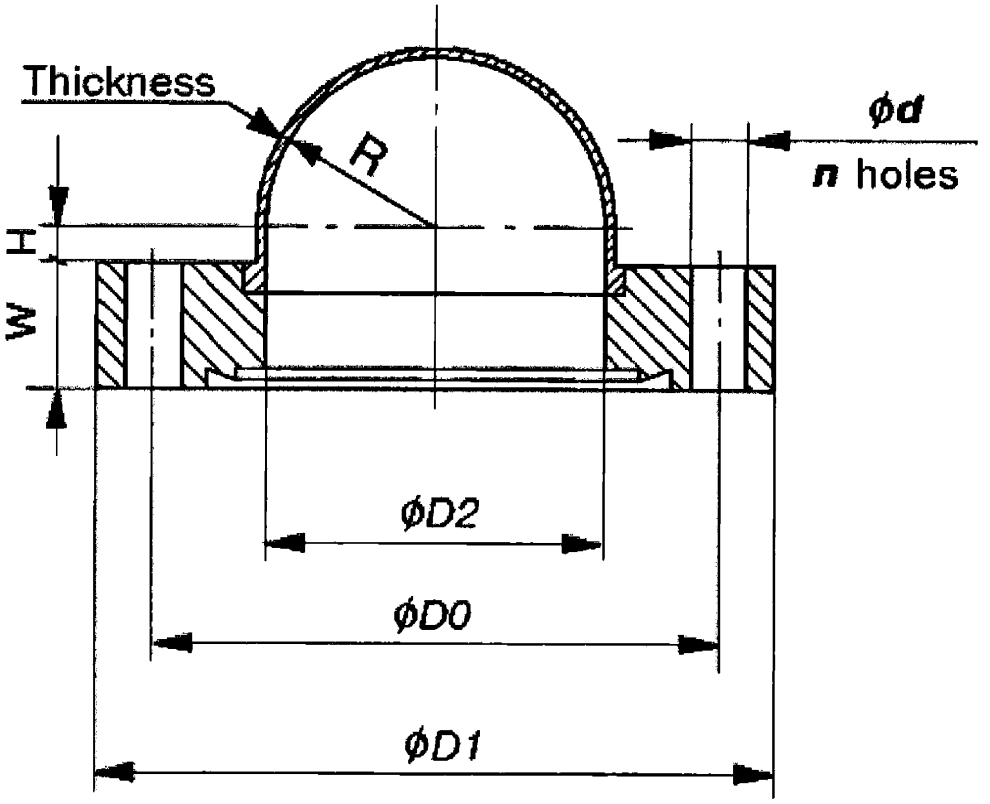

Beryllium Window				Stainless Steel Flange				
Thickness	R	D2	Flange Index	D1	D0	W	d	n
0.4	8	16	DN16CF34mm	34	27	8	4.4	6
0.4	17.5	35	DN35CF70mm	70	58.7	13	6.6	6
0.4	30	60	DN63CF114mm	114	92.1	18	8.4	8
0.4	50	100	DN100CF152mm	152	130.2	21	8.4	16
0.6	75	150	DN160CF203mm	202	181	22	8.4	20
0.6	100	200	DN200CF254mm	253	231.8	25	8.4	24

All dimensions in millimeters

Figure 3-71. Schematic of prefabricated hemispherical beryllium target available from K-TEK International of Portland, OR. Illustration and data come from website: www.ktekintl.com[73]

For spherical shells it is conventional to express stresses as $\sigma_{\theta\theta}$ (meridional) or $\sigma_{\phi\phi}$ (azimuthal or hoop). There are also radial stresses σ_{rr} although these are usually negligible in shells which have a very small thickness. Under a pressure load, the meridional and hoop stresses are equal and can be expressed as

$$\sigma_{\theta\theta} = \sigma_{\phi\phi} = P\,R / 2t \tag{3.47}$$

where,

P: Pressure (Pa)

R: radius from the center to the midpoint of the shell (m)

t: thickness of the shell (m)

To illustrate the reduction in stress resulting from using spherical shape Equations 3.39 and 3.47 can be used to compare the stresses for similar dimensions. A fixed-edge beryllium plate having a radius of 0.03 m and a thickness of 400 μm under a pressure load of 10^5 Pa would experience a maximum stress of 227.8 MPa at its center. A spherical beryllium shell of the same thickness and radius under the same pressure load would experience a stress of only 7.55 MPa.

The simply-supported hemispherical beryllium target model, which is pictured in Figure 3-72, was used to determine the power limits of a 400 μm-thick hemispherical beryllium target having a radius of 2.6 cm. This radius was selected so that the entire structure, including the edges used to mount the target on a beamline would have a diameter of 6 cm. A uniform heat transfer coefficient of 10^5 W/m^{2}K at a bulk temperature of 35 °C was imposed on the cooled side of the target. Implicit in these simulations was the assumption that cooling jets could be oriented to impinge normally on the target in order to form an array which covered the entire surface. For a beam with a standard deviation of 12 mm, a maximum power of 20.2 kW was achieved. This is nearly 2.6 times higher than the 7.85 kW achieved using a simply-supported beryllium disk. Figures 3-73 a,b plot the stresses and temperatures in the target resulting from a power of 20 kW. With this heat load the temperature at the center of the cooled side was 285 °C and remained in excess of 200 °C out to a y-coordinate of 0.01 m. The necessity for using gallium in this case is apparent considering the pressure required for T_{sat}=200 °C with water is 1.55 MPa (15.3 atm) and for T_{sat}=285 °C is 6.91 MPa (68.2 atm).

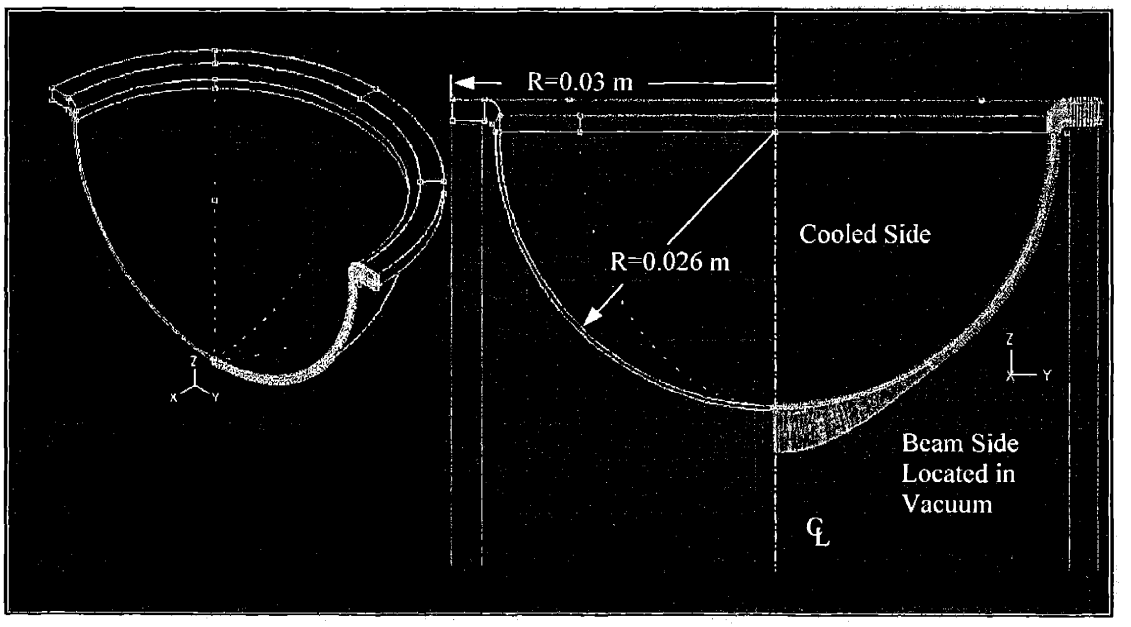

Figure 3-72. Schematic of the spherical target as it might exist mounted on the end of a beamline. This illustration shows the axisymmetric model used to calculate the stresses resulting from the thermal and mechanical loads. The blue region indicates the portion of the spherical shell used in the simulation, while a heat load resulting from a beam having a standard deviation of 7.2 mm is shown in pink.

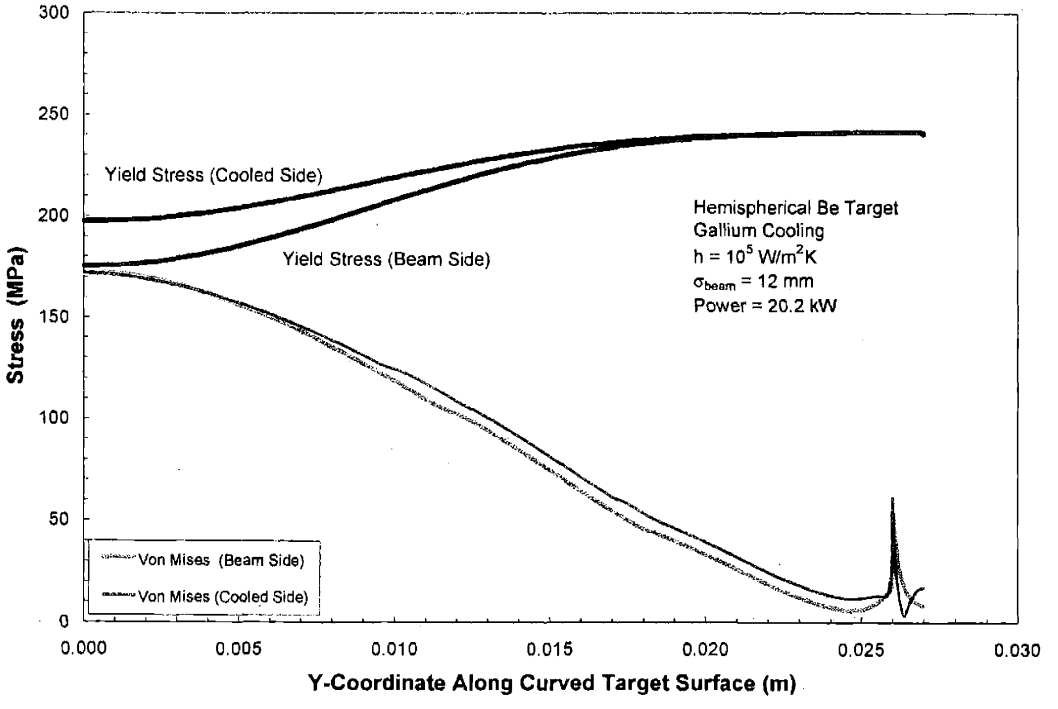

a)

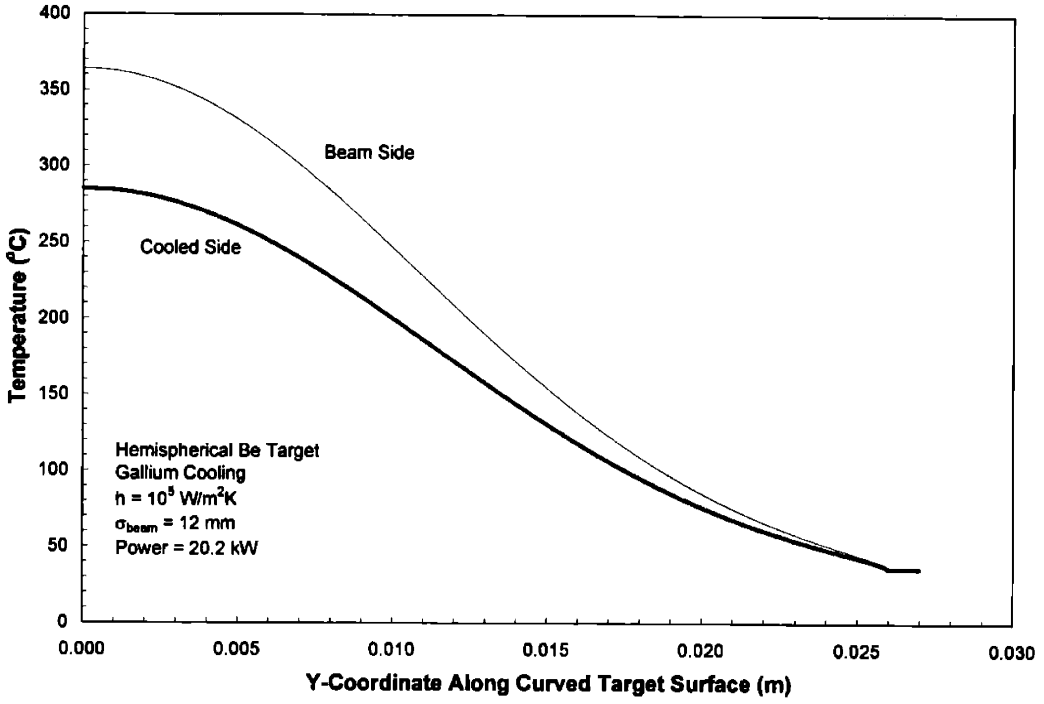

b)

Figure 3-73. (a) Von Mises stresses and (b) temperatures resulting from a 20 kW beam having a standard deviation of 12 mm striking a hemispherical beryllium target. A heat transfer coefficient of 10^5 W/m^{2}K at a bulk temperature of 35 °C was used on the cooled side. The abscissa plots the y-coordinate along the cooled and beam sides of the spherical shell, with y=0 corresponding to the target centerline. For y-values greater than 0.026 (cooled side) and 0.0264 (beam side) the coordinate applies to the fillets used to transition from the hemispherical shell to the edge supports. These fillets are visible in Figure 4-72.

For other beams having smaller standard deviations, the hemispherical target improved the maximum power by a factor of ≈3. At σ_{beam}= 6 mm the hemispherical target cooled with gallium (h= 10^5 W/m^{2}K) achieved a power of 6.95 kW compared to 2.3 kW with a circular beryllium disk. At σ_{beam}= 7.2 mm, the hemispherical target achieved a maximum power of 10.1 kW versus only 3.4 kW with the circular target. For all cases studied covering all types of beryllium-based targets, the 7.2 mm standard deviation was the smallest for which a power of over 10 kW was possible.

3.5 Conclusions

A great deal of information has been presented in this chapter regarding the thermal and mechanical constraints involved in designing a high-power target for use in neutron capture therapy. By examining the axial deposition of heat combined with the concomitant production of neutrons, it was illustrated that under most conditions, the thickness of the neutron producing layer should be just enough so that the energy of the charged-particle falls below the reaction threshold upon exiting the layer. For the 4.0 MeV ^{9}Be(p,n) reaction this thickness is 110 μm. The appropriate thickness for the 2.5 MeV ^{7}Li (p,n) reaction is 85 μm. Initial small-scale tests using single jets of liquid metal and water indicated that stagnation point heat transfer with gallium was superior to water at reduced flowrates. A gallium jet (d= 3.91 mm) at a velocity of 0.64 m/s generated a stagnation point heat transfer coefficient of 37544±2784 W/m^{2}K compared to an h_o of 32448±3645 W/m^{2}K from a water jet at 2.43 m/s. Numerical simulations using the K-ε RNG model confirmed that the heat transfer from the gallium jet was superior. These simulations illustrated that gallium jets are subject to a wetting effect which reduce the overall heat transfer. Simulations also indicated that the heat transfer from gallium could fall below that of water at large r/d values. In order to overcome the reduction in heat transfer at large r/d distances, which is typical for single submerged jets, experiments were carried out using a jet-array. These experiments found that the average heat transfer from gallium over areas typical of accelerator targets was superior to water for Reynolds numbers greater than 13500. At a Reynolds number of 35000 gallium produced an average heat transfer coefficient of $\approx 10^5$ W/m^{2}K while water produced an $\bar{h}$ of 55000 W/m^{2}K. Nusselt number correlations were presented for both water and gallium jet arrays. An attempt was made to use theoretical predictions for the spreading of liquid metal on a surface to quantify the wetting effect. A quantity known as the spreading ration, β_{max}, was introduced as an additional parameter in the gallium Nusselt number correlations. Finally, thermal and mechanical stresses were examined both analytically and numerically in order to develop a procedure whereby target dimensions could be optimized to allow the maximum amount of power to be placed on a target for a given set of conditions. In the case of beryllium-based targets, optimizing a target generally involves the balancing of stresses on the hot and cold faces so that both sides reach the failure point at similar powers. Hemispherical targets were shown to permit the largest amounts of total power for any of the beryllium-based targets. Under similar conditions, hemispherical targets having a thickness of only 400 μm achieved powers which were nearly 3 times greater than cylindrical targets. The optimization of lithium-based targets was simplified because of the low melting point of target material. Maintaining the temperature of the lithium below the melting point rather than balancing stresses in the target is the primary design criterion. Substrates which are excessively thin result in unnecessarily large stresses with only small increases in maximum power.

3.6 References

1. W. B. Howard, J. C. Yanch, S. M. Grimes, T. N. Massey, S. I. Al-Quaraishi, D. K. Jacobs and C. E. Brient, "Measurement of the ^{9}Be(p,n) thick target spectrum for use in accelerator-based boron neutron capture therapy," Nucl. Sci. Tech., submitted (1998).

2. W.B. Howard, J.C. Yanch, S.M. Grimes, T.N. Massey, A.I. Al-Quaraishi, D.K. Jacobs and C.E. Brent, "Measurement of the ^{9}Be(p,n) thick target spectrum for use in accelerator-based BNCT," Med Phys, **23:** 1233-1235 (1996).

3. N. Colonna, L. Beaulieu, L Phair, G.J. Wozniak, L.G. Moretto, W.T. Chu and B.A. Ludewigt, "Measurements of low-energy (d,n) reactions for BNCT," Med Phys, **26:** 793-798 (1999).

4. S M White, "Beam Characterization for Accelerator-Based Boron Neutron Capture Therapy using the 9Be(d,n) Nuclear Reaction," M.S. thesis, Massachusetts Institute of Technology, 1998.

5. J.F. Ziegler and J.P. Biersack, "Stopping and Range of Ions in Matter," Yorktown, NY, (2000) Computer Code.

6. J.H. Gibbons and R.L. Macklin, "Total neutron yields from light elements under proton and alpha bombardment.," Journal of Physical Review, **114:** 571-580 (1959).

7. V.A. Vukolov, E.A. Koltypin, Y.D. Molchanov and G.B. Yankov, "Energy spectra for neutrons in 6Li(d,n)3He and 9Be(d,n)10B reactions at deuteron energy up to 2 MeV," Yadernaya Fizika (Russia), **58:** 1539 (1995).

8. E. Koltay, "Investigation on the excitation function of the nuclear reaction 9Be(d,n)10B by artificially accelerated particles in the 0.5-1.6 MeV energy range.," Acta Physica Hungarica, **16:** (1963).

9. K.K. Sekharan, H. Laumer, B.D. Kern and F. Gabbard, "A neutron detector for measurement of total neutron production cross sections.," Nuclear Instruments and Methods, **133:** 253-257 (1976).

10. H. Liskien and A. Paulsen, "Neutron production cross sections and energies for the reaction ^{7}Li(p,n)^{7}Be and ^{7}Li(p,n)^{7}Be*," Atomic Data and Nuclear Data Tables, **15:** 57-84 (1975).

11. J.H. Lienhard and D.S. Napolitano, "Yield limits of plates at extremely high heat flux.," Journal of Heat Transfer, **120:** 253-258 (1998).

12. N. Zuber, "On the stability of boiling heat transfer," Trans. ASME, **80:** 711 (1958).

13. D.P. Gierga, "Neutron delivery for boron neutron capture synovectomy," Ph.D., Massachusetts Institute of Technology, 2001.

14. S. M. White, "Biological Dosimetry of Neutron Beams for Neutron Capture Therapies," Ph.D., Massachusetts Institute of Technology, 2001.

15. JAHM Software, "Material Properties Database," (1999) Computer Code

16. J.H. Keenan, F.G. Keyes, P.G. Hill and J.G. Moore, *Steam Tables*New York: Wiley, 1969.

17. H. Sun, C.F. Ma and W. Nakayama, "Local characteristics of convective heat transfer from simulated microelectronic chips to impinging submerged round water jets," Jounal of Electronic Packaging, **115:** 71-77 (1993).

18. J.W. Gauntner, J.N.B. Livingood and P. Hrycak, "Survey of literature of flow characteristics of a single trubulent jet impinging on a flat plate," NASA TN D-5652, 1969.

19. X.J. Liu, J.H. Lienhard and J.S. Lombara, "Convective heat transfer by impingement of circular liquid jets," Journal of Heat Transfer, **113:** 571 (1991).

20. J.H. Lienhard, R.S. Dahbura, H.F. Younis and C.H. OH, "Large area jet-array cooling modules for high heat fluxes," High Heat Flux Engineering III, **SPIE 2855:** 66-81 (1996).

21. J.H. Lienhard, H.F. Younis, R.S. Dahbura and D. Michels, "Liquid jet-array cooling modules for high heat fluxes.," AIChe, **44, No.4:** 769-779 (1998).

22. S.V. Garimella and R.A. Rice, "Confined and submerged liquid jet impingement heat transfer.," Journal of Heat Transfer, **117:** 871-877 (1995).

23. S.V. Garimella and B. Nenaydykh, "Nozzle-geometry effects in liquid jet impingement heat transfer," International Journal of Heat /Mass Transfer, **39:** 2915-2933 (1996).

24. K. Garrett and B.W. Webb, "The effect of drainage configuration on heat transfer under an impinging liquid jet," Journal of Heat Transfer, **121:** 803-810 (1999).

25. L.A. Gabour and J.H. Lienhard, "Wall roughness effects on stagnation-point heat transfer beneath impinging liquid jets," Journal of Heat Transfer, **116:** 81-87 (1994).

26. Y. Pan and B.W. Webb, "Heat transfer characteristics of arrays of free-surface liquid jets," Journal of Heat Transfer, **117:** 878-883 (1995).

27. R.A. Seban, "Heat transfer to a fluid flowing turbulently between parallel walls and asymmetric wall temperatures.," Trans. ASME, **72:** 789 (1950).

28. R.N. Lyon, "Liquid metal heat transfer coefficients," Chem. Eng. Prog., **47:** 75-79 (1951).

29. R.N. Lyon, *Liquid Metals Handbook*, 2nd ed. Washington, D.C.: Atomic Energy Commision, 1952.

30. V. Y. Prokhorenko, V.V. Roshchupkin, M.A. Pokrasin, S.V. Prokhorenko and V.V. Kotov, "Liquid gallium: potential uses as a heat-transfer agent," High Temperature, **38:** 954-968 (2000).

31. K. Sato, A. Furutani, M. Saito, M. Isozaki, K. Suganuma and S. Imahori, "Melting attack of solid plates by a high-temperature liquid jet [II]- Erosion behavior by a molten metal jet.," Nuclear Enginerring and Design, **132:** 171-186 (1991).

32. J.A. Green, T.N. Dinh and B.R. Sehgal, "Molten metal jet impingement: Insights from experiments and analysis," in *5th International Conference on Nuclear Engineering*, Nice, France, ICONE 5, pp. 1-8,1996.

33. J.H. Lienhard, *Annual Review of Heat Transfer*, Vol. 6, edited by C.L. Tien et al (Begell House Inc. ,New York, (1995) .

34. Xin Liu, "Liquid Jet Impingement Heat Transfer and its Potential Applications at Extremely High Heat Fluxes," Ph.D. Thesis, Massachusetts Institute of Technology, 1992.

35. Omega Engineering, "Pressure, Flow and Level, pH and Conductivity Catalog," 1999.

36. P.A. Durbin and B.A. Pettersson Reif, *Statistical Theory and Modeling for Turbulent Flows*, West Sussex, England: John Wiley & Sons LTD., 2001.

37. V. Yakhot and S.A. Orszag, "Renormalization group analysis of turbulence," Journal of Scientific Computing, **1:** 3-51 (1986).

38. C.J. Freitas, "Perspective: Selected benchmarks from commercial CFD codes," Journal of Fluid Engineering, **117:** 209 (1995).

39. S.S. Thakre and J.B. Joshi, "CFD Modeling of heat transfer in turbulent pipe flows," AIChE Journal, **46:** 1798-1812 (2000).

40. B. Weigand, J.R. Ferguson and M.E. Crawford, "An extended Kays and Crawford turbulent Prandtl number model," International Journal of Heat and Mass Transfer, **40:** 4191-4196 (1996).

41. Xiaodong Wang, "Analytical and computational approaches for some fluid-structure interaction analyses.," Computers and Structures, **72:** 423-433 (1999).

42. T.S. Park and H.J. Sung, "Development of a near-wall turbulence model and application to jet impingement heat transfer," International Journal of Heat and Fluid Flow, **22:** 10-18 (2001).

43. P.A. Durbin, "On the k-epsilon stagnation point anomaly," International Journal of Heat and Fluid FLow, **17:** 89-90 (1996).

44. C.H. Oh, J.H. Lienhard, H.F. Younis, R.S. Dahbura and D. Michels, "Liquid jet-array cooling modules for high heat fluxes," AIChE Journal, **44:** 769-779 (1998).

45. J. Lee and S.J. Lee, "Turbulent heat transfer characteristics in a stagnation region of axi-symmetric jet impingement," in *Heat Transfer 1998 Proceedings of 11th IHTC*, Kyongju, Korea5, pp. 433-438,1998.

46. J.D. Bernardin, I. Mundawar, C.B. Walsh and E.I. Franses, "Contact andlge temperature dependence for water droplets on practical aluminum surfaces," International Journal of Heat and Mass Transfer, **40:** (1996).

47. J.V. Naidich and J.N. Chuvashov, "Wettability and contact interaction of gallium-containing melts with non-metallic solids," Jounal of Materials Science, **18:** 2071-2080 (1983).

48. M. Hida, A. Sakakibara and H. Kamiyabu, "Surface tension and supercooling phenomenon of liquid gallium.," Journal of Japan Institute of Metals, **53:** 1263-1267 (1989).

49. A.V. Ivanov, T.S. Ivanova, L.I Kostenetskaya, Y.I. Smirnov and M.M. Churakov, "Wetting and infiltration of porous tungsten and molybdenum by liquid gallium.," Test Methods and Properties of Powder Metallurgical Materials, **6:** 471-472 (1983).

50. Carborundum, "Material Properties of SA Silicon Carbide," 2000.

51. D.E. Wolfe and J. Singh, *Functionally graded ceramic/metallic coatings for gas turbine components by high-energy beams for high-temperature applications*, Y. Pauleau and P.B. Barna, in *Protective Coatings and Thin Films*. Kluwer Academic Publishers, Netherlands 441-465, (1997).

52. M.R. Pais, J.E. Leland, W.S. Chang and L.C. Chow, "Single-phase heat transfer characteristic of submerged jet impingement cooling using JP-5," in *Conference on Thermal Phenomena in Electronic Systems*pp. 178-183.,1994.

53. N.T. Obot and T.A. Trabold, "Impingement heat transfer within arrays of circular jets: Part I- effects of minimum, intermediate, and complete crossflow for small and large spacings," Journal of Heat Transfer, **109:** 872-879 (1987).

54. D.M. Kercher and W. Tabakoff, "Heat transfer by a square array of round air jets impinging perpendicular to a flat surface including the effect of spent air," Journal of Engineering for Power, **92:** 73-82 (1970).

55. W.M. Healy, J.G. Hartley and S.I. Abdel-Khalik, "Surface wetting effects on the spreading of liquid droplets and impacting a solid surface at low Weber numbers.," International Jounal of Heat and Mass Transfer, **44:** 235-240 (2000).

56. D. Attinger, Z. Zhao and D. Poulikakos, "An experimental study of molten microdroplet surface deposition and solidification: transient behavior and wetting angle dynamics.," Journal of Heat Transfer, **122:** 544-556 (2000).

57. S.D. Aziz and S. Chandra, "Impact, recoil and splashing of molten metal droplets," International Journal of heat and Mass Transfer, **43:** 2841-2857 (1999).

58. M. Pasandideh-Fard, R. Bhola, S. Chandra and J. Mostaghimi, "Deposition of tin droplets on a steel plate: simulations and experiments.," International Jounal of Heat and Mass Transfer, **41:** 2929-2945 (1998).

59. W.M. Healy, J.G. Hartley and S.I. Abdel-Khalik, "Comparison between theoretical models and experimental data for the spreading of liquid droplets impacting a solid surface," International Journal of Heat and Mass Transfer, **39:** (1996).

60. V. Laurent, C. Rado and N. Eustathopoulos, "Wetting kinetics and bonding of Al and Al alloys on alpha-SiC," Material Science and Engineering-A, **205:** 1-8 (1996).

61. D.R. Lide ed., *Handbook of Chemistry and Physics 73ed.*, CrC Press, Boca Raton, (1992).

62. S.Amada, M. Haruyama, T. Ohyagi and K. Tomoyasu, "Wettability effect on the flattening ratio of molten metal droplets.," Surface and Coating Technology, **138:** 211-219 (2001).

63. V.S. Kelkar and R.T. Sewell, *Fundamentals of the Analysis and Design of Shell Structures*Englewood Cliffs, N.J.: Presntice-Hall Inc., 1987.

64. D.J. Johns, *Thermal Stress Analyses*Oxford: Pergammon Press, 1965.

65. D.S. Napolitano, "Stress Induced Failure in Materials Subjected to Extremal Heat Fluxes," S.M., M.I.T., 1995.

66. J.N. Goodier, "Thermal stress and deformation.," ASME Journal of Applied Mechanics., **9:** 467-474 (1957).

67. J.R. Barber, *Intermediate Mechanics of Materials.* New York: McGraw-Hill, 2001.

68. Brush Wellman Inc., "Designing With Beryllium," MB-001, 2001.

69. A.J. Stonehouse, "Physics and chemistry of beryllium.," Journal of Vacuum Science and Technology, **3:** 1163-1170 (1986).

70. J.M. Marder, "Beryllium in stress-critical environments," Journal of Materials for Energy Systems, **8:** 17-26 (1986).

71. A.A. Macieka and R.K. Skema, "Boiling crisis burnout in the zone of interaction of a circular submerged water jet with a flat wall.," Heat Tansfer- Soviet Research, **22:** 587-594 (1989).

72. Brush Wellman Electrofusion Products, "Brush Wellman website:www.beminc,com/web/bpdweb.nsf/," 2002.

73. Inc. K-TEK International, "K-TEK International Website: www.ktekintl.com," 2002.

Chapter 4 Comparing the Neutronics of Water and Gallium-Cooled Targets

Any discussion of an accelerator target, which is intended for use in neutron capture therapy, would be incomplete without a description of how the neutronics are affected as a result of integrating a complete target assembly. This is especially true when considering a cooling fluid such as gallium which has significantly different moderating and absorption properties compared to water. For example, thermal (0.025 eV) neutrons have a macroscopic (Σ_s) incoherent scattering cross-section in H_2O of 13.9 cm^{-1} and an absorption cross-section (Σ_a) of 0.0222 cm^{-1}. Gallium, on the other hand, has an incoherent scattering cross-section of 0.00843 cm^{-1} and a macroscopic thermal neutron cross-section of 0.145 cm^{-1}.[1] Figure 4-1 plots the total (σ_T), scattering (σ_s), and radiative capture (σ_γ) microscopic cross-sections of natural gallium versus neutron energy.[2] These cross-sections, which come from the Evaluated Nuclear Data File (ENDF-VI) maintained at Brookhaven National Laboratory, are the values used in MCNP4B.

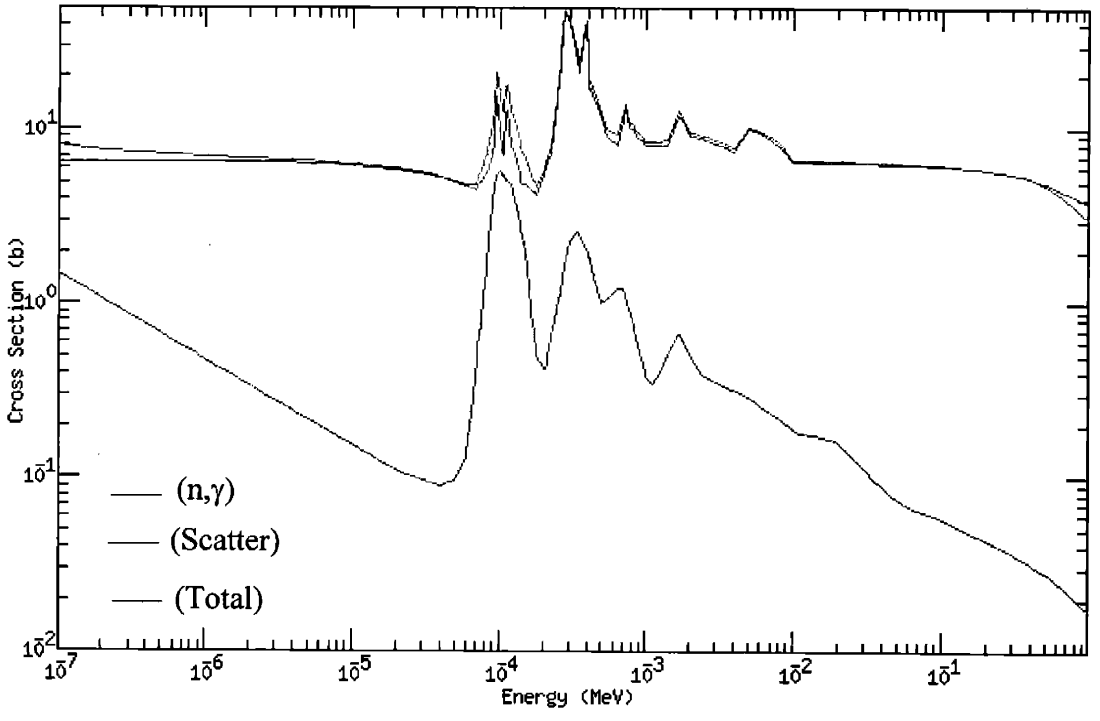

Figure 4-1. ENDF-VI microscopic cross-sections for naturally occurring gallium.[2]

The initial section of this chapter describes a jet impingement cooling system that was built to cool an all-beryllium target for use at LABA. Since 1997, this target and associated cooling system has served as the primary neutron production source for experiments including animal irradiations for the study of BNCS[3], whole-body dose studies[4], and dosimetric studies of the biological effect of accelerator beams for BNCT[5]. Not only will the description of this prototype illustrate some practical lessons which have been learned, it will also highlight some of the fundamental thermal and mechanical concerns which have been developed since the target was built.

One of the major findings of this thesis is that liquid gallium metal is an attractive alternative to water as a coolant for a high-power NCT target. While a complete neutronic optimization study is certainly beyond the scope of the present work, it is important to illustrate that initial MCNP simulations have found little or no detrimental effects which would preclude the use of gallium. To this end, six different cases will be presented (3 relating to BNCS; 3 relating to BNCT) which utilize various figures of merit to compare a cooling system based on gallium to one using water. Attention will also be given to the activation of the gallium resulting from exposure to the neutron field.

4.1 The Current Target and Cooling System In Use At LABA

Figure 4-2 illustrates the entire moderator/reflector assembly (MRA) along with the target and cooling system which has been in use at LABA. The MRA is composed of graphite in the shape of a right circular cylinder having an outer diameter of 45 cm and a length of 41 cm. A cylindrical cavity, 9 cm in diameter, is located within the graphite in order to hold the liquid D_2O moderator. By using a liquid as opposed to a solid, the adjustment of moderating length is greatly simplified. Further simplification is facilitated by enclosing the target and entire cooling system in a single assembly which is inserted through the back of the reflector. In order to prevent leaking of the moderator Delrin and plexiglass seals are located on the front and rear of the graphite. Filling of the moderator is accomplished once the cooling assembly is place through the inlet at the front of the reflector.

The entire assembly is composed of two outer stainless steel cylinders and an inner cylinder of aluminum welded into a 10 cm x 10 cm x 7.6 cm block which serves as a coolant outlet, instrument cable feedthrough, and connecting flange to the rest of the beamline. Two concentric annuli are formed from the three cylinders and run nearly the entire 61.3 cm length of the cooling tube. Coolant enters the outer annuli between the stainless steel cylinders through a single fitting welded on to the outermost tube and travels toward the target end of the assembly. At the end of

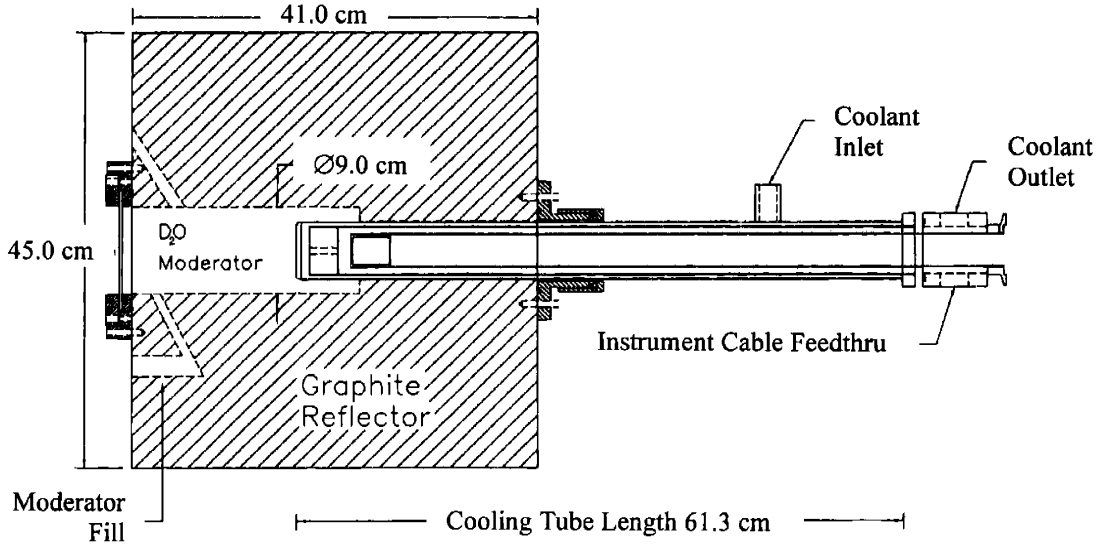

Figure 4-2. Scale drawing of the moderator/reflector with target and cooling system currently in use at the LABA facility. An all-beryllium target is cooled by a single submerged jet of heavy water which passes through two concentric annuli.

the assembly fluid is redirected and passed through a Teflon plug drilled with a 6.35 mm diameter hole to form a single jet. The end of this nozzle is located at a z/d spacing of 2 from the target surface. After exiting the nozzle coolant impinges normally on the target before traveling back down the length of the tube in the inner annulus. A closeup of the target end of the cooling line is shown in Figure 4-3, and a schematic of the target itself is pictured in Figure 4-4.

Under bombardment from an ion-beam, electrons of a few tens of eV are ejected from the surface. The number of electrons which are ejected per charged particle is dependent on the energy, charge, and incident angle of the incoming ion as well as the nature of the target material. If these electrons ultimately strike a material other than the target a false positive current is measured. Experiments conducted at LABA have found that this can vary the measured beam current by as much as 20-30%. The cup-like shape of the target is designed as a passive, geometric means of increasing the likelihood that a secondary electron would strike the tubular portion of the target before interacting with another structure. In addition to the purely geometrical means of suppressing secondary electrons, maintaining the target at a slightly higher potential than the surrounding materials can also be used to reduce the secondary electron effect. The combination of geometry and biasing is the principle behind a Faraday cup.

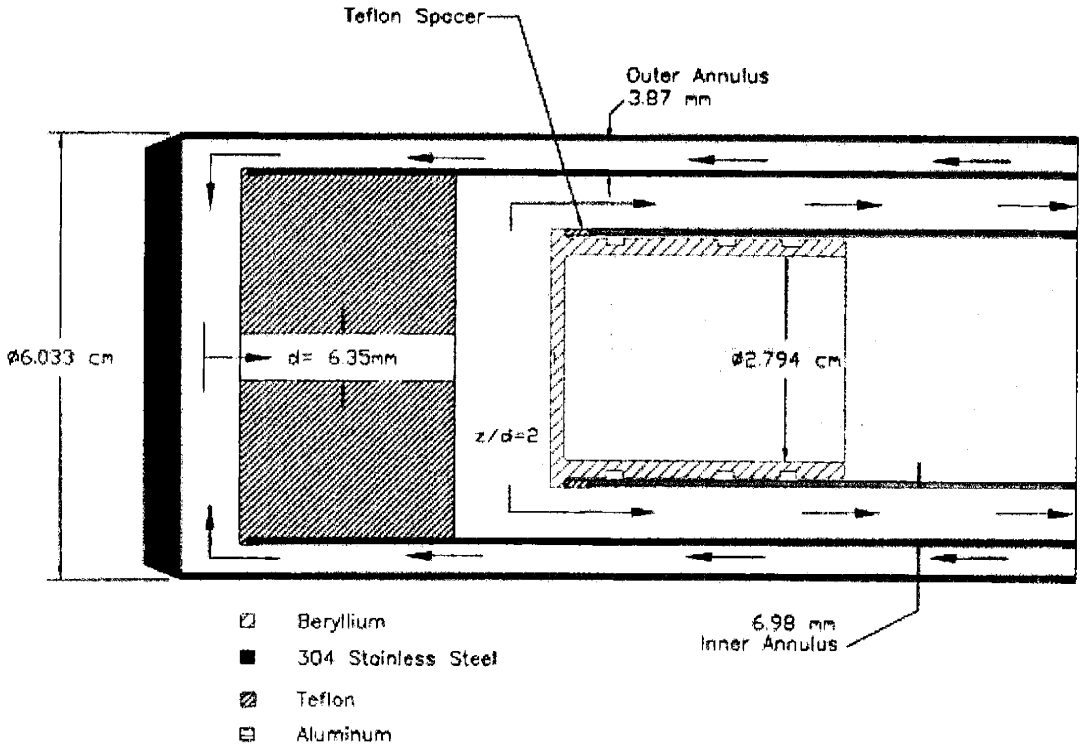

Figure 4-3. Closeup of the target-end of the cooling assembly. Coolant passes through the outer annulus, is formed into a jet by the Teflon plug, impinges on the beryllium target, and travels back in the inner annulus.

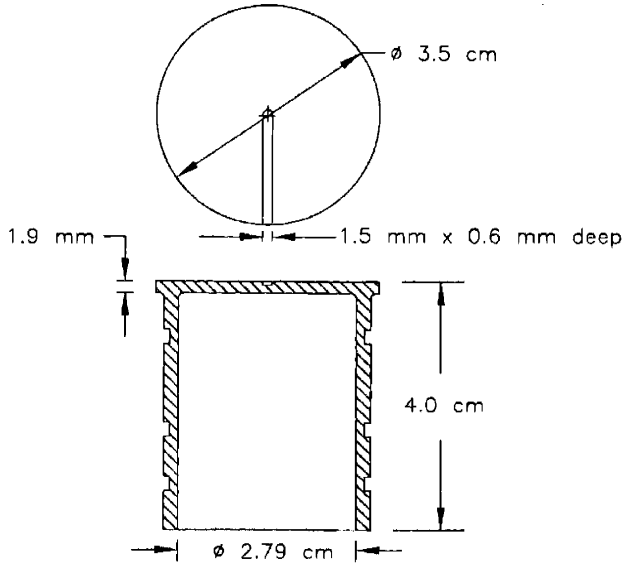

Figure 4-4. Beryllium target used in current accelerator-NCT experiments at LABA. Although the target rests on the inner aluminum beam tube, it is electrically isolated by O-rings and a Teflon spacer. Current and heat are measured from a single stainless steel thermocouple epoxied into the groove cut on the upper face.

The cup-like shape of the target is designed as a passive means of dealing with secondary electrons. Under bombardment from an ion-beam, electrons of a few tens of eV are ejected from the surface. The number of electrons which are ejected per charged particle is dependent on the energy, charge, and incident angle of the incoming ion as well as the nature of the target material. If these electrons ultimately strike a material other than the target a false positive current is measured. Experiments conducted at LABA have found that this can vary the measured beam current by as much as 20-30%. In addition to the purely geometrical means of suppressing secondary electrons, maintaining the target at a slightly higher potential than the surrounding materials can also be used to reduce the secondary electron effect. The combination of geometry and biasing is the principal behind a Faraday cup.

Accurate current measurement requires that the target is insulated from the surrounding beam tube, and in the case where gallium coolant is used, a thermally conductive yet electrically insulating layer such as diamond, beryllium oxide, or silicon carbide would be required on the cooled side of the target. Thin coatings of these materials are routinely deposited by a number of different methods. Temperature measurement is also critical for monitoring the target performance during an irradiation. During experiments at LABA, current and temperature are measured with a single thermocouple which is epoxied into the thin groove cut into the face of the target as shown in Figure 4-4. The probe has a stainless steel sheath which is insulated from the actual thermocouple wires. Temperature is monitored through the inner wires, while current is read from the sheath. The thermocouple is fixed to the innermost aluminum tube and runs the length of the cooling assembly to the point where it is extracted from the block shown in Figure 4-2.

A final note regarding the design of the target is warranted before moving to the neutronic comparisons. Although the target pictured in Figure 4-4 is not mounted to the beamline with screws or a weld, it behaves as a fixed-edge target because of its cup-like shape. Section 4.4 describes in detail the need for a simply-supported target which allows for radial expansion to alleviate the thermal stress. This is crucial for achieving high beam power, especially with beryllium-based targets. With that being said, however, a calculation of the power limit of a gallium-cooled, fixed-edge beryllium target having the diameter shown in Figure 4-4 which is irradiated with a beam having a standard deviation of 1 cm could achieve a power of $\approx$3 kW before failure. This equates to nearly 2 mA of current when using the 1.5 MeV (d,n) reaction and 750 μA using the 4.0 MeV (p,n) reaction. A hemispherical target, however, could achieve a power of 9.4 kW under the same conditions. A fixed-edge lithium target (a C15715 copper alloy

substrate is assumed) can achieve a power of 4.7 kW assuming the same heating and cooling conditions. At 2.5 MeV, this would allow 1.88 mA of current to be placed on target.

4.2 The Neutronic Effect of Using Gallium as Coolant

A detailed optimization study was conducted by Gierga[4, 6] to determine the proper moderator and reflector dimensions for a variety of neutron producing reactions. As a result of those studies, the moderator pictured in Figure 4-2 was constructed at the LABA facilities. Further Monte Carlo studies by Gierga and White[4,5] were conducted to show that a single dedicated facility could be used for both BNCS and BNCT. In terms of cost and facility requirements, the ability to use the same assembly for both types of treatments greatly enhances the capabilities of an ABNCT system. Dimensions of this new MRA were slightly different from those given in Figure 4-2. Table 4-1 lists the dimensions of the original BNCS and modified BNCS/BNCT MRA.

Table 4-1. Comparison of the dimensions of the original and modified MRA. The original assembly was constructed for use at LABA in experiments involving BNCS. The modified assembly has been shown to be useful for both BNCS and BNCT.

	Original MRA Dedicated to BNCS	Combined BNCS/BNCT Moderator
Moderator	D_2O	D_2O
Moderator Diameter	9.0 cm	20.0 cm
Max. Moderator Length	23.0 cm	30.0 cm
Reflector	Graphite	Graphite
Reflector Diameter	45.0 cm	56.0 cm
Reflector Length	41.0 cm	48.0 cm

Although the combined BNCS/BNCT moderator provides enough space for a target with a diameter of up to 6 cm, the studies of Gierga and White modeled a target and cooling system which reflected the dimensions given in Figure 4-3. This was done in order to accommodate the effect of the cooling system on the neutronics at the patient position. Both the BNCS and BNCT studies used light water as the cooling material. It is doubtful that the neutronics would vary considerably for target diameters between 3 and 6 cm. A study by Allen et. al found no

significant detrimental effects on therapy parameters when considering a proton beam which varied in size from 0 to 7.5 cm.[7]

In order to examine the neutronic effect of replacing the light water coolant with gallium, six different MCNP simulations were carried out and compared with the studies of Gierga and White. In order to make an equitable comparison, no optimization of the moderator or reflector dimensions was attempted. For each simulation using gallium as coolant, RBE values, moderator diameter, and length were held at the quantities used in the original studies. In cases where the z/d length was changed in the gallium studies the amount of D_2O between the target and patient position was not affected. This was done under the assumption that neutron moderation by the gallium was negligible.

4.2.1 Comparing Results for BNCS Simulations of a Human Knee Using ^{9}Be(d,n)

Studies of BNCS therapy on a human knee were originally presented by Gierga[4]. Figure 4-5 illustrates geometric models used in the MCNP simulations in order to determine BNCS figures of merit. For the 1.5 MeV ^{9}Be(d,n) reaction, which has a relatively hard neutron spectrum, 23 cm was determined as the optimal moderator length based on the following figures of merit: (1) therapy time (min) required to deliver a dose of 10^4 RBE-cGy to all parts of the synovium assuming 1 mA on target; (2) skin dose (RBE-cGy); (3) ratio of synovium to bone dose.

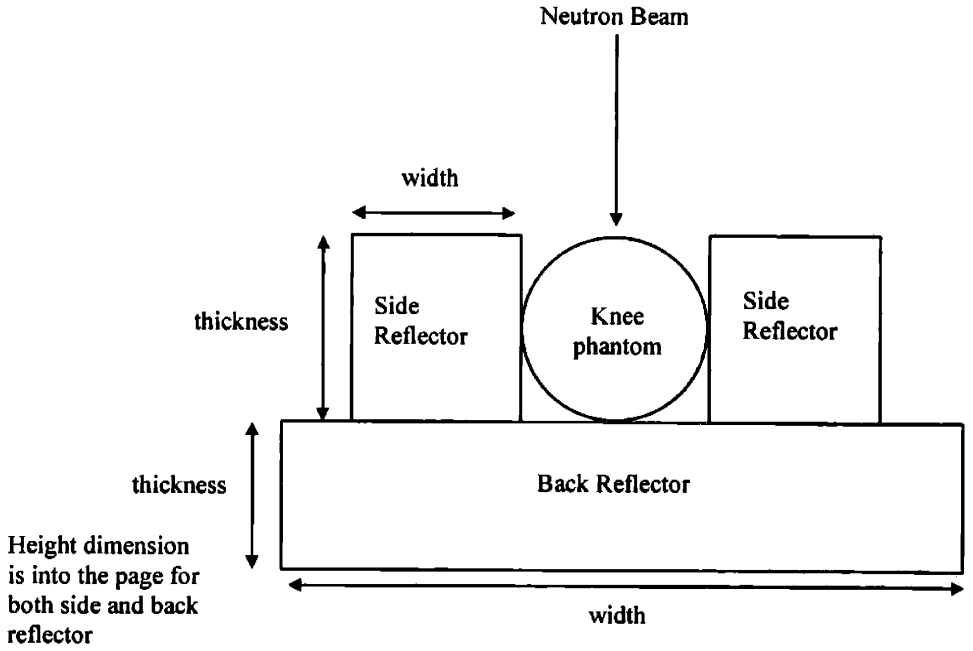

a)

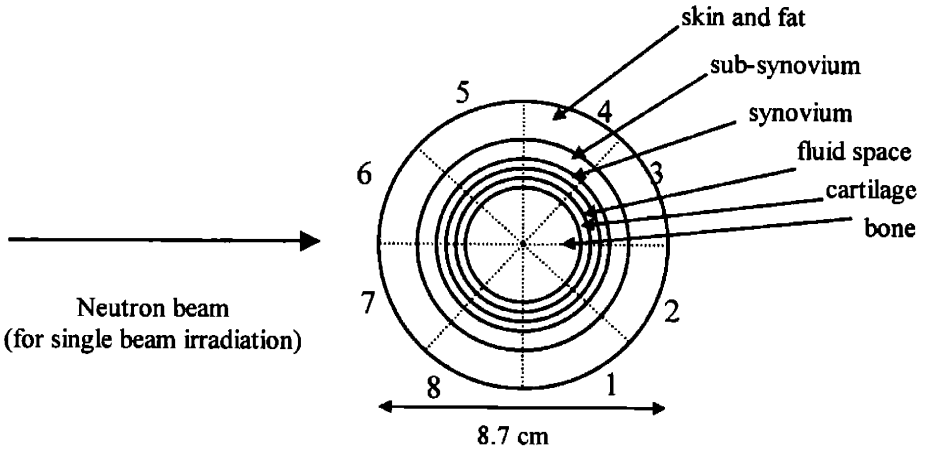

b)

Figure 4-5. Model of the a) irradiation orientation and b) tissue components of the human knee used in the MCNP studies of BNCS.

Three different MCNP studies were conducted which involved replacing the light water coolant with gallium. Figures of merit were calculated and compared to the original simulations. A summary of the changes made in each of the three different cases is listed below. Figure 4-3 should be referenced when considering the changes of dimension.

Case (1) Light water coolant replaced with gallium

Case (2) Light water coolant replaced with gallium; z/d distance increased from 2 to 6

Case (3) Light water coolant replaced with gallium; z/d distance increased from 2 to 6; stainless steel tubes changed to Delrin plastic; inner aluminum tube changed to tantalum

The rationale for changes in Cases 2 and 3 deserve brief explanations. Increasing the z/d distance from 2 to 6 results in more efficient heat transfer for a single submerged impinging jet. This is explained in more detail in §3.3. Modifications in the coolant tubes in Case 3 stem from concerns of material compatibility and activation. As described in Chapter 3, interaction with gallium causes rapid loss of mechanical strength in aluminum. Tantalum, however, is not affected by liquid gallium up to temperatures of 450 °C.[8] Tantalum also reduces the secondary radiation level produced by deuterons striking the beam tube below that of aluminum. LABA currently uses tantalum in certain locations along the beamline to reduce the secondary radiation caused by stray deuterons. Delrin plastic, which is composed of carbon, hydrogen, and oxygen, is subject to less activation than the iron, chromium, and nickel in stainless steel.

The data presented in Figure 4-6 compare the dose rates in each knee section for a single beam irradiation in the original simulation with Cases 1-3 which use gallium cooling. Because of the symmetry of the model, the single beam irradiation case can also be used to calculate parameters for multiple irradiation therapies such as a parallel opposed configuration.

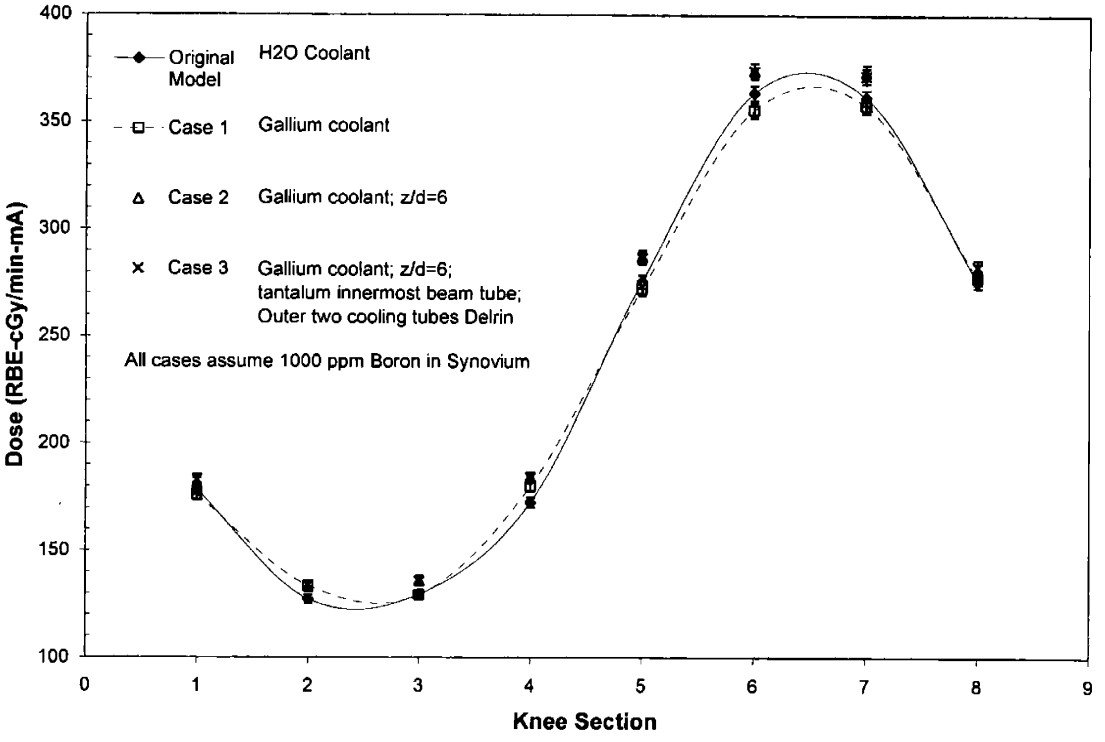

Figure 4-6. Dose rate to the synovium in various sections of the knee for a single beam BNCS therapy using the ^{9}Be(d,n) reaction with a moderator length of 23 cm. Error bars are given at a 1σ uncertainty.

In each of the three cases using gallium as the cooling fluid the majority of the data points fall within the 1σ uncertainty and all are within the 2σ. This translates to figures of merit, presented in Tables 4-2 and 4-3, which show no significant differences between a system cooled with light water and one cooled with gallium. Even in cases 2 and 3, which introduce an additional 2.54 cm of gallium between the target and knee, deleterious neutronic effects are quite small. Even though the effects are small, it should be noted that Cases 2 and 3 had shorter therapy times and higher bone ratios, albeit with higher skin doses. This is primarily due to the increased photon contribution from the n,γ reactions in the gallium. When averaged over all knee sections, the photon dose contribution to the synovium, skin, and bone increased by 10.2%, 15.0%, and 12.1%, respectively, in Case 2. These values were 10.0%, 14.3%, and 11.7% in Case 3. All other components varied by less than 5% between the original simulations and Cases 1-3.

Table 4-2. Comparison of the figures of merit for single beam irradiation of the knee using the 1.5 MeV ^{9}Be(d,n) reaction with 23 cm of moderator. A 1000 ppm boron concentration and 1 mA current are assumed.

	Original Case With H_2O Coolant	Case 1	Case 2	Case 3
Therapy Time (min)	78.6 ± 1.2	77.3 ± 1.1	75.1 ± 1.1	74.7 ± 1.1
Max. Skin Dose (RBE-cGy)	714 ± 16	726 ± 16	722 ± 16	718 ± 16
Min. Bone Ratio	31.8 ± 1.3	31.7 ± 1.2	32.0 ± 1.2	32.4 ± 1.2

Table 4-3. Comparison of the figures of merit for a parallel beam irradiation of the knee using the 1.5 MeV ^{9}Be(d,n) reaction with 23 cm of moderator. A 1000 ppm boron concentration and 1 mA current are assumed.

	Original Case With H_2O Coolant	Case 1	Case 2	Case 3
Therapy Time (min)	44.0 ± 0.4	44.6 ± 0.4	42.9 ± 0.3	42.8 ± 0.3
Max. Skin Dose (RBE-cGy)	268 ± 5	280 ± 5	279 ± 5	278 ± 5
Min. Bone Ratio	39.9 ± 1.1	39.1 ± 1.0	42.2 ± 1.0	41.7 ± 1.0

4.2.2 Comparing Results for BNCT Simulations of an Ellipsoidal-Head Phantom

The same procedures utilized in the BNCS comparisons were used to compare results of a simulated BNCT irradiation of an ellipsoidal-head phantom using both the 4.0 MeV ^{9}Be(p,n) and 2.5 MeV ^{7}Li(p,n) reactions. Details of the original simulations can be found in White.[5] The original simulations performed by White used the modified graphite/D_2O MRA, which is described at the beginning of §5.2, and considered the irradiation of an ellipsoidal head phantom pictured in Figure 4-7.[5] A 40 ppm B-10 concentration was assumed in the tumor and 7.5 ppm was assumed in the healthy tissue. An ion beam current of 1 mA was assumed in order to assign the neutron yields. The figures of merit included for comparison were the advantage depth, tumor dose rate at a depth of 4 cm, and the ratio of the fast to tumor dose rates at a depth of 1 cm. These quantities were tallied in cells located along the brain centerline as shown in Figure 4-7. Advantage depth refers to the point at which the tumor dose falls to a level corresponding to the highest dose in the healthy tissue.

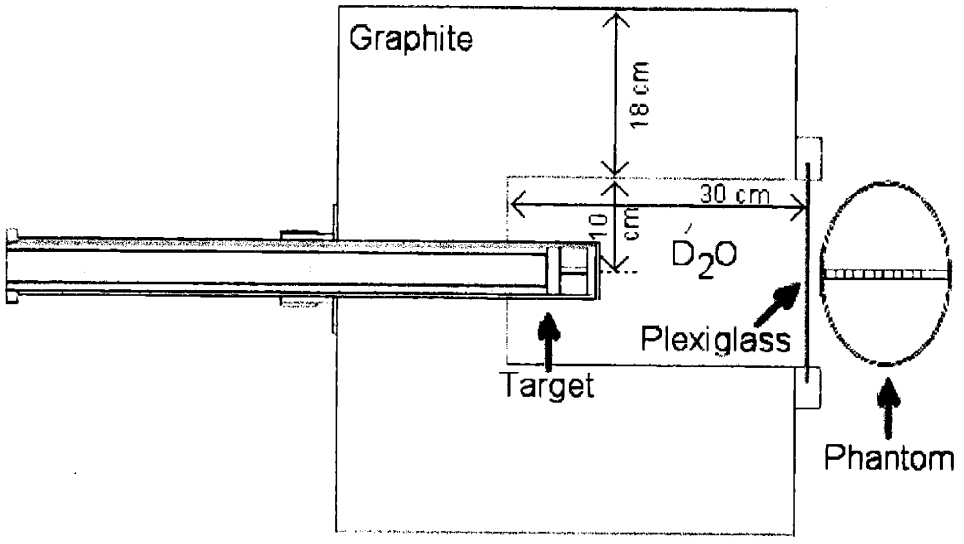

Figure 4-7. Schematic of the water-filled ellipsoidal head phantom used to compare BNCT simulations using the 4.0 MeV ^{9}Be(p,n) and 2.5 MeV ^{7}Li(p,n) reactions in a system cooled by light water and gallium.

Two simulations with gallium-cooling were conducted using the ^{9}Be(p,n) reaction for comparison to the original simulation, while a single comparison was made utilizing the ^{7}Li(p,n) reaction. The cases are numbered 4 through 6 to delineate them from the BNCS cases already mentioned.

Original ^{9}Be(p,n) Case: Moderator length 26 cm
Light water coolant
Single submerged jet at a z/d=2

Case 4: Light water coolant replaced with gallium

Case 5: Beryllium target in the shape of a hemisphere
Light water coolant replaced with gallium
4 additional jets included in Teflon
z/d spacing increased to 4

Original ^{7}Li(p,n) Case: Moderator length 21 cm
Light water coolant
Single submerged jet at a z/d=2

Case 6: Light water coolant replaced with gallium

Figures 4-8 a,b,c plot the total and individual components which make up the tumor dose rate for both the light water and gallium-cooled cases. Figures of merit for these simulations are presented in Table 4-4. All figures of merit, with the exception of the fast/tumor ratio in Case 5, fall within the 1σ uncertainty. The most noticeable differences occur for Case 5 which replaces a large portion of the Teflon plug with gallium as well as increasing the amount of gallium between the nozzle plug and the target. When components of dose rate are compared between the original case and Case 5 the largest differences occur in the fast neutron and photon components. At the surface, the gallium-cooled system photon dose is larger by 14.3% while the other components vary by less than 1.5%. At a depth of 4 cm, however, the fast neutron component of the gallium cooled case is a factor of 2.7 higher than the original while the thermal neutron and boron doses are 9.4% and 10.5% lower.

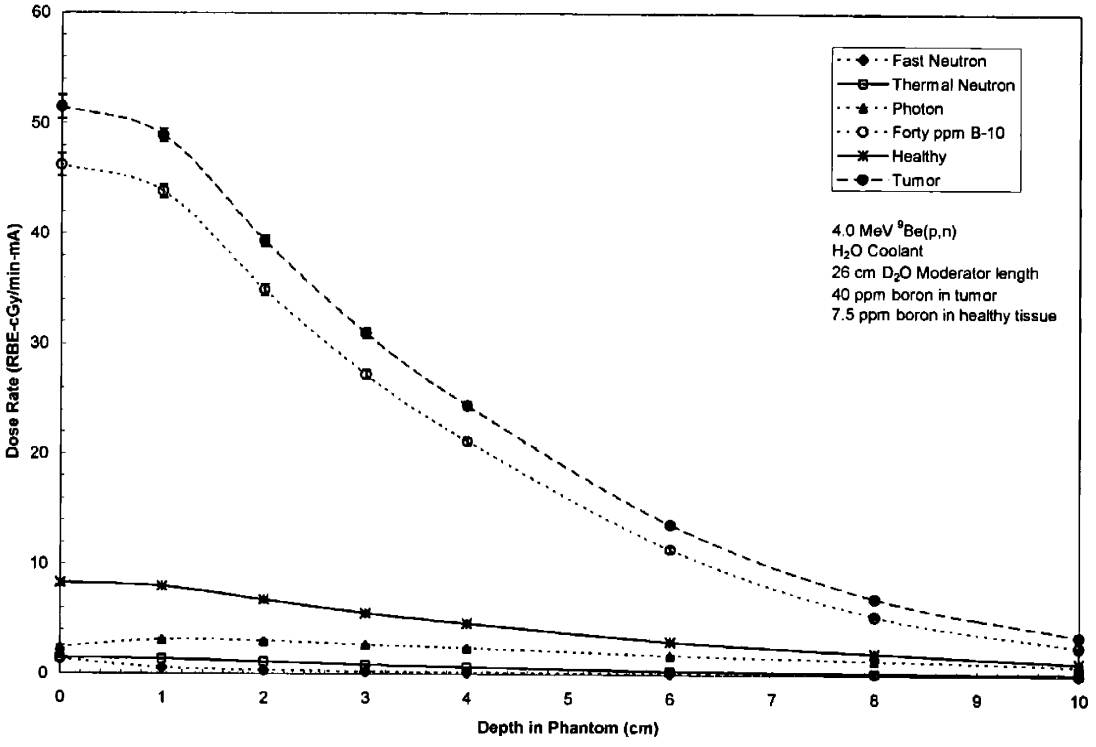

Figure 4-8 a) Original ^{9}Be(p,n) Case

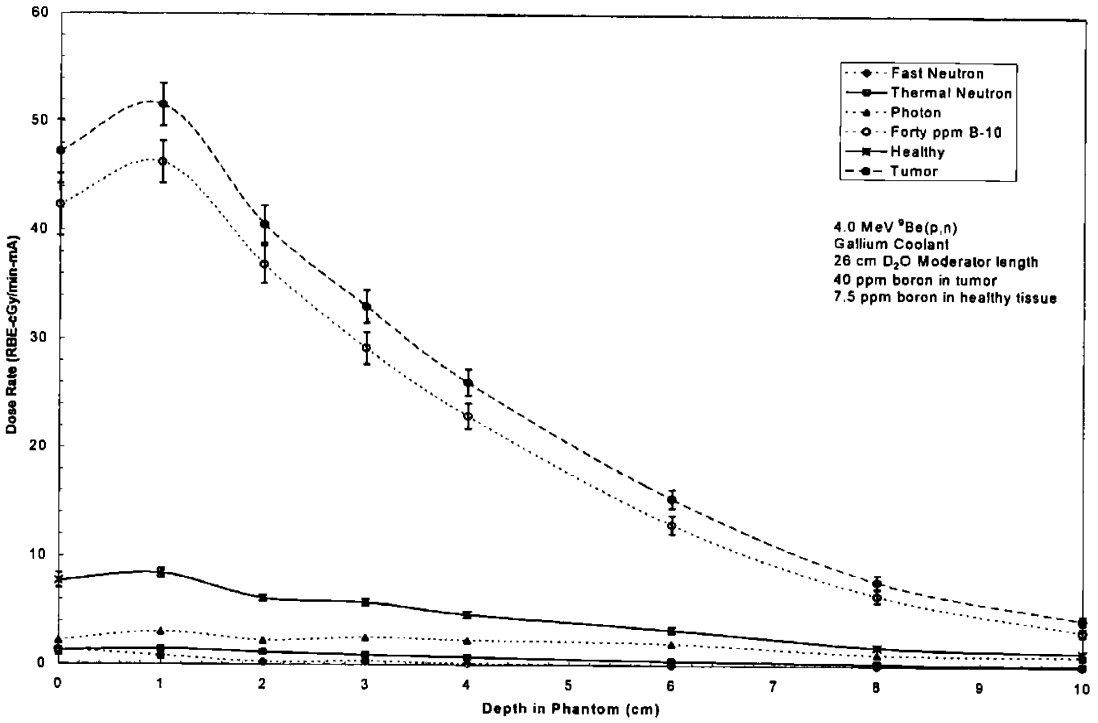

Figure 4-8 b) ^{9}Be(p,n) Case 4

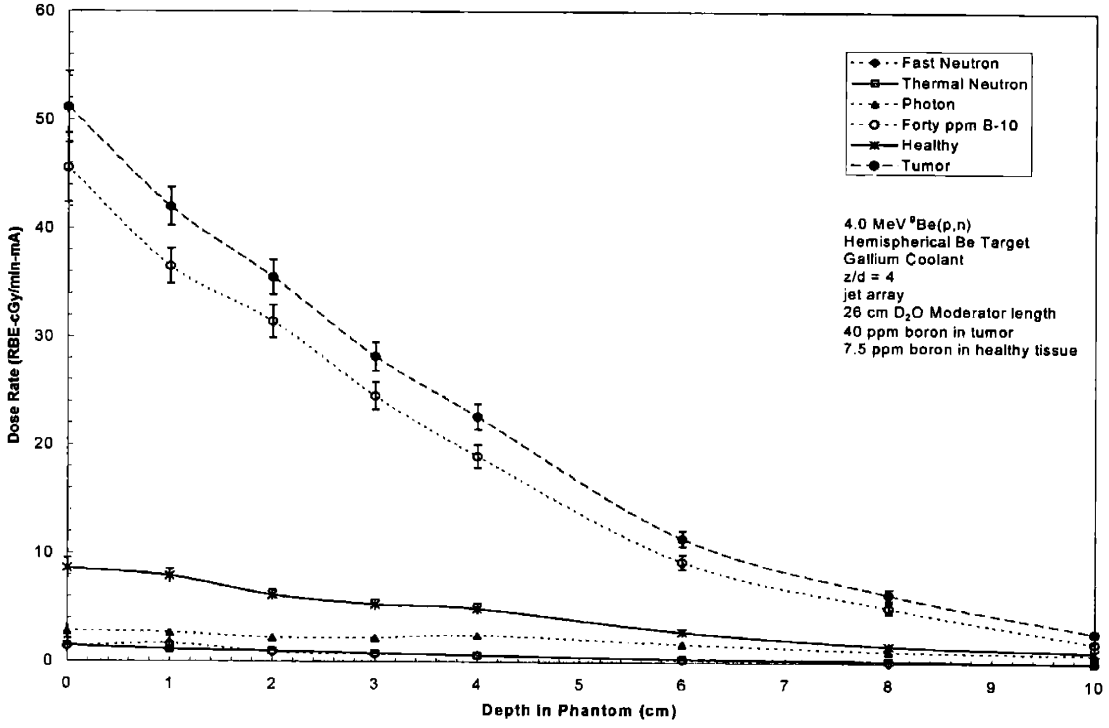

Figure 4-8. Plots at increasing depth for the various components which contribute to the overall tumor dose rate for the original ^{9}Be(p,n) case (a) and the subsequent simulations replacing the light water coolant with gallium (b) Case 4 (c) Case 5.

Table 4-4. Comparison of the figures of merit from the simulated irradiation of an ellipsoidal water-filled phantom using the 4.0 MeV $^{9}Be(p,n)$ reaction with 26 cm of D_2O moderator. A 40 ppm boron concentration and 1 mA current are assumed.

	Original $^{9}Be(p,n)$ With H_2O Coolant	Case 4	Case 5
Advantage Depth (cm)	7.5 ± 0.3	7.8 ± 0.9	6.9 ± 0.9
Tumor Dose Rate at 4 cm (RBE-cGy/min-mA)	24.4 ± 0.4	26.1 ± 1.2	22.6 ± 1.4
Ratio of Fast/Tumor Dose Rate at 1 cm	0.012 ± 0.002	0.016 ± 0.006	0.039 ± 0.014

Figures of merit relating to the lithium reaction, which has a softer neutron spectrum than the beryllium reaction, were less affected by an increase in fast neutrons. Dose rate curves for the original and gallium cooled case are given in Figures 4-9 a, b, while figures of merit are presented in Table 4-5.

Table 4-5. Comparison of the figures of merit from the simulated irradiation of an ellipsoidal water-filled phantom using the 2.5 MeV $^{7}Li(p,n)$ reaction with 21 cm of D_2O moderator. A 40 ppm boron concentration and 1 mA current are assumed.

	Original $^{7}Li(p,n)$ With H_2O Coolant	Case 6
Advantage Depth (cm)	7.7 ± 0.3	8.0 ± 0.3
Tumor Dose Rate @ 4 cm (RBE-cGy/min-mA)	39.1 ± 0.7	42.7 ± 0.8
Ratio of Fast/Tumor Dose Rate at 1 cm	0.018 ± 0.003	0.029 ± 0.002

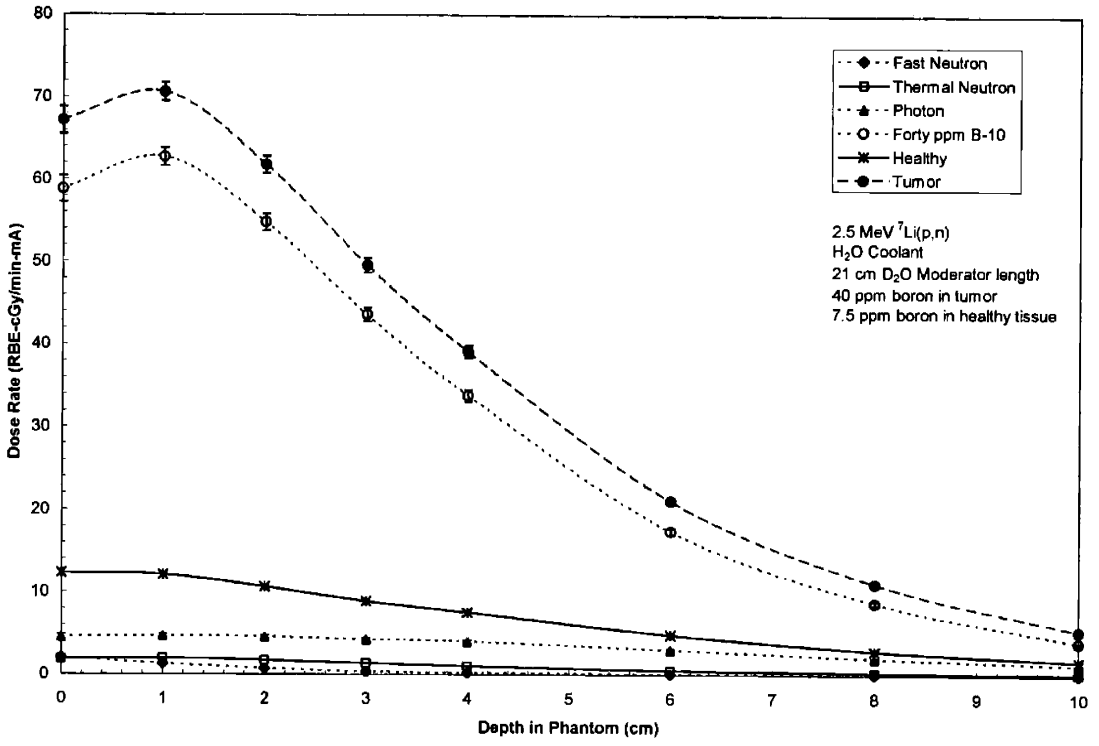

Figure 4-9 a) Original ^{7}Li(p.n) case

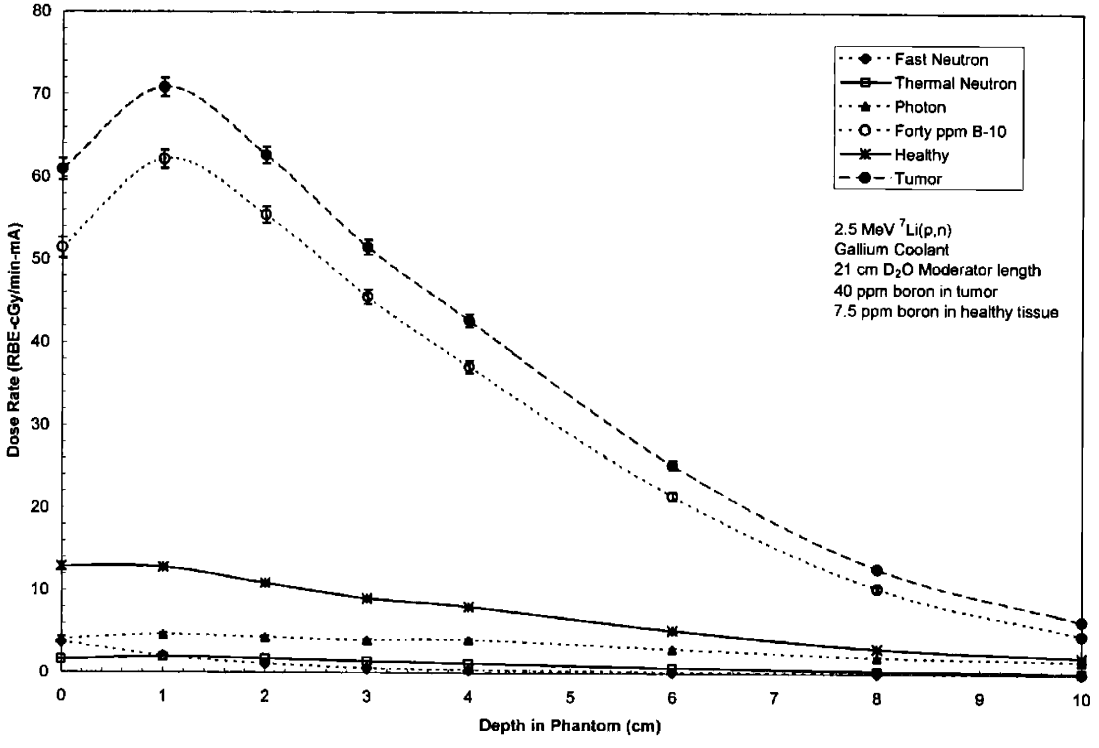

Figure 4-9. Original (a) and gallium-cooled (b) head phantom simulations using the ^{7}Li(p.n) with a moderating length of 21 cm.

At the surface the fast neutron component of the gallium cooled case increased by 86.7% over the original simulation while at a depth of 4 cm the fast neutron component is higher by only 64.9%. Thermal neutron and boron doses for the gallium-cooled case are also increased at the 4 cm depth by 9.8% over the water-cooled simulation. Because the spectrum is slightly harder at the surface, less low energy neutrons would have been lost in the moderator due to absorption.

4.2.3 Gallium Activation

Upon irradiation by neutrons, natural gallium produces two isotopes: $^{70}Ga(T_{1/2} = 21.1$ min) and $^{72}Ga(T_{1/2} = 14.1$ hr). ^{70}Ga is produced by the (n,γ) reaction with ^{69}Ga which makes up 60.1% (atom percent) of natural gallium. ^{70}Ga is primarily a β^- emitter with 98.9% of all decays leading to emission of an electron with a maximum energy of 1656 keV. Only two gammas from ^{70}Ga have intensities over 0.1%. A low energy 176.2 keV photon is emitted 0.29% of the time, and a 1039 keV photon is emitted 0.65% of the time. ^{72}Ga is produced from ^{71}Ga which makes up the remaining 39.9% of natural gallium. The decay structure of ^{72}Ga is considerably more complex than ^{70}Ga. When the energy and intensities of all β^- particles are considered, on average each decay of ^{72}Ga emits a 501.6 keV electron. Among the photons which are emitted, nine have intensities over 5%. Their energies and intensities are listed as follows: 601 keV (5.5%), 630 keV(24.8%), 834 keV (95.6%), 894 keV (9.9%), 1050 keV (6.9%), 1861 keV (5.3%), 2201 keV (25.9%), 2491 keV(7.7%), 2507 keV(12.8%).

In order to examine the activation of the gallium by the neutrons produced during a therapy, MCNP was used to tally the (n,γ) reactions in all gallium cells for cases 2, 5, and 6. These cases were chosen since they contained the greatest volume of gallium for each of the reactions used. Since the activity in gallium results from two different isotopes with different characteristic radiations and half-lives, activity is plotted as a function of irradiation time for both ^{70}Ga and ^{72}Ga in Figures 4-10 a, b, c.

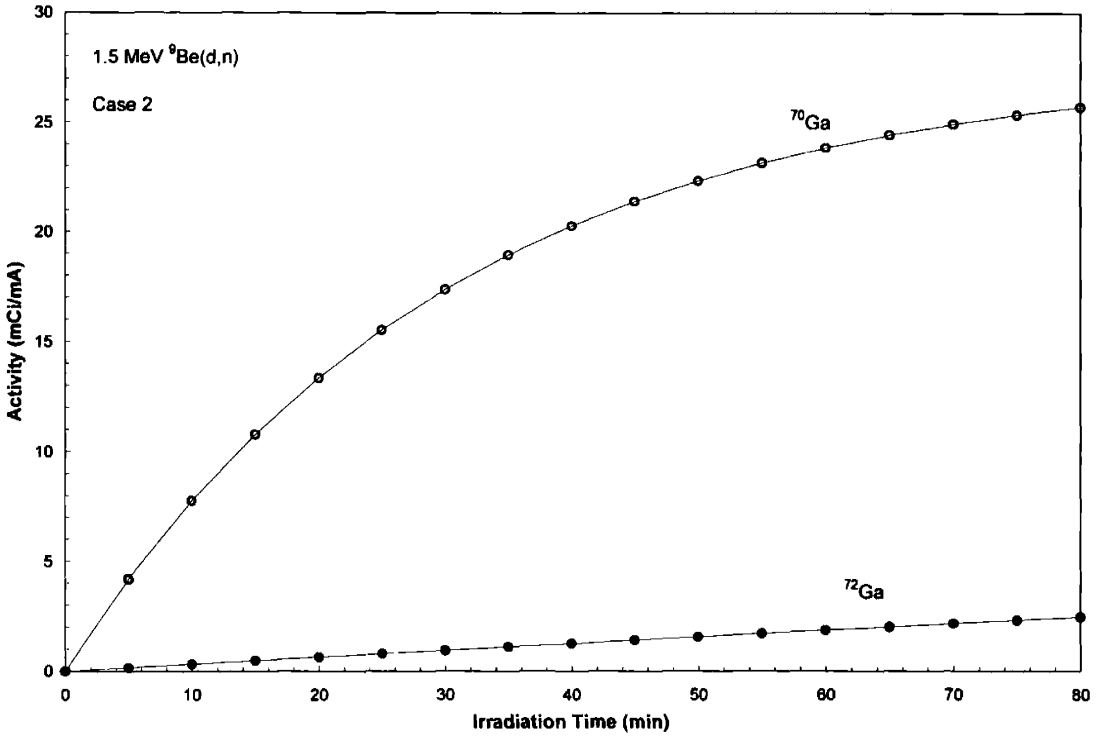
1.5 MeV ^{9}Be(d,n)
Case 2
^{70}Ga
^{72}Ga
Activity (mCi/mA)
Irradiation Time (min)
0
5
10
15
20
25
30
0
10
20
30
40
50
60
70
80

a)

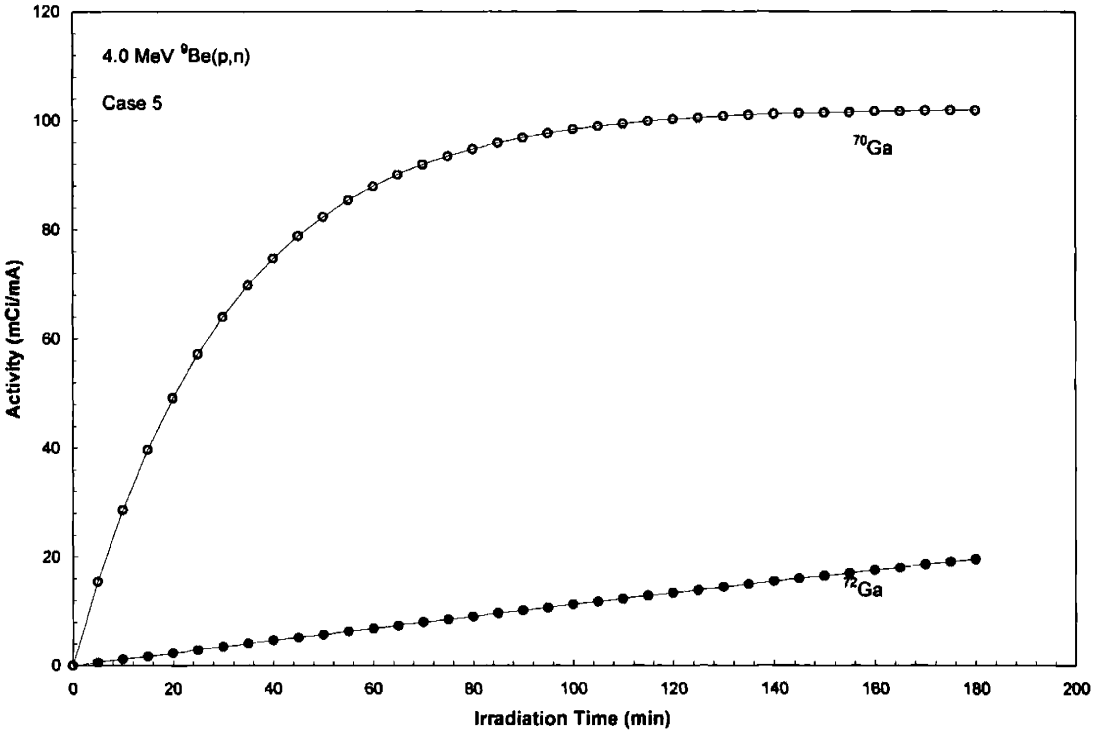
4.0 MeV ^{9}Be(p,n)
Case 5
^{70}Ga
^{72}Ga
Activity (mCi/mA)
Irradiation Time (min)
0
20
40
60
80
100
120
0
20
40
60
80
100
120
140
160
180
200

b)

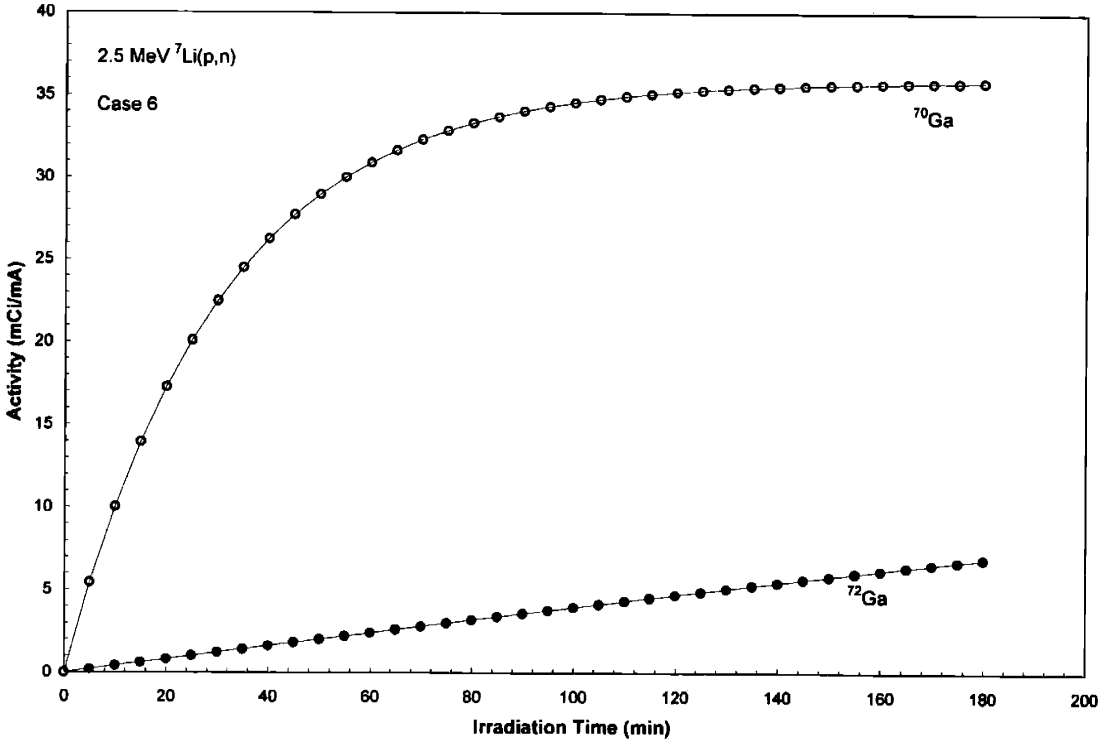

Figure 4-10. a) Gallium activation for 1 mA of beam current as a function of irradiation time using the geometry presented in Case 2. b) Gallium activation for 1 mA of beam current as a function of irradiation time using the geometry presented in Case 5. c) Gallium activation for 1 mA of beam current as a function of irradiation time using the geometry presented in Case 6.

From the levels of activity presented in these figures, it is evident that an ABNCT system cooled with gallium must consider the induced radiation in the gallium coolant especially from the standpoint of system maintenance. Fortunately, the majority of the activity comes from the β^- emissions of ^{70}Ga and would not likely affect the dose rate at the therapy position. This radiation would be of concern, however, to individuals working with the cooling system, especially for the 1-3 hours following an irradiation. For long irradiations where there is buildup of the longer-lived ^{72}Ga, it might be necessary to change out the coolant to allow for decay.

4.3 REFERENCES

1. National Institute of Standards and Technology, "NIST Center for Neutron Research," 2002.

2. J.F. Briesmeister, "MCNP - A general Monte Carlo N-Particle transport code, Version 4B," Los Alamos National Laboratory Report, LA-12625-M, 1997.

3. E. Binello, "Efficacy of Boron Neutron Capture Synovectomy in an Animal Model," Ph.D. thesis, Massachusetts Institute of Technology, 1999.

4. D.P. Gierga, "Neutron delivery for boron neutron capture synovectomy," Ph.D., Massachusetts Institute of Technology, 2001.

5. S. M. White, "Biological Dosimetry of Neutron Beams for Neutron Capture Therapies," Ph.D., Massachusetts Institute of Technology, 2001.

6. D.P. Gierga, J.C. Yanch and R.E. Shefer, "Development and construction of a neutron beamline for accelerator-based neutron capture synovectomy," Med Phys, **27:** 203-214 (2000).

7. D.A. Allen, T.D. Beynon and S. Green, "Design for an accelerator-based orthogonal epithermal neutron beam for boron neutron capture therapy," Med Phys, **26:** 71-76 (1999).

8. R.N. Lyon, "Liquid metal heat transfer coefficients," Chem. Eng. Prog., **47:** 75-79 (1951).

Chapter 5 Conclusions and Future Work

5.1 Summary of Conclusions

This thesis has investigated various aspects of high-power target design for Accelerator-Based Neutron Capture Therapy. Areas of interest presented in this work included the development of a technique which can be used to measure and map the current intensity profile for high current beams. Additionally, thermal and mechanical aspects of target design were considered using analytic calculations, numerical simulations, and experiments. The primary focus was to present an alternative to conventional water cooling by using liquid gallium metal as the working fluid. Based on the superior thermal and mechanical performance of a target cooled with gallium, comparisons of such a system against a conventional water-cooled target were investigated with Monte Carlo simulations to uncover any detrimental neutronic effects which would preclude the use as a coolant.

Chapter 2 developed a technique which allows the measurement of the current intensity profile in beams which have powers that can far exceed 100 W. This is crucial for the development of accelerator targets capable of handling high heat loads. Determination of the current density allows local values of the heat flux to be determined simply through multiplying the measured value by the beam energy. Methods currently available for beam profiling, such as helical profilers and harps, are limited to low overall beam powers of around 100 W. At energies of 1-4 MeV, this translates to beam currents of 100 μA or less. The technique developed in this chapter was used to interrogate beams having powers in excess of 350 W. In order to measure the current density, activity is induced in a target of ^{12}C or ^{11}B depending on whether deuterons or protons are being used. The former can be used with deuterons having energies of 0.7 MeV or higher, while the latter requires protons with energies greater than 3.0 MeV. MD-55-2 radiochromic film was used to measure a dose profile resulting from the emission of positrons from the activated target. This dose profile was converted to a map of current intensity by scanning the film with a desktop scanner. A calibration curve was generated which plotted the optical density measured with the scanner as a function of dose. Because of the linearity of the dose deposited in the film with the current intensity, the calibration curve allowed the conversion of the net optical density to current intensity. The resolution of this technique was investigated through the use of SRIM-2000 and Monte Carlo techniques and was found to be 0.22±0.01 mm, which is on the same order as the current beam measurement techniques which have resolutions on the order of 0.5-2 mm. This technique was used to measure current density in beams exceeding 1.4 mA/cm^2.

Chapter 3 presented various thermal and mechanical components of target design. Based on the axial deposition of heat and the concomitant production of neutrons, it was shown that the minimum temperature increases occurred in neutron producing layers which had thicknesses which did not exceed the point at which neutron production ceased. For the 4.0 MeV ^{9}Be(p,n) reaction this thickness was 110 μm. For the 2.5 MeV ^{7}Li (p,n) reaction the thickness was 85 μm. Initial small-scale tests using single jets having a diameter of 3.19 mm and a z/d of 1.75 compared the stagnation point heat transfer coefficient of gallium and water. Gallium at a velocity of 0.64 m/s generated a stagnation point heat transfer coefficient of 37544±2784 W/m^{2}K compared to an h_o of 32448±3645 W/m^{2}K from a water jet at 2.43 m/s. Numerical simulations using the K-ε RNG model were utilized to quantify the local behavior of the heat transfer coefficient. While the simulations of the water jets predicted the experimental data to within 10%, the gallium data differed by factors of over 5 as a result of the non-wetting of the target surface. By matching the experimental gallium data with simulations, the magnitude of the wetting effect was quantified. These simulations also indicated that the heat transfer from gallium could fall below that of water at large r/d values. Large-scale tests using an array of submerged jets were conducted at powers (0-11 kW) and flowrates which were representative of the levels expected in NCT. Experiments found that the average heat transfer from gallium over areas typical of accelerator targets was superior to water for Reynolds numbers greater than 13500. At a Reynolds number of 35000 gallium produced an average heat transfer coefficient of $\approx 10^5$ W/m^{2}K while water produced an $\bar{h}$ of 55000 W/m^{2}K. Nusselt number correlations were presented for both water and gallium jet arrays. For a water jet array a correlation of $\overline{Nu} = 0.032\ Re^{0.82}\ Pr^{1/3}$ was developed. The correlation for the submerged gallium jet array was $\overline{Nu} = 0.0113\beta^2_{max}Pe^{0.54}$. The spreading ratio, β_{max}, was introduced as a correlating parameter as a means of incorporating the non-wetting effect in the predicted heat transfer. Finally, thermal and mechanical stresses were examined both analytically and numerically. Target dimensions were optimized in order to maximize the amount of power which could be handled by a target without failing either as a result of thermal stress or melting. Using gallium as a coolant, disk-shaped beryllium targets achieved power levels up to 9.3 kW with water targets achieving power levels ~3 kW less. Beryllium targets failed as a result of exceeding the yield stress. Hemispherical beryllium targets having a thickness of only 400 μm achieved powers which were nearly 3 times greater than cylindrical targets. A hemispherical target cooled by gallium could safely handle a beam of up to 20.2 kW. Optimization of lithium-based targets was simplified because of the low melting point of the target material. Maintaining the temperature of the lithium below the melting

point rather than balancing stresses in the target is the primary design criterion. In order to achieve a power of 10 kW on a target composed of 85 μm lithium on a 865 μm-thick C15715 substrate and cooled by a gallium jet at 35 °C which generates a heat transfer coefficient of 10^5 W/m^2K, the power density of the beam had to be kept below 11.6 W/m^2K.

Chapter 4 presented numerical comparisons between previous BNCS and BNCT simulations using light water as the cooling fluid and simulations in which the water was replaced with gallium. Figures of merit such as therapy time, skin dose, bone ratio, advantage depth, and tumor dose rate were used to compare the two coolants. All comparisons using gallium were done with the same moderator lengths and reflector thicknesses as the water cases. For the BNCS simulations, decreases in therapy times were caused by increased photon doses resulting from the capture of neutrons in the gallium. This increased photon dose resulted in slightly higher skin doses, but never exceeded the skin reddening threshold. Comparison of the figures of merit between the two coolants for both single beam and parallel beam irradiations yielded values which were within the 2σ uncertainty level in all cases. Likewise, comparisons with previous BNCT simulations yielded figures of merit in the case of gallium coolant which were within the 2σ uncertainty level for all cases presented. In both the BNCS and BNCT comparison no significant difference was seen which would preclude the use of gallium as a coolant for neutronic reasons. Activation of the gallium was investigated by considering the (n,γ) captures tallied in the MCNP simulations. Activation in the gallium is due primarily to ^{70}Ga which is almost exclusively a β^- emitter. Of all cases considered a maximum activity level of 100 mCi/mA was calculated for a BNCT therapy using the 4.0 MeV $^9Be(p,n)$. For BNCT using the 2.5 MeV $^7Li(p,n)$ reaction and BNCS using 1.5 MeV $^9Be(d,n)$ ^{70}Ga activity levels of 35 mCi/mA and 25 mCi/mA were calculated.

5.2 Recommendations for Future Work

This work has opened up the possibility of designing accelerator-NCT targets which are capable of withstanding irradiation by high power ion beams through the use of gallium cooling. Regarding the measurement of current beam intensity profiles, the target design presented in Chapter 2 should be altered by examining a method to place very thin (1 μm) layers on a working target. This would allow the technique to be used with beams having powers considerably higher than used in this study. It would also improve the resolution by limiting the degree to which the incoming charged-particles are scattered as they travel through the target.

For submerged-gallium jets, a study investigating the local heat transfer from a single nozzle at varying z/d spacings is warranted. If the local heat transfer coefficients were realized,

corrections could be made to the numerical simulations which would allow the thorough investigation of target design through the use of the ADINA package. Further experiments are needed to investigate the nature of the non-wetting effect on the heat transfer of gallium jets. An empirical relation is needed which specifically relates to submerged-jets. It is likely that the non-wetting effect is dependent not only on the jet velocity but also on r/d. Investigation of the heat transfer and wetting effect at jet Reynolds numbers in excess of 40000 would illustrate whether the improvement of using gallium compared to water continues to increase at higher jet velocities or whether the non-wetting effect reaches a constant value.